

DISS. ETH Nr. 16366

EXTRACTING PHYSICS FROM WEAK SIGNALS  
IN LATTICE GAUGE THEORY

A dissertation submitted to the  
SWISS FEDERAL INSTITUTE OF TECHNOLOGY ZURICH

for the degree of  
DOCTOR OF NATURAL SCIENCES

presented by

SLAVO KRATOCHVILA

Dipl. Phys. ETH

born February 8<sup>th</sup>, 1976

citizen of Winterthur (ZH), Pratteln (BL)

accepted on the recommendation of  
Prof. Dr. Matthias Troyer, examiner  
Dr. Philippe de Forcrand, co-examiner

2005



# Abstract

Recent relativistic particle collider experiments at very high energies are probing a new phase of matter. This so-called quark-gluon plasma contains quarks and gluons, just as ordinary matter does. However, while in ordinary matter the quarks are confined by the strong interaction, in the quark-gluon plasma, the quarks are deconfined. We use Lattice Quantum Chromodynamics (Lattice QCD), which provides a regularisation of QCD, the theory of the strong interaction, on a discrete, hypercubic lattice in Euclidean space-time without any assumption on the strong coupling. In this framework, non-perturbative phenomena, such as confinement and its disappearance through the phase transition above, can be computed by Monte Carlo simulations from first principles.

This thesis mainly deals with the following two physical problems: (i) the phenomenon of string breaking in the context of 3-dimensional  $SU(2)$  Lattice Gauge Theory, by measuring the groundstate energy of a gluonic system with two static adjoint colour-charges; (ii) the thermodynamics of Lattice QCD at finite temperature and matter density, by studying the canonical ensemble rather than the more commonly used grand-canonical ensemble. Both projects have in common that standard numerical methods fail to reveal relevant information, because the signal is drowned into noise before reaching the physically interesting distance/energy scale. In other words, we have to deal with “weak signals”. Techniques that provide a substantial variance reduction are thus needed. We improve state-of-the-art methods for variance reduction and develop a new canonical approach to QCD.

String breaking, ie. the creation of a matter-antimatter pair from the energy stored in the flux tube between two static colour-charges, has been observed in older studies, however, a controversial multichannel technique has been used. Here, we show this “string breaking”-effect in an uncontroversial way by considering the Wilson

loop observable only, which we show to have a non-vanishing overlap with both the unbroken and the broken string state. This task is numerically challenging, because the signal to be observed is of order  $\mathcal{O}(10^{-40})$ , while a single measurement is of order  $\mathcal{O}(1)$ . An efficient variance reduction is needed if we want to avoid the unfeasible number of  $10^{80}$  measurements. We take the Lüscher-Weisz variance reduction technique as a starting point. This method focuses on the correlation of Polyakov loops and provides an error reduction exponential in their length by averaging temporal link-link correlators. We generalise this technique to adjoint Wilson loops by introducing an additional error reduction on the spatial transporters. We succeed in measuring the energy of the groundstate, first- and second excited state as a function of the spatial separation  $R$  up to  $R \sim 1.2\text{fm}$ . We find that in our model, string breaking occurs at  $R \sim 1.0\text{fm}$ .

Lattice QCD at finite temperature  $T$  and finite chemical potential  $\mu$  lacks algorithms to study thermodynamic systems with  $\frac{\mu}{T} \gtrsim 1$ . The difficulty is caused by the “sign problem”, which is absent at  $\mu = 0$ , but gains strength with increasing  $\mu$ . We present a new approach to Lattice QCD thermodynamics, where we focus on the matter density  $\rho$  rather than the chemical potential. We provide a variance reduction by calculating the Fourier coefficients of the fermion determinant on each configuration. This makes the approach numerically expensive so that we can only study small lattices due to limited computer budget. However, in our particular case of QCD with four flavours of staggered quarks with mass  $\frac{m}{T} = 0.2$ , the regime  $\frac{T}{T_c} \gtrsim 0.8$  and  $\frac{\mu}{T} \lesssim 2$  becomes accessible on a  $6^3 \times 4$  lattice. We determine the Helmholtz free energy, from which all thermodynamic properties of QCD follow. In particular, we locate the phase transition between ordinary matter and the quark gluon plasma in the  $T$ - $\rho$  as well as  $T$ - $\mu$  plane. In contrast to the literature, we observe a “bending down” of the critical line at  $\frac{\mu}{T} \gtrsim 1.3$ . We argue that this bending must happen, if the critical line is to reach expectations from a strong coupling analysis at zero temperature.

# Zusammenfassung

Kürzlich wurde mit Hilfe relativistischer Teilchenbeschleuniger ein neuer Zustand der Materie bei sehr hohen Energien entdeckt. Dieses sogenannte Quark-Gluonen-Plasma setzt sich, wie unsere Umwelt, aus Quarks und Gluonen zusammen. Im Gegensatz zu normaler Materie ist jedoch im Plasma das Confinement der Quarks aufgehoben. Wir benutzen Lattice Quantum Chromodynamics (Lattice QCD) um QCD, die Theorie der starken Wechselwirkung, welche für das Confinement verantwortlich ist, zu regularisieren. Diese Regularisierung wird erreicht, indem die Kontinuumstheorie auf einem hyper-kubischen Euklidischen Raumzeit-Gitter diskretisiert wird, ohne eine Annahme über die Stärke der starken Wechselwirkung zu machen. Dadurch ermöglicht Lattice QCD mit Hilfe von Monte Carlo Simulationen das Studium nicht-perturbativer Phänomene, wie dem Confinement und Phasenübergängen, direkt mittels der QCD Lagrange-Dichte.

Diese Dissertation befasst sich hauptsächlich mit den folgenden zwei physikalischen Problemen: Wir studieren (i) das Phänomen “string breaking” im Rahmen drei-dimensionaler  $SU(2)$  Gitter-Eichtheorie, indem wir die Grundzustands-Energie eines gluonischen Systems mit zwei statischen adjungierten Farb-Ladungen messen; (ii) die Thermodynamik von Lattice QCD bei endlicher Temperatur und Teilchendichte, indem wir, anstatt wie gewöhnlich das grosskanonische, das kanonische Ensemble untersuchen. Es ist beiden Projekten gemeinsam, dass herkömmliche numerische Methoden unzureichend sind, um relevante Informationen zu sammeln. Das Signal verschwindet im Rauschen bevor physikalisch interessante Distanz- oder Energie-Skalen erreicht wurden. Mit anderen Worten, wir haben ”schwache Signale” aufzulösen. Wir verbessern Algorithmen zur Varianz-Reduktion, welche auf dem neuesten Stand der Technik sind, und entwickeln für QCD einen neuen kanonischen Ansatz.

“String breaking”, d.h. die Bildung eines Materie-Antimaterie Paares aus der Energie, welche im String zwischen zwei statischen Farb-Ladungen gespeichert ist, wurde vor einigen Jahren durch Gitter-Eichtheorie-Simulationen beobachtet. Allerdings wurde bis anhin ein umstrittener Ansatz, die Multi-Kanal-Technik, verwendet. Wir werden diesen “String-breaking”-Effekt auf eine unumstrittene Art und Weise demonstrieren, indem wir nur “Wilson loops” betrachten. Wir zeigen, dass der “Wilson loop” einen nicht-verschwindenden Überlapp mit dem Zustand des gebrochenen, wie jenem des ungebrochenen Strings hat. Diese Aufgabe ist aus numerischer Sicht eine Herausforderung, da das zu betrachtende Signal der Grössenordnung  $\mathcal{O}(10^{-40})$ , eine einzelne Messung hingegen der Ordnung  $\mathcal{O}(1)$  ist. Will man die unrealistische Anzahl von  $10^{80}$  Messungen vermeiden, muss eine effiziente Methode zur Reduktion der Varianz angewendet werden. Wir starten mit dem Algorithmus von Lüscher-Weisz, welcher auf die Messung von “Polyakov loop”-Korrelationen spezialisiert ist. Der Fehler wird hierbei exponentiell in der Länge des “Polyakov loop” verkleinert, indem man über temporale Link-Link Korrelatoren mittelt. Wir verallgemeinern diese Methode, so dass sie auch für adjungierte Wilson loops verwendet werden kann. Wir erreichen dies, indem wir eine zusätzliche Fehler-Reduzierung für die räumlichen Komponenten entwickeln. Dieser Weg ist von Erfolg gekrönt: Wir können die Energie des Grundzustandes, wie auch jene des ersten und zweiten angeregten Zustandes, als Funktion der räumlichen Distanz  $R$  der beiden Ladungen bis  $R \sim 1.2\text{fm}$ , messen. Der String bricht in unserem Modell bei der Länge  $R \sim 1.0\text{fm}$  auseinander.

Es fehlen Algorithmen, um die Thermodynamik der Lattice QCD bei endlicher Temperatur  $T$  und bei endlichem chemischen Potential  $\mu$  für Systeme mit  $\frac{\mu}{T} \gtrsim 1$  zu simulieren. Die Schwierigkeit wird vom “sign problem” verursacht, welches bei  $\mu = 0$  nicht auftaucht, allerdings mit grösserem  $\mu$  stärker wird. Wir präsentieren einen neuen Ansatz, indem wir die Teilchendichte  $\rho$ , anstatt das chemische Potential betrachten. Die Methode reduziert die Varianz, indem sie die Fourier-Koeffizienten

der fermionischen Determinante für jede einzelne Konfiguration berechnet. Dadurch wir sie numerisch sehr kostspielig, und aufgrund unserer beschränkten Computer-Ressourcen konzentrieren wir uns auf die Untersuchung kleinerer Systeme. Konkret betrachten wir QCD mit vier Arten von Kogut-Susskind Fermionen der Masse  $\frac{m}{T} = 0.2$  auf einem Gitter der Grösse  $6^3 \times 4$ . Wir können dieses System im Bereich  $\frac{T}{T_c} \gtrsim 0.8$  und  $\frac{\mu}{T} \lesssim 2$  studieren. Wir bestimmen die Helmholtz Freie Energie, von welcher die gesamte Thermodynamik der QCD abgeleitet werden kann. Beispielsweise lokalisieren wir den Phasenübergang von der gewöhnlichen Materie zum Quark-Gluonen-Plasma, sowohl als Funktion von  $T$  und  $\rho$ , wie auch als Funktion von  $T$  und  $\mu$ . Im Gegensatz zur Literatur sehen wir, dass diese Phasenlinie, bei  $\frac{\mu}{T} \gtrsim 1.3$  startend, rasch in  $T$  abfällt. Wir denken, dass dieser Effekt eintreten muss, um konsistent mit Erwartungen von “strong coupling”-Rechnungen bei  $T = 0$  zu sein.





# Contents

<b>Abstract</b>	<b>i</b>
<b>Zusammenfassung</b>	<b>iii</b>
<b>1 Introduction</b>	<b>1</b>
1.1 Formulation of QCD on the Lattice . . . . .	4
1.1.1 QCD Lagrangian and its Symmetries . . . . .	5
1.1.2 Gauge Fields on the Lattice . . . . .	9
Haar Measure . . . . .	11
1.1.3 Fermion Fields on the Lattice . . . . .	12
Naive Discretisation . . . . .	12
Wilson Fermions . . . . .	16
Kogut-Susskind Fermions . . . . .	17
Fermion field measure . . . . .	18
1.1.4 Continuum Limit . . . . .	21
1.1.5 Temperature and Chemical Potential . . . . .	23
1.2 QCD Thermodynamics . . . . .	28
1.2.1 $Z_{N_c}$ Centre Symmetry . . . . .	30
1.2.2 Partition Functions . . . . .	33
1.2.3 QCD Phase Diagram . . . . .	36
1.3 Outlook for the following Chapters . . . . .	41

<b>2</b>	<b>String Breaking</b>	<b>45</b>
2.1	Motivation . . . . .	45
2.2	Static potential . . . . .	47
2.3	The three approaches . . . . .	50
2.4	Technical details . . . . .	53
2.4.1	Adjoint smearing . . . . .	54
2.4.2	Exponential error reduction . . . . .	55
	Multihit-method . . . . .	56
	Multilevel-method . . . . .	57
	Improved spatial transporter . . . . .	60
2.4.3	Diagonalisation procedure . . . . .	61
2.4.4	Gluelumps . . . . .	62
2.4.5	Multichannel Ansatz . . . . .	66
2.4.6	Polyakov loops . . . . .	66
2.5	Results . . . . .	67
2.5.1	Wilson loops only . . . . .	68
	Static potential . . . . .	69
	Excited states . . . . .	73
2.5.2	Gluelumps . . . . .	75
2.5.3	Multichannel Ansatz . . . . .	76
	Static potential . . . . .	77
	Excited states . . . . .	78
2.5.4	Polyakov loops . . . . .	80
2.5.5	Casimir scaling . . . . .	80
2.6	Conclusions - String Breaking . . . . .	82
<b>3</b>	<b>QCD Toy Model</b>	<b>85</b>
3.1	Motivation . . . . .	85
3.2	The Model: 0-dim Quantum Field Theory . . . . .	87

3.2.1	Sign Problem . . . . .	87
3.2.2	Overlap Problem . . . . .	88
3.3	Methods and Results . . . . .	89
3.3.1	Brute-Force Method . . . . .	89
3.3.2	Factorisation Method . . . . .	90
	Sign problem . . . . .	94
	Overlap problem . . . . .	95
3.3.3	Contour Integral . . . . .	96
	Discussion: $t_0$ . . . . .	97
	Discussion: $y_0$ . . . . .	98
3.4	Conclusions - QCD Toy Model . . . . .	100
<b>4</b>	<b>Canonical Approach to Lattice QCD</b>	<b>103</b>
4.1	Motivation . . . . .	103
4.1.1	State of the Art . . . . .	104
4.1.2	Scope of this project . . . . .	108
4.2	Models . . . . .	111
4.2.1	Hadron Resonance Gas . . . . .	112
4.2.2	Quark-Gluon Gas . . . . .	114
4.3	The Two Methods . . . . .	116
4.3.1	Fourier Transformation . . . . .	116
4.3.2	Zero Baryon Number . . . . .	117
4.3.3	Non-Zero Baryon Number . . . . .	119
4.3.4	Baryon density versus chemical potential . . . . .	126
4.4	Results - Zero Baryon Number . . . . .	128
4.4.1	Polyakov Loop in the Canonical Ensemble . . . . .	129
4.4.2	Confinement-Deconfinement Transition . . . . .	131
4.4.3	The Free Energy $F(T, \mu_I)$ . . . . .	133
4.5	Results - Non-Zero Baryon Number . . . . .	138

4.5.1	The Free Energy $F(T, \mu)$ and $F(T, B)$ . . . . .	140
4.5.2	$\frac{F(T, B) - F(T, B-1)}{3T} = \frac{\mu(B)}{T}$ . . . . .	148
4.5.3	Maxwell Construction . . . . .	151
4.5.4	Phase Diagrams . . . . .	152
4.5.5	Chiral Condensate . . . . .	155
4.5.6	Latent Heat . . . . .	158
4.5.7	Interface Tension . . . . .	160
4.6	Conclusions - Canonical Approach to Lattice QCD . . . . .	161
<b>5</b>	<b>3-state Potts Model</b> . . . . .	<b>165</b>
5.1	Motivation . . . . .	165
5.2	Method . . . . .	167
5.3	Real Chemical Potential . . . . .	169
5.4	Imaginary vs Real Chemical Potential . . . . .	172
5.5	Canonical Ensemble . . . . .	173
5.6	Conclusions - 3-state Potts Model . . . . .	174
<b>6</b>	<b>Outlook</b> . . . . .	<b>177</b>
<b>A</b>	<b><math>r_I</math> and the free scalar propagator</b> . . . . .	<b>185</b>
<b>B</b>	<b>Error analysis</b> . . . . .	<b>187</b>
B.1	Binned Jackknife Error Estimation . . . . .	187
B.2	Example: Statistical Error Estimate in the Reweighting Procedure . . . . .	189
<b>C</b>	<b>Stochastic Estimator</b> . . . . .	<b>191</b>
<b>D</b>	<b>Ferrenberg-Swendsen reweighting</b> . . . . .	<b>192</b>
D.1	The Self-Consistency Equation . . . . .	193
D.1.1	Gauge action . . . . .	194
D.1.2	Fermion determinant . . . . .	194

D.2	Autocorrelation-Time . . . . .	195
D.3	Reweighting to Arbitrary Coupling . . . . .	196
D.4	Zero Baryon Density . . . . .	197
D.5	Canonical Partition Functions . . . . .	198
D.6	Canonical Observables . . . . .	199
	<b>Bibliography</b>	<b>201</b>
	<b>List of Tables</b>	<b>212</b>
	<b>List of Figures</b>	<b>223</b>
	<b>Acknowledgments</b>	<b>225</b>
	<b>Curriculum vitae</b>	<b>227</b>



# Chapter 1

## Introduction

Today's knowledge about the elementary constituents of matter and the interaction between them is summarised in a model called "The Standard Model", see Fig. 1.1. Matter consists of 12 fundamental fermions - 6 leptons (electron, muon, tau and the corresponding neutrinos) and 6 quarks (up, down, strange, charm, bottom and top). The forces between these particles are mediated by bosons. The electromagnetic force involves a massless "photon" that is either absorbed or emitted by any particle with non-zero electric charge.

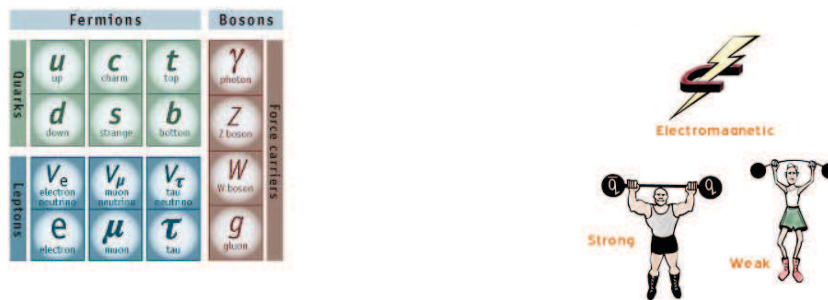


Figure 1.1: The fundamental particles in the standard model (left). The four interactions in nature are the gravity, the electromagnetic force, the weak force and the strong force. Note that gravity is not part of the standard model (right, taken from <http://particleadventure.org/particleadventure>).

The massive bosons  $Z^0$ ,  $W^+$  and  $W^-$  are assigned to the weak interaction and interact with themselves. The  $W$  bosons also couple to the photon due to their electromagnetic charge. The strong force is mediated by eight “gluons”. Each gluon is characterised by a colour and an anti-colour charge. They couple to the quarks, but also to each other. In our world, there are three colours. Unlike the coupling in the electromagnetic or the weak force, the strong coupling is, well, strong, which makes this interaction very complicated. We will discuss this in more detail below.

The quantum field theory Quantum Electrodynamics (QED) had enormous success in describing the electromagnetic interactions. This theory has the structure of an Abelian  $U(1)$  gauge theory, ie. a theory that allows for a local  $U(1)$  symmetry transformation<sup>1</sup>. The corresponding bosonic gauge field is the electromagnetic field, from which the photon (“gauge boson”) emerges. This success has been a great motivation to extend the notion of a gauge field to the other interactions, such as the strong force. The resulting theory is called Quantum Chromodynamics (QCD) - a Non-Abelian<sup>2</sup>  $SU(3)$  gauge theory that couples the six species (called “flavours”) of quarks to the eight gauge bosons via the colour charge. The world of QCD is tremendously rich and fascinating, but more difficult to deal with than QED, which can be solved using perturbative methods. This well-known mathematical tool depends on the existence of a small expansion parameter, usually the coupling constant. In QCD, the strong coupling constant  $\alpha_s$  is small only in the limit of very high energy ( $\gg 1$  GeV) - a fact which is known as asymptotic freedom. However, the typical scale of phenomenological interest is of order of the size of a nucleon, which is

---

<sup>1</sup>A reminder: the QED Lagrangian, which describes the physics of the electromagnetic interaction, is invariant under the local transformation of the matter field  $\Psi(x) \rightarrow e^{i\phi(x)}\Psi(x)$  and of the bosonic gauge field  $A_\mu(x) \rightarrow e^{i\phi(x)}A_\mu(x)e^{-i\phi(x)}$ .

<sup>2</sup>Non-Abelian physics is completely different from Abelian physics: the force is short-range rather than long-range; and the gauge bosons self-interact, which is not the case for photons. In the following part of the introduction, we generalise our notation to  $N_c$  colours unless otherwise specified.



about one Fermi or 200 MeV. In this low-energy regime,  $\alpha_s$  is large and perturbative methods fail. As a consequence an alternative, non-perturbative approach has to be used. Many non-perturbative phenomena in QCD have still to be understood, foremost among them is colour confinement: the dynamics of the gluon sector of QCD contrives to eliminate asymptotic quark states and other states with a non-trivial colour charge from the spectrum. Indeed, all the strongly-interacting particles observed so far are colour-neutral and can be viewed as bound states of quarks and gluons.

Kenneth G. Wilson[1] transcribes gauge theories *without any assumption on the coupling constant* (this is how we define “non-perturbative”) on a four-dimensional hypercubic lattice rather than in continuous space-time. The lattice sites are separated by a distance called “lattice spacing”  $a$ . First, this formulation provides a regularisation of the ultraviolet (and infrared, if any) divergences and second, preserves the “holy grail” of gauge theories, namely the local gauge invariance, *exactly*. Within this framework, non-perturbative calculations can be carried out, for example by numerical simulations (“Monte Carlo simulations”). However, in order to recover the continuum field theory, two limits have to be taken one after the other: the volume  $V \rightarrow \infty$  (“thermodynamic limit”, since space-time is infinite), then the lattice spacing  $a \rightarrow 0$  (“continuum limit”, to remove the cut-off). Renormalised physical quantities will show a finite, well behaved limit, thus QCD can be studied non-perturbatively.

In the following part of the introduction, we show how QCD can be formulated on the lattice in an exactly gauge-invariant way, and we discuss the notions of temperature and chemical potential. Subsequently, we will present the conjectured phase diagram of QCD. Finally, having established these preliminaries, we motivate the projects and give an outlook for the chapters in this thesis.

## 1.1 Formulation of QCD on the Lattice

A suitable starting point for our discussion about the formulation of QCD on the lattice, called “Lattice QCD”, is the path integral formulation of a quantum field theory given by the Lagrangian  $\mathcal{L}$  with the field  $\phi$  *in continuous Euclidean space*, where real time  $t$  has been analytically continued to imaginary time  $x_4 = it$  (“Wick rotation”). The functional integral  $Z$ , often also referred to as “partition function”, is given in this framework by the path integral over all possible field configurations  $[D\phi]$

$$Z = \int [D\phi] e^{-\frac{1}{\hbar} \int dx_4 \int d^3\vec{x} \mathcal{L}(\phi, \partial_\mu \phi)} . \quad (1.1)$$

We define the “action”

$$S(\phi, \partial_\mu \phi) \equiv \int dx_4 \int d^3\vec{x} \mathcal{L}(\phi, \partial_\mu \phi) , \quad (1.2)$$

which is real in general. Note that this is of crucial importance: Monte Carlo simulations, the tool we are using in this thesis exclusively, require  $e^{-\frac{1}{\hbar} S(\phi, \partial_\mu \phi)}$  to be real and positive, since this factor is interpreted as a probability! We write the “expectation values” of a functional  $\hat{O}(\phi)$  of the fields  $\phi$  as

$$\langle \hat{O}(\phi) \rangle = \frac{1}{Z} \int [D\phi] \hat{O}(\phi) e^{-\frac{1}{\hbar} S(\phi, \partial_\mu \phi)} . \quad (1.3)$$

One question arises about the Euclidean domain: is it physical? Time-independent quantities, like the spectrum of the theory have a well defined meaning: the Eigenstates of the Hamiltonian are damped exponentially with imaginary time instead of oscillating with real time. On a more axiomatic level, the Osterwalder-Schrader reflection positivity condition[2] ensures the reconstruction of Minkowski Green functions via analytical continuation from Euclidean Green functions. On the lattice, strict constraints on the form of the discretised action are imposed. M. Lüscher[3] has shown that for Lattice QCD, discretised in the usual way, reflection positivity holds.

### 1.1.1 QCD Lagrangian and its Symmetries

We specify the (continuum) Lagrangian of QCD and discuss its two main symmetries<sup>3</sup>: the local “gauge symmetry” and the global “chiral symmetry”. This is of prime importance since the discretisation of the theory (Euclidean space  $\rightarrow$  hypercubic lattice, continuum Lagrangian  $\rightarrow$  discretised Lagrangian) may break symmetries explicitly. Wilson had the intuition to promote local gauge invariance, rather than for example Lorentz invariance, to something unbreakable when discretising the theory.

The local gauge invariance of the Lagrangian is fundamental and defines the gauge theory as such. The motivation to discuss the global symmetry is more diversified. On the one hand, the transcription of the fermion fields to the lattice raises technical problems and may break global symmetries explicitly. On the other hand, we will study QCD at finite temperature and finite density, introduced in subsection 1.1.5: a phase transition, which might occur if we vary the temperature, often is related to a different realisation of a global symmetry of the Lagrangian; an observable, which transforms not trivially under the symmetry, thus operates as an order parameter. Furthermore, once the relevant degrees of freedom are identified, effective theories, which are more easily solvable, help to predict the order of the phase transition.

---

<sup>3</sup>We will not discuss Lorentz invariance in detail. A remnant of this symmetry is present “on the lattice”, namely the rotations of the cubic group and the translations by  $a$ . This is sufficient for its restoration when taking the continuum limit.

The Euclidean Lagrange density of QCD is

$$\mathcal{L}(A, \bar{\Psi}, \Psi) = \frac{1}{4} F_{\mu\nu}^a F_{\mu\nu}^a + \sum_{\text{flavour } f} \bar{\Psi}_f (\not{D} + m_f) \Psi_f \quad (1.4)$$

with

$F_{\mu\nu}^a = \partial_\mu A_\nu^a - \partial_\nu A_\mu^a + ig f_{bc}^a A_\mu^b A_\nu^c$  : Field-strength tensor.

$\not{D} = \gamma^\mu (\partial_\mu + ig A_\mu^a \lambda_a)$  : Dirac operator.

$\Psi_\mu^{f,c}$  : Quark field.

$A_\mu^a$  : Gluon field.

$c$  : Colour index (“fundamental”),  $1, \dots, N_c$ .

$a$  : Colour index (“adjoint”),  $1, \dots, N_c^2 - 1$ .

$f$  : Flavour index,  $1, \dots, N_f$ .

$\mu$  : Dirac index,  $1, \dots, 4$ .

$g$  : Bare coupling.

$m_f$  : Bare quark mass.

$\gamma^\mu$  : Dirac’s Gamma matrices ( $\gamma^4 = i\gamma^0$ ).

$\lambda_a$  : Generators of the Lie Group  $SU(N_c)$ .

$f_{bc}^a$  : Structure constant:  $[\lambda_b, \lambda_c] \equiv if_{bc}^a \lambda_a$ .

(1.5)

In our world, the number of colours is  $N_c = 3$ . Thus, the colour indices  $a = 1, \dots, 8$ , the generators  $\lambda_a$  are the Gell-Mann matrices and  $f_{12}^3 = 2, f_{45}^8 = f_{67}^8 = \sqrt{3}, f_{14}^7 = f_{16}^5 = f_{24}^6 = f_{25}^7 = f_{34}^5 = f_{37}^6 = 1$  and zero otherwise. The number of quark flavours is  $N_f = 6$ . However, at the scale of a few hundred MeV, the dynamics of QCD is completely dominated by the three lightest quarks, namely “up” ( $m_u=1.5-4$  MeV) and “down” ( $m_d=4-8$  MeV) and “strange” ( $m_s=80-130$  MeV).

The Lagrangian is invariant under the local gauge transformation

$$\Psi(x) \rightarrow \Omega(x)\Psi(x) \quad (1.6)$$

$$A_\mu(x) \rightarrow \Omega(x)A_\mu(x)\Omega^{-1}(x) - \frac{i}{g}\Omega(x)\partial_\mu\Omega^{-1}(x) \quad (1.7)$$

where  $\Omega(x) \in SU(N_c)$ , while the gluons fields are elements of the corresponding algebra  $A_\mu(x) = A_\mu^a \lambda_a \in su(N_c)$ . On the lattice, this fundamental symmetry will be preserved *exactly*.

For the massless classical theory, a global  $U_V(N_f) \times U_A(N_f) = SU_V(N_f) \times SU_A(N_f) \times U_V(1) \times U_A(1)$  flavour symmetry is realised. The  $U_V(1)$  symmetry

$$\Psi \rightarrow e^{i\theta}\Psi, \quad \bar{\Psi} \rightarrow \bar{\Psi}e^{-i\theta} \quad (1.8)$$

provides the baryon number (or rather quark number) conservation via the conserved current

$$J^\mu = \bar{\Psi}\gamma^\mu\Psi \quad (1.9)$$

and will be discussed later, see subsection 1.1.5. Due to quantum corrections (the notorious ‘‘triangle’’-anomaly[4]) the axial  $U(1)_A$  symmetry ( $\Psi \rightarrow e^{i\gamma^5\theta}\Psi$ , with  $\gamma^5 \equiv -\gamma^1\gamma^2\gamma^3\gamma^4$ ,  $\{\gamma^5, \gamma^\mu\} = 0$ ) is broken. We thus will discuss just the symmetry group  $SU_V(N_f) \times SU_A(N_f)$  in more detail. The Lagrangian with *degenerate* quark masses is invariant under the global vector transformation

$$\Psi \rightarrow e^{iT^a\theta_a}\Psi, \quad \bar{\Psi} \rightarrow \bar{\Psi}e^{-iT^a\theta_a}, \quad (1.10)$$

where  $\Psi = (\Psi^1, \dots, \Psi^{N_f})$ , each  $\Psi^f = \Psi_{\text{Dirac } \mu}^{\text{flavour } f, \text{colour } c}$ , and  $T^a$  are the generators of the  $SU(N_f)$  Lie group. The conserved current is

$$V_\mu^a = \bar{\Psi}\gamma_\mu T^a\Psi. \quad (1.11)$$

This vector symmetry  $SU_V(N_f)$  is called flavour symmetry. In addition, the *massless* Lagrangian is also invariant under the global axial-vector transformation, which is

given by

$$\Psi \rightarrow e^{i\gamma_5 T^a \theta_a} \Psi, \quad \bar{\Psi} \rightarrow \bar{\Psi} e^{i\gamma_5 T^a \theta_a}, \quad (1.12)$$

and the corresponding conserved current is

$$A_\mu^a = \bar{\Psi} \gamma_\mu \gamma_5 T^a \Psi. \quad (1.13)$$

This  $SU_V(N_f) \times SU_A(N_f)$ -symmetry of the massless Lagrangian is called the chiral symmetry, and we say that

$$\gamma_5 \Psi_R = +\Psi_R : \quad \Psi_R \text{ has right-handed chirality} \quad (1.14)$$

$$\gamma_5 \Psi_L = -\Psi_L : \quad \Psi_L \text{ has left-handed chirality,} \quad (1.15)$$

$$\text{with } \Psi_{R/L} = \frac{1}{2} (1 \pm \gamma_5) \Psi. \quad (1.16)$$

In order to refer to the chiral basis  $(\Psi_R, \Psi_L)$ , one often writes  $SU_R(N_f) \times SU_L(N_f)$  rather than  $SU_V(N_f) \times SU_A(N_f)$ .

This chiral symmetry can be spontaneously broken to  $SU_V(N_f)$ . As a consequence, a non-vanishing ‘‘chiral condensate  $\bar{\Psi}\Psi$ ’’ has formed: the vacuum expectation value

$$\langle 0 | \bar{\Psi}\Psi | 0 \rangle = \langle 0 | \bar{\Psi}_R \Psi_L + \bar{\Psi}_L \Psi_R | 0 \rangle \quad (1.17)$$

does not transform trivially under  $SU_A(N_f)$ , and thus is zero if the  $SU_A(N_f)$ -symmetry is realised in the vacuum, but non-zero if broken:

$$\bar{\Psi}\Psi \xrightarrow{SU_V(N_f)} \bar{\Psi}\Psi \quad (\text{‘‘trivial’’}) \quad (1.18)$$

$$\bar{\Psi}\Psi \xrightarrow{SU_A(N_f)} \bar{\Psi} e^{2i\gamma_5 T^a \theta_a} \Psi \quad (\text{‘‘non-trivial’’}) \quad (1.19)$$

Therefore, the chiral condensate is an order parameter. The spontaneous breaking gives rise to  $N_f^2 - 1$  massless Goldstone bosons, identified with the pions.

Let us take the real world as an example. The ‘‘up’’ and ‘‘down’’ quarks are approximately massless and have an *approximate*  $SU_V(2) \times SU_A(2)$  chiral symmetry. By the spontaneous breaking of the axial-vector symmetry, three Goldstone bosons are

created:  $\pi^0, \pi^\pm$ . However, due to Eq.(1.18), we know that a mass term explicitly breaks the chiral symmetry. Since the quarks are not exactly massless, the  $\pi$ -meson acquires a mass of about 135 MeV, which is small compared to the nucleon mass ( $\sim 1$  GeV). This smallness of the pion mass (often called a quasi-Goldstone or pseudo-Goldstone boson) is the motivation for an expansion about the massless limit, called chiral perturbation theory[5].

### 1.1.2 Gauge Fields on the Lattice

We proceed as follows. In this subsection, we discretise the gauge field part of the QCD Lagrangian, ie. QCD without quarks, and discuss its symmetries *on the lattice*. We then define the path integral measure of the gauge fields, which completes the construction of the partition function of this “Yang-Mills theory”, also called “pure gauge theory”. In the next subsection, we discretise the fermion field part of the QCD Lagrangian and discuss the (possible) breaking of symmetries; this is followed by the definition of the fermionic path integral measure. We then discuss in detail the notion of the continuum limit, and close this section by defining the concepts of “temperature” and “chemical potential” on the lattice.

In order to start the construction of Wilson’s formulation of Lattice QCD, we introduce the four-dimensional hypercubic lattice  $\Lambda$  with lattice spacing  $a$  as

$$\Lambda = \{x = (x_1, x_2, x_3, x_4) \mid 1 \leq n_\mu = \frac{x_\mu}{a} \leq N_\mu, N_\mu \in \mathbb{N}\} . \quad (1.20)$$

The elements  $x$  are called sites, and a link  $l = \{x; \mu\}$  describes the line, which connects two neighbouring sites. The “plaquette” is the elementary square  $p = \{x; \mu, \nu\}$  on a lattice, which is bounded by four links, see Fig. 1.2. Local gauge invariance has to be implemented exactly, as required by Wilson. He thus put the gauge field on the links by assigning a “phase factor” to a given link  $l$

$$U_\mu(x) = \mathcal{P}e^{ig \int_x^{x+\hat{\mu}a} dx' A_\mu^a(x')\lambda_a} \approx e^{igaA_\mu^a(x+\frac{a}{2}\hat{\mu})\lambda_a} \in SU(N_c) . \quad (1.21)$$

$\mathcal{P}$  denotes the path ordering, which can be defined by dividing the path into  $N$  segments  $(x_n, x_{n+\Delta n})$  of size  $\Delta n = \frac{\hat{\mu}a}{N}$ , with  $n = 0, \dots, N-1$  and taking the ordered product,

$$U_\mu(x) = \lim_{N \rightarrow \infty} e^{-ig \int_{x_{N-1}}^{x+\hat{\mu}a} dx' A_\mu^a(x') \lambda_a} e^{-ig \int_{x_{N-2}}^{x_{N-1}} dx' A_\mu^a(x') \lambda_a} \dots e^{-ig \int_x^{x_1} dx' A_\mu^a(x') \lambda_a} . \quad (1.22)$$

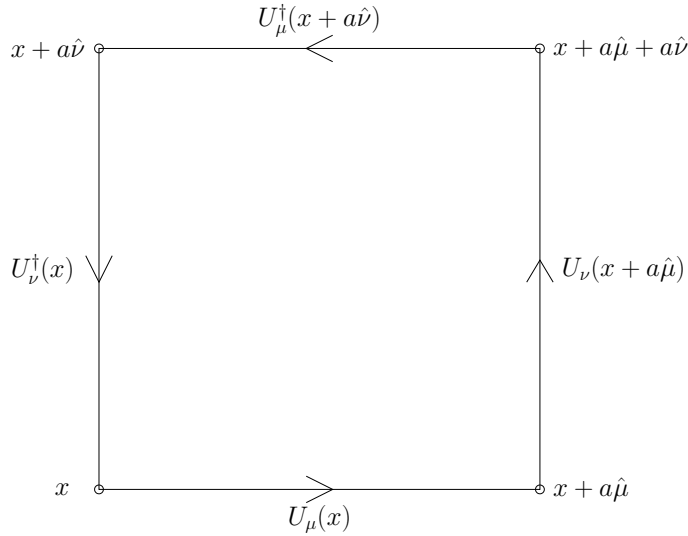


Figure 1.2: A plaquette and its contour.

The “plaquette variable” is the phase factor of the transporter around a plaquette  $p$

$$U(\partial p) = U_\nu^\dagger(x) U_\mu^\dagger(x + a\hat{\nu}) U_\nu(x + a\hat{\mu}) U_\mu(x) , \quad (1.23)$$

and usually called “plaquette” as well. Based on this simple object, we can show the two most crucial requirements in constructing a lattice formulation of the pure gauge theory:

- local gauge invariance. We can build an object  $\text{Tr } U(\partial p)$ , commonly also called “plaquette”, which is exactly gauge invariant under the lattice gauge transformation

$$U_\mu(x) \rightarrow \Omega(x + a\hat{\mu}) U_\mu(x) \Omega^{-1}(x) , \quad \Omega(x) \in SU(N_c) \quad (1.24)$$



By an expansion in  $a$

$$\begin{aligned} & 1 + i g a A_\mu(x) + \mathcal{O}(a^2) \\ & \rightarrow 1 + i g a [\Omega(x + a\hat{\mu}) A_\mu(x) \Omega^{-1}(x)] + a \Omega(x + a\hat{\mu}) \partial_\mu \Omega^{-1}(x) + \mathcal{O}(a^2) \end{aligned} \quad (1.25)$$

we can recover the continuum expression for  $a \rightarrow 0$

$$A_\mu(x) \rightarrow \Omega(x) A_\mu(x) \Omega^{-1}(x) - \frac{i}{g} \Omega(x) \partial_\mu \Omega^{-1}(x) \quad (1.26)$$

- correct continuum limit. Based on this gauge invariant object, we can construct a lattice action, which recovers the correct Yang-Mills action in the naive continuum limit  $a \rightarrow 0$

$$S_g[U] = \beta \sum_p \left[ 1 - \frac{1}{2N_c} (\text{Tr } U(\partial p) + \text{Tr } U^\dagger(\partial p)) \right] \xrightarrow{a \rightarrow 0} \int d^4x \frac{1}{4} F_{\mu\nu}^a F_{\mu\nu}^a + \mathcal{O}(a^2) \quad (1.27)$$

by identifying  $\beta = \frac{2N_c}{g^2}$ .

## Haar Measure

The quantum expectation value of an observable functional of the fields  $\hat{O}(U)$  is obtained by averaging its value over all field configurations  $\{U\}$  with a “sampling weight”<sup>4</sup> proportional to  $e^{-S_g[U]}$

$$\langle \hat{O}(U) \rangle = \frac{1}{Z} \int [DU] \hat{O}(U) e^{-S_g[U]}, \quad (1.28)$$

where the partition function  $Z$  is given by

$$Z = \int [DU] e^{-S_g[U]}. \quad (1.29)$$

Link by link, the integrals involved in the construction of  $Z$  are ordinary integrals  $[DU] = \prod_l dU_l$ . We require the measure  $dU_l$  to preserve local gauge invariance and

---

<sup>4</sup>We use the term “sampling weight” in order to refer to Monte Carlo simulations.

to be normalised

$$\text{normalisation} \quad \int dU_l \quad = 1 \quad (1.30)$$

$$\text{invariance} \quad \int dU_l f(U_l) \quad = \int dU_l f(\Omega U_l) = \int dU_l f(U_l \Omega) . \quad (1.31)$$

The measure is determined uniquely and identified as the  $SU(N_c)$  Haar measure. The local gauge invariance and the following property of group integration

$$\int dU_l U_l = 0 \quad (1.32)$$

are sufficient to ensure that only gauge invariant objects have non-zero expectation values. If we deal with pure gauge theories, such an observable has to be the trace of a closed loop of gauge links.

### 1.1.3 Fermion Fields on the Lattice

The treatment of “dynamical” fermions<sup>5</sup> is not unique, and by itself involves conceptual problems, which arise from the first-order derivative in the Dirac operator. We first present the “naive discretisation” formulation for an illustration of these difficulties. Then, we discuss other formulations. A summary of the various advantages and disadvantages can be found in Table.1.1 on page 15.

#### Naive Discretisation

The fermion part of the continuum action for *one continuum flavour* in the free case  $A_\mu(x) = 0$  is

$$S_F[\bar{\Psi}, \Psi] = \int dx_4 \int d^3\vec{x} \bar{\Psi}(\gamma^\mu \partial_\mu + m)\Psi . \quad (1.33)$$

---

<sup>5</sup>It is worth noting, what we understand under the term “dynamical”. We can measure expectation values of (external) fermion field functionals *in a vacuum, which contains gluons only*. (so-called “quenched” simulations). Real QCD, however, allows for *virtual fermion loops* in the QCD vacuum, ie. “feedback” of the quarks back to the gluons. We then speak of simulations with “dynamical” fermions.

We discretise and write the derivative  $\partial_\mu$  naively by the central difference

$$S_F^{naive} = a^4 \sum_x \bar{\Psi}(x) \sum_{\mu=1}^4 \gamma^\mu \frac{\Psi(x + a\hat{\mu}) - \Psi(x - a\hat{\mu})}{2a} + m \bar{\Psi}(x) \Psi(x), \quad (1.34)$$

which, in the chiral limit  $m \rightarrow 0$ , is invariant under the global chiral transformation

$$\Psi(x) \rightarrow e^{i\gamma^5 T^a \theta_a} \Psi(x), \quad \bar{\Psi}(x) \rightarrow \bar{\Psi}(x) e^{i\gamma^5 T^a \theta_a}. \quad (1.35)$$

Thus, the naive discretisation does not break the chiral symmetry explicitly. However, if we solve for the spectrum of the discrete Dirac operator, we find that the lowest energy states, which dominate at large distance, show a 16-fold degeneracy. As we will show now, each of these states corresponds to a Dirac particle of mass  $m$  in the continuum. In other words, although the naive discretisation is supposed to correspond to one continuum flavour, it actually describes *16 continuum flavours*, when we let  $a \rightarrow 0$ . This is known as the ‘‘doubler problem’’.

We extract the spectrum, ie. the energy Eigenvalues, by solving for the poles in the fermion field propagator.  $\mathcal{S}^{naive}(p)$ , where  $p$  is the momentum, is obtained by taking the Fourier transformation of the Dirac operator Eq.(1.34) and inverting it:

$$\mathcal{S}^{naive}(p) = \frac{1}{i\gamma^\mu \frac{\sin p_\mu a}{a} + m} = \frac{-i\gamma^\mu \frac{\sin p_\mu a}{a} + m}{\frac{\sin^2 p_\mu a}{a^2} + m^2}. \quad (1.36)$$

The 16-fold degeneracy is most easily shown for  $m = 0$ . One pole is at  $p = (0, 0, 0, 0)$ , as expected in the continuum. There are, in principle, infinitely many more poles at  $p = (n_1\pi, n_2\pi, n_3\pi, n_4\pi)$  with  $(n_1, n_2, n_3, n_4) \in \mathbb{Z}^4$ . However, due to the translation invariance of the lattice, the Brillouin zone is  $[0, \frac{2\pi}{a})$ . In addition to the continuum solution, we thus have 15 more solutions:  $p = (\frac{\pi}{a}, 0, 0, 0), (0, \frac{\pi}{a}, 0, 0), \dots, (\frac{\pi}{a}, \frac{\pi}{a}, \frac{\pi}{a}, \frac{\pi}{a})$ . Each pole corresponds to a Dirac particle, characterised via its dispersion relation. This can be illustrated nicely for a non-zero mass  $m$ . We set  $p_4 = iE$ . The denominator in Eq.(1.36)

$$\sinh^2 Ea = m^2 a^2 + \sum_{i=1}^3 \sin^2 p_i a \quad (1.37)$$

reduces in the continuum limit to the dispersion relation of Dirac particles  $E = \sqrt{m^2 + \sum_{i=1}^3 p_i^2}$  near the origin of the momentum space, but also for any of these 15 poles, for which we obtain  $E = \sqrt{m^2 + \sum_{i=1}^3 (p_i - n_i \frac{\pi}{a})^2}$ . These additional modes also contribute to the partition function and the expectation values, and thus, survive as relevant degrees of freedom in the continuum limit. In principle, this would not be a problem, if our world consisted of 16 degenerate flavours of quarks. However, we know our world consists of six quarks with very different masses: two very light quarks “up” ( $m_u=1.5-4$  MeV) and “down” ( $m_d=4-8$  MeV), a light quark “strange” ( $m_s=80-130$  MeV) and three more, but heavy quarks: “charm” ( $m_c=1150-1350$  MeV), “bottom” ( $m_b=4100-4400$  MeV) and “top” ( $m_t=174300 \pm 5100$  MeV).

We cannot simply get rid of these doublers without some sacrifice. The Nielsen-Ninomiya “No Go”-theorem[8] states rigorously, that in any local lattice theory with chiral symmetry, there exists species doubling of fermions. An escape route from to the “No Go”-theorem must violate either locality or chiral symmetry. In other words, the following properties cannot hold simultaneously:

1. The Dirac operator is local, ie. the non-vanishing contributions to the sum  $D\Psi(x) = a^4 \sum_y D(x, y)\Psi(y)$  come from the points  $y$  exponentially decaying, ie.  $|D(x, y)| \leq e^{-\gamma|x-y|/a}$ . Note that the usual discretisation schemes (Naive, Kogut-Susskind and Wilson fermions) even fulfill ultra-locality, ie. the contributions to  $D\Psi(x) = a^4 \sum_y D(x, y)\Psi(y)$  come from the points  $y$  in a finite neighbourhood of  $x$ .
2. Chiral symmetry is not violated, ie. the Dirac operator anti-commutes with  $\gamma_5$ ,  $D\gamma_5 + \gamma_5 D = 0$ .
3. There are no doublers, ie. the Dirac operator is invertible for all non-zero momenta (within the first Brillouin zone).
4. The Dirac operator actually describes Dirac particles, ie.  $\not{D}(p) = i\gamma^\mu p_\mu$  for small  $p$ .

In Table 1.1, we summarise for the most common discretisations of the Dirac operator the sacrifice. For example, naive fermions are invariant under a global vector and axial-vector transformation and the Dirac operator is ultra-local, but doublers appear.

<b>Discretisation Scheme</b>	<b>Continuum Species</b>	<b>Chiral Symmetry</b>	<b>Flavour Symmetry</b>	<b>Ultra-Locality</b>
Naive fermions	16	✓	✓	✓
Kogut-Susskind fermions	4	✓	×	✓
Wilson fermions	1	×	✓	✓
Ginsparg-Wilson fermions	1	✓ (minimal violation)	✓	×

Table 1.1: Various transcriptions of the Dirac operator and their relation to doublers, chiral symmetry, flavour symmetry and ultra-locality.

Several proposals have been made during the years to formulate fermions on the lattice. Commonly, Wilson fermions and Kogut-Susskind fermions (staggered fermions) are used, and we will briefly discuss them. A recent, third major proposal, called Ginsparg-Wilson fermions, is under intense investigation. This transcription allows for a lattice theory without doublers and the minimal violation of the chiral symmetry, as shown by P. H. Ginsparg and K. G. Wilson[9]. The sacrifice is the ultra-locality. This may not be crucial, and we argue as follows (see Ref. [10] and references therein). As long as the rate of decay in  $|D(x, y)| = |D(|x-y|)|$  for  $|x-y|$  can be shown to be proportional to the cutoff  $\frac{1}{a}$ , the sum  $D\Psi(x) = a^4 \sum_y D(x, y)\Psi(y)$  is dominated by the contributions from a bounded region around  $x$  with a fixed diameter in lattice units. It is argued that this is as good as the strict ultra-locality requirement, thus leading to the same continuum physics. Indeed, it has been shown rigorously for smooth gauge field configuration<sup>6</sup> that the Dirac opera-

<sup>6</sup>A smooth gauge field configuration refers to a configuration in which the gauge links differs

tor in the Ginsparg-Wilson formalism has exponentially decaying tails in  $D(x, y)$ , ie.  $|D(x, y)| \leq C e^{-\gamma|x-y|/a}$  with  $C, \gamma > 0$ . In practice it seems that all configurations are allowed for lattices, which are fine enough ( $\beta$  has to be large enough).

## Wilson Fermions

Wilson himself introduced a modification of the naive action in order to suppress the doublers in the continuum limit. Essentially, he added a second derivative to the action

$$S_F^{Wilson} = S_F^{naive} - \frac{r}{2} a^5 \sum_x \bar{\Psi}(x) \sum_\mu \frac{\Psi(x + \hat{\mu}) + \Psi(x - \hat{\mu}) - 2\Psi(x)}{a^2} \quad (1.38)$$

with  $r$  the Wilson parameter. The free fermion field propagator becomes

$$\mathcal{S}^{Wilson}(p) = \frac{1}{i\gamma^\mu \left( \frac{\sin p_\mu a}{a} - r \frac{1 - \cos p_\mu a}{a} \right) + m} = \frac{1}{i\gamma^\mu \left( \frac{\sin p_\mu a}{a} - 2r \frac{\sin^2(p_\mu a/2)}{a^2} \right) + m}. \quad (1.39)$$

The expansion of the denominator around  $p = (0, 0, 0, 0)$  leads to

$$\frac{1}{\mathcal{S}^{Wilson}(p)} = i\gamma^\mu p_\mu + m + \frac{ra}{2} \sum_{\nu=1}^4 p_\nu^2 + \dots \quad (1.40)$$

where the extra-term vanishes for  $a \rightarrow 0$ . If instead we expand around a specific doubler at  $p = (\pi, 0, 0, 0)$ , we obtain

$$\frac{1}{\mathcal{S}^{Wilson}(p)} = i\gamma^\mu p_\mu + m + \frac{2r}{a} + \dots \quad (1.41)$$

As we approach the continuum limit, the mass of the doubler  $m + \frac{2r}{a}$  diverges. We recover a local formulation of the Dirac operator with no doublers. However, the chiral symmetry of continuum QCD is explicitly broken on the lattice even for  $m \rightarrow 0$ . The term  $\frac{ra}{2}$  in Eq.(1.40) is manifested in the Lattice Dirac operator by an additional mass term  $\frac{ra}{2} \bar{\Psi} \Psi$ , which is not invariant under the chiral transformation Eq.(1.35):

$$\bar{\Psi} \Psi \xrightarrow{\text{chiral transformation}} \bar{\Psi} e^{2i\alpha\gamma^5} \Psi. \quad (1.42)$$

---

“little” from their neighbouring gauge links. In particular this is fulfilled by free case  $A_\mu(x) = 0$ .

### Kogut-Susskind Fermions

We now describe another formulation, where the resulting fermion fields are known as “Kogut-Susskind fermions” or “staggered fermions”. The number of doublers can be reduced by a factor four, while preserving a part of the chiral symmetry in the naive formulation, at the cost of mixing the lattice flavours[11]. In chapter 4 we will simulate dynamical fermions based on this formulation.

We substitute

$$\Psi(x) = \gamma_1^{\frac{x_1}{a}} \gamma_2^{\frac{x_2}{a}} \gamma_3^{\frac{x_3}{a}} \gamma_4^{\frac{x_4}{a}} \rho(x) , \quad (1.43)$$

for which the naive fermion action Eq.(1.34) becomes diagonal with respect to the spinor indices  $i$

$$S_F^{naive} = a^4 \sum_x \sum_{\mu=1}^4 \eta_\mu(x) \sum_{i=1}^4 \bar{\rho}_i(x) \frac{\rho_i(x + \hat{\mu}) - \rho_i(x - \hat{\mu})}{2a} , \quad (1.44)$$

with

$$\begin{aligned} \eta_1(x) &= 1 \\ \eta_2(x) &= (-1)^{\frac{x_1}{a}} \\ \eta_3(x) &= (-1)^{\frac{x_1}{a} + \frac{x_2}{a}} \\ \eta_4(x) &= (-1)^{\frac{x_1}{a} + \frac{x_2}{a} + \frac{x_3}{a}} . \end{aligned}$$

Each spinor index adds the same contribution to the action, since  $\eta_\mu(x)$  is independent of the spinor index, and therefore, the idea is to leave only one component of  $\rho_i(x)$  in order to reduce the degeneracy, ie.  $\rho_1(x) = \chi(x)$ :

$$S_F^{KS} = a^4 \sum_x \sum_{\mu=1}^4 \eta_\mu(x) \bar{\chi}(x) \frac{\chi(x + \hat{\mu}) - \chi(x - \hat{\mu})}{2a} + m \bar{\chi}(x) \chi(x) \quad (1.45)$$

We thus reduce the degeneracy by a factor four, and say, one flavour of staggered fermions corresponds to 4 degenerate flavours of continuum quarks[12]. For completeness, since we are using this formulation in chapter 4, we now turn on the gauge

field. The Kogut-Susskind action is given by

$$\begin{aligned}
S_F^{KS} &= a^4 \sum_x \sum_{\mu=1}^4 \eta_\mu(x) \bar{\chi}(x) \frac{U_\mu(x) \chi(x + \hat{\mu}) - U_\mu^\dagger(x - \hat{\mu}) \chi(x - \hat{\mu})}{2a} + m \bar{\chi}(x) \chi(x) \\
&\equiv a^4 \sum_x \sum_{x'} \bar{\Psi}(x) M^{KS}(x, x') \Psi(x')
\end{aligned} \tag{1.46}$$

with the ‘‘fermion matrix’’  $M^{KS}(x, x')$

$$\begin{aligned}
M^{KS}(x, x') &= am \delta_{x, x'} + \mathcal{D}(x, x') \\
&= am \delta_{x, x'} + \frac{1}{2} \sum_{\mu=1}^4 \eta_\mu(x) [U_\mu(x) \delta_{x, x' - \hat{\mu}} - U_\mu^\dagger(x - \hat{\mu}) \delta_{x, x' + \hat{\mu}}] .
\end{aligned} \tag{1.47}$$

We conclude our discussion of the construction of Kogut-Susskind fermion fields on the lattice by a comment about the chiral symmetry. With the substitution given in Eq.(1.43), we have obfuscated the notion of chiral symmetry

$$M \gamma_5 + \gamma_5 M = 0 \Leftrightarrow \gamma_5 M^\dagger \gamma_5 = M \text{ and } \mathcal{D} \text{ anti-hermitian.} \tag{1.48}$$

Chiral symmetry in the case of Kogut-Susskind fermions is the invariance of the Kogut-Susskind Lagrangian under the continuous  $U_A(1)$  transformation

$$\chi(x) \rightarrow e^{i\theta\epsilon(x)} \chi(x), \quad \bar{\chi}(x) \rightarrow \bar{\chi}(x) e^{i\theta\epsilon(x)}, \tag{1.49}$$

with  $\epsilon(x) = (-1)^{\sum_\mu \frac{x_\mu}{a}}$ , which plays the role of  $\gamma_5$ . Notabene,  $\epsilon(x) (M^{KS}(x, x'))^\dagger \epsilon(x') = M^{KS}(x, x')$ . The spontaneous breaking of this symmetry gives rise to one Goldstone pion.

### Fermion field measure

The complete QCD partition function with a discretised action with Kogut-Susskind fermions is given by

$$Z = \int [DU][D\bar{\chi}][D\chi] e^{-S_g[U] - S_F[U, \bar{\chi}, \chi]}, \tag{1.50}$$



where

$$\begin{aligned}
S_g[U] &= \beta \sum_p \left[ 1 - \frac{1}{2N_c} (\text{Tr } U(\partial p) + \text{Tr } U^\dagger(\partial p)) \right] \\
S_F[U] &= a^4 \sum_x \sum_{x'} \bar{\chi}(x) M^{KS}(x, x') \chi(x') .
\end{aligned} \tag{1.51}$$

We have discussed the path integral measure  $[DU]$  already in subsection 1.1.2. Here, we define  $[D\bar{\chi}][D\chi]$  and then integrate out the fermion fields analytically. This effective description of the fermion fields is the standard approach in Lattice QCD, because Grassmann variables cannot be directly simulated. The fermion field  $\chi(x)$  is represented by anti-commuting Grassmann variables  $\chi(x)\bar{\chi}(y) = -\bar{\chi}(y)\chi(x)$ . The path integral is defined as

$$[D\bar{\chi}][D\chi] \equiv \prod_x d\bar{\chi}(x) d\chi(x) , \tag{1.52}$$

with the following Grassmann integration rules:

$$\int d\chi(x) (a + b\chi(x)) = b \tag{1.53}$$

$$\int d\bar{\chi}(x) (a + b\bar{\chi}(x)) = b \tag{1.54}$$

$$\int d\bar{\chi}(x) d\chi(x) \bar{\chi}(x)\chi(x) = -1 . \tag{1.55}$$

The partition function Eq.(1.50) can be tremendously simplified to

$$Z = \int [DU] e^{-S_g[U]} \det M^{KS}(U) . \tag{1.56}$$

The determinant of the Kogut-Susskind matrix is real and positive (see below), hence appropriate for Monte Carlo simulations. However, since we have to calculate<sup>7</sup> the determinant for the large fermion matrix for *each* configuration  $\{U\}$ , the simulation of fermions is computationally expensive.

---

<sup>7</sup>In practice, the determinant is often estimated rather than calculated exactly[7].

We show the required property  $\det M^{KS}(U) > 0$  as follows. First, we order the matrix in even  $((-1)^{\sum_\mu \frac{x_\mu}{a}} = 1)$  and odd sites  $((-1)^{\sum_\mu \frac{x_\mu}{a}} = -1)$ . Then,

$$\det M^{KS}(x, x') = \det \begin{pmatrix} am\mathbb{1}_{ee} & M_{eo} \\ M_{oe} & am\mathbb{1}_{oo} \end{pmatrix} = \det \begin{pmatrix} \mathbb{1}_{ee} & 0 \\ 0 & D_{oo} \end{pmatrix}, \quad (1.57)$$

where  $M_{oe}$  ( $M_{eo}$ ) is the matrix from odd sites to even sites (even sites to odd sites) and  $D_{oo} = (am)^2\mathbb{1}_{oo} - M_{oe}M_{eo} = (am)^2\mathbb{1}_{oo} + M_{eo}^\dagger M_{eo}$ . Finally, we exploit the anti-hermiticity of the Dirac operator.  $D_{oo}$  is nothing else than the odd-sites part of

$$\begin{aligned} (M^{KS})^\dagger M^{KS} &= \begin{pmatrix} am\mathbb{1}_{ee} & M_{oe}^\dagger \\ M_{eo}^\dagger & am\mathbb{1}_{oo} \end{pmatrix} \begin{pmatrix} am\mathbb{1}_{ee} & M_{eo} \\ M_{oe} & am\mathbb{1}_{oo} \end{pmatrix} \\ &= \begin{pmatrix} (am)^2\mathbb{1}_{ee} + M_{oe}^\dagger M_{oe} & 0 \\ 0 & (am)^2\mathbb{1}_{oo} + M_{eo}^\dagger M_{eo} \end{pmatrix}. \end{aligned}$$

The eigenvalues of  $M^\dagger M$  are real and positive, which completes the proof.

It is displeasing however that one Kogut-Susskind lattice flavour corresponds to four degenerate continuum flavours. If we want to use the staggered formulation to simulate  $N_f$  degenerate continuum flavours, there is a simple, but controversial, trick[13]:

$$\det \frac{N_f}{4} M^{KS}(U) = e^{\frac{N_f}{4} \text{Tr} \log M^{KS}(U)} \quad (1.58)$$

reduces the contribution of the degenerate flavours to the action by a factor  $\frac{N_f}{4}$ , which corresponds to the contribution of  $N_f$  continuum flavours. This expression is certainly valid if  $N_f$  is a multiple of 4, e.g. we recover the determinant of the Kogut-Susskind fermion matrix  $\det M^{KS}(U)$  for  $N_f = 4$ . However, for two flavours, the expression becomes  $e^{\frac{2}{4} \text{Tr} \log M^{KS}(U)} = \sqrt{\det M^{KS}(U)}$ . Hence, this ad-hoc approach is often referred to as the ‘‘square-root trick’’. The problem is whether there exists a fermion operator  $\tilde{D}$  (matrix  $\tilde{M}$ ) with kernel

$$\tilde{D}\chi(x) = a^4 \sum_y \tilde{D}(x, y)\chi(y), \quad (1.59)$$

which satisfies  $\det \tilde{M}(U) = \sqrt{\det M^{KS}(U)}$  and *locality*. Such an operator has not yet been found. In this thesis, we will not make use of this trick, but study four degenerate flavours of continuum quarks, also called “four degenerate flavours of staggered quarks”. Note that this common terminology is slightly misleading, since we are simulating only one Kogut-Susskind lattice flavour (ie.  $N_c$  complex components per site).

### 1.1.4 Continuum Limit

An important issue has to be treated carefully: the continuum limit. We remove the ultraviolet cutoff provided by the lattice by taking the limit  $a \rightarrow 0$ . Since  $a$  is the only dimensionful quantity on the lattice<sup>8</sup>, every physical observable of mass dimension  $-d_{\hat{O}}$  will be expressed in units of the lattice spacing

$$\langle \hat{O}(U) \rangle = a^{d_{\hat{O}}} f_{\hat{O}}(\beta) \quad (1.60)$$

where  $f_{\hat{O}}$  is a *dimensionless* function of the parameters of the theory, here  $\beta$ . Without any statements about the function  $f_{\hat{O}}$ , if we naively set  $a \rightarrow 0$ , the expectation value will either be zero or infinity, except if  $d_{\hat{O}} = 0$ . In order to approach a finite value for the expectation value for a physical observable, we must require that  $f_{\hat{O}}$  goes to infinity or zero (depending on the sign of  $d_{\hat{O}}$ ). We can only vary the coupling  $\beta = \frac{2N_c}{g^2}$ , where  $g$  is the bare coupling. We can tune it such that we recover the physical results measured by experiments. This procedure is called renormalisation. A well defined continuum limit has to exist for all physical observables. Therefore, all the functions  $f_{\hat{O}}$  have to approach infinity or zero exponentially in  $-d_{\hat{O}}$  for the same  $\beta \rightarrow \beta_c$ , where  $\beta_c$  is thus called the “scaling critical point”. In the case of QCD we know the value of the scaling critical coupling due to asymptotic freedom: in the regime of small distances  $a \rightarrow 0$ , the coupling constant  $g \rightarrow g_c = 0$  or  $\beta \rightarrow \beta_c = \infty$ . Perturbation theory can be applied and provides the relation between the cut-off  $a$

---

<sup>8</sup>The coupling  $g$  is dimensionless in dimension  $d = 4$ .

and coupling constant  $g$  by solving the Callan-Symanzik equation. For QCD[6],

$$a(g) = \frac{1}{\Lambda_{QCD}} e^{-\frac{1}{2\beta_0 g^2}} (\beta_0 g^2)^{-\frac{\beta_1}{2\beta_0^2}} (1 + \mathcal{O}(g^2)) \quad (1.61)$$

$$a(\beta) = \frac{1}{\Lambda_{QCD}} e^{-\frac{\beta}{4N_c\beta_0}} \left( \frac{2N_c\beta_0}{\beta} \right)^{-\frac{\beta_1}{2\beta_0^2}} (1 + \mathcal{O}(\beta^{-1})) \quad (1.62)$$

with the constants

$$\beta_0 = \frac{1}{16\pi^2} \left[ \frac{11}{3} N_c - \frac{2}{3} N_f \right]$$

$$\beta_1 = \frac{1}{(16\pi^2)^2} \left[ \frac{34}{3} N_c^2 - \left( \frac{13}{3} N_c - \frac{1}{N_c} \right) N_f \right]$$

where  $N_f$  is the number of fermion species. To establish that the Lattice Gauge Theory indeed defines a continuum quantum theory for  $\beta \rightarrow \infty$ , the behaviour of Eq.(1.60) has to be verified. If this is found to occur, the actual dimensionless value of the physical observable (in the continuum theory)  $O$  can be expressed in terms of the dimensionful constant  $\Lambda_{QCD}$  as

$$\langle \hat{O}(U) \rangle = O \Lambda_{QCD}^{-d_{\hat{O}}} . \quad (1.63)$$

$\Lambda_{QCD}$  has to be determined, and one “fixes the scale” by measuring one expectation value on the lattice and comparing it with its physical value. A conventional way in pure gauge theory is the measurement of the string tension in the quark potential (see for a detailed discussion subsection 1.2.3 and chapter 2) and compare it with the physical value from spectroscopy of the quarkonia. In full QCD, ie. with fermions, one measures the  $\rho$ -meson mass in lattice units  $ma$ . The physical value of the  $\rho$ -meson mass is the reference observable used to fix the scale  $\Lambda_{QCD}$ . An intuitive picture of the continuum limit is the following: Approaching  $\beta \rightarrow \beta_c$  in the coupling parameter space will cause a divergence of the  $\rho$ -meson-correlation length  $\xi$  in lattice units, which is defined via  $\langle \rho^\dagger(r)\rho(0) \rangle \sim e^{-\frac{r/a}{\xi}}$ , where  $\rho^\dagger(r)\rho(0)$  describes the creation of a  $\rho$ -meson at position  $x = (0, 0, 0, 0)$  and its annihilation at position  $r = (0, 0, 0, r)$ . In other words, a second (or higher) order phase transition takes places at  $\beta_c$  in coupling space, since  $\frac{\xi}{a} \rightarrow \infty$ . Note that details of the underlying lattice action,

ie. details of the microscopic theory, do not affect the critical phenomena due to the universality property. Thus, translation invariance as well as rotational symmetry is restored in the continuum limit, because the physics becomes insensitive to the particular choice of the lattice discretisation.

### 1.1.5 Temperature and Chemical Potential

We formally can identify the Euclidean path integral Eq.(1.1) with the partition function of a three dimensional quantum statistical system. As a consequence, the sampling weight is often referred to as a “Boltzmann weight”. In thermal equilibrium at a certain temperature  $T$ , the probability for a state  $|\phi\rangle$  to occur in a quantum system is just the Boltzmann factor  $e^{-\frac{1}{T}E}$  with  $k_B = 1$ , and  $E$  has to be interpreted as the energy eigenvalue of  $|\phi\rangle$  in a quantum system given by an Hamiltonian  $\hat{H}$ . In quantum statistical mechanics, the integration over the phase space is replaced by a sum over states. The formal identity with a quantum statistical system given can be obtained by compactifying the imaginary time dimension and by periodicising the fields:

$$Z = \text{Tr}_{|\phi\rangle} e^{-\frac{1}{T}\hat{H}} = \int_{bc} [D\phi] e^{-\int_0^{\frac{1}{T}} d\tau \int d^3\vec{x} \mathcal{L}(\phi, \partial_\mu\phi)}, \quad (1.64)$$

where  $bc$  abbreviates the boundary conditions in the temporal direction, which the fields  $\phi$  have to fulfill: periodic for boson fields  $\phi(\vec{x}, \frac{1}{T}) = +\phi(\vec{x}, 0)$ , antiperiodic for fermion fields  $\phi(\vec{x}, \frac{1}{T}) = -\phi(\vec{x}, 0)$ . This follows from the path integral formalism. We show it here for bosonic degrees of freedom. We introduce the conjugate momentum  $\hat{\pi}$  with the Eigenstate  $|\pi\rangle$  and divide the imaginary time  $\frac{1}{T}$  in  $N$  elements  $\Delta\tau = \frac{1}{NT}$ .

The identity is given by  $1 = \int d\varphi_N(\vec{x})|\varphi_N\rangle\langle\varphi_N| = \int \frac{d\pi_N(\vec{x})}{2\pi}|\pi_N\rangle\langle\pi_N|$ .

$$\begin{aligned}
\int d\phi\langle\phi|e^{-\frac{1}{T}\hat{H}}|\phi\rangle &= \lim_{N\rightarrow\infty} \int d\phi\langle\phi| \left( \int \frac{d\pi_N(\vec{x})}{2\pi}|\pi_N\rangle\langle\pi_N| \right) e^{-\Delta\tau\hat{H}} \left( \int d\varphi_N(\vec{x})|\varphi_N\rangle\langle\varphi_N| \right) \cdots \\
&\quad \left( \int \frac{d\pi_1(\vec{x})}{2\pi}|\pi_1\rangle\langle\pi_1| \right) e^{-\Delta\tau\hat{H}} \left( \int d\varphi_1(\vec{x})|\varphi_1\rangle\langle\varphi_1| \right) |\phi\rangle \\
&= \lim_{N\rightarrow\infty} \int d\phi \int d\varphi_{N+1}(\vec{x})\langle\phi|\varphi_{N+1}(\vec{x})\rangle \int \prod_{k=1}^N \frac{d\pi_k(\vec{x})}{2\pi} d\varphi_k(\vec{x}) \langle\varphi_{N+1}|\pi_N\rangle \cdots \\
&\quad \underbrace{\left( e^{+\int d^3\vec{x} \pi_k(\vec{x})\varphi_{k+1}(\vec{x})} \right)}_{\langle\varphi_{k+1}|\pi_k\rangle} \underbrace{\left( e^{-\Delta\tau\int d^3\vec{x} H(\pi_k,\varphi_k)} e^{-\int d^3\vec{x} \pi_k(\vec{x})\varphi_k(\vec{x})} \right)}_{\langle\pi_k|e^{-\Delta\tau\hat{H}}|\varphi_k\rangle} \langle\varphi_1|\phi\rangle \\
&= \lim_{N\rightarrow\infty} \int d\phi \int \prod_{k=1}^N \frac{d\pi_k(\vec{x})}{2\pi} d\varphi_k(\vec{x}) \delta(\phi - \varphi_{N+1})\delta(\varphi_1 - \phi) \times \\
&\quad \times e^{-\Delta\tau\sum_{k=1}^N \int d^3\vec{x} H(\pi_k,\varphi_k) - \pi_k(\vec{x})\frac{\varphi_{k+1}(\vec{x}) - \varphi_k(\vec{x})}{\Delta\tau}} \\
&\equiv \int [D\pi] \int_{\varphi(\vec{x},x_4=0)=\phi(\vec{x})}^{\varphi(\vec{x},x_4=\frac{1}{T})=\phi(\vec{x})} [D\varphi] e^{-\int_0^{\frac{1}{T}} d\tau d^3\vec{x} \left[ \pi_k(\vec{x},t)\frac{\partial\varphi_k(\vec{x},t)}{\partial\tau} - H(\pi_k,\varphi_k) \right]}
\end{aligned} \tag{1.65}$$

If the Hamiltonian allows to simply integrate out the momentum fields, we obtain

$$\int d\phi\langle\phi|e^{-\frac{1}{T}\hat{H}}|\phi\rangle = \mathcal{N} \int_{\varphi(\vec{x},x_4=0)=\phi(\vec{x})}^{\varphi(\vec{x},x_4=\frac{1}{T})=\phi(\vec{x})} [D\varphi] e^{-\int_0^{\frac{1}{T}} d\tau d^3\vec{x} \mathcal{L}(\pi_k,\varphi_k)} \tag{1.66}$$

with  $\mathcal{N}$  a constant. The same calculation for fermions with  $\int d\phi^\dagger d\phi$ , where  $\phi$  are Grassmann variables, results in antiperiodic boundary conditions. This can be illustrated by considering the two-point Green function  $G_2$ . With  $\tau \in ]0, \frac{1}{T}[$  and the time-ordering

$$\mathcal{T}_\tau [\phi(\vec{x}, \tau_1)\phi(\vec{y}, \tau_2)] \equiv \phi(\vec{x}, \tau_1)\phi(\vec{y}, \tau_2)\Theta(\tau_1 - \tau_2) + \eta \phi(\vec{x}, \tau_2)\phi(\vec{y}, \tau_1)\Theta(\tau_2 - \tau_1), \tag{1.67}$$

where  $\eta = +1$  for bosons, and  $\eta = -1$  for fermions due to the respective commutation relations, we can calculate ( $\tau > 0$ )

$$G_2(\vec{x}, \tau; \vec{y}, 0) \equiv \frac{1}{Z} \text{Tr} \left( e^{-\frac{1}{T} \hat{H}} \mathcal{T}_\tau [\phi(\vec{x}, \tau) \phi(\vec{y}, 0)] \right) = \frac{1}{Z} \text{Tr} \left( e^{-\frac{1}{T} \hat{H}} e^{+\frac{1}{T} \hat{H}} \phi(\vec{y}, 0) e^{-\frac{1}{T} \hat{H}} \phi(\vec{x}, \tau) \right) \quad (1.68)$$

$$= \frac{1}{Z} \text{Tr} \left( e^{-\frac{1}{T} \hat{H}} \phi(\vec{y}, \frac{1}{T}) \phi(\vec{x}, \tau) \right) = \eta \text{Tr} \left( e^{-\frac{1}{T} \hat{H}} \mathcal{T}_\tau \left[ \phi(\vec{x}, \tau) \phi(\vec{y}, \frac{1}{T}) \right] \right) \quad (1.69)$$

$$= \eta G_2(\vec{x}, \tau; \vec{y}, \frac{1}{T}) \quad (1.70)$$

This implies  $\phi(\vec{x}, 0) = \eta \phi(\vec{x}, \frac{1}{T})$ .

For QCD, the corresponding formal identification is as follows

$$Z = \text{Tr} e^{-\frac{1}{T} \hat{H}} = \int_{bc} [DU][D\bar{\Psi}][D\Psi] e^{-\int_0^{\frac{1}{T}} d\tau \int d^3\vec{x} \mathcal{L}(U, \bar{\Psi}, \Psi)}, \quad (1.71)$$

where the gluon fields obey periodic boundary conditions, the fermion fields anti-periodic boundary conditions, see Fig. 1.3. The lattice extents are asymmetric with  $N_s$  sites in the spatial directions and  $N_t$  sites in the temporal direction. The thermodynamic limit is given by  $N_s \rightarrow \infty$ . For practical purposes, however, it is enough to demand

$$N_s \gg N_t. \quad (1.72)$$

The QCD temperature  $T$  (not to be confused with the above temperature  $T$ ) is given by

$$T(N_t, \beta) = \frac{1}{N_t a(\beta)}, \text{ with } \beta = \frac{2N_c}{g^2}. \quad (1.73)$$

The introduction of an additional quark chemical potential leads to QCD at finite temperature and density, or short ‘‘Finite Density QCD’’. In quantum field theory, particles can be created and destroyed, and thus we couple the chemical potential to the fermion charge operator, ie. the difference of the number of fermions and

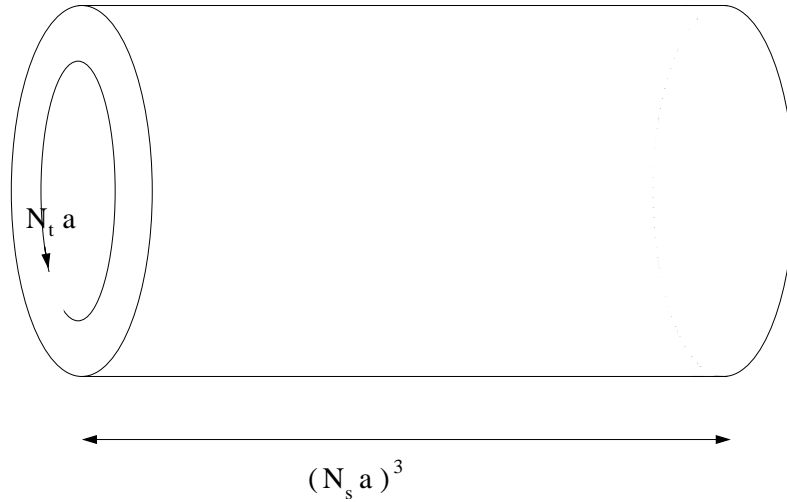


Figure 1.3: Field Theory at Finite Temperature. The cylinder represents the periodic boundary conditions in the temporal direction.

antifermions, from now on referred to as “fermion number”, which is given as

$$\hat{N} = \int d^3\vec{x} \bar{\Psi} \gamma^0 \Psi. \quad (1.74)$$

Its conservation can be shown: The Noether current  $J^\mu = \bar{\Psi} \gamma^\mu \Psi$ , associated to the global  $U(1)_V$  transformation  $\Psi \rightarrow e^{i\theta} \Psi$ , is conserved:  $\partial_\mu J^\mu = 0$ . It follows that  $\partial_0 \hat{N} = \int d^3\vec{x} \partial_0 J^0 = \int d^3\vec{x} \partial_i J^i = 0$ . Therefore, the chemical potential will appear in the Hamiltonian as a term  $\mu \int d^3\vec{x} J_0$

$$\hat{H} \rightarrow \hat{H} - \mu \hat{N} = \hat{H} - \mu \int d^3\vec{x} \bar{\Psi} \gamma^0 \Psi = \hat{H} - \mu \int d^3\vec{x} \Psi^\dagger \Psi. \quad (1.75)$$

It seems straight-forward to transcribe the continuum chemical potential to the lattice, since we could treat the corresponding term like the mass term. However, the naive discretisation is not adequate. Its failure can be seen when calculating the internal energy[15]

$$\epsilon(\mu) \equiv \frac{1}{V} \frac{\partial \log Z(\mu)}{\partial (\frac{1}{T})} = \frac{1}{4\pi^4} \int d^4 p \frac{\vec{p}^2 + m^2}{(p_4 - i\mu)^2 + \vec{p}^2 + m^2}, \quad (1.76)$$

which shows for massless fermions in the zero temperature limit  $T = 0$  the behaviour<sup>9</sup>

<sup>9</sup>This follows from a dimensional argument: since  $m = 0$  and  $T = 0$ , the only dimensionful



$\epsilon \sim \mu^4$ . The lattice expression correspondingly is

$$\epsilon(\mu) = \frac{1}{4\pi^4 a^4} \int_{-\pi}^{\pi} d^4 p \frac{\sum_{j=1}^3 \sin^2(p_j a) + (ma)^2}{[\sin(p_4 a) - i\mu a]^2 + \sum_{j=1}^3 \sin^2(p_j a) + (ma)^2}, \quad (1.77)$$

which is quadratically divergent  $(\frac{\mu}{a})^2$  in the continuum limit  $a \rightarrow 0$ . This apparent difficulty of putting a chemical potential on the lattice actually is easily solved by going back to the discrete Dirac operator. The derivative is implemented as a central difference

$$\partial_{\mu} = \frac{\delta_{x,x'+\hat{\mu}} - \delta_{x,x'-\hat{\mu}}}{2a} \xrightarrow{\text{Fourier transformation}} \frac{e^{ip_{\mu}a} - e^{-ip_{\mu}a}}{2a} = i \frac{\sin(p_{\mu}a)}{a}. \quad (1.78)$$

In the continuum, the chemical potential is introduced by a shift in the fourth component of the momentum  $p_4 \rightarrow p_4 - i\mu$ , which imposes the following change in the lattice expression of the internal energy

$$\epsilon(\mu) = \frac{1}{4\pi^4 a^4} \int_{-\pi}^{\pi} d^4 p \frac{\sum_{j=1}^3 \sin^2(p_j a) + (ma)^2}{\sin^2(p_4 a - i\mu a) + \sum_{j=1}^3 \sin^2(p_j a) + (ma)^2}, \quad (1.79)$$

and shows the correct behaviour in the continuum limit[16]. We go back to position space by the (inverse) Fourier transformation in Eq.(1.78), and it follows

$$\begin{aligned} \delta_{x,x'+\hat{\mu}} &\rightarrow \delta_{x,x'+\hat{\mu}} e^{-\mu a} \\ \delta_{x,x'-\hat{\mu}} &\rightarrow \delta_{x,x'-\hat{\mu}} e^{\mu a}. \end{aligned} \quad (1.80)$$

The modification of the discrete Kogut-Susskind fermion matrix is then given by

$$M^{KS}(x, x', \mu) = am\delta_{x,x'} + \frac{1}{2} \sum_{i=1}^3 \eta_i(x) \left[ U_i(x) \delta_{x,x'-\hat{i}} - U_i^{\dagger}(x - \hat{i}) \delta_{x,x'+\hat{i}} \right] \quad (1.81)$$

$$+ \frac{1}{2} \eta_4(x) \left[ \frac{1}{2} U_4(x) (\delta_{x,x'-\hat{4}} e^{\mu a}) - U_4^{\dagger}(x - \hat{4}) (\delta_{x,x'+\hat{4}} e^{-\mu a}) \right]. \quad (1.82)$$

In other words, introduce a chemical potential  $\mu$  on the lattice by

$$\begin{aligned} U_4(x) &\rightarrow e^{\mu a} U_4(x) \\ U_4^{\dagger}(x) &\rightarrow e^{-\mu a} U_4^{\dagger}(x). \end{aligned} \quad (1.83)$$

---

parameter is  $\mu$ ; since the dimensionality of  $\epsilon(\mu) \sim a^{-4}$ , the internal energy has to be proportional to  $\mu^4$ .

It is interesting to note that the resulting energy density (in the naive continuum limit) is four times larger than the usual finite energy density of one continuum flavour at zero temperature, which reflects the presence of the doublers.

The fermion matrix at zero chemical potential  $M(\mu = 0)$  fulfills  $\gamma_5$ -hermiticity

$$M^{KS}(\mu = 0) = \gamma_5 (M^{KS})^\dagger (\mu = 0) \gamma_5, \quad (1.84)$$

in other words, the determinant is real

$$\det M^{KS}(\mu = 0) = \det (M^{KS})^\dagger (\mu = 0). \quad (1.85)$$

In contrast, the fermion matrix at non-zero chemical potential is not symmetric, since the forward components “ $\delta_{x,x'-4}$ ” pick up a factor  $e^{\mu a}$ , while the backward components “ $\delta_{x,x'+4}$ ” are assigned a factor  $e^{-\mu a}$ . Therefore, the determinant becomes complex. If  $\mu$  is chosen to be pure imaginary,  $\mu = i\mu_I$ , the determinant still fulfills the  $\gamma_5$ -hermiticity, since  $e^{i\mu a} U_4(x)$  is the complex conjugate of  $e^{-i\mu a} U_4^\dagger(x)$ .

Note that we have required a positive definite sampling weight in order to be able to perform Monte Carlo simulations. Obviously, this is not fulfilled anymore, if we turn on a chemical potential. We thus have to define a new sampling weight. A usual choice is

$$e^{-S_g[U]} \det M(U; \mu) = e^{-S_g[U]} |\det M(U; \mu)| e^{i\phi(U; \mu)} \rightarrow e^{-S_g[U]} |\det M(U; \mu)|, \quad (1.86)$$

where the phase factor  $e^{i\phi(U; \mu)}$  will be treated as an observable. This approach, known as “reweighting”, introduces a severe numerical problem, the so-called “sign problem”, which we will discuss in detail in chapter 3.

## 1.2 QCD Thermodynamics

Recent experiments offer the exciting possibility to create temperature and density conditions under which the dynamics of QCD can bring ordinary matter into a new

state, the so called “quark-gluon plasma”. Unfortunately, the regime of the phase transition is not accessible by analytical calculations, which are limited to very large ( $\sim$  infinite) temperature and/or density. Lattice QCD at finite temperature and density provides the framework to characterise the different phases and study phase transitions from first principles. The thermodynamic study of Lattice QCD at finite temperature, but zero density is a well established field. However, progress in the study of Finite Density QCD has only been made recently. The hindrance is of algorithmic nature, and we will provide a new numerical technique within the context of this thesis.

Lattice QCD at finite temperature and density is given by the grand canonical partition function

$$Z_{GC}(T, V, \mu) = \int [DU][D\bar{\Psi}][D\Psi] e^{-S_g[U;T,V] - S_F[U,\bar{\Psi},\Psi;T,V,\mu]} \quad (1.87)$$

$$S_g[U] = \beta \sum_p \left[ 1 - \frac{1}{2N_c} (\text{Tr } U(\partial p) + \text{Tr } U^\dagger(\partial p)) \right]$$

$$S_F[U] = a^4 \sum_x \sum_{x'} \bar{\Psi}(x) M^{KS}(x, x') \Psi(x') . \quad (1.88)$$

where the path integral is taken with the temporal boundary conditions

$$U_\mu(\vec{x}, \frac{1}{T}) = +U_\mu(\vec{x}, 0)$$

$$\Psi(\vec{x}, \frac{1}{T}) = -\Psi(\vec{x}, 0) \quad (1.89)$$

and periodic spatial boundary conditions. After integrating out the fermion fields, we obtain the commonly used grand canonical partition function

$$Z_{GC}(T, \mu) = \int [DU] e^{-S[U;T]} \det M^{KS}(U; \mu) . \quad (1.90)$$

The thermodynamic state of the system is completely determined from the free

energy and its derivatives

$$\text{free energy } F = -T \log Z_{GC}(T, \mu) \quad (1.91)$$

$$\text{free energy density } f = \frac{F}{V} \quad (1.92)$$

$$\text{pressure } P = -\frac{\partial F}{\partial V} \quad (1.93)$$

$$\text{matter density } \rho = -\frac{1}{V} \frac{\partial F}{\partial \mu} \quad (1.94)$$

In this thesis, we are particularly interested in the phase diagram of QCD in the  $T$ - $\mu$  and  $T$ - $\rho$ -plane. In order to understand the phase structure, we first have to discuss another symmetry of the Yang-Mills Lagrangian, which only plays a significant role at finite temperature: the  $Z_{N_c}$ -symmetry. In addition, we discuss properties of the grand canonical partition function by enlarging the phase space to imaginary chemical potential. This leads to an explicit construction of canonical partition functions, which we will need for our different approach to Finite Density QCD as presented in chapter 4. These notions are important prerequisites for our discussion of the QCD phase diagram in subsection 1.2.3.

### 1.2.1 $Z_{N_c}$ Centre Symmetry

The Yang-Mills Lagrangian is invariant under any local gauge transformation, in particular trivially under the following global transformation

$$A_\mu(x) \rightarrow z(k)A_\mu(x)z(k)^\dagger, \quad (1.95)$$

where  $z(k) \equiv e^{i\frac{2\pi k}{N_c}} \mathbb{1}_{N_c}$  with  $k = 0, \dots, N_c - 1$  are the centre elements of the gauge group  $SU(N_c)$ . Note that the group built by the elements  $z(k)$  is isomorphic to  $Z_{N_c}$ . The gluon fields are in the adjoint representation and therefore, they commute with the centre elements  $z(k)A_\mu(x)z(k)^\dagger = A_\mu(x)$ . Hence, the Lagrange density remains the same. At finite temperature, this symmetry becomes relevant, since it can be spontaneously broken and thus may be related with a phase transition that occurs at a critical temperature. We now show the construction of an order parameter.

Remember that the fields are required to obey boundary conditions in the temporal direction given by quantum statistics, ie.  $A_\mu(\vec{x}, \frac{1}{T}) = +A_\mu(\vec{x}, 0)$  for the gluon fields and  $\Psi(\vec{x}, \frac{1}{T}) = -\Psi(\vec{x}, 0)$  for the fermion fields. A proper gauge transformation *must* respect these boundary conditions. For the gluon fields, as noticed by 't Hooft[17], it is sufficient to demand (for notation compare with the local gauge transformation Eq.(1.6))

$$\Omega(\vec{x}, \frac{1}{T}) = z(k) \Omega(\vec{x}, 0) , \quad (1.96)$$

since

$$\begin{aligned} \Omega(\vec{x}, \frac{1}{T}) A_\mu(\vec{x}, \frac{1}{T}) \Omega^{-1}(\vec{x}, \frac{1}{T}) &= z(k) A_\mu^\Omega(\vec{x}, \frac{1}{T}) z(k)^\dagger \\ &= A_\mu^\Omega(\vec{x}, \frac{1}{T}) = A_\mu^\Omega(\vec{x}, 0) , \end{aligned} \quad (1.97)$$

where  $A^\Omega = \Omega(\vec{x}, 0) A_\mu \Omega^{-1}(\vec{x}, 0)$ , for example  $\Omega(\vec{x}, 0) = \mathbb{1}_{N_c}$ . Having this in mind, a “ $Z_{N_c}$ -transformation” on the lattice can be realised by multiplying all temporal links originating at sites of a given temporal hyperplane  $x_4$  by  $z(k)$ . This leaves the Yang-Mills Lagrangian invariant, but a simple object can be found that does not transform trivially under this transformation: the Polyakov loop,

$$\begin{aligned} Pol(\vec{x}) &= \sum_{\vec{x}} \frac{1}{N_c} \text{Tr} \prod_{n_4 < N_t} U_4(\vec{x}, x_4 = n_4 a) \\ &\rightarrow z(k) Pol(\vec{x}) , \end{aligned} \quad (1.98)$$

which is a closed loop thanks to the compactness of the temporal direction. This implies that the expectation value of the Polyakov loop is zero if the  $Z_{N_c}$  symmetry is present, but can be non-zero if spontaneously (or explicitly) broken. Hence, the Polyakov loop is an order parameter of this discrete symmetry. Note that the  $Z_{N_c}$ -transformation is not a gauge transformation, since it changes the value of the gauge-invariant Polyakov loop. Nevertheless, because of its origin Eq.(1.96), it is often called a “singular gauge transformation”.

The inclusion of dynamical fermion fields in the usual grand-canonical formulation<sup>10</sup> breaks this symmetry *explicitly*. This can be most easily seen in the following way:

$$\begin{aligned} \Omega(\vec{x}, \frac{1}{T}) \Psi(\vec{x}, \frac{1}{T}) &= z(k) \Omega(\vec{x}, 0) \Psi(\vec{x}, \frac{1}{T}) \\ &= \Omega(\vec{x}, 0) \left( z(k) \Psi(\vec{x}, \frac{1}{T}) \right) \neq \Omega(\vec{x}, 0) \left( - \Psi(\vec{x}, 0) \right) . \end{aligned} \quad (1.99)$$

We now show the breaking explicitly. We write the Kogut-Susskind fermion matrix given in Eq.(1.47) as  $M^{KS}(U; m) = am \left( \mathbb{1} + \frac{1}{2am} \epsilon(U) \right) = am \left( \mathbb{1} + \epsilon(U; m) \right)$ . Then,

$$\det M^{KS}(U; m) = e^{3VN_t \log(am)} e^{\text{Tr} \log(\mathbb{1} - \epsilon(U; m))} = e^{3VN_t \log(am)} e^{\text{Tr}[-\epsilon(U; m) - \frac{1}{2}\epsilon^2(U; m) + \dots]} , \quad (1.100)$$

if we expand the logarithm in terms of  $\epsilon(m)$ . Assume for simplicity that the number of spatial sites is  $N_s \rightarrow \infty$  and the number of temporal sites is  $N_t = 2$ . The first term  $\int [DU] e^{-\text{Tr} \epsilon(U; m)} = 0$  since the group measure fulfills  $\int dU_\mu(x) U_\mu(x) = 0$ . The second term can be decomposed into  $U_\mu(x) U_\mu^\dagger(x) = \mathbb{1}$  (overall factor),  $U_i(x) U_i(x + \hat{i})$  ( $i$ =spatial index, integral is zero),  $U_i^\dagger(x) U_i^\dagger(x - \hat{i})$  (integral is also zero) and Polyakov loops  $Pol(\vec{x})$  and  $Pol^\dagger(\vec{x})$ , whose integrals are not zero. These considerations lead to an expansion in the Polyakov loop

$$\det M^{KS}(U; m) = e^{3VN_t \log(am)} e^{-\frac{1}{2(2am)^2} \sum_{\vec{x}} (Pol(\vec{x}) + Pol^\dagger(\vec{x}))(-1) + \dots} \quad (1.101)$$

where the explicit  $(-1)$  refers to the antiperiodic boundary condition of the fermions. The exponent is maximised if the Polyakov loop is close to  $\mathbb{1}$ . Therefore, these values of the Polyakov loop are preferred due to the larger Boltzmann weight, and the  $Z_{N_c}$ -symmetry is explicitly broken. Since the Polyakov loop is real, we call the corresponding vacuum the “real sector”.

---

<sup>10</sup>In chapter 4, we will discuss an equivalent canonical formalism of Finite Density QCD, in which the  $Z_{N_c=3}$  symmetry is realised for *any* temperature, ie. the Polyakov loop expectation value is zero for *any* temperature. This subtle issue that in the presence of dynamical fermions the Polyakov loop is always either zero or non-zero will be resolved in detail in subsection 4.4.1.

We remember that a chemical potential is built into the fermion matrix by the substitution  $U_4(x) \rightarrow e^{\mu a} U_4(x)$ ,  $U_4^\dagger(x) \rightarrow e^{-\mu a} U_4^\dagger(x)$  respectively. Thus, we can break the  $Z_{N_c}$ -symmetry into any of the  $N_c$   $Z_{N_c}$ -vacua by applying an imaginary chemical potential  $a\mu = ai\mu_I = -i\frac{2\pi k}{N_c N_t}$ . We label the corresponding vacuum by the integer  $k$  and call it “ $k$ -sector”.

### 1.2.2 Partition Functions

In this section, we will discuss symmetries of the grand canonical partition function  $Z_{GC}(T, \mu)$  as a function of an imaginary chemical potential  $\mu = i\mu_I$ , following Ref. [18]. The main purpose is to provide an explicit construction of the canonical partition function  $Z_C(T, Q)$ . The motivation for this derivation is at hand: In chapter 4 we present a canonical approach to Finite Density QCD.

Important properties of  $Z_{GC}(T, \mu = i\mu_I)$ , see Fig. 1.4 for an illustration, are

- Evenness:  $Z_{GC}(-i\mu_I) = Z_{GC}(+i\mu_I)$ .

The transformation  $\mu \rightarrow -\mu$  can be compensated by time-reversal, ie. by interchanging particles and anti-particles. Time reversal is equivalent to CP symmetry (since CPT is always a good symmetry), and thus does not change the thermodynamics in the absence of CP violating terms.

- $\frac{2\pi T}{N_c}$ -periodicity in  $\mu_I$ :  $Z_{GC}(i(\mu_I + \frac{2\pi T}{N_c})) = Z_{GC}(i\mu_I)$ .

It follows from the previous subsection that a shift in the imaginary chemical potential  $\mu_I \rightarrow \mu_I + \frac{2\pi k}{N_c}$  can be compensated by a  $Z_{N_c}$ -transformation with  $-k$ , ie. by a rotation of the Polyakov loop  $Pol(\vec{x}) \rightarrow z(-k)Pol(\vec{x})$ . Since the path integral sums over all possible gauge fields, the partition function stays the same.

These properties lead to an expectation of the phase structure in the  $T - \mu_I$ -plane:

In a phase, where the  $Z_{N_c}$ -symmetry is realised (“disorder”), the periodicity in  $\mu_I$  is smoothly realised. However, there is a phase, where this  $Z_{N_c}$ -symmetry is spontaneously broken into one of the sectors (“order”). The existence of these distinct phases forces the appearance of phase transitions. Naturally, these discontinuities appear at  $\mu_I = \frac{2\pi kT}{N_c} + \frac{\pi T}{N_c}$ .

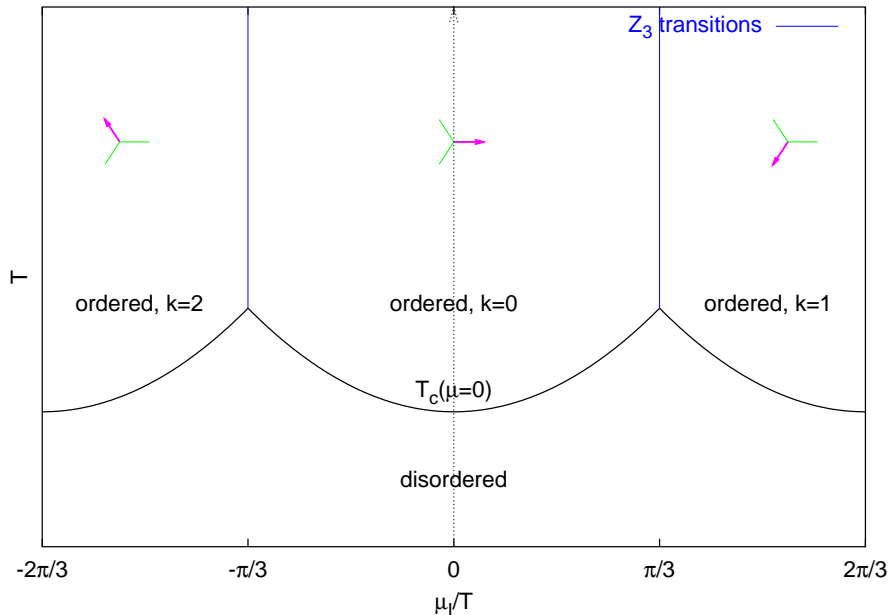


Figure 1.4: Phase diagram of  $Z_{GC}(i\mu_I)$  in the  $(\mu_I, T)$ -plane for  $N_c = 3$ . The arrows indicate the orientation of the Polyakov loop. The vertical lines signals the “order-order”  $Z_3$  transitions, which are first order. Properties of the “order-disorder”  $Z_3$  transitions (curved lines) depend on the parameters (number of flavours, quark mass) of the theory.

We obtain the canonical partition function  $Z_C(T, Q)$  when we fix the number of quarks  $\hat{N} = \int d^3\vec{x} \bar{\psi}(\vec{x}) \gamma_0 \psi(\vec{x})$  to  $Q$ , by inserting a  $\delta$ -function in the grand canonical partition function:

$$Z_C(T, Q) = \int [DU][D\bar{\Psi}][D\Psi] e^{-S_g[U;T] - S_F[U, \bar{\Psi}, \Psi; T]} \delta(\hat{N} - Q) . \quad (1.102)$$



The  $\delta$ -function admits a Fourier representation with the new variable  $\bar{\mu}_I$

$$\begin{aligned}
Z_C(T, Q) &= \mathcal{N} \int_{-\infty}^{\infty} d\bar{\mu}_I e^{-iQ\bar{\mu}_I} \times \int [DU][D\bar{\Psi}][D\Psi] e^{-S_g[U;\beta] - S_F[U,\bar{\psi},\psi] + i\bar{\mu}_I \hat{N}} \\
&= \mathcal{N} \int_{-\infty}^{\infty} d\bar{\mu}_I e^{-iQ\bar{\mu}_I} \times \int [DU][D\bar{\Psi}][D\Psi] \times \\
&\quad \times e^{-S_g[U;\beta] - S_F[U,\bar{\psi},\psi] + i\bar{\mu}_I \int d^3\vec{x} \bar{\psi}(\vec{x}) \gamma_0 \psi(\vec{x})} \\
&= \mathcal{N} \int_{-\infty}^{\infty} d\bar{\mu}_I e^{-iQ\bar{\mu}_I} \times \int [DU][D\bar{\Psi}][D\Psi] \times \\
&\quad \times e^{-S_g[U;\beta] - S_F[U,\bar{\psi},\psi] + i\bar{\mu}_I T \int_0^{\frac{1}{T}} d\tau \int d^3\vec{x} \bar{\psi}(\vec{x}) \gamma_0 \psi(\vec{x})}, \tag{1.103}
\end{aligned}$$

where  $\mathcal{N}$  is a normalisation factor. In the last line, we have used the fact that  $Q$  is conserved. One recognises  $i\mu_I = i\bar{\mu}_I T$  as an imaginary chemical potential,

$$Z_C(T, Q) = \mathcal{N} \int_{-\infty}^{\infty} d\bar{\mu}_I e^{-iQ\bar{\mu}_I} Z_{GC}(T, i\bar{\mu}_I T) = \frac{N_c}{2\pi} \int_{-\frac{\pi}{N_c}}^{\frac{\pi}{N_c}} d\bar{\mu}_I e^{-iQ\bar{\mu}_I} Z_{GC}(T, i\bar{\mu}_I T), \tag{1.104}$$

where we have exploited the  $\frac{2\pi T}{N_c}$ -periodicity in  $\mu_I$  of  $Z_{GC}(i\mu_I)$  in the last step. From this periodicity, it follows that  $Z_C(T, Q) = 0$  except for  $\frac{Q}{N_c} \equiv B \in \mathbb{Z}$ , where  $B$  is the baryon number. For convenience, we write

$$Z_C(T, B) = \frac{1}{2\pi} \int_{-\pi}^{\pi} d\left(\frac{\mu_I}{T}\right) e^{-i3B\frac{\mu_I}{T}} Z_{GC}(T, i\mu_I). \tag{1.105}$$

In principle, we can reconstruct the grand canonical partition function from the canonical ones using the fugacity expansion in  $B$

$$Z_{GC}(T, \mu) = \sum_{B=-\infty}^{\infty} e^{3B\frac{\mu}{T}} Z_C(T, B). \tag{1.106}$$

In the infinite volume, the baryon density  $\rho_B = \frac{B}{V}$  is a continuous variable, and we obtain the Laplace transformation

$$Z_{GC}(T, \mu) \underset{V \rightarrow \infty}{=} \int_{-\infty}^{\infty} d\rho_B e^{3V\rho_B\frac{\mu}{T}} Z_C(T, \rho_B) \tag{1.107}$$

$$= \int_{-\infty}^{\infty} d\rho_B e^{-\frac{V}{T}(f(T, \rho_B) - 3\mu\rho_B)} \tag{1.108}$$

with the Helmholtz free energy density  $f(T, \rho_B) = -\frac{T}{V} \log Z_C(T, \rho_B)$ .

### 1.2.3 QCD Phase Diagram

Historically the roots of QCD are in nuclear physics and the description of ordinary matter - understanding what protons and neutrons are and how they interact. Nowadays, we know that nucleons are composite particles, made of quarks and gluons. At first sight however, it appears to be confusing that we have not seen single quarks in experiments, for example via the trajectories of a particle with a fractional electric charge. Neither have we observed gluons - massless particles mediating the long-range strong force. Therefore, QCD must explain why quarks and gluons cannot exist as isolated particles - we say that they are confined. Confinement is the property of a certain phase. In QCD, the relevant thermodynamic variables for the phase diagram are the temperature  $T$  and the chemical potential  $\mu$  (or density  $\rho$ ). It may happen that confinement gets lost if we increase either the density or the temperature. In the latter, there is a rigorous proof as to why a “confinement-deconfinement phase transition” must occur in QCD - even in the absence of dynamical quarks[20]. On the one hand, at  $\beta = 0$ , Wilson[1] shows confinement in the regime of strong coupling. On the other hand, at  $\beta = \infty$ , perturbation theory can be applied, which does not confine quarks.

In the following, we give a description of the *conjectured* QCD phase diagram. The confined phase, also called hadronic phase is located at low temperature and small chemical potential, see Fig. 1.5. Quarks are confined, and the chiral symmetry is spontaneously broken, which is reflected in the non-vanishing expectation value of the chiral condensate. At low temperature we expect a vacuum-nuclear matter phase transition, which occurs at a quark chemical potential close to  $\frac{m_{\text{proton}}}{3}$ , where  $m_{\text{proton}}$  is the mass of the proton, and is first order because it takes some energy to extract a proton or neutron from a nucleus.

In relativistic heavy-ion collisions, as performed at RHIC (Brookhaven) or planned at LHC (CERN), we can probe higher temperatures. The protons and neutrons start to

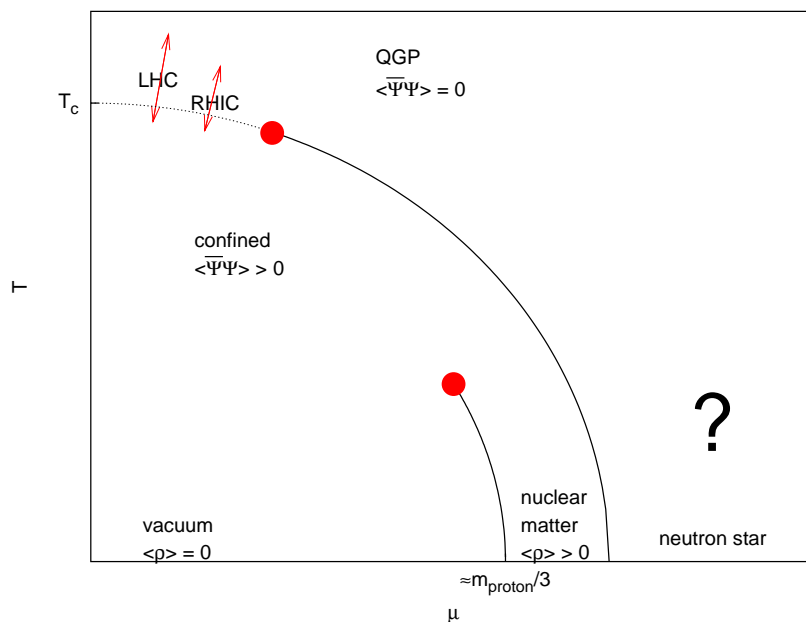


Figure 1.5: Conjectured phase diagram of real-world QCD in the  $(T, \mu)$ -plane.

overlap, and their constituents cannot be assigned to one hadron or another. Quarks are no longer confined, and furthermore, chiral symmetry is restored. Experimental hints for the formation of such a quark-gluon plasma are accumulating[21], and we may succeed in the coming years to confirm descriptions of this plasma being a gas of quarks and gluons. Numerical simulations at realistic quark masses indicate, that the temperature driven transition at zero chemical potential is a rapid, but smooth crossover. The  $\mu$ -driven transition at zero temperature, on the other hand, is a strong first order transition, where the baryon density  $\rho$  jumps from zero to non-zero. For an recent review of various model calculations, see Ref. [22]. The existence of a second order endpoint follows from the fact that the  $\mu$ -driven first order critical line starting at zero temperature cannot end at zero chemical potential. The search for this endpoint currently is an important goal in the community of Lattice QCD and experimental heavy-ion physics.

At low temperature and high density, as it might be realised in the interior of neutron stars, the description is more speculative[23]. This regime is of particular theoretical

interest, since the relevant scale is given by a large chemical potential. The coupling becomes small due to asymptotic freedom, and analytic calculations are feasible. It is predicted that matter may form a colour-superconducting phase.

The nature of the phase transition, such as the order and details of the critical behaviour, is related to global symmetries of the QCD Lagrangian. Here, we discuss the phase transition between hadronic matter and quark-gluon plasma in two limits: the regime of static quarks, where the  $Z_3$ -symmetry is realised and the case of massless quarks, for which the chiral symmetry is relevant. Note that only in these limits global symmetries exist and for any non-zero, finite value of quark masses, the global symmetries are explicitly broken. In Fig. 1.6, we indicate the order of the phase transition at  $\mu = 0$  in the plane of the degenerate “up/down”-quark masses  $m_u = m_d$  and “strange”-quark mass  $m_s$ . In Fig. 1.5 the quark masses were physical and the phase transition at zero chemical potential was a crossover. Thus, at the corresponding position, denoted by the blue “X”, we are in the crossover region.

In QCD with infinitely heavy quarks, which corresponds to pure  $SU(3)$  gauge theory with static test charges, the phase transition is first order. Effectively, it can be described by the  $Z_3$ -symmetric 3-state Potts model[24, 25], which confirms this numerical finding of the order of the transition. Unlike QCD, the Potts model can be numerically treated at arbitrary chemical potentials  $\mu$ . We can extend this figure in a third dimension  $\mu$ , as we will present in chapter 5. This first order nature of the transition persists for large, but finite quark masses. It terminates with a critical line of second order endpoints, because numerical simulations show that the phase transition actually is a crossover for intermediate quark masses.

The effective sigma-model[26, 27] describes QCD in the chiral regime, since  $SU_V(N_f) \times SU_A(N_f) = O(2N_f)$ . It has been found that for three or more flavours, the phase transition is first order. Therefore, it also has to end at a line of second order endpoints.

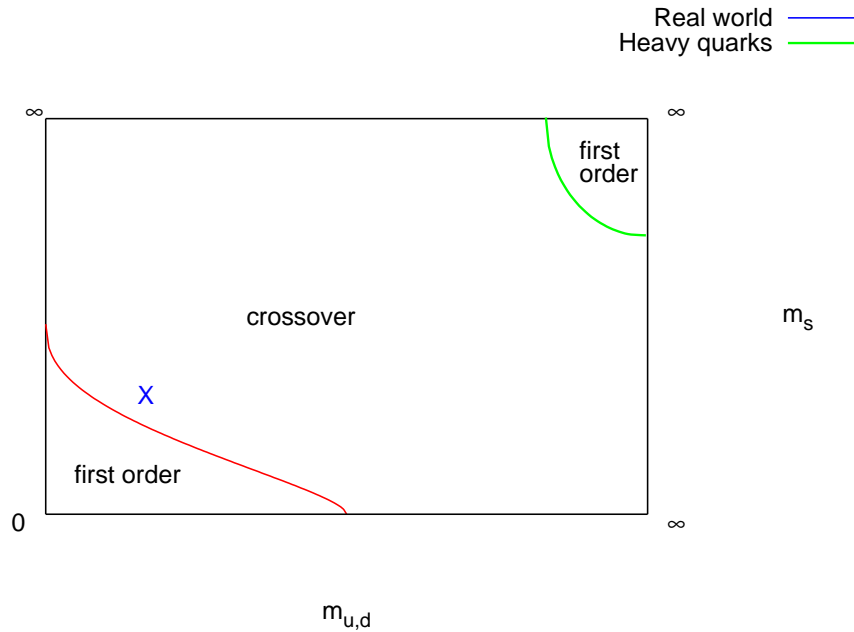


Figure 1.6: The order of the phase transition from the hadronic matter phase to the quark-gluon plasma one in the plane of the degenerate “up/down”-quark masses  $m_u = m_d$  and “strange”-quark mass  $m_s$ . The blue  $X$  refers to real-world physics, ie. physical quark masses.

We have discussed the order of the phase transition, but what are the mechanisms which drive the transition? We cover the two limits separately, starting with infinite quark mass. In this limit, the phase transition is called confinement-deconfinement transition. Quarks are confined in the low-temperature phase, while they are not at high temperature. At zero temperature, confinement is detected by Wilson’s criterion[1]: linear confinement, ie. a linearly increasing quark-antiquark potential  $V(R)$ , can be detected by the area law behaviour of the Wilson loop

$$W(R, T) \underset{T \rightarrow \infty}{\sim} e^{-V(R)T} = e^{-\sigma RT} \quad (1.109)$$

where  $R$  is the spatial extent and here,  $T$  the temporal extent of the rectangular Wilson loop  $W(R, T)$ , and  $\sigma$  is called the string tension. For details see

chapter 2. However, this criterion is inappropriate at non-zero temperature. A temperature sensitive criterion for Yang-Mills theories is given by associating the confinement-deconfinement transition with the spontaneous breaking of the global  $Z_3$  symmetry[28]. The Polyakov loop, which represents one static quark world line wrapping around the lattice, is related to the free energy of a single quark via  $\langle Pol(\vec{x}) \rangle = e^{\frac{1}{T}F_q}$ :

$$T < T_c \quad \langle Pol(\vec{x}) \rangle = 0 \rightarrow \quad F_q = \infty \rightarrow \quad \text{confinement} \quad (1.110)$$

$$T > T_c \quad \langle Pol(\vec{x}) \rangle \neq 0 \rightarrow \quad F_q < \infty \rightarrow \quad \text{deconfinement} \quad (1.111)$$

However, this seems ill-defined, since the left hand side can be complex. The clean way to study the transition is by measuring correlators of Polyakov loops, see Eq.(2.15), as a function of the distance  $R$ , ie. we measure the quark-antiquark potential, or rather the free energy of a system with a quark and an antiquark, as a function of the temperature. A linearly increasing potential as a function of  $R$  shows linear confinement. However, for finite quark masses, the long distance behaviour of the quark-antiquark potential can no longer serve as an order parameter, since the heavy quark free energy stays finite for all temperatures[29], indicating the screening of the static charges by dynamical quark-antiquark pairs. Up to date there is no known order parameter for finite quark masses[30], because there is no known symmetry.

In the massless quark regime, the Lagrangian is invariant under the chiral transformation. At low temperature, the chiral symmetry is spontaneously broken. As we have seen in Eq.(1.18), the order parameter is the chiral condensate

$$T < T_c \quad \langle \bar{\Psi}\Psi \rangle \neq 0 \rightarrow \quad \text{spontaneously broken symmetry} \quad (1.112)$$

$$T > T_c \quad \langle \bar{\Psi}\Psi \rangle = 0 \rightarrow \quad \text{symmetry restored} . \quad (1.113)$$

As outlined, two properties of QCD are playing a central role for the structure of the QCD phase diagram at finite temperature: confinement and chiral symmetry breaking. While the former explains why we observe colour-singlet states in the spectrum the latter describes the presence of light Goldstone particles, the pions.

### 1.3 Outlook for the following Chapters

The first project, “String Breaking”, is aimed at observing the creation of a matter-antimatter pair  $g\bar{g}$  in  $SU(2)$  gauge theory from the energy between two static colour charges  $Q$  and  $\bar{Q}$ , which is stored in a flux tube due to the self-interaction of the gluons, see Fig. 1.7. The energy in the flux tube, which is a string-like object, increases linearly with the spatial separation  $R$  of the two static charges, reflecting the confining property of QCD. At a certain distance  $R_b$ , it will be energetically favourable to create a matter-antimatter pair out of the vacuum using the accumulated energy stored in the string. The two static charges become screened and the energy remains constant under a further increase of the distance. We say, the string is broken.

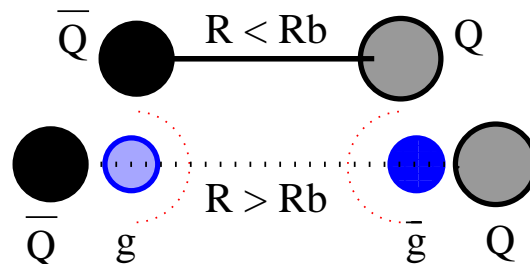


Figure 1.7: Two static charges  $Q$  and  $\bar{Q}$  will be screened, if the energy stored in the flux tube of length  $R$  is large enough to create a matter-antimatter pair  $g\bar{g}$ .

An uncontroversial observation at *zero* temperature from first principles can be achieved by measuring the groundstate of the system by the Wilson loop observable, which has a small, but non-vanishing overlap with the broken-string groundstate. In

Euclidean field theory, the groundstate energy can be extracted uniquely by evolving an arbitrary initial state in *imaginary time*  $T$  and taking the limit  $T \rightarrow \infty$ . The difficulty arises, since the magnitude of a single Wilson loop is of  $\mathcal{O}(1)$ , while its expectation value is of  $\mathcal{O}(10^{-40})$ . In Monte Carlo simulations, this would require  $N = 10^{80}$  measurements, since the statistical error on the expectation value of the Wilson loop decreases like  $\frac{1}{\sqrt{N}}$ . Thus, a strong variance reduction technique is needed.

The goal of the second project is to extract and understand certain aspects of QCD thermodynamics, e.g. its rich phase diagram as a function of temperature and matter density or chemical potential<sup>11</sup>. In particular, we study the nature of the so-called “confined phase” and the “quark-gluon plasma phase”, which is of experimental relevance (RHIC<sup>12</sup>, LHC<sup>13</sup>), and is discussed in detail in section 1.2.3. In the literature[31, 32, 33, 34], the two phases are often described by two simple models - the hadron resonance gas model in the confined phase, a weakly-interacting gas of light-quarks in the quark-gluon phase. We will compare our findings with predictions of these two models as well.

In contrast to the first project, the study of Finite Density QCD requires the numerical treatment of dynamical fermions, which is, as we will see later, computationally expensive. In addition, the simulation at non-zero chemical potential suffers from the so-called “sign-problem” - a known and serious obstacle for Lattice QCD with a real chemical potential. We propose a canonical approach to Finite Density QCD, which allows to investigate interesting physical regimes, without actually solving

---

<sup>11</sup>Unless otherwise specified, the chemical potential  $\mu$  refers to the *quark* chemical potential, the matter density  $\rho$  refers to the *baryon* matter density

<sup>12</sup>RHIC is the acronym of Relativistic Heavy Ion Collider, located at and operated by the Brookhaven National Laboratory in Upton, New York.

<sup>13</sup>LHC is the acronym of Large Hadron Collider, a high-energy proton-proton or ion-ion collider located at CERN with a collision energy of 7 TeV per proton, currently under construction and scheduled to operate in 2007.



the “sign problem”. The major part of the difficulties to explore the regime of finite matter density are due to the so-called “overlap-problem”, which often accompanies the “sign-problem”, but is less well known. This issue can be naturally addressed within the framework of our method. We will illustrate the “sign problem” and “overlap problem” in the context of a simple QCD toy model in an introductory chapter.

In QCD, the number of flavours and the masses of the involved quarks can be treated as parameters. In particular, we can make all quark flavours very heavy. This theory can be effectively described by the 3-state Potts model, for which the “sign problem” is mild, and simulations are feasible for arbitrary chemical potential. It thus provides an excellent laboratory to study heavy-quark QCD at finite chemical potential.



# Chapter 2

## String Breaking

### 2.1 Motivation

Quarks are linearly confined inside hadrons by a force called the strong interaction. Therefore, we cannot see single quarks. One can study this force by analysing the energy between a static colour charge and a static anticharge. Unlike in the case of the electromagnetic force, this energy is, as a consequence of linear confinement, squeezed into a long flux tube. This flux tube is a string-like object. Therefore, one can ask whether this string actually breaks when it reaches a certain length. This breaking of the string corresponds to the screening of the static charges by a virtual matter-antimatter pair created from that very energy stored in the string. The energy of the groundstate of the system, the so-called static potential, completely changes its qualitative behaviour as a function of the distance between the two static charges and can therefore be used to detect string breaking. There are two main situations where string breaking can be studied: *(i)* when one deals with static charges in the fundamental representation, which can only be screened by other fundamental particles, such as dynamical quarks or fundamental Higgs fields; *(ii)* when one considers static charges in the adjoint representation which can be screened by the gluons of the gauge field. To avoid the simulation of costly dynamical quarks

or of Higgs fields, we consider here adjoint static charges. The bound state of a gluon and an adjoint static charge is called a “gluelump”. Therefore, the breaking of the adjoint string leads to the creation of two of these gluelumps.

Three approaches have been used to measure the static potential and study string breaking:

- Correlation of Polyakov loops, at finite temperature [35].
- Multichannel Ansatz (also known as Variational Ansatz) using two types of operators: one for the string-like state and one for the broken-string state [36, 37].
- Wilson loops [38, 39].

String breaking has been seen using the first two methods, but no clear signal has been observed using the third one. The failure of the Wilson loop method seems to be due to the poor overlap of the Wilson loop operator with the broken-string state. It has even been speculated that this overlap is exactly zero [40]. This is why we have a closer look at this problem, taking advantage of recent, improved techniques to measure long Wilson loops. The results already are published in Ref. [41, 42]. Recently, [43] succeeded in measuring string breaking, using Wilson loops only, in a three-dimensional  $Z_2$ -Higgs model.

In the following section we recall notions about the static potential and its relation to the Wilson loop. In section 2.3, we take the three methods into more detailed consideration, to be able to discuss our results in all approaches. We explain the difficulties of measuring string breaking using Wilson loops only. In section 2.4, we present the techniques we applied, such as adjoint smearing and improved exponential error reduction for Wilson loops. We also discuss the methods used to analyse our data. For all three methods, results are shown in section 2.5, followed by the conclusion.

## 2.2 Static potential

We consider a pure  $SU(2)$  gauge system with a static charge and a static anticharge separated by a distance  $R$ . Although we mainly focus on measuring the static potential using Wilson loops only, we also consider the Multichannel Ansatz. Therefore, here we discuss the issue of measuring the groundstate and excited-state energies in a more general way.

The Hilbert space of the Hamiltonian is spanned by its orthonormal eigenbasis  $\Psi^{(n)}(R)$ . The corresponding energies are  $E_0 < E_1 < \dots$ , where  $E_0$ , the ground-state energy, is called the static potential. If we knew these eigenstates, we could extract the energies by measuring their Euclidean time evolution:

$$\Gamma^{(n)}(R, T) = \langle \Psi^{(n)}(R) | \hat{\mathbf{T}}^T | \Psi^{(n)}(R) \rangle = e^{-E_n(R)T}, \quad (2.1)$$

where  $\hat{\mathbf{T}}$  is the transfer operator,  $\hat{\mathbf{T}} = \sum_{n=0}^{\infty} |\Psi^{(n)}(R)\rangle e^{-E_n(R)} \langle \Psi^{(n)}(R)|$ . Since we do not know these eigenstates explicitly, let us consider an arbitrary linear combination  $\Phi(R)$ . We can expand this state in the eigenbasis

$$|\Phi(R)\rangle = \sum_n \langle \Psi^{(n)}(R) | \Phi(R) \rangle |\Psi^{(n)}(R)\rangle. \quad (2.2)$$

The temporal evolution is given by

$$\langle \Phi(R) | \hat{\mathbf{T}}^T | \Phi(R) \rangle = \sum_n |\langle \Phi(R) | \Psi^{(n)}(R) \rangle|^2 e^{-E_n(R)T} \equiv \sum_n c_n e^{-E_n(R)T}. \quad (2.3)$$

Let us introduce a finite set of states  $\phi_i(R)$  which we know how to measure. We set

$$\Phi(R) = \sum_i a_i(R) \phi_i(R). \quad (2.4)$$

To be explicit, let us expand Eq.(2.3) and define the correlation matrix  $V_{ij}(R, T)$

$$V_{ij}(R, T) = \langle \phi_j(R) | \hat{\mathbf{T}}^T | \phi_i(R) \rangle. \quad (2.5)$$

so that

$$\langle \Phi(R) | \hat{\mathbf{T}}^T | \Phi(R) \rangle = \sum_{i,j} a_j(R) a_i(R) V_{ij}(R, T). \quad (2.6)$$

A lemma, which is proven in Ref. [44], states for the eigenvalues  $\lambda^{(n)}(R, T)$  of the correlation matrix  $V_{ij}$

$$\lambda^{(n)}(R, T) \underset{T \rightarrow \infty}{=} f^{(n)}(R) e^{-E_n T} (1 + O(e^{-T \Delta E_n})) \quad (2.7)$$

where  $f^{(n)}(R) > 0$  and  $\Delta E_n = \min_{m \neq n} |E_n - E_m|$ . In general, the correction term cannot be neglected and it will play an essential role in our study. The way to determine the eigenvalues  $\lambda^{(n)}(R, T)$  and estimate the energies  $E_n$  is described in subsection 2.4.3.

The finite set of states  $\phi_i(R)$  is created by applying some operators on the vacuum. These states are chosen to model the expected ones, the unbroken-string and the broken-string state. We can build a string-like state  $\phi_s(R)$  by a spatial line  $S_s(R)$  of links of length  $R$  where  $s$  denotes the number of spatial smearing iterations (see subsection 2.4.1), or a broken-string state  $\phi_G(R)$  of length  $R$ , using  $G(R)$ , a "clover" discretisation of  $F_{\mu\nu}$  around the two static charges (see subsection 2.4.4). The correlation matrix is then

$$V_{ij}(R, T) = \langle \phi_j(R) | \hat{\mathbf{T}}^T | \phi_i(R) \rangle, \quad i, j = s, G \quad (2.8)$$

$$= \begin{pmatrix} \begin{array}{c} \square \\ \text{---} \\ \text{---} \\ \text{---} \\ \text{---} \\ \diamond \end{array} & \begin{array}{c} \diamond \\ | \\ \text{---} \\ | \\ \diamond \end{array} & \begin{array}{c} \diamond \\ | \\ \text{---} \\ | \\ \diamond \end{array} \\ \begin{array}{c} \text{---} \\ \text{---} \\ \text{---} \\ \text{---} \\ \diamond \end{array} & \begin{array}{c} \diamond \\ | \\ \text{---} \\ | \\ \diamond \end{array} & \begin{array}{c} \diamond \\ | \\ \text{---} \\ | \\ \diamond \end{array} \end{pmatrix} = \begin{pmatrix} S_s S_s(R, T) & S_s G(R, T) \\ G S_s(R, T) & G G(R, T) \end{pmatrix} \quad (2.9)$$

Using the diagonalisation procedure<sup>1</sup> (see subsection 2.4.3) one can reconstruct  $\Gamma^{(n)}(R, T)$  (Eq.(2.1)) for small  $n$ , the lowest energies, hence the static potential,

---

<sup>1</sup>Throughout this project, we call the *multichannel Ansatz* the approach to obtain eigen-energies and -states using a multichannel approach, i.e. measuring correlations between states created by a finite set of operators. We call the *diagonalisation procedure* the numerical procedure we use to extract information about eigen-energies and -states from a given correlation matrix of type Eq.(2.5).

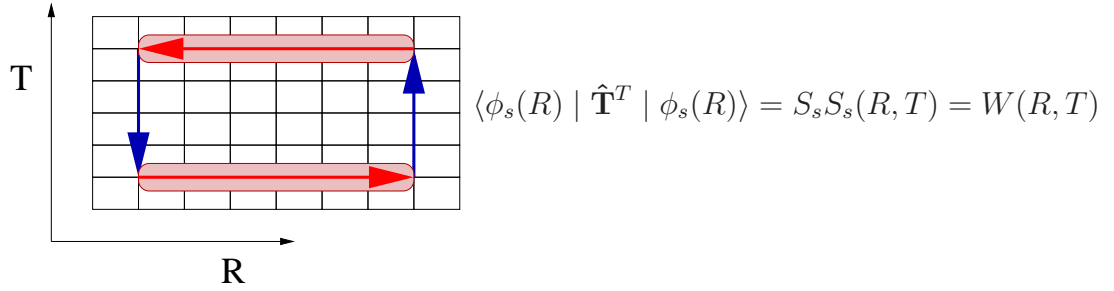


Figure 2.1: The Wilson loop channel. Information about the groundstate energy, the so-called static potential, can be extracted.

and the overlaps of the string-like state and the broken-string state with the corresponding eigenstates. In previous studies [36, 37], this correlation matrix has been used in the multichannel Ansatz to show string breaking. We will confirm these results. But since the multichannel Ansatz has been objected to (see next section), we will also show that the full information about the static potential can be extracted using only the  $GG$ -channel or only the  $S_s S_s(R, T)$  channel (the Wilson loop  $W(R, T)$  (see Fig. 2.1)). Using the above notation, this corresponds to setting  $a_s = 1$ , the other  $a_i = 0$ . Eq.(2.3) is now given by

$$\begin{aligned} \langle \phi_s(R) | \hat{\mathbf{T}}^T | \phi_s(R) \rangle &= S_s S_s(R, T) = W(R, T) \\ &= \sum_n |\langle \phi_s(R) | \Psi^{(n)}(R) \rangle|^2 e^{-E_n(R)T} = \sum_n c_n e^{-E_n(R)T} . \end{aligned} \quad (2.10)$$

We can truncate this sum of exponentials at  $n = l$  if all the states we neglect are strongly suppressed. For all  $k > l$ , we demand

$$1 \gg \frac{c_k(R)}{c_l(R)} e^{-(E_k(R) - E_l(R))T_{\min}(R)} , \quad (2.11)$$

which defines a  $T_{\min}(R)$  implicitly. In particular, we consider the following two-mass Ansatz ( $l = 1$ )

$$W(R, T) = c_0 e^{-V(R)T} + c_1 e^{-E_1(R)T} , \quad T > T_{\min} , \quad (2.12)$$

where  $c_0$  and  $c_1$  are the overlaps of the state  $|\phi_s\rangle$  with the groundstate, which is the static potential, and the first excited state respectively.

## 2.3 The three approaches

The adjoint Wilson loop shows a good overlap with the unbroken-string but not with the broken-string state. This is natural: The Wilson loop observable creates a static quark-antiquark pair together with a flux tube joining them. Therefore, the broken-string state, which consists of two isolated gluelumps, has poor overlap with the flux-tube state, hence with the Wilson loop. For  $R < R_b$  the unbroken-string state is the groundstate, therefore in Eq.(2.12)  $c_0$  is large compared to  $c_1$ . In this regime, additionally  $E_1 > V$  by definition, therefore the second exponential in Eq.(2.12) is negligible for  $T > T_{\min}$ . An important issue is what happens for  $R$  larger than  $R_b$ . The broken-string state becomes the groundstate. Its energy  $V(R)$  is smaller than the unbroken-string state energy  $E_1(R)$  (level crossing has occurred). But for small  $T$ , the unbroken-string state still dominates over the broken-string state because  $c_0 \ll c_1$ . Of course, this domination holds only up to a temporal extent  $T = T_P$ , where  $T_P$  is the turning point defined by the equality of both terms on the right-hand side of (2.12). For  $T > T_P$ , the broken-string groundstate becomes "visible" in the exponential decay of Eq.(2.12). The value of this  $T_P$  is crucial to be able to detect string breaking using Wilson loops only.

$$T_P = \frac{\log \frac{c_1}{c_0}}{E_1(R) - V(R)}. \quad (2.13)$$

Based on the heavy quark expansion, the strong coupling model[45] leads to estimates of the ratio  $\frac{c_1}{c_0}$  and of  $T_P$ . As an example we consider the distance  $R = 12a = 1.228(1)$  fm, whereas string breaking occurs at  $R_b \approx 10a = 1.023(1)$  fm (The lattice spacing  $a$  is calculated in the beginning of section 2.5). The energy of the broken-string state is  $V(R) \approx 2 \times M(Qg)$ , where  $M(Qg) = 1.03(2)a^{-1}$  is the mass of a gluelump (measured independently in subsection 2.4.4). Within the model[45], the ratio  $\frac{c_1}{c_0}$  is around  $\frac{c_1}{c_0} \sim e^{M(Qg)R} \underset{R=12a}{\approx} 2 \times 10^5$ . Therefore, the turning point is estimated to be

$$T_P^{(est)} = \frac{M(Qg)R}{E_1(R) - 2M(Qg)} \underset{R=12a}{\approx} 42a \quad (2.14)$$



using the value  $E_1(R = 12a) = 2.34(1)a^{-1}$  of our results in advance. Wilson loops of size  $12a \times 42a$ , i.e. about  $1.2\text{fm} \times 4.3\text{fm}$ , or larger are needed to observe string breaking according to this model.

Based on a topological argument, Ref. [40] even suggests that there may be no overlap at all:  $c_0 = 0$  for  $R > R_b$ . Adding matter fields gives rise to the formation of holes in the world sheet of the Wilson loop, reflecting pair creation. The average hole size leads to two different phases of the world sheet. In the normal phase, holes are small and the Wilson loop still fulfills an area law,  $W(R, T) \sim e^{-\sigma RT}$ , where  $\sigma$  is the string tension renormalised by the small holes. This phase corresponds to the unbroken-string case and a screening of the static charges cannot be observed. The other phase is called the tearing phase, where holes of arbitrarily large size can be formed. As a consequence, the Wilson loop follows a perimeter law,  $W(R, T) \sim e^{-cT}$ . This corresponds to the broken-string state, since the groundstate energy remains constant. Ref. [40] speculates that the Wilson loop is in the normal phase, and analyticity prevents it from changing phase, so that string breaking cannot be seen. This would explain why, for instance, the authors of Ref. [39] could not observe string breaking even at a distance  $R \approx 2R_b$ . Note however, that their temporal extent was  $T \leq 3$ .

A simple argument gives a necessary condition for the observation of string breaking if we only use ordinary (non-smear) Wilson loops  $W(R, T)$ . If  $R > R_b$ , where  $R_b$  is the string breaking distance, but  $T < R_b$ , we can relabel the  $R$  and  $T$  directions, so that now  $R < R_b$  and  $T > R_b$ . In that case, string breaking is not visible since the new spatial extent is  $R < R_b$ , and the Wilson loop must still fulfill the area law. Therefore, *both* sides  $R$  and  $T$  should be larger than  $R_b$ . Replacing ordinary Wilson loops by spatially smeared ones may relax this requirement somewhat.

As already mentioned in the previous section, an improved determination of the static potential can be achieved by a variational superposition of the unbroken-string and the broken-string states. In other words, the multichannel Ansatz enlarges the

operator space to a multichannel approach. The unbroken-string state is realised via the flux tube of the Wilson loop, the broken-string state is modelled by considering two gluelumps - separated static charges surrounded by gluons which screen the "interior" colour charge. We end up with the two-channel transfer matrix  $V_{ij}$  of Eq.(2.9).

Nevertheless, this method has been criticised [46]. One may claim that string breaking is *built into* the multichannel Ansatz due to the explicit inclusion of both states. Moreover, the behaviour in the continuum limit ( $\beta \rightarrow \infty$ ) must be considered. If the off-diagonal element  $S_s G(R, T) = G S_s(R, T)$  is zero in this limit, string breaking does not actually happen: the Wilson loop does not communicate with the broken-string state; the eigenvalues merely cross each other at  $R = R_b$ . It is only if the off-diagonal elements are different from zero, that the eigenstates are a mixture of both states. A small overlap at different  $\beta$ -values has indeed been confirmed by the mixing analysis in the multichannel Ansatz, as can be seen in Ref. [36, 37], which deal with this issue. However, whether this overlap vanishes or not for  $a \rightarrow 0$  still has to be checked in detail. Here, we do not address this question of continuum extrapolation due to technical difficulties: The method we use is more efficient at smaller  $\beta$ . Therefore we consider only one  $\beta$ -value, which we choose as small as possible while staying in the scaling region.

The Wilson loop method and the multichannel Ansatz work at zero temperature, where the question to be answered is: What is the groundstate of a system with two static charges? In the context of the Polyakov loop method we have contributions of temperature-dependent effects, and the question to be answered is different: What is the free energy of a system with two static charges coupled to a heat-bath? Nevertheless, it is an interesting issue and, as a by-product, we can also measure the correlations of Polyakov loops, which are in our case of adjoint charges  $Pol(\mathbf{x}) = \frac{1}{3} \text{Tr} \prod_{i=0}^{N_t-1} U_{\text{adj}}^{(t)}(\mathbf{x}, i)$ . This results in a temperature-dependent potential

$V_T(R)$  [47]:

$$\langle Pol(0)Pol^*(R) \rangle = e^{-V_T(R)/T} . \quad (2.15)$$

The flattening of the potential  $V_T(R)$  at large  $R$  has been seen in QCD with dynamical fermions, although in practice only at temperatures close to or above the critical deconfinement temperature. Unlike the multichannel Ansatz, this method builds in no prejudices about the structure of the groundstate wave function.

## 2.4 Technical details

We are considering Wilson loops in the adjoint representation (for a definition see the following subsection). The choice of the representation has a direct impact on the static potential, which is, at lowest order in perturbation theory in (2+1) dimensions [48]

$$V_P(R) \sim -C_2 \frac{g_0^2}{2\pi} \log R\Lambda + O(g_0^4/\Lambda) . \quad (2.16)$$

$C_2$  is the value of the quadratic Casimir operator of the representation of the static charges, i.e.

- fundamental representation:  $C_2(F) \mathbb{1}_{2 \times 2} = \frac{3}{4} \mathbb{1}_{2 \times 2}$
- adjoint representation:  $C_2(A) \mathbb{1}_{3 \times 3} = 2 \mathbb{1}_{3 \times 3}$

The important point is that, in the regime of perturbation theory, i.e. at small distances  $R$ , at lowest order, the adjoint static potential  $V_{\text{adj}}(R)$  differs from the fundamental static potential  $V_{\text{fund}}(R)$  by a factor  $\frac{8}{3}$ . Assuming, for simplicity, that the ratio remains the same at larger  $R$  (this issue is discussed in subsection 2.5.5), the adjoint potential is much more difficult to measure than the fundamental one: The Wilson loop is  $W(R, T) \sim e^{-V(R)T}$ , therefore the signal decreases much faster with  $R$  or  $T$  in the adjoint representation. This is the price to pay if we consider adjoint static charges instead of fundamental static charges in order to avoid the simulation of dynamical quarks. We need a sophisticated method of exponential error reduction

(see subsection 2.4.2) to detect very small signals: The magnitude of each measured Wilson loop is  $W_i(R, T) \sim O(1)$  while the average to be detected, as it will turn out, is  $W(R, T) \sim O(10^{-40})$ . Using ordinary methods,  $10^{80}$  measurements would be needed.

### 2.4.1 Adjoint smearing

It is very desirable to reduce contributions from excited states  $\Psi^{(n \neq 0)}$  to the Wilson loop  $W(R, T)$ : The turning point Euclidean time  $T_P$  (Eq.(2.13)) is reduced, and the accuracy on the groundstate potential is greatly improved. To this end, we smear adjoint links spatially. In  $SU(2)$ , a matrix  $U_{\text{fund}}$  in the fundamental representation can be mapped onto a  $3 \times 3$  real link matrix  $U_{\text{adj}}$  in the adjoint representation by

$$U_{\text{adj}}^{\alpha\beta}(U_{\text{fund}}) = \frac{1}{2} \sigma_{li}^{\alpha} U_{\text{fund},ij} \sigma_{jk}^{\beta} U_{\text{fund},kl}^{\dagger} . \quad (2.17)$$

where the  $\sigma^{\alpha}$  are the Pauli matrices;  $\alpha, \beta = 1..3$ ;  $i, j, k, l = 1..2$ .

The smearing can be done by setting the new adjoint link as the  $SO(3)$  projection of the old link plus a weighted sum of the spatial staples:

$$U'_{\text{adj}}(x) = \text{Proj}_{SO(3)} \left( U_{\text{adj}}(x) + \alpha \sum_{i=1}^4 \text{Adjoint Spatial Staple}_i \right) \quad (2.18)$$

where we choose  $\alpha = 0.5$ . We consider three different smearing levels: 15, 30 and 60 iterations of Eq.(2.18). For details and usage, see subsection 2.4.2. We define our projection of an arbitrary matrix  $\tilde{A}$  onto  $A \in SO(3)$  by maximising  $\text{Tr} \tilde{A}^{\dagger} A$ . This can be performed using the singular value decomposition: Every  $M \times N$  matrix  $\tilde{A}$  ( $M \geq N$ ) can be written as the product of a column-orthogonal  $M \times N$  matrix  $U$ , a diagonal  $N \times N$  matrix  $\Delta$  with positive or zero elements (the singular values), and an orthogonal  $N \times N$  matrix  $V^{\dagger}$

$$\tilde{A} = U \Delta V^{\dagger} . \quad (2.19)$$

Since in our case  $M = N = 3$ , both  $U$  and  $V$  are elements of  $SO(3)$ , and we get the projection of  $\tilde{A}$  onto  $SO(3)$  by

$$A = \text{Proj}_{SO(3)}(\tilde{A}) = UV^\dagger. \quad (2.20)$$

For completeness we also describe the fundamental smearing procedure used in subsection 2.4.4. Instead of considering adjoint links, we use the same method but in the fundamental representation:

$$U'(x) = \text{Proj}_{SU(2)}\left(U(x) + \alpha \sum_{i=1}^4 \text{Spatial Staple}_i\right), \quad (2.21)$$

where we take  $\alpha = 0.5$  and project back onto  $SU(2)$  by

$$U'(x) = \text{Proj}_{SU(2)}(\tilde{U}'(x)) = \frac{\tilde{U}'(x)}{\sqrt{\det \tilde{U}'(x)}}. \quad (2.22)$$

### 2.4.2 Exponential error reduction

An adjoint  $R$  by  $T$  Wilson loop in the  $(x, t)$ -plane consists of two adjoint spatial transporters of length  $R$ , which we call  $\mathbf{L}(0)$  and  $\mathbf{L}(T)^\dagger$ , and two temporal sides of length  $T$ , which we write explicitly<sup>2</sup> as  $\mathbf{U}(0)^\dagger = \prod_{i=0}^{T-1} U_{\text{adj}}^{\dagger(t)}(x, y, t + i)$  and  $\mathbf{U}(R) = \prod_{j=T-1}^0 U_{\text{adj}}^{(t)}(x + R, y, t + j)$ . The expectation value of the Wilson loop can be written as

$$W(R, T) = \frac{1}{\mathcal{Z}} \int [DU] \text{Tr}\{\mathbf{U}(0)^\dagger \mathbf{L}(T)^\dagger \mathbf{U}(R) \mathbf{L}(0)\} e^{-S[U]} \quad (2.23)$$

An exponential error reduction is possible because of the locality of the action, which in our case is the Wilson plaquette action. The main idea is to write the average of a product as a product of averages.

---

<sup>2</sup>To make clearer the distinction between the two temporal sides of the Wilson loop, we use separate indices  $i$  and  $j$  for the two running time-coordinates.

## Multihit-method

One possibility to reduce the variance of the Wilson loop observable, is to reduce the variance of a single link contribution. The Multihit method [49] takes the average of many samples of one particular link with all other links held fixed. As we will show now, all the temporal links<sup>3</sup>  $U_{\text{adj},k}^{(t)}$  in Eq.(2.23) can be treated like this for Wilson loops with a spatial extent  $R \geq 2$ . In the first step we split the action as  $S = S'[U'] + \sum_k S''_k[U_k]$ .  $S''_k[U_k]$  is the local part of the action that contains the fundamental link  $U_k$  corresponding to  $U_{\text{adj},k}$ . The Multihit-method can be applied also to  $U_{\text{adj},l}$  if  $S''_k[U_k]$  does not depend on  $U_l$  for  $k \neq l$ . Therefore, since we use the Wilson plaquette action, this condition is satisfied if  $R \geq 2$ . We can then apply the Multihit-method on all time-like links and Eq.(2.23) can be rewritten as

$$\frac{1}{Z} \int [DU'] \text{Tr} \left( \prod_{i=0}^{T-1} \int dU_i U_{\text{adj},i}^\dagger e^{-S''_i[U_i]} \right) \mathbf{L}(T)^\dagger \times \quad (2.24)$$

$$\left( \prod_{j=T-1}^0 \int dU_j U_{\text{adj},j} e^{-S''_j[U_j]} \right) \mathbf{L}(0) e^{-S'[U']} =$$

$$\frac{1}{Z} \int [DU] \text{Tr} \left( \prod_{i=0}^{T-1} \bar{U}_{\text{adj},i}^\dagger \right) \mathbf{L}(T)^\dagger \left( \prod_{j=T-1}^0 \bar{U}_{\text{adj},j} \right) \mathbf{L}(0) e^{-S[U]}, \quad (2.25)$$

where the Multihit-average is given by the one-link integral

$$\bar{U}_{\text{adj},i} = \frac{\int dU_i U_{\text{adj},i} e^{-S''_i[U_i]}}{\int dU_i e^{-S''_i[U_i]}}. \quad (2.26)$$

In simple cases, as in pure  $SU(2)$ , the Multihit-average can even be calculated analytically. Namely,  $S''_i[U_i] = -\beta \frac{1}{2} \text{Tr} U_i W^\dagger$ , where  $W$  is the sum of the four (in  $3d$ ) fundamental staples, and

$$\bar{U}_{\text{adj},i} = \hat{W}_{\text{adj}} \frac{I_3(\beta w)}{I_1(\beta w)}, \quad (2.27)$$

where  $w = \sqrt{\det W}$ ,  $\hat{W} = W/w$  is the projection of the staple-sum onto  $SU(2)$  and  $\hat{W}_{\text{adj}}$  represents  $\hat{W}$  in the adjoint representation via Eq.(2.18).

---

<sup>3</sup>The situation is different considering spatial links: Since we have smeared them spatially, we cannot "hold all the other links fixed".

Since the variance of each time-like link entering  $W(R, T)$  is reduced, the variance reduction in  $W(R, T)$  is exponential in  $T$ . The coefficients have been estimated in Ref. [50]. For fundamental Wilson loops, the reduction is about  $(0.8^2)^T = e^{-0.45T}$ , and for adjoint loops about  $(0.5^2)^T = e^{-1.39T}$ .

### Multilevel-method

Although the Multihit-method was revolutionary in 1983, the error reduction was not strong enough to enlarge measurable Wilson loops to temporal extents  $T$  sufficient to observe string breaking. In section 2.3, we suggested a heuristic argument, that  $T$  should be at least as large as the string breaking distance, which in our case is at  $R_b \sim 10a$ . The heavy quark expansion even results in an estimation of  $T_P^{(est)} \approx 42a$  (see Eq.(2.14)).

M. Lüscher and P. Weisz generalise the Multihit method from single time-like links to link-link correlators  $\mathbf{T}(R, t' = na)$  [51]. Using our notation from above,

$$\mathbf{T}(R, t' = na)_{\alpha\beta\gamma\delta} = U_{\text{adj}}^{*(t)}(x, y, t + i = na)_{\alpha\beta} U_{\text{adj}}^{(t)}(x + R, y, t + j = na)_{\gamma\delta}. \quad (2.28)$$

A single Wilson loop  $W_s(R, T)$  can be written, using the tensor multiplication defined by

$$\{\mathbf{T}(R, na)\mathbf{T}(R, (n+1)a)\}_{\alpha\beta\gamma\delta} = \mathbf{T}(R, na)_{\alpha\lambda\gamma\epsilon} \mathbf{T}(R, (n+1)a)_{\lambda\beta\epsilon\delta} \quad (2.29)$$

as

$$W_s(R, T) = \mathbf{L}(0)_{\alpha\gamma} \{\mathbf{T}(R, 0)\mathbf{T}(R, 1a)\dots\mathbf{T}(R, (T-1)a)\}_{\alpha\beta\gamma\delta} \mathbf{L}(T)_{\beta\delta}^*. \quad (2.30)$$

Just like in the Multihit-method where we considered the average links  $\bar{U}_i$ , here time-slice expectation values of a link-link-correlator  $\mathbf{T}(R, na)$ , denoted by  $[\cdot]$ , can be obtained by sampling over the corresponding sublattice which is in this case the time-slice at time  $t' = na$ . This sublattice can be studied independently of the surrounding lattice provided the spatial link variables at the boundaries are

held fixed. This is a consequence of the time-locality of the gauge action. Using a self-explanatory notation:

$$[\mathbf{T}(R, na)] \equiv \frac{1}{Z_{\text{sub}}} \int [DU]_{\text{sub}} \mathbf{T}(R, na) e^{-S[U]_{\text{sub}}} , \quad (2.31)$$

the expectation value of the Wilson loop can be written in the form

$$W(R, T) = \langle \mathbf{L}(0)_{\alpha\gamma} \{ [\mathbf{T}(R, 0)] [\mathbf{T}(R, 1a)] \dots [\mathbf{T}(R, (T-1)a)] \}_{\alpha\beta\gamma\delta} \mathbf{L}(T)_{\beta\delta}^* \rangle . \quad (2.32)$$

The restriction of fixed spatial links at the boundaries becomes manifest in the fact that only the *temporal* links on the time-slice at time  $t' = na$  are allowed to be updated when evaluating  $[\dots]$  with Monte Carlo methods. For our project, this is a severe obstacle which limits the efficiency of the exponential error reduction. It can be circumvented by using a hierarchical scheme based on identities like

$$\begin{aligned} & [\mathbf{T}(R, na)] [\mathbf{T}(R, (n+1)a)] = \\ & \left[ \mathbf{T}(R, na) \mathbf{T}(R, (n+1)a) \right] = \left[ [\mathbf{T}(R, na)] [\mathbf{T}(R, (n+1)a)] \right] \end{aligned} \quad (2.33)$$

The impact on the Monte Carlo method is, that we are also allowed to sample over spatial links on the time-slice  $(n+1)a$  since the boundary of the so-called second-level average  $[\dots]$  now consists of the spatial links in the time-slices  $na$  and  $(n+2)a$ . The possibility to use this two-level scheme allows us to measure long Wilson loops almost up to the desired accuracy. We actually implement the following three-level scheme illustrated in Fig. 2.2, where  $T$  is restricted to be a multiple of 4:

$$\begin{aligned} W(R, T) = \langle \mathbf{L}(0)_{\alpha\gamma} \{ \dots \left[ [\mathbf{T}(R, na)] [\mathbf{T}(R, (n+1)a)] \right] \right. \\ \left. \left[ [\mathbf{T}(R, (n+2)a)] [\mathbf{T}(R, (n+3)a)] \right] \dots \}_{\alpha\beta\gamma\delta} \mathbf{L}(T)_{\beta\delta}^* \rangle \end{aligned} \quad (2.34)$$

As a result of a rough optimisation process in the error reduction, based on minimising the CPU time versus the error, we choose the following parameters (see also [52]): The innermost averages  $[\mathbf{T}(R, na)]$  are calculated from 10 sets of time-like *Multihit*-links, each obtained after  $n_1 = 10$  updates. The updates alternate



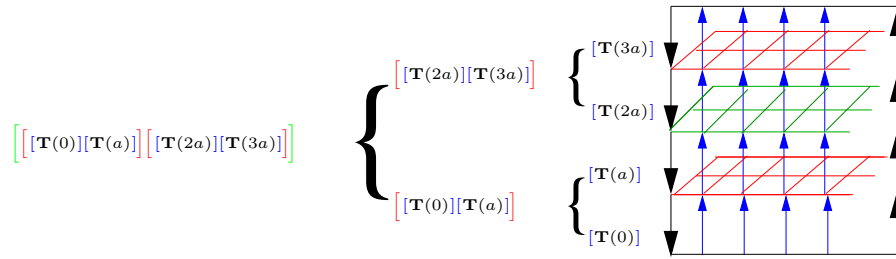


Figure 2.2: Hierarchical scheme. Using the three-level method as described in the text decreases the statistical error exponentially. While a one-level approach only allows to sample over the temporal links, a multi-level approach also makes it possible to update the interior spatial links, which improves the error reduction.

heatbath and overrelaxation steps in the proportion 1:4. The second-level averages,  $[[\mathbf{T}(R, na)][\mathbf{T}(R, (n+1)a)]]$  are calculated from  $n_2 = 160$  averages of  $[\mathbf{T}(R, na)]$  and  $[\mathbf{T}(R, (n+1)a)]$ , separated by 200 updates of the spatial links on time-slice  $(n+1)a$ . Finally, the third-level averages are calculated from  $n_3 = 165$  second-level averages separated by 200 updates of the spatial links on time-slice  $(n+2)a$ .

$n_1 = 10$  seems rather small, but can be explained using the confinement-deconfinement phase transition. For the ratio  $\frac{T_c}{\sqrt{\sigma}}$ , [53] finds a value

$$\frac{T_c}{\sqrt{\sigma}} = 1.065(6) \quad (2.35)$$

with periodic boundary conditions. The corresponding critical temporal extent (in lattice units) for our coupling  $\beta = 6.0$  is then

$$N_c^{(p)} = \frac{a(\beta = 6.0)}{T_c} \approx 3.76 \quad (2.36)$$

As a rule of thumb, one can estimate that a slice with fixed boundary conditions with a temporal extent of  $\gtrsim \frac{1}{2}N_c^{(p)}$  will be "confined" [54]. On the first level, we deal with time slices of extent 1, a high temperature regime, corresponding to the deconfined phase. Then the link-link-correlator has a large finite value, even at large  $R$ , and its determination is easy:  $n_1 = 10$  Multihit-averages are sufficient, and increasing  $n_1$  further does not reduce the final error as  $1/\sqrt{n_1}$ . On the next level, time

slices of extent 2 are in the confined phase. The signal then decreases exponentially at large  $R$ . We adjust  $n_2$  so that the signal to noise ratio is about 1 for the distance  $R = 13a$  which we are interested in. On the third level, the situation becomes more complicated and the best choice of all three parameters can only be found using optimisation, to minimise CPU time versus error. We find that a three-level scheme is more efficient than a one- or two-level scheme.

In Eq.(2.34), we have a product of  $N$  tensors, the three-level link-link-correlators with a temporal extent  $4a$ . Just like in the case of the Multihit-method, the variance of each tensor is reduced by a factor  $\delta(R)$ . Thus, the variance of the Wilson loop average can be reduced by as much as  $\delta(R)^N$  for an effort  $\propto N\delta(R)^{-2}$ . Variance reduction exponential in  $N = T/4$  is achieved.

### Improved spatial transporter

Using the above technique, we are able to reduce exponentially the error coming from the temporal links of the Wilson loop. But there is still the intrinsic noise, coming from the frozen spatial links at time-slices  $t = 0 \pmod{4}$ , which is relatively large [52]. How can we decrease it? This is what we do: To provide additional error reduction also in the spatial transporter, we replace the spatial transporters  $\mathbf{L}(0)_{\alpha\gamma}$  and  $\mathbf{L}(T)_{\beta\delta}^*$  with staple-shaped transporters, which are constructed in the following way (see Fig. 2.3):

(i) After each calculation of second-level averages, denoted as  $\begin{array}{|c|} \hline \\ \hline \end{array}$ , we form the smeared spatial links,  $\text{---}$ , at time-slice  $(n+2)a$ . (ii) We multiply them with the second-level averages to obtain the staple-shaped transporter  $\begin{array}{|c|} \hline \text{---} \\ \hline \end{array}$ ,  $\begin{array}{|c|} \hline \text{---} \\ \hline \end{array}$ . (iii) This procedure is repeated  $n_3 = 165$  times, each time after updating the spatial links on time-slice  $[(n+2)a]$  during the calculation of the third-level average. These error-reduced staple-shaped transporters replace the naive spatial transporters  $\mathbf{L}(0)_{\alpha\gamma}$  and  $\mathbf{L}(T)_{\beta\delta}^*$  and by contracting them with none, one, two, etc... third-level-averages one

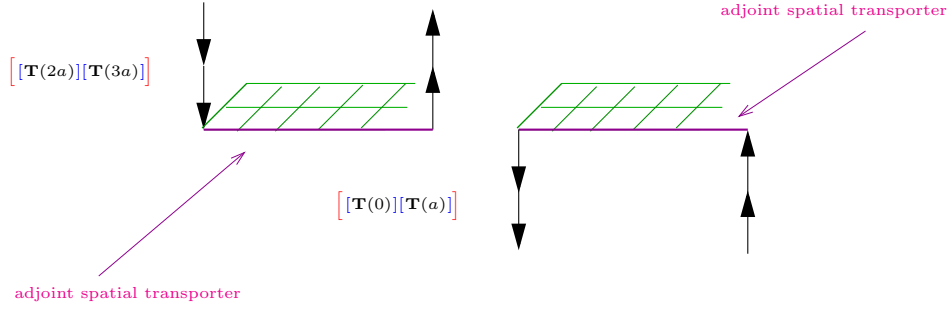


Figure 2.3: The improved spatial transporters. After each calculation of second-level averages  $\left[ \mathbf{T}(R, na) \right] \left[ \mathbf{T}(R, (n+1)a) \right]$ , we form staple-shaped transporter including smeared spatial links at the time-slice  $(n+2)a$ .

obtains Wilson loops at a fixed  $R$  with temporal extent  $T = 4, 8, 12$ , etc...

### 2.4.3 Diagonalisation procedure

Given a set of states  $\phi_i$  and the correlation matrix  $V_{ij}(R, T)$  as introduced in section 2.2, one can approximate the eigenstates correlation matrix  $\Gamma$  defined in Eq.(2.1), get information on the eigenstates  $\Psi^{(n)}$  and extract the lowest energies  $E_n$  using a diagonalisation procedure.

For a given separation  $R$ , the correlation matrix is defined in Eq.(2.5) as

$$V_{ij}(R, T) = \langle \phi_j(R) | \hat{\mathbf{T}}^T | \phi_i(R) \rangle . \quad (2.37)$$

A naive determination of the lowest energies  $E_n$  is obtained by looking for a plateau in the ratio of eigenvalues  $\frac{\lambda^{(n)}(R, T)}{\lambda^{(n)}(R, T+1)}$  of  $V_{ij}(R, T)$  for increasing  $T$  (see Eq.(2.7)):

$$E_n(R, T) = \lim_{T \rightarrow \infty} \log \frac{\lambda^{(n)}(R, T)}{\lambda^{(n)}(R, T+1)} . \quad (2.38)$$

This simple method works very well, especially in the multichannel Ansatz. Nevertheless, we want to increase the signal of the desired state as much as possible. For a finite basis, for small  $T$ , the eigenstates change with  $T$ . To improve  $T$ -convergence, we apply a variational diagonalisation which consists of solving the generalised eigen-

value problem

$$V_{ij}(R, T) v_j^{(n)}(R, T, T_0) = \lambda^{(n)}(R, T, T_0) V_{ij}(R, T_0) v_j^{(n)}(R, T, T_0) , \quad T > T_0 . \quad (2.39)$$

The eigenvalues  $\lambda^{(n)}(R, T, T_0)$  also fulfill Eq.(2.7) but their coefficients  $f^{(n)}(R)$  are enhanced by construction, compared to the previous ones. Once the eigenvectors  $\mathbf{v}^{(n)}$  and eigenvalues  $\lambda^{(n)}$  are known, one may approximate the eigenstates as a superposition of the operator states using

$$\Psi^{(n)}(R, T) = N^{(n)}(R, T, T_0) \sum_j v_j^{(n)}(R, T, T_0) \phi_j(R, T) \equiv \sum_j a_j^{(n)}(R, T, T_0) \phi_j(R, T) , \quad (2.40)$$

where the constants  $N^{(n)}$  are chosen such that the  $\Psi^{(n)}$  are normalised to unity.

It is well known from the literature, that the groundstate energy can be extracted nicely using a single-mass Ansatz even in the broken-string regime  $R > R_b$ , starting with  $T_0 = 0$ , *if* broken-string state operators are included in the multichannel (variational) basis. Indeed, we can confirm this observation. The situation is different when one uses a pure Wilson loop operator basis, at  $R > R_b$ . Because the overlap of the Wilson loop with the broken-string state is so weak, one must choose  $T_0$  very large to ensure that the lowest-lying eigenstates at  $T_0$  and  $T$  are both broken-string states. Then, the high sensitivity of Eq.(2.39) to statistical noise renders the analysis delicate: The matrix  $V_{ij}(R, T_0)$  may not be invertible. As a trade-off, we choose a small value of  $T_0$ ,  $T_0 = 4a$ , but must use a two-mass Ansatz to account for all data points.

#### 2.4.4 Gluelumps

In order to fully implement the multichannel Ansatz, we must consider the two-gluelump correlator, which is in the notation of Eq.(2.9)

$$\begin{array}{c} \diamond \\ | \\ \diamond \end{array} \begin{array}{c} \diamond \\ | \\ \diamond \end{array} = GG(R, T) . \quad (2.41)$$

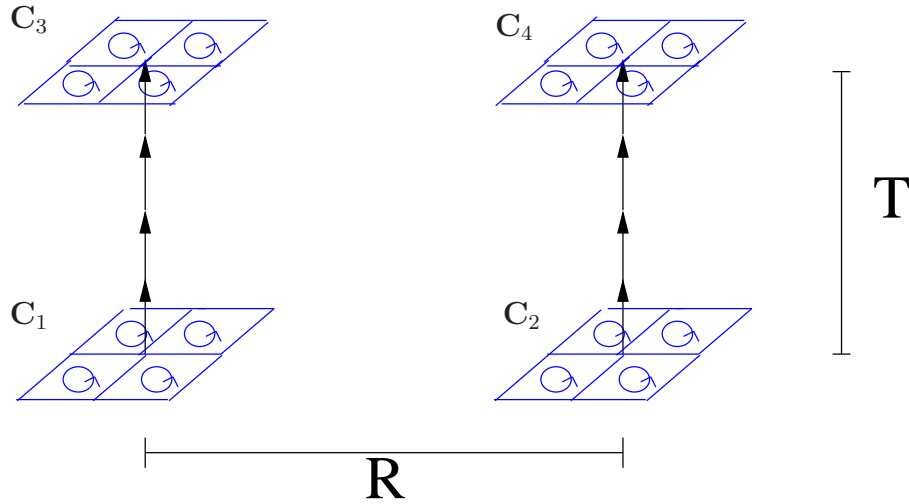


Figure 2.4: Interacting gluelumps at distance  $R$ . Four "clovers" are stuck on a link-link-correlator tensor of temporal extent  $T$ .

The broken-string state can be described by the presence of two gluelumps, each formed by the coupling of adjoint glue to an adjoint static charge [50]. It is of interest to measure the mass and the correlator of gluelumps. A simple way to probe the gluon field distribution, denoted as  $\diamond$ , around the adjoint static charge is the so-called clover-discretisation of  $F_{\mu\nu}$ , denoted as  $\mathbf{C}_{m,\mu\nu} = \mathbf{C}_{1,\mu\nu}, \dots, \mathbf{C}_{4,\mu\nu}$  in Fig. 2.4.

$$\begin{aligned} \mathbf{C}_{m,\mu\nu} &= \frac{1}{4} \sum_{i=1}^4 \text{Smeared Spatial Plaquette}(m, \mu, \nu)_i \\ &= C_{m,\mu\nu}^0 \mathbb{1}_{2 \times 2} + i C_{m,\mu\nu}^\alpha \sigma^\alpha, \end{aligned} \quad (2.42)$$

where the index  $i$  labels the four plaquettes of the clover  $\mathbf{C}_m$ . The anti-hermitian part of the clover  $\mathbf{C}_m$  approximates  $F_{\mu\nu}$

$$\frac{1}{2i} (\mathbf{C}_{m,\mu\nu} - \mathbf{C}_{m,\mu\nu}^\dagger) = C_{m,\mu\nu}^\alpha \sigma^\alpha = g_0 a^2 F_{\mu\nu} + O(a^4), \quad (2.43)$$

where the  $\sigma^\alpha$  are the Pauli matrices and we average over the four oriented spatial plaquettes that share a corner with one end of the time-like line. We choose the orientation of Fig. 2.4 (all four staples clockwise), whose symmetry selects the lowest-lying gluelump mass [39]. The plaquettes are built using fundamentally smeared

links (as described in Eq.(2.21)).

To measure the gluelump mass, one considers only one gluelump, e.g. the left side ( $\mathbf{C}_1 - \mathbf{C}_3$ ) in Fig. 2.4. The gauge-invariant operator  $CC(T)$  is an adjoint time-like line of length  $T$  using Eq.(2.17),  $A^{\alpha\beta}(T)$ , which is coupled at the two ends to the clovers ( $\mathbf{C}_1$  and  $\mathbf{C}_3$ )

$$CC(T) = C_1^\alpha(0)A^{\alpha\beta}(T)C_3^\beta(T) . \quad (2.44)$$

The adjoint time-like line can be measured using the Multihit-method or by applying the Multilevel-idea to this particular problem. The mass  $M(Qg)$  can then be extracted using

$$CC(T) \sim e^{-M(Qg)T} . \quad (2.45)$$

The overlap with the lowest-lying state is enhanced by using smeared links to build the clover observable Eq.(2.42). We would like to mention at this point that the gluelump mass by itself has no real physical meaning, since it contains a UV-divergence in the continuum limit due to the self-energy of the time-like links. Only the difference between this divergent mass and another similarly divergent one, like the static potential, makes physical sense. As a consequence, the string breaking distance  $R_b$  remains constant in physical units, while the energy of the level-crossing diverges as  $\beta \rightarrow \infty$ .

To measure the correlation of two gluelumps, one has to consider the full object in Fig. 2.4. The four clovers  $\mathbf{C}_1, \dots, \mathbf{C}_4$  are measured as described above. The correlation  $GG(R, T)$  of two gluelumps separated by a distance  $R$  can be measured by contracting the four clovers to the link-link-correlator tensors with temporal extent  $T$ ,  $\mathbf{T}(R, T)$ . The same tensors, obtained with the Multilevel algorithm and used for Wilson loops, are also used here

$$GG(R, T) = C_2^\gamma(0)C_1^\alpha(0)\mathbf{T}_{\alpha\beta\gamma\delta}(R, T)C_3^\beta(T)C_4^\delta(T) . \quad (2.46)$$

$GG(R, T)$  can be used in two ways: On the one hand, as mentioned in the beginning of this section, it is a contribution to the multichannel matrix; on the other hand, we can try to extract, from it alone, the energies of the unbroken-string and of the broken-string states since presumably the two-gluelump correlator has projection on both states.

$$GG(R, T) \sim g_0 e^{-V(R)T} + g_1 e^{-E_1(R)T}, \quad T > T_{\min}, \quad (2.47)$$

where  $V(R)$  is the static potential and  $E_1(R)$  the first excited state energy. The operator has obviously a good overlap with the broken-string state, but a poor one with the unbroken-string state. This situation mirrors that of the Wilson loop, described in the beginning of section 2.3. For  $R < R_b$ , the unbroken-string state is the groundstate. Therefore  $g_0$  is expected to be small compared to  $g_1$ , and the first excited state, with the energy of two gluelumps, is dominating for small  $T$ . Since the groundstate will be visible for large temporal extents only, we need a two-mass Ansatz to describe the correlator. At large distances,  $R \geq R_b$ , the broken-string state is the groundstate and also the dominating one ( $g_0 \gg g_1$ ), therefore a single-mass  $g_0 e^{-V(R)T}$  will suffice.

In the case of Wilson loops, we attach improved spatial transporter to the link-link-correlators. Here, we use non-improved clovers for simplicity. Therefore, we have more statistical noise, which makes it difficult to extract the groundstate, if the turning point is large. This is the case, for distances  $R$  close to but below the string breaking distances  $R_b$ . For details see subsection 2.5.2.

### 2.4.5 Multichannel Ansatz

To complete the multichannel Ansatz, we must also consider the off-diagonal elements in Eq.(2.9), denoted  $S_{s_1}G(R, T)$  and  $GS_{s_2}(R, T)$ .

$$S_{s_1}G(R, T) = \mathbf{L}_{s_1}(0)_{\alpha\gamma} \mathbf{T}_{\alpha\beta\gamma\delta}(R, T) C_3^\beta(T) C_4^\delta(T) \quad (2.48)$$

$$GS_{s_2}(R, T) = C_2^\gamma(0) C_1^\alpha(0) \mathbf{T}_{\alpha\beta\gamma\delta}(R, T) \mathbf{L}_{s_2}(T)_{\beta\delta}^* \quad (2.49)$$

To extract their values at  $T = 0 \pmod{4}$ , we use the non-improved spatial transporter  $\mathbf{L}_{s_1}(0)$  and  $\mathbf{L}_{s_2}(T)$ , where we smeared the links beforehand using  $s_1$  respectively  $s_2$  smearing iterations. The clovers are denoted as  $\mathbf{C}_1, \dots, \mathbf{C}_4$ . We attach them to the link-link-correlators  $\mathbf{T}(R, T)$ . The complete multichannel matrix is

$$V_{ij}(R, T) = \begin{pmatrix} \begin{array}{|c|} \hline \square \\ \hline \end{array} & \begin{array}{|c|} \hline \diamond \\ \hline \end{array} & \begin{array}{|c|} \hline \diamond \\ \hline \end{array} \\ \hline \begin{array}{|c|} \hline \square \\ \hline \end{array} & \begin{array}{|c|} \hline \diamond \\ \hline \end{array} & \begin{array}{|c|} \hline \diamond \\ \hline \end{array} \end{pmatrix} = \begin{pmatrix} S_{s_1}S_{s_2}(R, T) & S_{s_1}G(R, T) \\ GS_{s_2}(R, T) & GG(R, T) \end{pmatrix} \\ = \begin{pmatrix} S_{15}S_{15} & S_{15}S_{30} & S_{15}S_{60} & S_{15}G \\ S_{30}S_{15} & S_{30}S_{30} & S_{30}S_{60} & S_{30}G \\ S_{60}S_{15} & S_{60}S_{30} & S_{60}S_{60} & S_{60}G \\ GS_{15} & GS_{30} & GS_{60} & GG \end{pmatrix}, \quad (2.50)$$

since we consider three different smearing levels (15,30 and 60 smearing steps). This  $4 \times 4$  matrix can be analysed using the diagonalisation procedure described in subsection 2.4.3. We end up with enhanced signals for the three lowest-lying states, plus effective information about higher states.

### 2.4.6 Polyakov loops

According to Eq.(2.15) we can extract a temperature-dependent potential  $V_T(R)$ . The correlator of two adjoint Polyakov loops can be easily built by using the link-link



correlator tensors and the tensor-multiplication defined in Eq.(2.29)

$$\begin{aligned} \langle Pol(0)Pol^*(R) \rangle &= \langle \{ \cdots \left[ [\mathbf{T}(R, na)][\mathbf{T}(R, (n+1)a)] \right] \\ &\quad \left[ [\mathbf{T}(R, (n+2)a)][\mathbf{T}(R, (n+3)a)] \right] \cdots \}_{\alpha\alpha\gamma\gamma} \rangle \\ &= e^{-V_T(R)/T} . \end{aligned} \quad (2.51)$$

## 2.5 Results

We are using a  $3d$ -lattice with extent  $(48a)^2 \times 64a$  at inverse coupling  $\beta = \frac{4}{ag^2} = 6.0$ . The lattice spacing  $a$  can be obtained from the Sommer scale<sup>4</sup>  $r_0$ [55], which is defined by

$$r_0^2 F_{\text{fund}}(r_0) = 1.65 . \quad (2.52)$$

Setting  $r_0 = 0.5$  fm and comparing with the lattice result for  $r_0/a$ , one obtains  $a = 0.1022(1)$  fm. A description of our procedure to extract the fundamental force  $F_{\text{fund}}$  is given in subsection 2.5.5.

We present our results in the following order:

1. The static potential and excited states extracted from Wilson loops only.
2. The static potential extracted from the two-gluelump correlator.

---

<sup>4</sup>The phenomenological interpretation of this scale is valid only for QCD. When extracting the lattice spacing  $a$  from the Sommer scale  $r_0 = 0.5$  fm, the resulting value of  $a$  depends on the Ansatz chosen for the potential, and on the fitting range for the force. We chose Ansatz Eq.(2.53), which includes a perturbative logarithmic term, because not including this term causes an unacceptably bad fit. Fitting the force over the interval  $3a \leq R \leq 7a$ , one obtains  $r_0/a$  is 4.890(1), and  $a = 0.1022(1)$  fm. This value changes by 0.5% under a variation of the fitting interval. Similar ambiguities arise when one tries to extract the lattice spacing from the string tension  $(\sigma a^2)$ . Setting  $\sqrt{\sigma} = 440\text{MeV} \approx (0.45\text{fm})^{-1}$ , one obtains  $a = 0.1136(1)$  fm, with a systematic variation of about 0.5% with the fitting range.

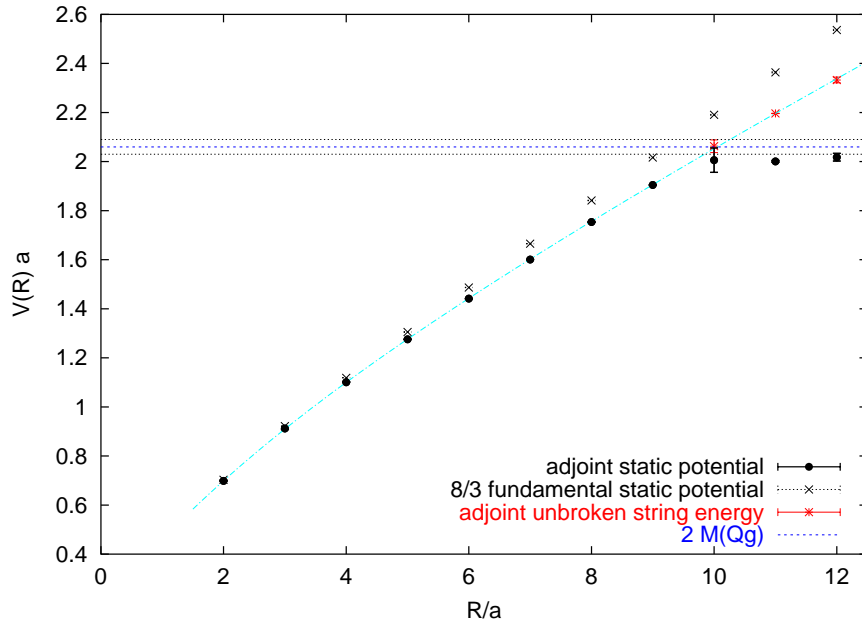


Figure 2.5: The adjoint and fundamental static potentials  $V(R)$  (the latter multiplied by the Casimir factor  $\frac{8}{3}$ ) versus  $R$  using Wilson loops only. The adjoint static potential remains approximately constant for  $R \geq R_b \approx 10a$  proving string breaking. The unbroken-string state energy is also drawn. The horizontal line at  $2.06(3)a^{-1}$  represents twice the mass of a gluelump.

3. The static potential and excited states obtained from the multichannel Ansatz.
4. The temperature-dependent potential obtained from the Polyakov loop correlators.
5. The comparison of fundamental and adjoint potentials and the issue of Casimir scaling.

We have analysed 44 configurations, which appear to be statistically uncorrelated. To extract the statistical errors we apply the jackknife method, see Appendix B.

### 2.5.1 Wilson loops only

We measure both the fundamental and the adjoint potential between two static charges. In the first case, string breaking cannot occur since the system does not

contain particles which can screen charges in the fundamental representation. Nevertheless, we can compare our results with accurate data available in the literature [38, 39]. We will also need these values later on, to discuss the issue of Casimir scaling (see subsection 2.5.5). In the case of adjoint static charges, string breaking should occur. A summary of our results is given in Fig. 2.5, where we show the fundamental potential multiplied by the Casimir ratio  $\frac{8}{3}$  (see Eq.(2.16)) and the adjoint static potential. It can clearly be seen that the adjoint static potential remains approximately constant for  $R \geq 10a$  proving string breaking at  $R_b \approx 10a$ . The unbroken-string potential is also shown.

The horizontal line at  $2.06(3)a^{-1}$  represents twice the mass of a gluelump, whose evaluation is described in subsection 2.4.4. This is the expected value of the static potential of the system, when the string is broken, since the broken-string state is modelled by the presence of two gluelumps whose interaction is screened.

Excited states are not visible for the fundamental case since the shortest Wilson loops we consider have a minimal temporal extent of  $T = 4a$  and excited states are already strongly suppressed. But they are clearly seen in the adjoint case for distances larger than the string breaking distance since the Wilson loop has very good overlap with the unbroken-string state which is an excited state for  $R > R_b$ . More about excited states can be found in subsection 2.5.1.

### Static potential

We start our discussion with the extraction of the fundamental static potential  $V_{\text{fund}}(R)$ . We consider only one level of fundamental smearing (30 iterations of Eq.(2.21)) of the fundamental spatial links and do not consider a Wilson loop matrix in the sense of Eq.(2.55). A single-mass Ansatz works nicely at all  $R$  in the temporal range  $T_{\text{min}} = 12a \leq T \leq 60a$ , where we have no measurable contribution of excited states. The extracted  $V_{\text{fund}}(R)$  is in full agreement with the literature.

From the static potential we can extract the string tension  $\sigma$ . This gives us a cross-

check with previous determinations [56] and a way to express the lattice spacing in physical units. We use a string-motivated Ansatz

$$V(R) \sim V_0 + l \log \frac{R}{a} - \frac{\gamma}{R} + \sigma R. \quad (2.53)$$

The Coulombic  $\log \frac{R}{a}$  term follows from  $3d$  perturbation theory (see Eq.(2.16)). The  $1/R$  term follows from the bosonic string model.  $\gamma$  is a universal constant with value  $\gamma = \frac{\pi}{24}(d-2)$  in  $d$  dimensions [57]. The linear term describes confinement, and  $\sigma$  is the string tension.

We fit all parameters and find for the string tension  $\sigma = 0.0625(5)a^{-2}$ . This value is stable and in full agreement with [56]. Using our Ansatz Eq.(2.53),  $\gamma$  cannot be reliably extracted by a global fit of the static potential. Using instead<sup>5</sup>

$$\gamma = -\frac{\partial^2 V(R)}{\partial R^2} R^3, \quad (2.54)$$

the extracted  $\gamma$  tends to the universal value  $\frac{\pi}{24} \approx 0.131$ :  $\gamma_{R=6a} = 0.126(12)$  and remains stable for  $R \geq 6a$  albeit with larger errors.

In the following case of the adjoint static potential, the Ansatz Eq.(2.53) does not result in stable parameters, with or without the Coulombic  $\log \frac{R}{a}$  term. Nevertheless, we include in Fig. 2.5 a best fit of the adjoint unbroken-string energy in the range  $2a \leq R \leq R_b$  using this Ansatz.

The extraction of the adjoint static potential works well using a single-mass Ansatz for  $T \geq 4$  and  $R < R_b$ . At larger distances  $R$ , it is a more complicated matter since the string breaks and the Wilson loop has a poor overlap with the broken-string. This makes the two-mass Ansatz mandatory. To extract the energies of the groundstate and first excited state, as shown in the figures, we use the diagonalisation procedure described in subsection 2.4.3. To illustrate that the static potential  $V(R)$

---

<sup>5</sup>We do observe an increase in  $\gamma$  with increasing  $R$ , visible until  $R \sim 6a$ . This increase can be understood as a  $1/R$ -correction to  $\gamma$  coming from the next-to-leading term in the bosonic string theory [57].

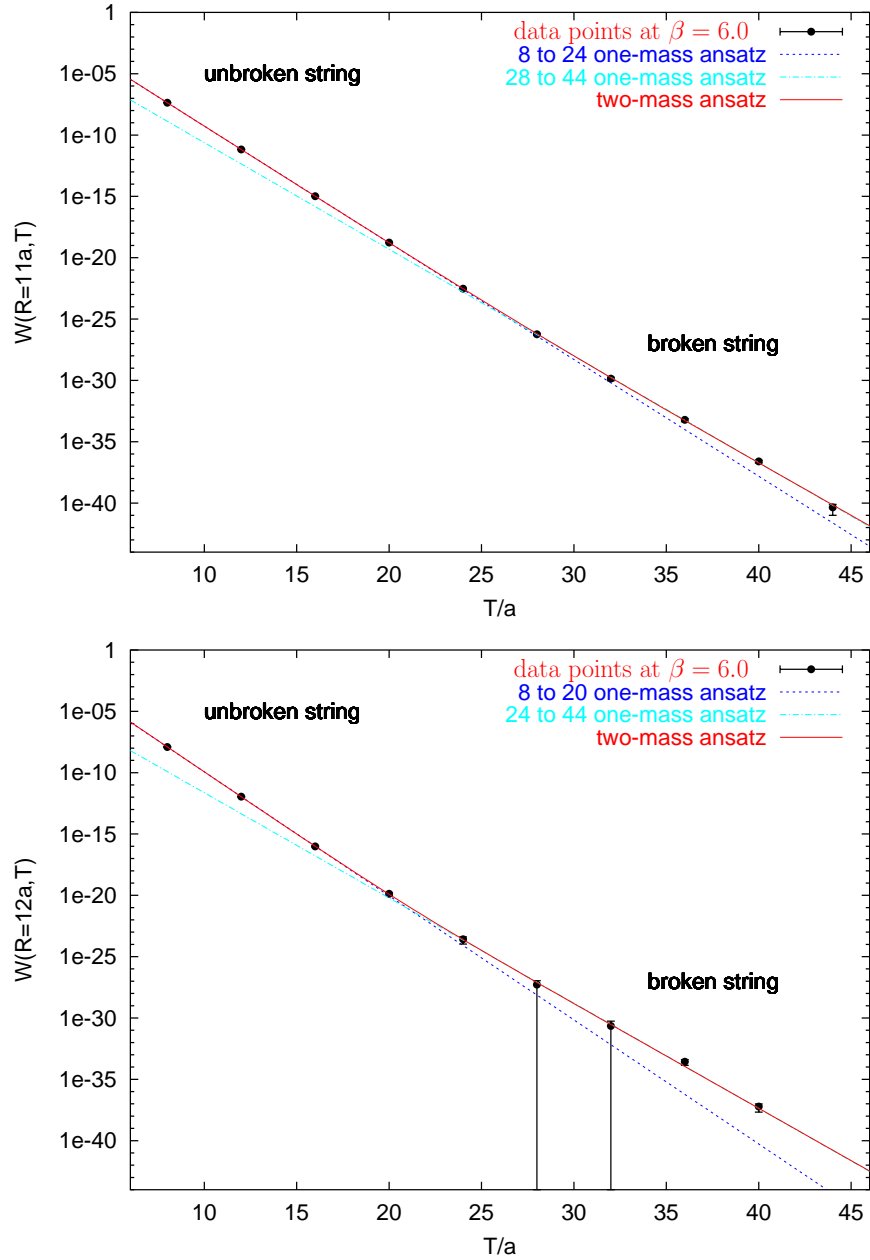


Figure 2.6: Adjoint Wilson loop data versus  $T$ , for  $R = 11a$  and  $R = 12a$ , obtained from a diagonalisation procedure Eq.(2.56), applied to Wilson loops, considering three different levels of smearing. A two-mass Ansatz accounts for all data points. Single-exponentials (dotted lines) do not. At large  $T$ , the broken-string groundstate is exposed. Note how small a signal can be measured.

at a fixed  $R > R_b$  cannot be determined by a single-mass, we show in Fig. 2.6  $W(R, T) = \lambda^{(0)}(R, T, T_0)$  (see Eq.(2.56)) at  $R = 11a$  and  $R = 12a$ . Here we want to

make use of the full Wilson loop data without distorting the ratio  $\frac{c_1}{c_0}$  of Eq.(2.12). We use a simplified version of the diagonalisation procedure to obtain  $\lambda^{(0)}(R, T, T_0)$  using Wilson loops only:

We have three types of staple-shaped transporter  $\sqcup, \sqcap$  as used in Eq.(2.50). In the same notation, the Wilson loops correlation matrix is

$$\square = S_{s_1} S_{s_2}(R, T) = \begin{pmatrix} S_{15} S_{15} & S_{15} S_{30} & S_{15} S_{60} \\ S_{30} S_{15} & S_{30} S_{30} & S_{30} S_{60} \\ S_{60} S_{15} & S_{60} S_{30} & S_{60} S_{60} \end{pmatrix} \quad (2.55)$$

1. For a fixed  $R$ , we diagonalise the matrix  $S_{s_1} S_{s_2}(R, T_0)$ , where we choose  $T_0$  so that the overlap with the desired state (e.g. the groundstate) is as large as possible and the signal still quite accurate. Setting  $T_0 \gtrsim T_P$  is a natural choice. E.g. at  $R = 12a$  we choose  $T_0 = 24a$ .
2. We use the eigenvectors  $\mathbf{v}_0(R, T_0)$ ,  $\mathbf{v}_1(R, T_0)$  and  $\mathbf{v}_2(R, T_0)$ , where the corresponding eigenvalues fulfill  $\lambda^{(0)}(R, T_0) > \lambda^{(1)}(R, T_0) > \lambda^{(2)}(R, T_0)$ , to project  $S_{s_1} S_{s_2}(R, T)$  to the different states at all  $T$  by

$$\lambda^{(n)}(R, T, T_0) = v_{n,s_1}(R, T_0) S_{s_1} S_{s_2}(R, T) v_{n,s_2}(R, T_0). \quad (2.56)$$

$\lambda^{(0)}(R, T, T_0)$ , the largest eigenvalue, contains amplified information about the groundstate and  $\lambda^{(1)}(R, T, T_0)$  information about the first excited state.  $\lambda^{(2)}(R, T, T_0)$  is some effective value containing information about the remaining excitations.  $W(R, T) = \lambda^{(0)}(R, T, T_0)$  has to be analysed with a two-mass Ansatz and the ratio  $\frac{c_1}{c_0}$  can be extracted.

$$W(R, T) = c_0 e^{-V(R)T} + c_1 e^{-E_1 T}, \quad T > T_{\min}. \quad (2.57)$$

$V(R)$  corresponds to the groundstate,  $E_1$  is the first excited state energy. The groundstate is the broken-string state and therefore,  $V(R)$  should be the energy of two gluelumps  $E(2Q\bar{g}) \approx 2M(Q\bar{g})$ . At small temporal extent  $T$  of the Wilson loop  $W(R, T)$  we get a larger slope than at large  $T$ , as visible in Fig. 2.6. This can be

explained as elaborated in section 2.3: At small  $T$  the signal is dominated by the unbroken-string state. The broken-string state can only be observed once  $T$  is large enough since the Wilson loop observable has a poor overlap with this groundstate. The ratio  $\frac{c_1}{c_0}$  quantifies the domination of the unbroken-string state signal versus the broken-string state and is related to the turning point  $T_P$  (see Eq.(2.13)). We obtain  $\frac{c_1}{c_0} \Big|_{R=12a} = 3.1(4)10^3$ , while the prediction of the strong coupling expansion [45] was  $\frac{c_1}{c_0} \Big|_{R=12a} \approx 2 \times 10^5$  and (see Eq.(2.14))  $T_P^{(est)} \Big|_{R=12a} \approx 42a$ . Our numerical determination of the turning point  $T_P \Big|_{R=12a} = 22(1)a$  is clearly below this estimate.

Note that we can detect signals down to  $10^{-40}$ , which corresponds to  $10^{80}$  ordinary measurements. Previously, only signals down to  $10^{-7}$  have been measured, i.e. in a regime where the unbroken-string state is dominating over the groundstate. This explains why string breaking has not been observed in Wilson loops up to now.

### Excited states

Excited states of the fundamental representation are suppressed too much for us to measure. But in the adjoint representation, we have clear information about the first excited state. Using the diagonalisation procedure Eq.(2.39), one source of information is the two-mass fit of  $W(R, T) = \lambda^{(0)}(R, T, T_0)$  at large distances  $R \geq R_b$  where the first excited state is the unbroken-string state. Another, related, source of information, also for smaller  $R$ , is  $W_1(R, T) = \lambda^{(1)}(R, T, T_0)$ .

In the same manner as for the static potential, we adopt here a two-mass Ansatz

$$W_1(R, T) = e_0 e^{-V(R)T} + e_1 e^{-V_1(R)T}, \quad T > T_{\min}, \quad (2.58)$$

where  $V(R)$  is the static potential and  $V_1(R)$  the energy of the first excited unbroken-string state (as it turns out). In Fig. 2.7, for distances smaller than the string breaking distance  $R_b$  we see a clear signal of the first excited state. However, at larger distance we expect contributions from at least three states: The two-gluelump groundstate, the unbroken-string state, and an excited unbroken- or broken-string

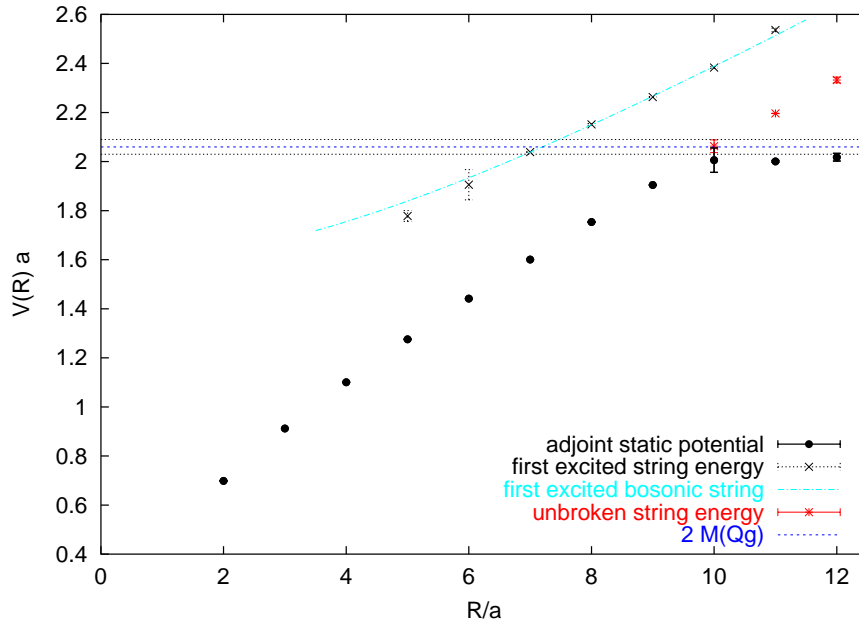


Figure 2.7: The static adjoint potential  $V(R)$  versus  $R$  (same as in Fig. 2.5) and the first excited unbroken-string state energy using Wilson loops only. We also show the energy  $\tilde{E}_1(R)$  (Eq.(2.59)) resulting from the relativistic Nambu string theory. The horizontal line at  $2.06(3)a^{-1}$  represents twice the mass of a gluelump.

state, since one expects a level-crossing of the latter two depending on the spatial distance  $R$ .

Surprisingly, at  $R = 8a$  and  $R = 9a$  we completely miss the broken-string state. The explanation lies in the spectrum at  $R = 8a, 9a$ . The first three terms entering the expansion of the Wilson loop Eq.(2.10) are:

- $c_0 e^{-E_0 T}$  groundstate: lowest-lying energy state of the unbroken-string,
- $c_1 e^{-E_1 T}$  first excited state: lowest-lying energy state of the broken-string,
- $c_2 e^{-E_2 T}$  second excited state: first excited state of the unbroken-string.

The overlap of the Wilson loop operator with the second excited state (unbroken-string),  $c_2$ , is larger than the overlap with the first excited state,  $c_1$ . In addition, the difference between the two corresponding energies  $E_1$  and  $E_2$  is small. In our case, the second excited state indeed dominates over the first in the accessible range of



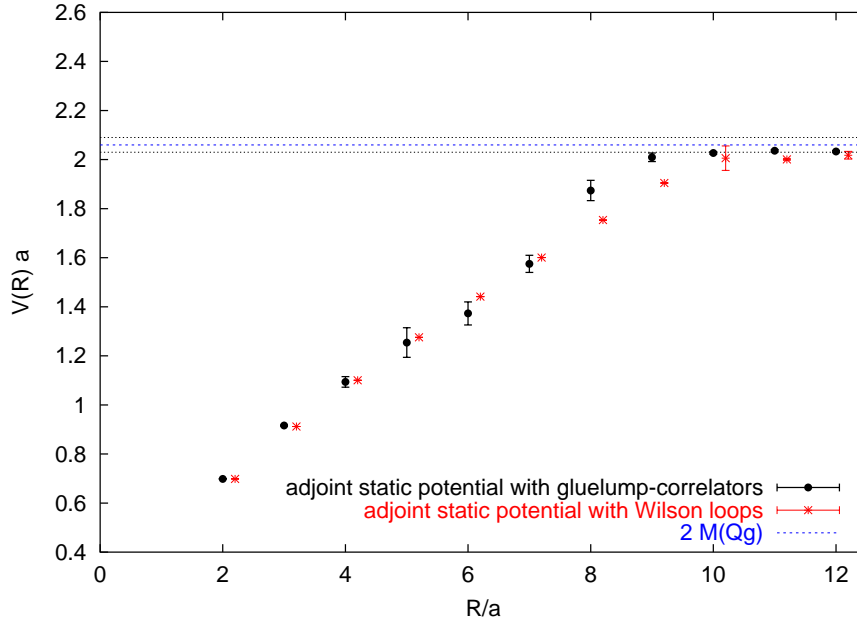


Figure 2.8: Agreement of the static adjoint potential  $V(R)$  versus  $R$ , extracted from the two-gluelump correlator and the one extracted from Wilson loops only (same as in Fig. 2.5, but shifted to the right for clarity). The deviations at  $R = 8a$  and  $R = 9a$  are due to a large value of the turning point  $T_P$ , as explained in the text.

Euclidean times. Therefore, we miss the broken-string state at  $R = 8a$  and  $R = 9a$ .

From our fit of the adjoint potential via Eq.(2.53) we have extracted the string tension  $\sigma$ . We then consider the relativistic Nambu string [58], which predicts for the first excited string energy

$$\tilde{E}_1(R) = \sqrt{\sigma^2 R^2 + 2\pi\sigma\left(1 - \frac{1}{24}\right)} + \text{const.} \quad (2.59)$$

This relativistic bosonic string theory prediction agrees with our measured first excited energy remarkably well, see Fig. 2.7.

## 2.5.2 Gluelumps

We have seen that the Wilson loop operator has an overlap with both states - the unbroken-string and the broken-string state. What about the two-gluelump

operator? At large distances  $R > R_b$ , a single-mass Ansatz is sufficient since the groundstate is the broken-string state, which has good overlap with the correlator of two gluelumps,  $GG(R, T)$ . Therefore, we cannot measure any signal of the unbroken-string state in this regime. At distances  $R < R_b$ ,  $GG(R, T)$  can be analysed using a two-mass Ansatz

$$GG(R, T) \sim g_0 e^{-V(R)T} + g_1 e^{-E_1(R)T}, \quad T > T_{\min}. \quad (2.60)$$

At small  $R$ , the turning point  $T_P$  is small, and the two-mass Ansatz Eq.(2.60) works fine. For  $R = 8a$  and  $R = 9a$ , which approaches the string breaking distance  $R_b$ , the energies of the unbroken-string and broken-string state are almost degenerate, and the turning point value is large. As mentioned in subsection 2.4.4, we used improved spatial transporters to measure Wilson loops. Here, we use non-improved clovers and have more noise. In addition, we have only one operator-state and cannot apply a diagonalisation procedure. Therefore, we have difficulties to measure the subleading groundstate exponential decay in this regime. We lose the signal of the unbroken-string state before it becomes visible and cannot extract the unbroken-string groundstate properly.

Fig. 2.8 shows the agreement between the static potential extracted from Wilson loops only and that extracted from the two-gluelump correlator. This confirms that  $GG(R, T)$  has a non-vanishing overlap with the unbroken-string state, similar to the fact, that the Wilson loop has a non-vanishing overlap with the broken-string state.

$GG(R, T)$  can also be used in the multichannel Ansatz as explained in section 2.3. It enters as a diagonal matrix element in the 4x4-matrix  $V_{ij}(R, T)$  Eq.(2.50). We will now consider this approach.

### 2.5.3 Multichannel Ansatz

The full multichannel matrix Eq.(2.50) is obtained by including the mixing terms  $S_i G(R, T)$  and  $G S_j(R, T)$ .

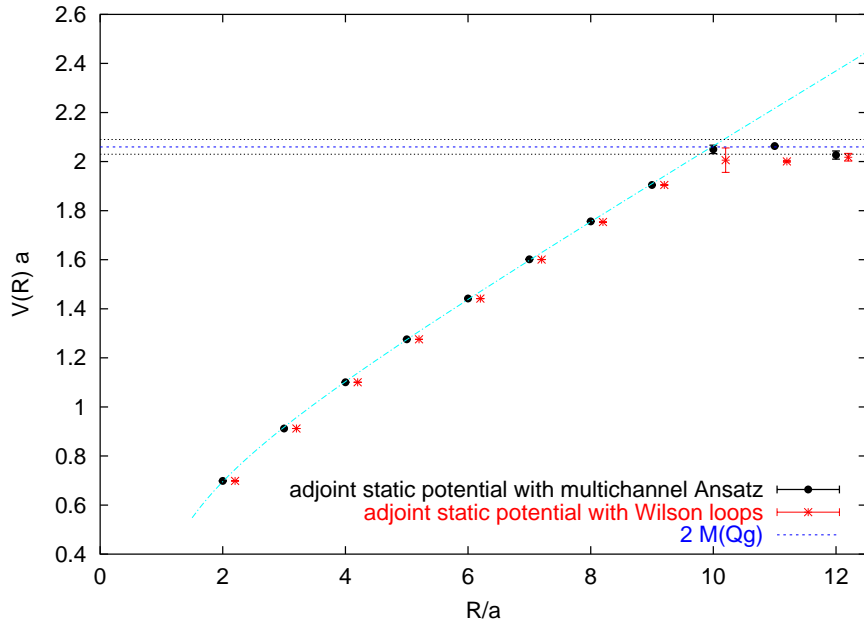


Figure 2.9: The static adjoint potentials  $V(R)$  versus  $R$  using the multichannel Ansatz. The agreement with the static potential extracted from Wilson loops only (same as in Fig. 2.5, shifted to the right for clarity) is good. The unbroken-string state energy is also drawn (dashed line). The horizontal line at  $2.06(3)a^{-1}$  represents twice the mass of a gluelump.

### Static potential

We analyse the  $4 \times 4$  matrix using the diagonalisation procedure Eq.(2.39) at  $T_0 = 4a$ , as described in subsection 2.4.3. As expected, a single-mass Ansatz can be applied for all  $R$  using  $\lambda^{(0)}(R, T, T_0 = 4a)$ . The results, presented in Fig. 2.9, agree with the static potential extracted from Wilson loops only, with improved accuracy for  $R > R_b$ .

The three Wilson loop operator states at different smearing levels have a good overlap with the unbroken-string state, but a poor one with the broken-string state. The opposite holds for the two-gluelump operator state. To confirm this statement, we analyse the overlaps  $a_j^{(n)}(R, T, T_0)$  of Eq.(2.40). We consider the overlap of all three Wilson loop operator states ( $j = S_{15}, S_{30}, S_{60}$ ) and the overlap of the two-

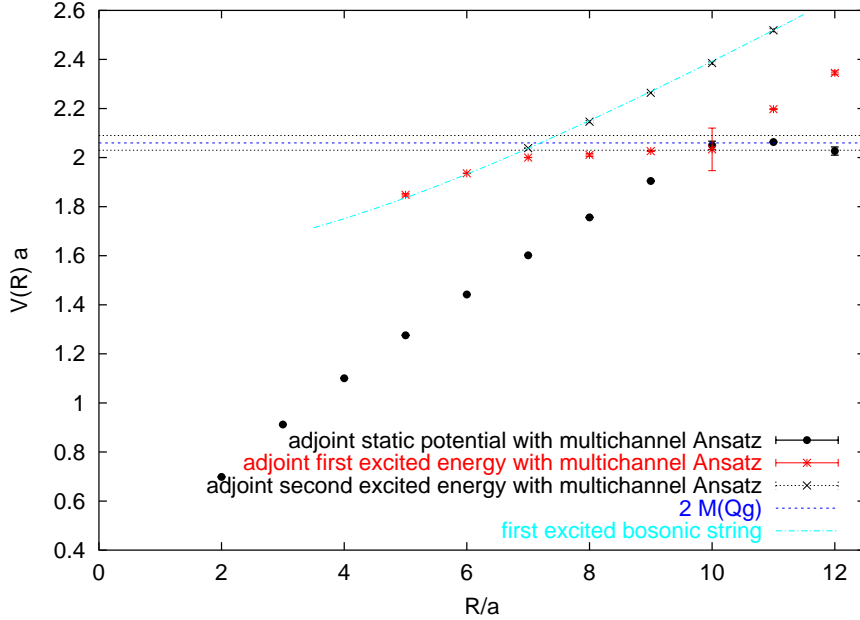


Figure 2.10: The static potential  $V(R)$ , the first and the second excited states energies using the multichannel Ansatz. We also show the energy  $\tilde{E}_1(R)$  (Eq.(2.59)) resulting from the relativistic bosonic string theory. The horizontal line at  $2.06(3)a^{-1}$  represents twice the mass of a gluelump.

gluelump operator state ( $j = G$ ) with the groundstate ( $n = 0$ )<sup>6</sup>. We observe for  $a_G^{(0)}(R, T, T_0)$  an abrupt change from  $O(10^{-3})$  ( $R \leq 10a$ ) to  $O(1)$  ( $R > 10a$ ) and vice versa for  $a_S^{(0)}(R, T, T_0)$ . This indicates that string breaking actually occurs at a distance slightly larger than  $10a$ .

### Excited states

Considering  $\lambda^{(1)}(R, T, T_0 = 4a)$ , we get information about excited states by applying a two-mass Ansatz. For  $R > R_b$ , we extract the lowest-lying unbroken-string state as expected. For  $R = 8a$  and  $R = 9a$ , the first excited state is the broken-string state. For  $R = 7a$ , the broken-string state and the excited unbroken-string state energies are almost degenerate. For  $R < 7a$  we extract the energy values of the

<sup>6</sup>In  $a_j^{(n=0)}(R, T, T_0 = 4a)$  of Eq.(2.40) we fix  $T = 8a$ . The results are stable for larger  $T$ , although with increasing errors.

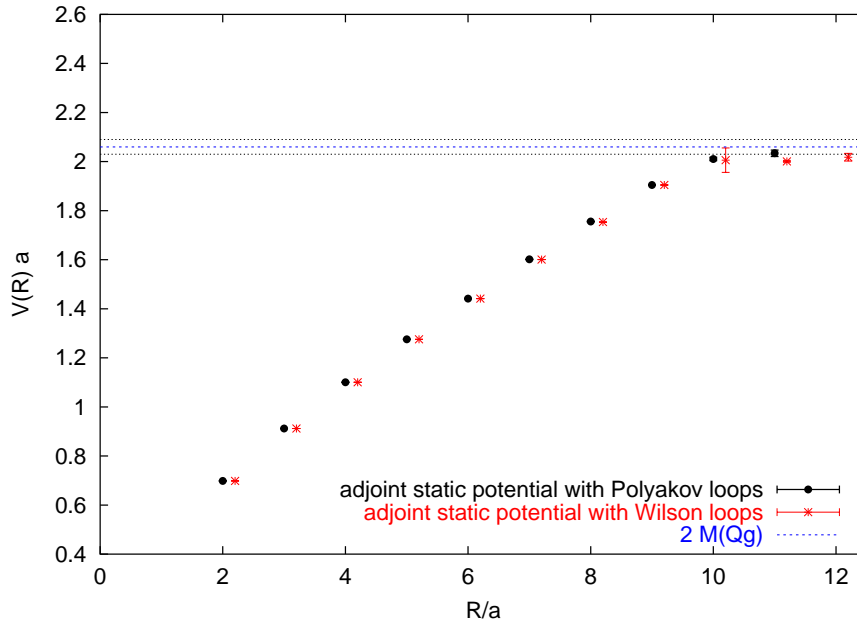


Figure 2.11: Polyakov loop method. The static adjoint potential  $V(R)$  versus  $R$  extracted from the correlator of two adjoint Polyakov loops agrees very well with that measured using Wilson loops only (same as in Fig. 2.5, shifted to the right for clarity). The flattening of the potential can be observed, although we cannot extract the value at  $R = 12a$  due to large fluctuations.

excited unbroken-string state which are in agreement with the ones extracted using Wilson loops only. For  $R < 5a$  we can no longer extract first excited state energies due to statistical noise. Finally, considering  $\lambda^{(2)}(R, T, T_0 = 4a)$ , for  $R \geq 7a$ , we obtain the energy of the second excited state, namely the excited unbroken-string state. For  $R < 7a$  we cannot extract the second excited energy due to statistical noise. In Fig. 2.10, we show the static potential extracted from  $\lambda^{(0)}(R, T, T_0 = 4a)$ , the first excited energy, extracted from  $\lambda^{(1)}(R, T, T_0 = 4a)$  and the second excited energy, extracted from  $\lambda^{(2)}(R, T, T_0 = 4a)$ .

### 2.5.4 Polyakov loops

The correlator of two adjoint Polyakov loops allows the extraction of a temperature-dependent potential  $V_{\mathcal{T}}(R)$  (see Eq.(2.15))

$$V_{\mathcal{T}}(R) \equiv -\frac{1}{N_t a} \log \langle \text{Pol}(0) \text{Pol}^*(R) \rangle . \quad (2.61)$$

The temperature of our system is  $\mathcal{T} = \frac{1}{N_t a} \approx 30$  MeV since  $N_t = 64$  is the temporal extent of the lattice and  $a = 0.1022(1)$  fm the lattice spacing. Since this temperature is quite low, contributions of excited states are negligible. Therefore, we observe a good match with the static potential measured using Wilson loops only (see Fig. 2.11).

In the regime of string breaking  $R \approx 10a$  we see flattening of the potential indicating string breaking. For  $R = 12a$ , the signal becomes very noisy and the average correlator is negative.

### 2.5.5 Casimir scaling

Since we measure the static potentials between fundamental and between adjoint charges with high accuracy, we can examine the hypothesis of Casimir scaling, which says that the ratio of the adjoint static potential over the fundamental static potential remains equal to the Casimir value  $\frac{8}{3}$  over a broad range of distances where both potentials grow more or less linearly with distance. Already in Fig. 2.5, we see clear deviations from Casimir scaling: The fundamental static potential, rescaled by the Casimir factor  $\frac{8}{3}$ , agrees with the adjoint static potential at small distances  $R \leq 2a$  only. This confirms earlier observations of Ref. [39], also at  $\beta = 6.0$ , and of Ref. [59] at  $\beta = 9.0$ . Therefore, we apply a more careful analysis considering forces, defined by

$$F(r_I) = -\frac{V(r) - V(r - a)}{a} , \quad (2.62)$$

where  $r_I$  is chosen such that the force evaluated from Eq.(2.62) coincides with the force in the continuum at tree level [55]. The procedure to determine the explicit

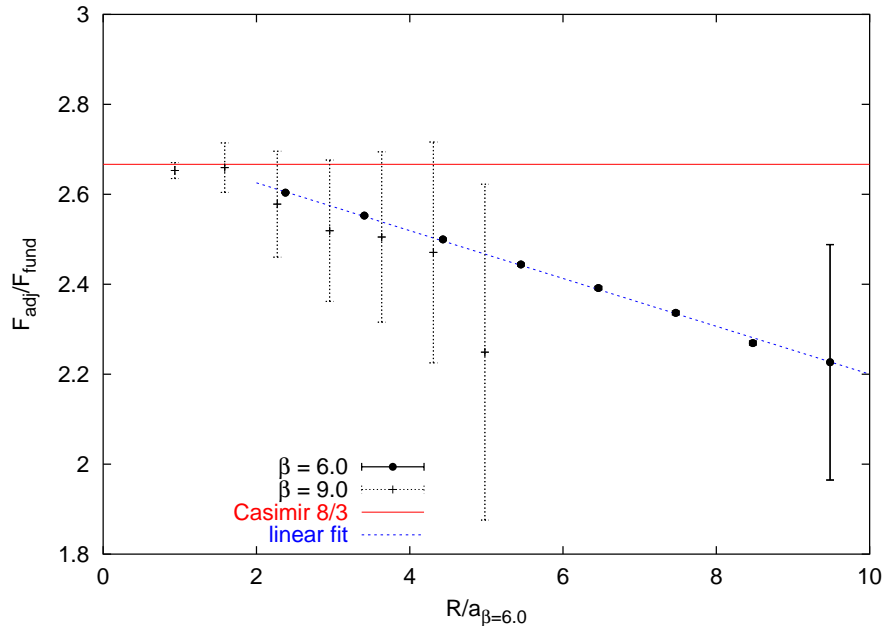


Figure 2.12: Ratio of forces  $\frac{F_{\text{adj}}(R)}{F_{\text{fund}}(R)}$  as a function of the spatial separation. The horizontal line at  $\frac{8}{3}$  indicates the Casimir ratio expected from perturbation theory. We see clear deviation at distances larger than  $R = 2a$ . The ratio seems to decrease linearly while increasing  $R$ .

values of  $r_I$  is described in Appendix A.

In Fig. 2.12, we show the ratio  $\frac{F_{\text{adj}}(R)}{F_{\text{fund}}(R)}$  at two different  $\beta$ 's. In the regime of perturbation theory, i.e. at small distances  $R$ , this ratio is  $\frac{8}{3}$  as expected. At larger distances, our  $\beta = 6.0$  data show clear deviations. The ratio appears to decrease linearly with increasing distance<sup>7</sup>  $R$ . The less precise data at  $\beta = 9.0$  of Ref. [59] seem to confirm this  $R$ -dependence, making it unlikely to be an artifact of the lattice spacing.

Our results do not necessarily contradict the work of Ref. [60], which found accurate Casimir scaling at large distances. [60] considers the  $4d$   $SU(3)$  theory, while we consider  $SU(2)$  in 3 dimensions. Rather, what we see might be specific to 3 dimensions.

<sup>7</sup>For  $R > R_b$ , the adjoint string breaks and the force  $F_{\text{adj}}$  is essentially zero. Large fluctuations at  $R \approx R_b$  induce the large error on the rightmost data point in Fig. 2.12.

## 2.6 Conclusions - String Breaking

We have demonstrated that string breaking can be observed, using only Wilson loops as observables to measure the static potential. This demonstration was performed in the computationally easiest setup: breaking of the adjoint string in the  $(2 + 1)$ -dimensional  $SU(2)$  theory. Even in this simple case, the unambiguous observation of string breaking, at a distance  $R_b \approx 1$  fm, required the measurement of adjoint Wilson loops of area in excess of  $4 \text{ fm}^2$ , with state-of-the-art variance reduction techniques. A similar study in  $(3 + 1)$  dimensions with a larger gauge group will be challenging.

The reason for such large loop sizes is as expected: the Wilson loop has very poor overlap with the broken-string. Even when the static adjoint charges are separated by  $R > R_b$  and the broken-string becomes the groundstate, its contribution to the Wilson loop area-law is subdominant. The temporal extent  $T$  of the Wilson loop must be increased beyond a characteristic distance, the turning point  $T_P$ , to weaken the unbroken-string state signal and reveal the true groundstate. We find  $T_P \sim 2$  fm, which explains why earlier studies, which did not use similar variance reduction methods, failed to detect string-breaking. While large, this turning point value stays well below the strong-coupling estimate of [45], which would predict a value about twice as large.

Of course, string-breaking is easy to observe, over a limited Euclidean time extent, if one uses a multichannel approach where a correlation matrix between unbroken- and broken-string states is formed and diagonalised, the latter being modelled by a pair of gluelumps. We reproduce in this case the results in the literature. We also consider the two-gluelump correlator, which has poor overlap with the unbroken-string state, and show that the unbroken-string groundstate can be extracted from that correlator alone, if one allows again for a large Euclidean time extent. Therefore, full information about the adjoint potential is contained in each of the diagonal elements of the multichannel matrix.



Finally, we looked in detail at the issue of Casimir scaling, by measuring the ratio of forces  $\frac{F_{\text{adj}}(R)}{F_{\text{fund}}(R)}$  as a function of  $R$ . We observe clear deviations of this ratio from the perturbative value  $\frac{8}{3}$ , and an apparent linear decrease with  $R$ . A consistent cross-check at a smaller lattice spacing makes this violation of Casimir scaling unlikely to be a lattice artifact. The situation, however, may be different in the  $(3+1)d$  theory.



# Chapter 3

## QCD Toy Model

### 3.1 Motivation

Monte Carlo simulations provide a powerful tool to understand properties of physical models from first principles, ie. based on the fundamental Hamiltonian  $\hat{H}$  rather than on effective descriptions. The hermiticity of the Hamiltonian ensures a positive Boltzmann weight  $e^{-\frac{1}{T}\hat{H}} \rightarrow e^{-S}$ , see Eq.(1.64). It may occur that the models are modified by putting in an external field by hand, which causes the weight to become complex, as in the case of a chemical potential in Lattice QCD. While this is not a conceptual problem, it causes technical difficulties when one attempts to study these systems by the usual Monte Carlo methods, which require a real and positive sampling weight. To gain insight how to treat such systems here we study a simple model with a complex phase.

A common approach is to take the absolute value of the complex weight as the sampling weight  $e^{-S(\mu)} = |e^{-S(\mu)}|e^{i\phi} \rightarrow |e^{-S(\mu)}|$ . The complex measure depends on some parameter called  $\mu$ . The expectation value of any observable in the physical system with volume  $V$  can be rewritten as

$$\langle \hat{O} \rangle_{\mu} = \frac{\langle \hat{O} e^{i\phi(V,\mu)} \rangle_{||}}{\langle e^{i\phi(V,\mu)} \rangle_{||}}, \quad (3.1)$$

where  $\langle \rangle_{||}$  refers to the sampled ensemble. The error becomes a contribution proportional to  $1/\langle e^{i\phi(V,\mu)} \rangle_{||}$ , which grows exponentially in  $V$  and  $\mu$ , see for example [61]<sup>1</sup>. To preserve statistical accuracy as  $V$  or  $\mu$  is increased, the Monte Carlo sample size  $N$  must grow exponentially, since the statistical error is proportional to  $\frac{1}{\sqrt{N}}$ . This is the “sign problem”. If we find a method such that the required statistics is polynomial in  $V$  and  $\mu$ , we say that the “sign problem” is solved. In general, this is not possible. However, by exploiting specific properties of a given model, in particular in zero or one dimensions, it may be feasible to find such a solution, as we will demonstrate. One should keep in mind, however, that generalisations, for example to higher dimensions, is usually not straight-forward or even possible.

The above choice to take the absolute value as the sampling weight is not unique. Any positive measure may be chosen. This general strategy is known under the name “reweighting”, since the weight given to each configuration in the Monte Carlo sample is no longer uniform. It is important to note that the “sign problem” is often accompanied by the lesser-emphasised “overlap problem”. There is a priori no guarantee that the sampled Monte Carlo partition function will produce a representative sample for the physical partition function, because the respective integrands may have poor overlap. A simple, but not foolproof way to detect whether there is an “overlap problem” is to monitor the distribution of the weights assigned to the various Monte Carlo configurations. In extreme situations, one configuration may dominate the partition function causing the complete breakdown of statistical sampling. A reasonable measure of the severity of this problem is thus provided by the width of the distribution of the logarithm of weights.

In the following section we present our simplified model, which encodes the main characteristics of the “sign problem”. In section 3.3, we present various methods to

---

<sup>1</sup>In short:  $\frac{Z(\mu)}{Z_{MC}} \sim e^{-V\Delta F(\mu)}$ , where  $Z(\mu)$  is the partition function with a complex weight and  $Z_{MC}$  is the sampled partition function. The ratio decreases exponentially in  $V$ . In addition  $\Delta F(\mu)$  increases if  $\mu$  grows.

tackle the “sign problem” and then discuss the difficulties we meet. Eventually, we find an approach to solve the “sign problem” in the context of our simple model, as demonstrated in subsection 3.3.3. We want stress that a generalisation of the strategy, in particular with respect to higher dimensions, seems not to be possible.

## 3.2 The Model: 0-dim Quantum Field Theory

We propose an analytically solvable model, given by the partition function

$$Z(\lambda) = \int dt_{-\infty}^{\infty} e^{-t^2+i\lambda t} \equiv \frac{1}{\sqrt{\pi}} e^{-\frac{\lambda^2}{4}}. \quad (3.2)$$

The goal of this study is to evaluate ratios of partition functions

$$\frac{Z(\lambda)}{Z(0)} = e^{-\frac{\lambda^2}{4}} \quad (3.3)$$

using several Monte Carlo approaches. Since the result is known, we can discuss systematic uncertainties such as the underestimation of statistical errors.

Ratios of partition functions can be measured in a MC simulation, for example by

$$\frac{Z(\lambda)}{Z(0)} = \frac{\int dt e^{-t^2} e^{i\lambda t}}{\int dt e^{-t^2}} = \langle e^{i\lambda t} \rangle_{\lambda=0}. \quad (3.4)$$

On the one hand, the measurement of  $e^{i\lambda t}$  in a certain configuration is of order one for any  $\lambda$ . On the other hand, the expectation value is exponentially decreasing, while increasing  $\lambda$ . Therefore, huge cancellations have to take place. This effect is the essence of the “sign problem”.

### 3.2.1 Sign Problem

At non-zero  $\lambda$ , the integrand of our model is oscillatory, and therefore cannot be used as a sampling weight in a Monte Carlo simulation. Instead, we measure

$$\langle \hat{O} \rangle_{\lambda} = \frac{\int dt \hat{O} e^{-t^2+i\lambda t}}{\int dt e^{-t^2+i\lambda t}} = \frac{\int dt \hat{O} e^{+i\lambda t} e^{-t^2}}{\int dt e^{+i\lambda t} e^{-t^2}} = \frac{\langle \hat{O} e^{i\lambda t} \rangle_{\lambda=0}}{\langle e^{i\lambda t} \rangle_{\lambda=0}}. \quad (3.5)$$

This expression results in the correct expectation value, if the statistics is large enough. Unfortunately, computational resources are limited, say, to  $N$  measurements, thus the above expectation value is biased. The question arises, how much can we increase  $\lambda$ ? The relative error, see Appendix B, is given by

$$\left(\frac{\Delta\langle\hat{O}\rangle_\lambda}{\langle\hat{O}\rangle_\lambda}\right)^2 = \left(\frac{\Delta\langle\hat{O}e^{i\lambda t}\rangle_{\lambda=0}}{\langle\hat{O}e^{i\lambda t}\rangle_{\lambda=0}}\right)^2 + \left(\frac{\Delta\langle e^{i\lambda t}\rangle_{\lambda=0}}{\langle e^{i\lambda t}\rangle_{\lambda=0}}\right)^2 + \dots > \left(\frac{\Delta\langle e^{i\lambda t}\rangle_{\lambda=0}}{\langle e^{i\lambda t}\rangle_{\lambda=0}}\right)^2. \quad (3.6)$$

The “sign problem” is encoded in the expectation value of the complex phase  $e^{i\lambda t}$ , which decreases exponentially

$$\langle e^{i\lambda t}\rangle_{\lambda=0} = e^{-\frac{\lambda^2}{4}} \xrightarrow{\lambda\rightarrow\infty} 0. \quad (3.7)$$

The error, however, remains constant

$$\Delta\langle e^{i\lambda t}\rangle_{\lambda=0} \sim \frac{1}{\sqrt{N}}. \quad (3.8)$$

For a given computer budget, the limiting  $\lambda$  is given by

$$N \sim e^{\frac{\lambda^2}{2}}. \quad (3.9)$$

If we succeed to find a method to measure  $\langle e^{i\lambda t}\rangle_{\lambda=0} = \frac{Z(\lambda)}{Z(0)}$  accurately for any  $\lambda$  without exponentially, but polynomially growing statistics, we have solved the “sign problem” for this particular case.

### 3.2.2 Overlap Problem

A less well known problem is the “overlap problem”. It comes from the fact, that the distribution function of the sampling model might have small or vanishing overlap with the one of the physical model.

In Fig. 3.1, we plot two different situations. A clear overlap problem is illustrated in the left sketch. The sampled distribution has an exponentially small overlap with the desired distribution. In a MC simulation with finite statistics, no or only a few configurations  $\{t\}$ , which are important for the integral, are sampled. This can lead

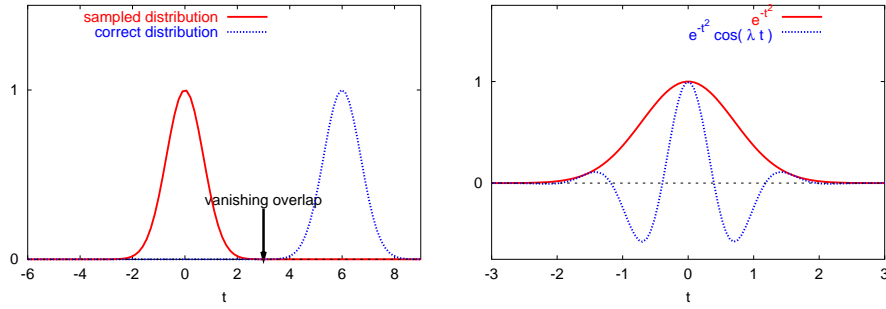


Figure 3.1: Simple illustration of the overlap problem. A typical example of a sampled distribution versus the correct distribution with vanishing overlap. No relevant “configurations” are sampled (left). The sampled distribution at  $\lambda = 0$  shows a rather good overlap with the distribution at  $\lambda \neq 0$  (right).

to unrealistic errors estimates, if the error analysis is not performed carefully. In the right plot, the sampled distribution versus the real part of the relevant distribution can be seen. The important configurations  $\{t\}$  are in the interval  $[-1 : 1]$ , which is well sampled with  $e^{-t^2}$ , ie.  $\lambda = 0$ . Thus, there is no overlap problem in our toy-model<sup>2</sup>.

### 3.3 Methods and Results

We now will discuss a variety of methods to tackle and finally solve the “sign problem”.

#### 3.3.1 Brute-Force Method

The Brute-Force method

$$\frac{Z(\lambda)}{Z(0)} = \langle e^{i\lambda t} \rangle_{\lambda=0} . \quad (3.10)$$

measures the complex phase  $e^{i\lambda t}$  in an ensemble generated at  $\lambda = 0$ , ie. the sampling weight used in the MC simulation is given by  $e^{-t^2}$ .

---

<sup>2</sup>Trivially, we can factorise the distribution  $e^{-t^2+i\lambda t} \rightarrow e^{-t^2} e^{i\lambda t}$ . While  $e^{-t^2}$  is exponentially decreasing,  $e^{i\lambda t}$  is of order one.

The ratio decreases exponentially while increasing  $\lambda$  and can only be computed accurately by this ordinary Monte Carlo if we gather extremely high statistics. Nevertheless, it is interesting to discuss a few quantities:

1. The histogram of sampled  $t$ 's (Fig. 3.2, top left) confirms that we are sampling the  $\lambda = 0$ -weight as intended. As it has been mentioned above, there is no “overlap problem”.
2. The expectation value of  $\cos(\lambda t)$  is the ratio of the partition functions (Fig. 3.2, top right). We have an excellent reproduction of the analytic result up to  $\lambda \approx 4.5$ . This is expected: Our simulation involves  $N = 50'000$  Monte Carlo steps. Using Eq.(3.9), we can estimate the maximal  $\lambda$  accessible:  $\lambda_{max} = 4.65$ . Note, that for higher  $\lambda$ 's, expectation values can become negative, and therefore are missing in the plot.
3. The histogram of  $\cos(\lambda t)$  (Fig. 3.2, bottom left) provides information about the strength of the “sign problem”. For  $\lambda = 1$ , most measurements of  $\cos(\lambda t)$  are in the positive regime, therefore, the “sign problem” is weak. Starting with  $\lambda = 4$ , the ratio of the partition functions is mainly obtained by cancellations, and the “sign problem” sets in.
4. The expectation value of  $\sin(\lambda t)$  (Fig. 3.2, bottom right) is a check of potential problems with ergodicity and verifies that the errors are estimated correctly: the partition function is a real number, therefore the expectation value of the imaginary part must be zero within errors.

### 3.3.2 Factorisation Method

The Brute-Force method for sure does not solve the “sign problem” as discussed in subsection 3.2.1. The Factorisation method may provide an improvement. It is a general trick which, for example, has helped to improve the efficiency in measuring



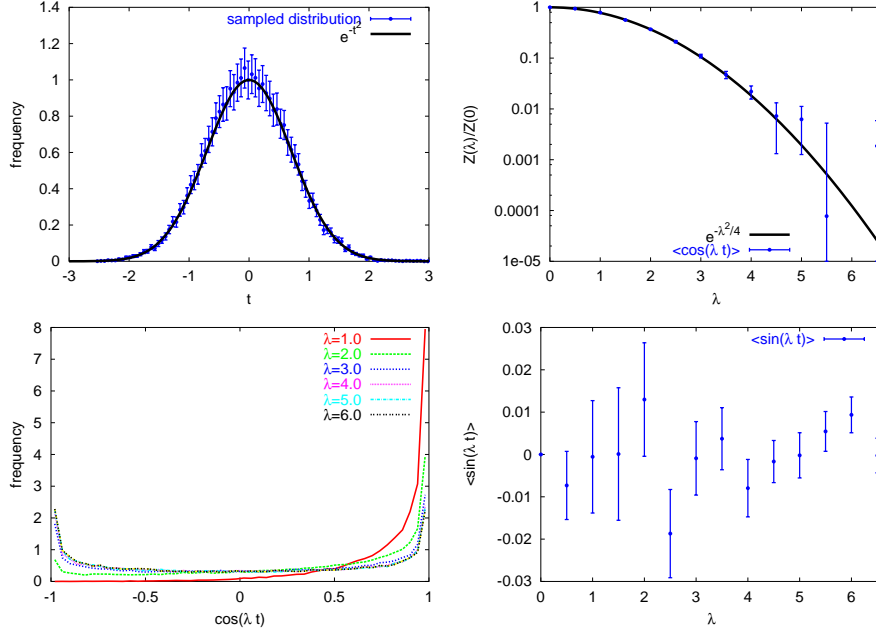


Figure 3.2: The Brute-Force method. The histogram of the sampling variable  $t$  in comparison with the exact integrand (top left). The expectation value  $\frac{Z(\lambda)}{Z(0)} = \langle \cos(\lambda t) \rangle$  in comparison with the exact result (top right). The histogram of the observable  $\cos(\lambda t)$  as a measure of the “sign problem” (bottom left). The expectation value  $\langle \sin(\lambda t) \rangle$  (bottom right) as an indicator for ergodicity, and a check of the correct evaluation of the statistical error.

the  $Z_{N_c}$ -“order-order” interface tension in lattice gauge theories immensely[19]. One evaluates the desired ratio by using the identity

$$\frac{Z(\lambda)}{Z(0)} \equiv \frac{Z_n}{Z_0} = \frac{Z_n}{Z_{n-1}} \frac{Z_{n-1}}{Z_{n-2}} \dots \frac{Z_1}{Z_0} \quad (3.11)$$

where  $Z_k = Z(\lambda_k)$ , for example  $\lambda_k = \frac{k}{n}\lambda$ . In general,  $\lambda_k$  should be chosen, such that each factor in Eq.(3.11) is of  $\mathcal{O}(1)$ .

We reformulate the calculation of  $\frac{Z(\lambda_1)}{Z(\lambda_2)}$  in a generic way. Let us define

$$\langle \hat{O} \rangle_f \equiv \frac{\int dt \hat{O} e^{-t^2} f(t)}{\int dt e^{-t^2} f(t)} \quad (3.12)$$

then

$$\frac{Z(\lambda_1)}{Z(\lambda_2)} = \frac{\int dt \frac{\cos(\lambda_1 t)}{f(t)} e^{-t^2} f(t)}{\int dt \frac{\cos(\lambda_2 t)}{f(t)} e^{-t^2} f(t)} = \frac{\langle \frac{\cos(\lambda_1 t)}{f(t)} \rangle_f}{\langle \frac{\cos(\lambda_2 t)}{f(t)} \rangle_f} = e^{-\frac{\lambda_1^2 - \lambda_2^2}{4}}, \quad (3.13)$$

where we have set to zero the imaginary part. We introduce a function  $f(t)$ , which is positive definite - examples, see Table 3.1. Each factor is a ratio of two expectation values, both very small for large  $\lambda$ . However, numerator and denominator are both estimated by sampling the same configurations  $\{t\}$ . It is hoped that there will be strong error cancellations when estimating the ratio.

$\lambda_1$	$\lambda_2$	$f(t)$	Method
$\lambda$	0	1	Brute-Force method
$\frac{k}{n}\lambda$	$\frac{k-1}{n}\lambda$	$\epsilon +  \cos(\frac{k-\frac{1}{2}}{n}\lambda t) $ , $\epsilon > 0$	Standard Factorisation method
$\frac{k}{n}\lambda$	$\frac{k-1}{n}\lambda$	1	Crompton Factorisation method
$\lambda_1$	$\lambda_2$	$\sqrt{\frac{\cos^2(\lambda_1 t)}{Z^2(\lambda_1)} + \frac{\cos^2(\lambda_2 t)}{Z^2(\lambda_2)}}$	Optimised Factorisation method

Table 3.1: Generalised Factorisation Method. An overview of various choices.

In the Standard and Crompton Factorisation methods, the latter following a suggestion of P. Crompton[62], the function  $f(t)$  has been chosen ad hoc. We have introduced an  $\epsilon > 0$  in the first case, such that the sampling weight does not become zero. By minimising the relative error for a given size  $N$  of the Monte Carlo sample, we determine  $f(t)$  in the Optimised Factorisation method approach. The (unjustified) assumption that the relative error on numerator ( $num$ ) and denominator ( $den$ ) in Eq.(3.13) can be added in quadrature allows for an analytic solution:

$$\Delta_{rel}^2[f] = \left(\frac{\Delta num[f]}{num[f]}\right)^2 + \left(\frac{\Delta den[f]}{den[f]}\right)^2. \quad (3.14)$$

We then apply the central limit theorem

$$\left(\frac{\Delta num[f]}{num[f]}\right)^2 \approx \frac{1}{N} \left( \frac{\langle (\frac{\cos(\lambda_1 t)}{f})^2 \rangle_f}{\langle \frac{\cos(\lambda_1 t)}{f} \rangle_f^2} - 1 \right), \quad (3.15)$$

and it would follow that the optimal function for the numerator is  $f_{num}(t) = \cos(\lambda_1 t)$  ( $f_{den}(t) = \cos(\lambda_2 t)$  for the denominator). By minimising the total relative error

$\Delta_{\text{rel}}[f]$ , we obtain the optimal function

$$f(t) = \sqrt{\frac{\cos^2(\lambda_1 t)}{Z^2(\lambda_1)} + \frac{\cos^2(\lambda_2 t)}{Z^2(\lambda_2)}} \quad (3.16)$$

The partition function  $Z(\lambda)$  is unknown in principle. In this study, we know it exactly and, for educational purposes, make use of this. The optimised function  $f$  has the nice feature, that it does not vanish, unless both cosines do. Moreover, one can compute the relative error, which is a function of  $\lambda_1$ ,  $\lambda_2$  and  $N$ . If one chooses  $N$  and  $\lambda_2$  in advance, then one can adjust  $\lambda_1$ , so that after  $N$  Monte Carlo measurements, the ratio  $\frac{Z(\lambda_1)}{Z(\lambda_2)}$  will be known to some prescribed accuracy. For the results presented in Fig. 3.3, we have chosen a fixed,  $\lambda_1 - \lambda_2 = 0.2$  for simplicity.

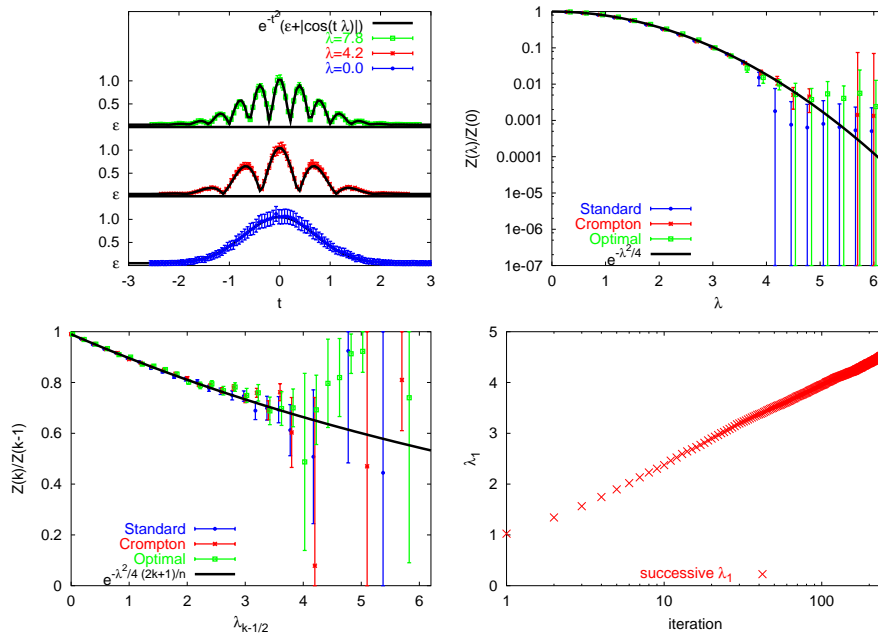


Figure 3.3: The Factorisation method. The histogram of the sampling variable  $t$  in comparison with the exact integrand (top left) for various  $\lambda$ . The expectation value  $\frac{Z(\lambda)}{Z(0)} = \langle \cos(\lambda t) \rangle$  in comparison with the exact result (top right). The expectation value  $\frac{Z(k)}{Z(k-1)}$  in comparison with the analytic result (bottom left). Successive values of  $\lambda_1$  in the Optimal Factorisation method (bottom right).

The sampled  $t$  (top left) are in nice agreement with the sampling function for various  $\lambda$ 's. Despite all the effort, the accessible range in  $\lambda$  could not be enlarged (top

right), based on the same statistics ( $N = 50'000$ ). We lose the signal at around  $\lambda = 4.0 \sim 4.5$ . This result is based on the intermediate factors (bottom left), which are of order one, but cannot be measured accurately for larger  $\lambda_k$ 's. We therefore think, there is no gain by further developing this type of approach - a “magical” cancellation of the error due to correlated measurements has not been observed: the numerator in Eq.( 3.13) can be negative while the denominator is positive or vice versa (see Fig. 3.4 (right)). We can give another, however related argument. Considering the Optimal Factorisation method, we can predict the successive value of  $\lambda_1$  for a given  $\lambda_2$ ,  $N$  and accuracy, which is shown in Fig. 3.3, bottom right. Initially,  $N$  and the accuracy are chosen such that for  $\lambda_2 = 0$  it follows  $\lambda_1 = 1$ . Then, we keep  $N$  and the accuracy fixed, set  $\lambda_2 \leftarrow \lambda_1 = 1$  and solve for the new value of  $\lambda_1$ . The result shows that the spacing ( $\lambda_1 - \lambda_2$ ) decreases exponentially. Therefore, an exponentially increasing effort still is needed to access larger  $\lambda$ 's.

### Sign problem

While discussing the Brute-force method, we have illustrated the “sign problem” by plotting the histogram of sampled  $\cos(\lambda t)$ , see Fig. 3.2, bottom left. More generally, we can do so by considering  $\frac{\cos(\lambda t)}{f(t)}$ . As an example, we want to measure the ratio of partition functions at  $\lambda = 6$ . For this, we use the Standard method with  $\epsilon = 0.05$  and  $n = 20$ . As per Eq.(3.13), we plot in Fig. 3.4

$$\frac{Z_{physical}}{Z_{sampled}} = \left\langle \frac{\cos(\lambda_1 t)}{\epsilon + \left| \cos\left(\left(\lambda_1 - \frac{\lambda}{2n}\right)t\right)\right|} \right\rangle_{Standard}, \quad (3.17)$$

as a function of  $\lambda_1$ . An interesting feature is the maximum of the ratio at  $\lambda_1 = 1$ . We thus can eliminate the “sign problem” for the particular choice  $\epsilon = 0.05$  and  $n = 20$  - however, this works for small  $\lambda_1 \lesssim 1.0$  only! For  $\lambda_1 \gtrsim 4.5$ , the expectation value is zero within errors. The “-”-contributions are thus as important as the “+”-contributions, which indicates that the expectation value is obtained by cancellations.

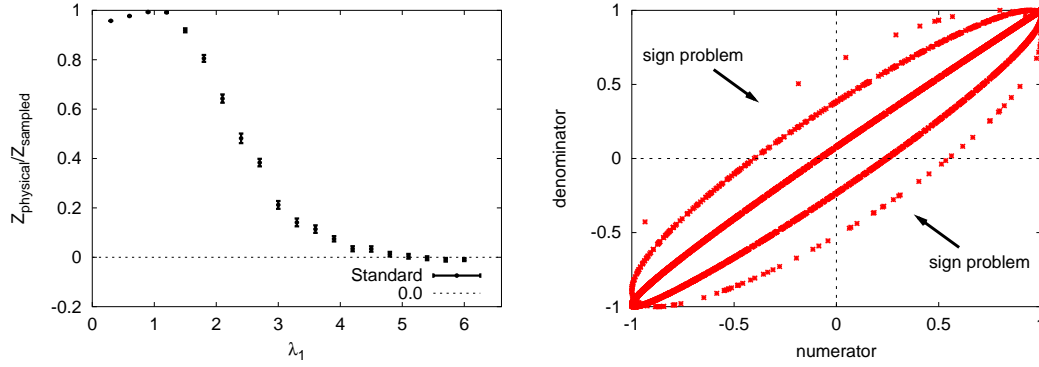


Figure 3.4: Quantification of the “sign problem”.  $\langle \frac{\cos(\lambda_1 t)}{\epsilon + |\cos((\lambda_1 - \frac{\lambda}{2n})t)|} \rangle_{Standard}$  drops to zero fast, while increasing  $\lambda_1$  (left). Another way to see the sign problem is by checking correlations between the numerator and the denominator. The more often the numerator has different sign than the denominator, the stronger the sign problem is. Here, we plot for  $\lambda_1 = 6.0$  (right). Note that we consider one factor of the factorisation formula Eq.(3.11). The expectation value of this factor thus is of order  $\mathcal{O}(1)$ .

### Overlap problem

It is clear that the Factorisation method does not solve the “sign problem”, since it is designed to address and solve the “overlap problem”, which as we saw is not a concern here. As an illustration for this claim, recall the distribution example we have given in subsection 3.2.2. We are interested in a Gaussian distribution  $d(t_{max})$ , which has the maximal contribution at the configuration  $t_{max} = 6$ . Assume that for some reason, we can sample this distribution for  $t_{max} \leq 4$  only, see Fig. 3.5, left.

This schematically should indicate, that the Factorisation method provides a mean to eliminate the overlap problem: Information from the physical distribution is tunnelled to the sampled distribution via intermediate steps, where neighbouring distributions show a good overlap.

In our particular case, Fig. 3.5, right, the important region is correctly sampled, such that we do not have an “overlap problem”.

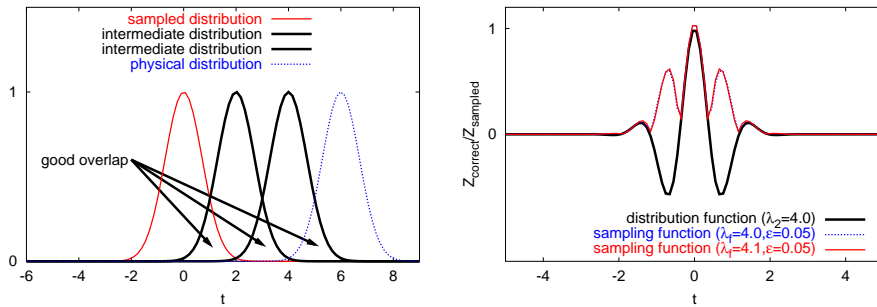


Figure 3.5: The Factorisation method as a mean to solve the “Overlap problem”. Schematically, the Factorisation method allows to conciliate the sampled distribution with the physical distribution, if we find a way to sample “intermediate” distributions (left). The toy model considered here does not suffer from an “overlap problem”: We sample preferably configurations  $\{t\}$ , which are important for the oscillating, correct distribution.

### 3.3.3 Contour Integral

Finally, we would like to test a deformation of the integral from  $-\infty$  to  $+\infty$  into the complex plane. Since the function to integrate  $e^{-t^2+i\lambda t}$  has no poles, the integral can be computed on any deformed contour. The idea is to have the deformed contour go through (or near) the saddle point  $t = i\lambda/2$ . Near the saddle, as expected from stationarity, the cosine stops oscillating, therefore the deformed contour should reduce the “sign problem” substantially, see Fig. 3.6.

We introduce a parametrisation with  $y(t) \xrightarrow{t \rightarrow \pm\infty} 0$  by

$$z(t) = x(t) + iy(t) \quad x(t) = t \quad y(t) = \frac{y_0}{1 + (t/t_0)^2}. \quad (3.18)$$

Analytic continuation leads to

$$Z(\lambda) = \int_{\gamma} dz e^{-z^2+i\lambda z} = \int dt \left( \frac{dz}{dt} \right) e^{-(x(t)+iy(t))^2+i\lambda(x(t)+iy(t))} \quad (3.19)$$

$$= \int dt e^{-x(t)^2+y(t)^2-\lambda y(t)} \left( \cos[x(t)(\lambda - 2y(t))] - \frac{\partial y(t)}{\partial t} \sin[x(t)(\lambda - 2y(t))] \right) \quad (3.20)$$

$$= \int dt e^{-x(t)^2+y(t)^2} H(t, \lambda), \quad (3.21)$$

where  $H(t, \lambda) = e^{-\lambda y(t)} \left( \cos[x(t)(\lambda - 2y(t))] - \frac{\partial y(t)}{\partial t} \sin[x(t)(\lambda - 2y(t))] \right)$ . As sam-

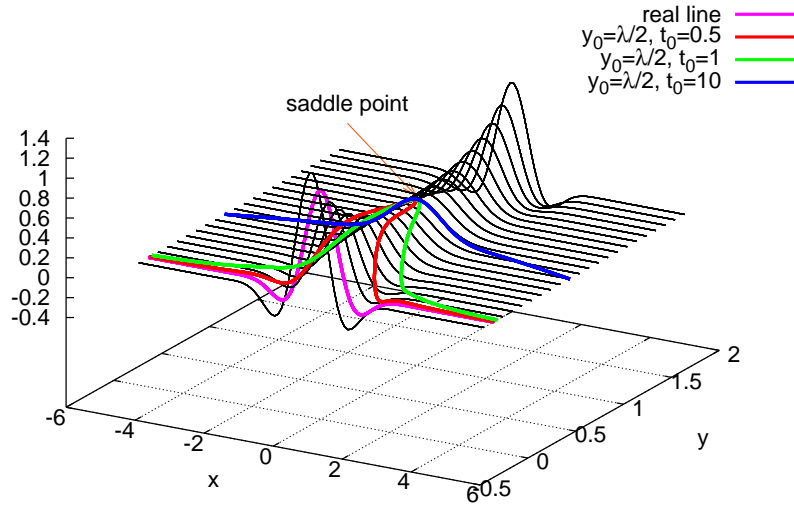


Figure 3.6: The Contour Integral. The integrand stops oscillating around the saddle point. A deformed contour may help to reduce the “sign problem” substantially. Here,  $\lambda = 2.0$  is plotted to increase the visibility.

pling weight we use  $e^{-x(t)^2+y(t)^2}$  (denoted by  $\langle \cdot \rangle_C$ ) and measure

$$\frac{Z(\lambda)}{Z(0)} = \frac{\langle H(x, \lambda) \rangle_C}{\langle H(x, 0) \rangle_C} \quad (3.22)$$

Based on our previous analysis of the Factorisation method, the Brute-Force approach should work fair enough if the Contour Integral method provides a reduction of the “sign problem”. We have two tuning parameters,  $t_0$  and  $y_0$ , where we assume that  $y_0$  should be close to the saddle point.

#### Discussion: $t_0$

Motivated by the observation, that the oscillations stop at the saddle point, we fix  $y_0 = \frac{\lambda}{2}$ . We vary the parameter  $t_0$ . By choosing a large  $t_0$ , we avoid the oscillating regime at the origin, see Fig. 3.6. We perform Monte Carlo simulations for  $t_0 = 1, 10, 100, 10000$ . The results are presented in Fig. 3.7.

In general, we lose the signal at  $\lambda \approx 4.5$  as with the previous methods, almost independently of the choice of  $t_0$ . For  $t_0 = 100$ , however, we have results for larger  $\lambda$ 's.

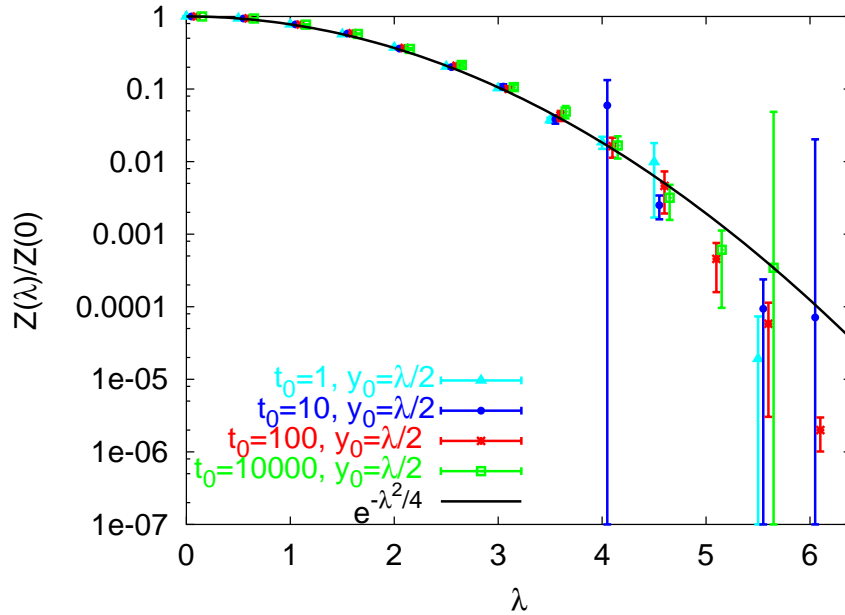


Figure 3.7: The Contour Integral. We fix  $y_0 = \frac{\lambda}{2}$  and vary  $t_0$ . Although we vary  $t_0$  in a huge range, the choice of  $y_0 = \frac{\lambda}{2}$  seems not to extend the range of  $\lambda$  measurable.

Unfortunately, they seem to disagree with the theoretical prediction, in particular at  $\lambda = 6$  within statistical errors. As a consequence, we suspect that the jackknife error underestimates the true error - a danger, one always should be aware of.

### Discussion: $y_0$

We fix  $t_0 = 100$  and vary  $y_0$ , from  $y_0 = \frac{\lambda}{10}$  to  $y_0 = \lambda$ . The results are shown in Fig. 3.8.

For  $y_0 \geq \frac{\lambda}{2}$ , we lose the signal already at small  $\lambda$ . For  $y_0 \leq \frac{\lambda}{10}$ , we are close to the undeformed contour, and also cannot measure beyond the naive limit  $\lambda \approx 4.5$ . In the range  $\frac{\lambda}{6} \leq y_0 \leq \frac{\lambda}{3}$ , we recover the analytic result. A further increase of  $\lambda$  reveals  $y_0 = \frac{\lambda}{4}$  to be the optimal choice, see Fig. 3.9.

At first sight, this result is surprising. We argued that oscillations disappear at the saddle point, which should substantially reduce the sign problem. This is true, but only for the *numerator* in the ratio of partition functions Eq.(3.22). In Fig. 3.10 we plot  $\langle H(x, \lambda) \rangle_C$  and  $\langle H(x, 0) \rangle_C$  for a few choices of  $y_0$  from  $\lambda = 6$  to  $\lambda = 12$ . For



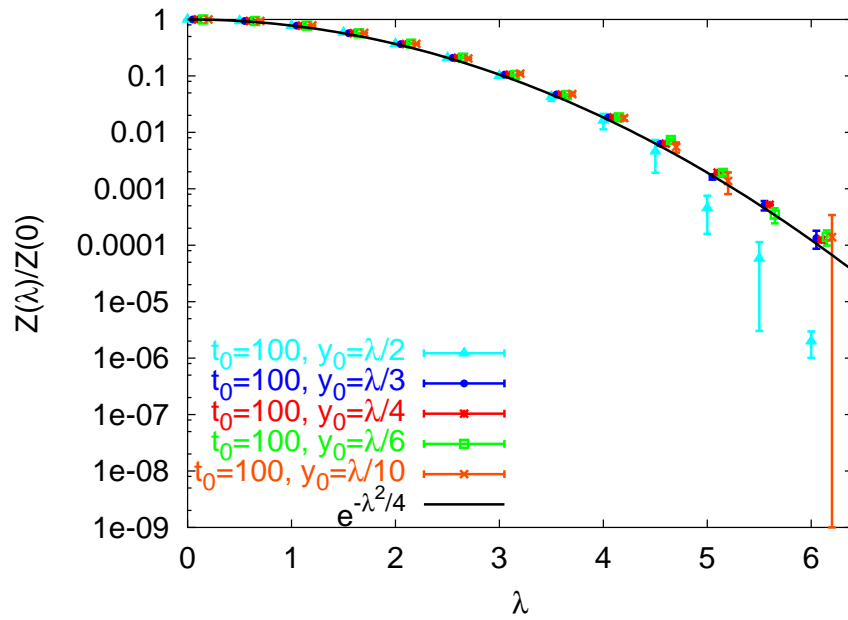


Figure 3.8: The Contour Integral. We fix  $t_0 = 100$  and vary  $y_0$ . For  $\frac{\lambda}{6} \leq y_0 \leq \frac{\lambda}{4}$ , we can recover the analytic result at least up to  $\lambda = 6$ .

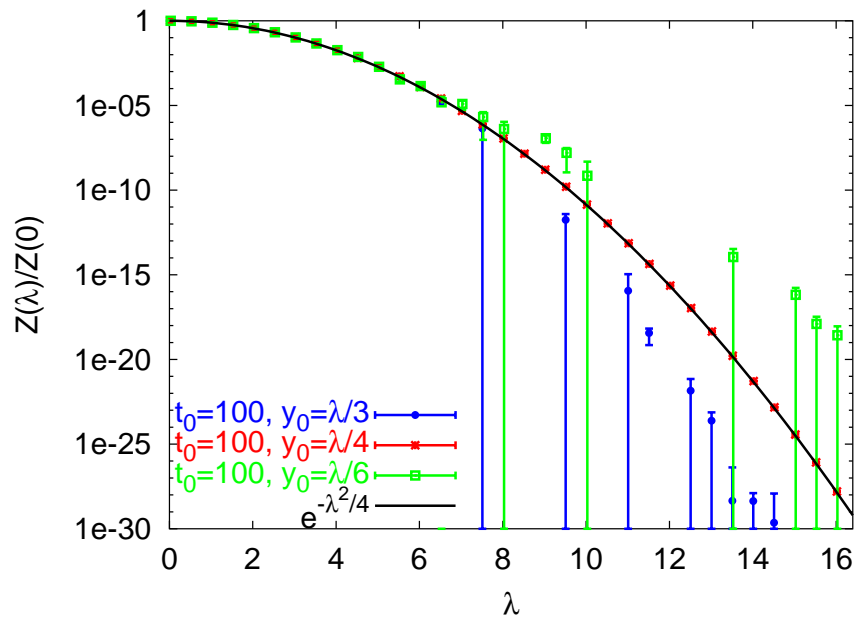


Figure 3.9: The Contour Integral. The choice  $y_0 = \frac{\lambda}{4}$  solves the “sign problem” for this toy model.

$y_0 = \frac{\lambda}{2}$ , the numerator is measured with high accuracy for any  $\lambda$ , while using an almost undeformed contour,  $y_0 = \frac{\lambda}{20}$ , the denominator is obtained with negligible statistical errors. The choice  $y_0 = \frac{\lambda}{4}$  is a trade-off, and indeed, a “magical” cancellation of the error due to correlated measurements is observed (unlike in the other methods). We present the correlation between the numerator and the denominator in a log-log plot. If the numerator is small/large/positive/negative, the denominator is small/large/positive/negative. There are only a few incidents where the numerator has different sign than the denominator: for  $t_0 = 100$ , 4-8 out of  $N = 50'000$ , for  $t_0 = 1000$ , 0-1 out of  $N = 50'000$ . In the limit  $t_0 \rightarrow \infty$ , we parameterise with  $y(t) = y_0$ , and we have perfect correlation due to the shape of  $H(t, \lambda)$ , see Eq.(3.19). In the case  $\frac{\partial y(t)}{\partial t} = 0$ , the signs of  $H(t, \lambda)$  and  $H(t, 0)$  are identical for all  $t$  since  $\cos[x(t)(\lambda - 2\frac{\lambda}{4})] = \cos[x(t)(-2\frac{\lambda}{4})]$ .

### 3.4 Conclusions - QCD Toy Model

We have investigated a simple model with a complex phase, which suffers from the “sign problem” due to oscillations, which are controlled by the parameter  $\lambda$ . We have tested various methods, of which most break down at a value of  $\lambda \sim \sqrt{2 \log N}$ , where  $N$  is the number of measurements. One strategy, the change of the integration contour, works beautifully and solves the “sign problem” in the context of the 0-dimensional quantum field theory by carefully tuning the contour parameters  $y_0 = \frac{\lambda}{4}$  and  $t_0 \gtrsim 100$ . The “overlap problem” has been illustrated, and a method to overcome this technical problem, namely the Factorisation method, has been introduced.

What can we learn from this study for our next project, QCD at Finite Density? Although it would be very interesting to generalise to QCD the strategy, which worked so well on the QCD toy model, we were not able to do so: in the contour integral method, we deform the (co)domain of our field from real ( $t$ ) into the complex plane ( $z(t) = x(t) + iy(t)$ ); in QCD, this would, for example, correspond to allow for non-

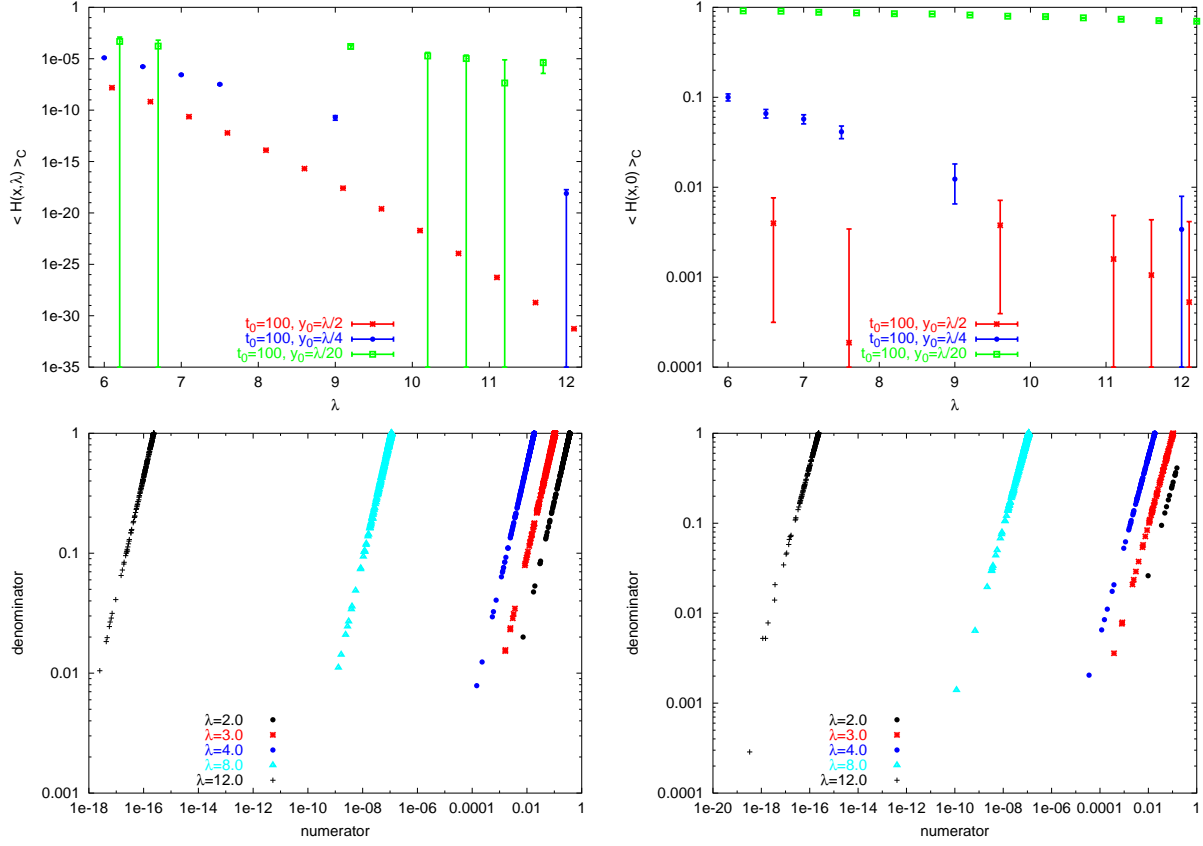


Figure 3.10: The Contour Integral. The numerator has small errors for  $y_0 = \frac{\lambda}{2}$  (top left), while the denominator has small errors for  $y_0 = \frac{\lambda}{20} \approx$  undeformed (top right). With the choice  $y_0 = \frac{\lambda}{4}$ , we observe strong correlation between the numerator and the denominator in Eq.(3.22). We plot the case “positive numerator” (bottom left) and “negative numerator” (bottom right).

unitary colour matrices, or to allow for a complex chemical potential. In the latter it is unclear what the integration contour should look like. Therefore, we have to find a different approach, which avoids the “sign problem”. The canonical framework, which depends on the baryon number  $B$  rather than the chemical potential  $\mu$ , seems to be a promising candidate. However, the difficulty we face is the “overlap-problem”: we would like to extract information about finite density physics, but we only know how to sample at zero matter density ( $\mu = 0$ ). We address this problem by making use of the idea of the Factorisation method.



# Chapter 4

## Canonical Approach to Lattice QCD

In this chapter, we discuss the main project of this thesis: Lattice QCD at finite matter density. In the following, we motivate this study and discuss the current state-of-the-art of numerical methods and the scope of our project. In section 4.2, we present in detail two models, which we want to test by comparison with our numerical results: the hadron resonance gas in the hadronic phase and the ideal gas of free quarks in the quark-gluon plasma phase. The canonical approach to Finite Density QCD is presented in section 4.3 and consists of two parts: first, we introduce a method aimed at zero baryon density, which is computationally inexpensive; second, we present a more costly technique to extract information about all canonical sectors. Results are discussed in sections 4.4 and 4.5, followed by the conclusions.

### 4.1 Motivation

The non-perturbative study of the thermodynamics of Yang-Mills theories via lattice calculations has shown the existence of the confinement-deconfinement transition[47]

25 years ago for  $SU(2)$ . In the late eighties, simulations of dynamical quarks have become feasible, and the chiral transition has been studied with respect to various quark flavours and masses, for a review see Ref. [63]. There was, however, no progress in the study of the QCD phase diagram at non-zero matter density  $\rho$  (or non-zero chemical potential  $\mu$ ) until recently. During the past few year various methods have been developed which work at small chemical potential  $\frac{\mu}{T} \lesssim 1$ . We briefly discuss the approaches and their limitations in the following subsection.

So far, Finite Density Lattice QCD calculations have been concentrating on determining the phase boundary  $T_c(\mu)$  between the low-temperature confined phase and the high-temperature quark-gluon plasma. We propose another approach, a canonical approach, which is designed to study systems with a few baryons at low temperature, but also allows to study the phase diagram for temperatures  $T \gtrsim 0.8 T_c(\mu = 0)$  in the  $T$ - $\rho$  plane with  $\rho \lesssim \frac{5 \text{ baryons}}{\text{fm}^3}$ , which corresponds in the  $T$ - $\mu$  plane to  $\frac{\mu}{T} \lesssim 2$ . We recall the relevant part of the conjectured QCD phase diagram in Fig. 4.1, which is discussed in subsection 1.2.3. Currently, simulations at approximately physical quark masses[64] show a crossover behaviour at small chemical potential. We have discussed in subsection 1.2.3 the existence of a second order endpoint. This critical point has not yet been found uncontroversially. At lower temperatures, the phase boundary becomes a first order transition line, which gives rise to a co-existence region in the  $T$ - $\rho$  plane as indicated in the plot.

### 4.1.1 State of the Art

1. Z. Fodor and S. D. Katz[65] propose a two-parameter reweighting (see Appendix D) in temperature  $T$  and chemical potential  $\mu$  following the critical line, which is determined by monitoring the Lee-Yang zeroes<sup>1</sup>: if the zeroes

---

<sup>1</sup>The critical line alternatively can be determined by identifying the peak in the specific heat or in the susceptibility of the chiral condensate.

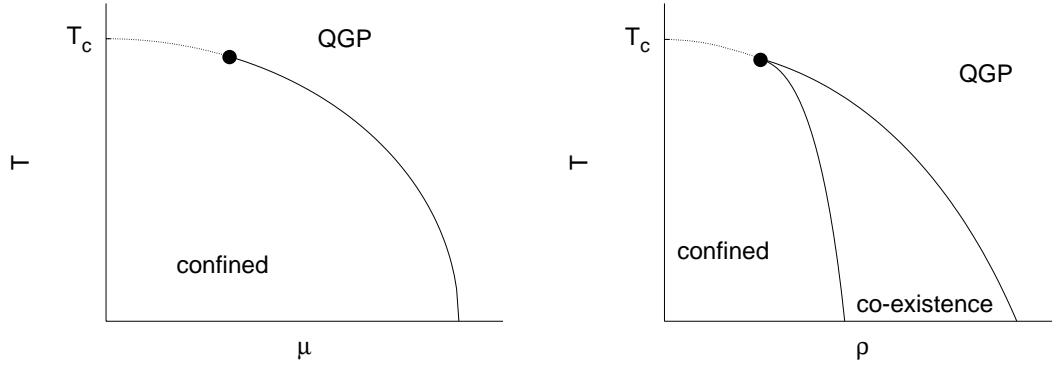


Figure 4.1: Simplified conjectured phase diagram of real-world QCD in the  $(T, \mu)$ -plane (left), in the  $(T, \rho)$ -plane (right). The dotted lines represent a crossover, the solid lines a first order phase transition. The single dots show the position of the second order critical endpoint.

of the grand canonical partition function touch the real axis for  $V \rightarrow \infty$ , the existence of a phase transition follows. In the case of a crossover, the zeroes tend in the thermodynamic limit to a value with a non-zero imaginary part.

The applicability of the method has been demonstrated for four degenerate flavours of staggered quarks and for three flavours of quarks at almost physical quark masses. In the case of four degenerate flavours, the phase transition at zero chemical potential is first order for their choice of quark mass  $\frac{m}{T} = 0.2$  and presumably does not develop a critical point, as we will discuss later. In the latter calculation the goal was to identify the critical point; however their findings are controversial[66]. Several years ago, there was a similar method in use, the so-called Glasgow method[67]. The essential difference is the following: To detect the  $\mu$ -driven phase transition at some fixed temperature  $T_0 < T_c(\mu = 0)$ , the Glasgow group sampled at  $T_0(\mu = 0)$  and increased the chemical potential by reweighting at fixed temperature. Unfortunately, the indicated onset of baryon density begins at a chemical potential smaller than the expected  $\frac{m_{\text{proton}}}{3}$ , see section 1.2.3. Ref. [68] noticed that this is due to the “overlap problem”: the ensemble generated at zero chemical potential

only has a few (or none at all) relevant configurations for the finite-density physics. Z. Fodor and S. D. Katz address this problem by sampling at the critical temperature at zero chemical potential  $T_c(\mu = 0)$ . The generated ensemble consists of configurations from both the confined and the deconfined phase, and thus, a much better overlap with the critical target ensemble is achieved. Still, the generic difficulty of reweighting methods, namely the reliable estimate of the statistical error, remains. See for more details subsection 4.5.4.

The systematic uncertainties become large at  $\mu \gtrsim \frac{m_\pi}{2}$  [69]. Simulations with the sampling weight  $|\det M(\mu)|^2$ , called “phase quenched” simulations, correspond to systems with finite isospin chemical potential, ie.  $\mu_{IS} = \mu_u = -\mu_d$  [70, 71] (see Appendix D.1.2). The phase diagram<sup>2</sup> at finite isospin chemical potential is sketched in Fig. 4.2. At small isospin chemical potential, the influence of the quenched phase is small, therefore one observes essentially the same curvature as at small chemical potential. At larger isospin chemical potential, ie.  $\mu_{IS} \gtrsim \frac{m_\pi}{2}$ , however, one probes a new phase at low temperature, called the “pion superfluid”, in which the expectation value of the chiral condensate is not zero, unlike in the quark-gluon plasma where  $\langle \bar{\Psi}\Psi \rangle = 0$ . Ref. [69] argues that reweighting methods are exceedingly delicate for values of  $T$  and  $\mu$ , where phase quenched QCD is in the pion superfluid phase, and shows that the critical endpoint found in Ref. [65] is close to the hadronic phase - pion superfluid transition.

2. Another approach [72, 73, 74] also samples at zero chemical potential, but instead of reweighting, which requires the (costly) exact determination of the fermion determinant, they determine the coefficients in the Taylor-expansion

---

<sup>2</sup>The Boltzmann weight at non-zero isospin chemical potential is positive and real, therefore the whole phase space is accessible via Monte Carlo methods.



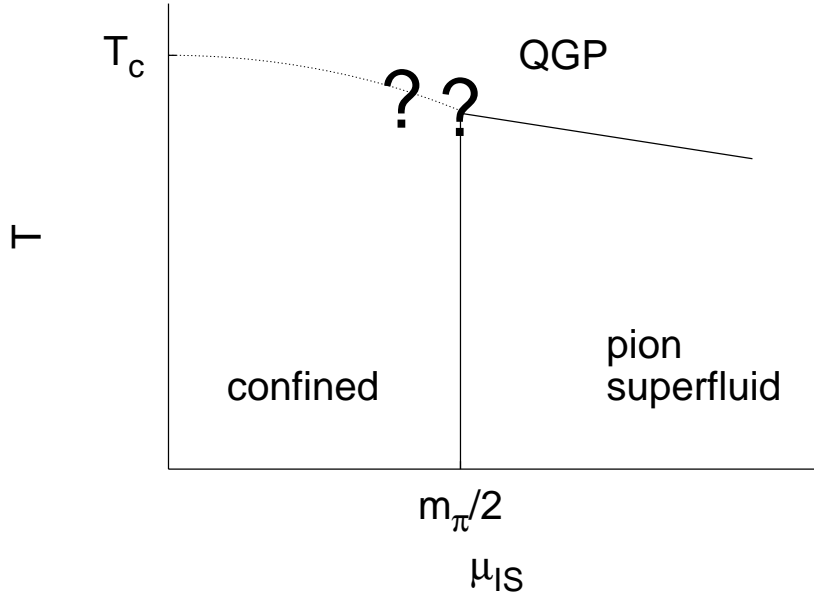


Figure 4.2: The conjectured phase diagram in the plane of temperature  $T$  and isospin chemical potential  $\mu_{IS}$ . For an isospin chemical potential  $\mu_{IS} > \frac{m_\pi}{2}$  a pion condensate is built.

of the free energy in  $\frac{\mu}{T}$  about  $\mu = 0$ . These coefficients can be expressed as observables in the  $\mu = 0$  ensemble, which can be estimated rather than computed exactly, and thus, the approach is computationally less intensive. Larger lattices can be tackled, however systematic uncertainties coming from the truncation of the Taylor series impose  $\frac{\mu}{T} \lesssim 1$ .

3. A third approach [75, 76, 77] samples at imaginary chemical potential, which preserves the  $\gamma_5$ -hermiticity of the Dirac operator, see Eq.(1.84), and therefore the fermion determinant remains real positive (for  $N_f$  even). Without a sign problem, accurate results can be obtained without enormous numerical effort, but there is a limitation in the analytic continuation to real chemical potential at  $|\mu|/T \leq \pi/3$ , due to non-analyticities in the partition function at  $\frac{\mu}{T} = (2k+1)\frac{\pi}{3}$ , as outlined in subsection 1.2.2.

Most of these methods initially have been tested for a particular theory, namely four degenerate flavours of staggered quarks. As it happens, all groups have chosen the quark mass to be  $\frac{m}{T} = 0.2$ . The resulting pion mass  $m_\pi \approx 350$  MeV is larger than the physical one (about 135 MeV). Interestingly, all approaches agree in the phase boundary  $T_c(\mu)$  for  $\frac{\mu}{T} \lesssim 1.0$ . One feature of the four flavour theory is that the phase transition at zero chemical potential is first order. This has been observed by direct lattice calculations, but is also in agreement with theoretical predictions of the sigma model, in which the phase transition is first order for four massless flavours, but gets weaker for less flavours, see subsection 1.2.3. For the particular choice of the quark mass, namely  $\frac{m}{T} = 0.2$ , the phase boundary remains first order presumably for all chemical potentials. This simplifies the detection of the phase boundary compared to a crossover, because the signatures of a first order transition are more pronounced. We will test our approach exclusively in the context of this model.

### 4.1.2 Scope of this project

We try to address the limitation of the previous approaches “ $\frac{\mu}{T} \lesssim 1.0$ ” by using a canonical approach, where we focus on the matter density  $\rho$  (or the baryon number  $B = \rho V$ ) rather than the chemical potential. With our improvements presented in this chapter, the Helmholtz free energy  $F(T, B)$  of successive baryon sectors

$$F(T, B) \equiv -T \log \frac{Z_C(T, B)}{Z_C(T, B=0)} \quad (4.1)$$

can be determined rather accurately on small systems down to relatively low temperatures  $T \approx 0.8T_c$  for a wide range of baryon number (up to 30 baryons). As elaborated in subsection 1.2.2, the canonical partition function  $Z_C(T, B)$  at fixed baryon number  $B$  is obtained from the grand canonical one using a Fourier trans-

form

$$Z_C(B) = \frac{1}{2\pi} \int_{-\pi}^{\pi} d\left(\frac{\mu_I}{T}\right) e^{-i3B\frac{\mu_I}{T}} Z_{GC}(\mu = i\mu_I). \quad (4.2)$$

Note that in this formulation the sign problem is explicitly visible in the oscillatory phase factor  $e^{-i3B\frac{\mu_I}{T}}$ , whereas the fermion determinant  $\det M(U; \mu = i\mu_I)$  in  $Z_{GC}(\mu = i\mu_I)$  is real positive.

So far, we have motivated the new approach mainly with respect to the phase diagram, but the range of applicability is much wider - new regimes can be explored, unsettled questions can be answered - and not much has been done beyond algorithmic testing[78, 79, 80, 81]. We proceed as follows:

- We explore the simplest canonical sector  $B = 0$ , which is equivalent to the grand canonical ensemble at  $\mu = 0$  in the thermodynamic limit[82, 83]. The “trivial” canonical sector  $B = 0$  is in particular interesting due to an unresolved paradox, which we call the “Polyakov loop paradox”. On the one hand, the grand canonical partition function  $Z_{GC}(T, \mu)$  with chemical potential  $\mu$  explicitly breaks the  $Z_3$  centre symmetry with the fermion determinant, as proven in subsection 1.2.1. As a consequence, the Polyakov loop expectation value is non-zero for all temperatures and volumes, see Fig. 4.3(top). On the other hand, the canonical partition function  $Z_C(T, B)$  at fixed baryon number  $B$  is manifestly  $Z_3$ -symmetric, see Fig. 4.3(bottom), since the transformation<sup>3</sup> $Pol(\vec{x}) \rightarrow z(k)Pol(\vec{x})$  can be compensated due to the  $\frac{2\pi T}{3}$ -periodicity of  $Z_{GC}(\mu = i\mu_I)$  (see subsection 1.2.2). Therefore, the Polyakov loop expectation value is exactly zero. This raises a fundamental question about the equivalence of the two ensembles and the role of the Polyakov loop as an order parameter[30, 84], which we will answer in subsection 4.4.1.

---

<sup>3</sup> $z(k) \equiv e^{i\frac{2\pi k}{3}}$  with  $k = 0, \pm 1$  are the centre elements of the gauge group  $SU(3)$

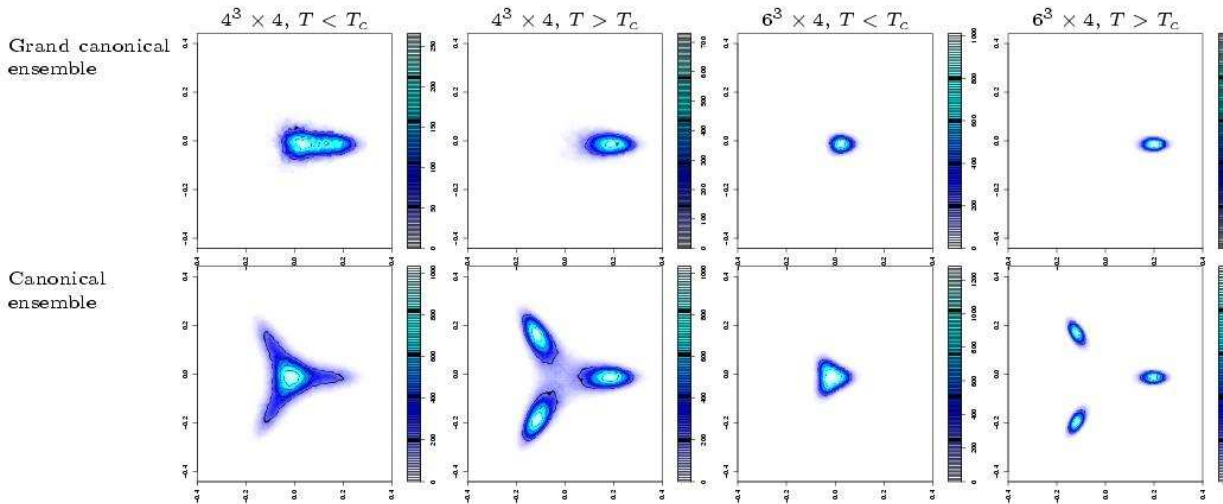


Figure 4.3: Distribution of the complex Polyakov loop in the grand canonical (top) and canonical (bottom) ensembles in the volumes  $4^3 \times 4$  (left),  $6^3 \times 4$  (right). In the thermodynamic limit, the distributions agree for both ensembles, up to two additional  $Z_3$ -rotations in the canonical ensemble.

- In heavy-ion collisions, as performed at RHIC (Brookhaven) or planned at LHC (CERN), a canonical framework is natural, since the net baryon number is fixed and conserved. It is a long-standing goal of lattice calculations to study the thermodynamics of few-nucleon systems. We initiate this field by measuring the Helmholtz free energy as a function of the baryon number in the quark-gluon plasma, and in particular also in the low-temperature hadronic phase. Prospects are the study of the bulk properties of nuclear matter from first principles, and the nuclear interaction, for example the binding energy of Deuteron. Nevertheless, the difference of scale between nuclear interactions (MeV) and nuclear masses (GeV) makes this goal extremely hard to reach. This search can be eased by a change in the parameters of QCD, namely the number and mass of the quark flavours, since the strength and even the order of a phase transition depend on these.

- The regime of higher matter density is also accessible. In our study, we can explore the phase diagram of QCD in the  $T$ - $\mu$  as well as in the  $T$ - $\rho$  plane for  $T \gtrsim 0.8T_c$  and  $\rho \lesssim \frac{5 \text{ baryons}}{\text{fm}^3}$ <sup>4</sup>. We compare the phase boundary  $T_c(\mu)$  with the literature and agree for  $\frac{\mu}{T} \lesssim 1.0$ . We determine the order and strength of the observed phase transition. We characterise the different phases: the measured Helmholtz free energy is compared with predictions from simple models, such as the hadron resonance gas and the free gas of massless quarks.

## 4.2 Models

Two non-interacting models have been found to provide an good description of the basic features of the  $T$ - and  $\mu$ -dependence of thermodynamic observables in the confined and in the quark-gluon plasma phase[31, 32, 33, 34] respectively: the hadron resonance gas and the free gas of massless quarks.

The starting point for both models is given by the grand canonical one-particle partition function of the continuum theory[15]

$$\log Z_{GC}(T, \mu) = \eta g \frac{V}{2\pi^2} \int_0^\infty dk k^2 \log \left( 1 + \eta e^{-\frac{1}{T}(\epsilon(k,m)-\mu)} \right) . \quad (4.3)$$

The parameter  $\eta$  is  $\eta = -1$  for bosons and  $\eta = 1$  for fermions,  $g$  is the spin-isospin degeneracy of the state,  $\mu$  is the chemical potential and the relativistic kinetic energy is

$$\epsilon(k, m) = \sqrt{k^2 + m^2} . \quad (4.4)$$

The contribution of the antiparticle is obtained by replacing  $\epsilon(k, m) - \mu$  by  $\epsilon(k, m) + \mu$ . The hadron resonance gas model is a model of a non-interacting gas of various bosonic and fermionic hadrons. Each kind of hadron is described by the one-particle partition function Eq.(4.3). The model of the free gas of quarks considers  $N_f$  degenerate flavours, each given by the one-particle partition function. It should be a

---

<sup>4</sup>Note, however, as  $V \rightarrow \infty$ , fixing the baryon number amounts to approach  $\rho = 0$

good approximation of QCD in the regime of asymptotic freedom, which holds at very high temperature.

### 4.2.1 Hadron Resonance Gas

The hadron resonance gas describes QCD bulk thermodynamics in terms of a non-interacting gas of hadron resonances, either bosonic mesons or fermionic baryons and exhibits a singularity, which is indicative of the hadronic matter quark-gluon plasma phase transition[85].

The *sum* of energies of relativistic Fermi and Bose particles is used as the Hamiltonian, ie. one assumes that the free energy density is given by the contributions of all the hadron resonances without explicit interactions. The hadron resonance gas model is an effective theory, which contains all relevant degrees of freedom of the confined matter, and implicitly contains the strong interaction by the inclusion of the heavy resonances as stable particles.

The grand canonical partition function  $Z_{HRG}$  can be split into bosonic and fermionic contributions

$$\begin{aligned} \log Z_{HRG}(T, V, \mu_B) = & \sum_{i \in \text{Mesons}} \log Z_i^M(T, V) + \sum_{i \in \text{Baryons}} \log Z_i^B(T, V, \mu_B) \\ & + (\text{particle} \longleftrightarrow \text{antiparticle}), \end{aligned} \quad (4.5)$$

with  $\mu_B$  the baryon chemical potential<sup>5</sup>. We are interested how the free energy depends on  $\mu_B$ , therefore we discuss the baryon contributions only. The relevant partition function of a hadron resonance with mass  $m_i$  is

$$\log Z_i^B(T, V, \mu_B) = g_i \frac{V}{2\pi^2} \int_0^\infty dk k^2 \log \left( 1 + z_i e^{-\frac{\epsilon(k, m_i)}{T}} \right) \quad (4.6)$$

---

<sup>5</sup>The baryon chemical potential is related to the quark chemical potential by  $\mu_B = 3\mu$

with the fugacity  $z_i = e^{\frac{\mu_B}{T}}$ . We expand the logarithm and obtain

$$\begin{aligned} \log Z_i^B(T, V, \mu_B) &= g_i \frac{V}{2\pi^2} \sum_{l=1}^{\infty} \frac{(-1)^{l+1} z_i^l}{l} \int_0^{\infty} dk k^2 e^{-l \frac{\epsilon(k, m_i)}{T}} \\ &= g_i \frac{VT m_i^2}{2\pi^2} \sum_{l=1}^{\infty} \frac{(-1)^{l+1} z_i^l}{l^2} K_2 \left( \frac{lm_i}{T} \right), \end{aligned} \quad (4.7)$$

where  $K_2$  is a modified Bessel function of second kind. With<sup>6</sup>  $m_i \gg T, \mu_B$  it follows that sectors with several resonances of the given type are exponentially suppressed, since  $K_2 \left( \frac{lm_i}{T} \right) \sim e^{-\frac{lm_i}{T}}$ :

$$\log Z_i^B(T, V, \mu_B) \approx_{l=1} g_i \frac{VT m_i^2}{2\pi^2} K_2 \left( \frac{m_i}{T} \right) e^{\frac{\mu_B}{T}}. \quad (4.8)$$

In dimensionless quantities the change in the free energy density due to a non-zero baryon chemical potential is given by

$$\begin{aligned} -\frac{F(T, V, \mu_B) - F(T, V, 0)}{VT^4} &\equiv -\frac{\Delta F(T, V, \mu_B)}{VT^4} = \frac{1}{VT^3} \log \frac{Z_{HRG}(T, V, \mu_B)}{Z_{HRG}(T, V, 0)} \\ &= \frac{1}{2\pi^2 T^2} \sum_{i \in \text{Baryons}} g_i m_i^2 K_2 \left( \frac{m_i}{T} \right) \left( e^{\frac{\mu_B}{T}} + e^{-\frac{\mu_B}{T}} - 2 \right) \\ &\approx f(T) \left( \cosh \left( \frac{\mu_B}{T} \right) - 1 \right). \end{aligned} \quad (4.9)$$

The so-called ‘‘sum of resonances’’  $f(T)$  is

$$f(T) \equiv \frac{1}{\pi^2} \sum_{i \in \text{Baryons}} g_i \left( \frac{m_i}{T} \right)^2 K_2 \left( \frac{m_i}{T} \right). \quad (4.10)$$

In subsection 4.5.2 we will numerically relate the baryon density  $\rho = \frac{B}{V}$  to the quark chemical potential  $\mu = \frac{\mu_B}{3}$ . In the hadron resonance gas, the baryon density is given in dimensionless quantities as

$$\frac{\rho}{T^3} \equiv -\frac{\partial \left( \frac{\Delta F(T, V, \mu_B)}{VT^4} \right)}{\partial \left( \frac{\mu_B}{T} \right)} = f(T) \sinh \left( \frac{\mu_B}{T} \right) = f(T) \sinh \left( \frac{3\mu}{T} \right). \quad (4.11)$$

---

<sup>6</sup>The lightest baryon is about 1 GeV, while the temperature scale is about 160 MeV

## 4.2.2 Quark-Gluon Gas

In the limit of high temperature (Stefan-Boltzmann (SB) limit), thermodynamic observables, like the free energy density, are expected to approach predictions of a free gas of quarks and gluons, due to asymptotic freedom. The gluonic contribution is independent of the chemical potential and contributes to the free energy with  $\frac{8\pi^2}{45}$ . We consider a system of  $N_f$  degenerate flavours of non-interacting quarks and antiquarks in the continuum. The free energy densities can be added and we obtain

$$\frac{F(T, V, \mu)}{VT^4} = -\frac{N_f}{2\pi^2 T^3} \int_0^\infty dk k^2 \log \left[ \left(1 + e^{-\frac{1}{T}(\epsilon(k, m) - \mu)}\right) \left(1 + e^{-\frac{1}{T}(\epsilon(k, m) + \mu)}\right) \right]. \quad (4.12)$$

For massless quarks one finds from an evaluation of the integral the free energy as a finite polynomial in  $\frac{\mu}{T}$ [34]

$$-\frac{F(T, V, \mu)}{VT^4} \approx \frac{8\pi^2}{45} + N_f \left( \frac{7\pi^2}{60} + \frac{1}{2} \left(\frac{\mu}{T}\right)^2 + \frac{1}{4\pi^2} \left(\frac{\mu}{T}\right)^4 \right) + \mathcal{O}(g^2). \quad (4.13)$$

The first term reflects the contribution of the gluon sector, which is independent of the (quark) chemical potential  $\mu$ , the  $N_f$ -dependent terms quantify the contribution of the fermion sector. We have indicated that interacting contributions start at order  $g^2$ [86]. We have seen in subsection 1.2.2 that CP symmetry implies that the series is even in  $\mu$ .

We are interested in the change of the free energy density with increasing chemical potential in dimensionless quantities

$$-\frac{\Delta F(T, V, \mu)}{VT^4} = \frac{N_f}{2} \left(\frac{\mu}{T}\right)^2 + \frac{N_f}{4\pi^2} \left(\frac{\mu}{T}\right)^4. \quad (4.14)$$

The quark density is given as  $\rho_q = -\frac{1}{V} \frac{\partial \Delta F(T, V, \mu)}{\partial \mu}$ . We here calculate the baryon density  $\rho = \frac{\rho_q}{3}$  as a function of the quark chemical potential in dimensionless quantities

$$\frac{\rho}{T^3} = \frac{\rho_q}{3T^3} \equiv -\frac{\partial \left( \frac{\Delta F(T, V, \mu)}{VT^4} \right)}{3\partial \left( \frac{\mu}{T} \right)} = \frac{N_f}{3} \left(\frac{\mu}{T}\right) + \frac{N_f}{3\pi^2} \left(\frac{\mu}{T}\right)^3. \quad (4.15)$$

These simple expressions are valid in the continuum theory at very high temperature, where the coupling  $g \approx 0$  and  $m \ll T$ . On the lattice we expect finite size corrections



( $N_s < \infty$ ) as well as cut-off corrections ( $T = \frac{1}{aN_t}$ ). Ref. [73] has calculated the free energy of free fermions with infinite spatial volume ( $N_s = \infty$ ) but finite temporal extent ( $N_t = 4$ ). Here, we also determine the corrections for finite spatial volume  $N_s = 4, 6, 8, 10$  for the free massless fermion gas on the lattice. We set the gauge fields  $A_\mu(x) = 0$ , ie. the gauge links to the identity, and solve for the free energy via

$$-\frac{\Delta F_{\text{latt}}^{\text{free}}(T, V, \mu)}{VT^4} = \frac{\log Z^{\text{free}}(T, V, \mu)}{VT^3} = \frac{\log \det M^{\text{free}}(T, V, \mu)}{VT^3} \approx C_2 \frac{N_f}{2} \left(\frac{\mu}{T}\right)^2 + C_4 \frac{N_f}{4\pi^2} \left(\frac{\mu}{T}\right)^4 \quad (4.16)$$

Table 4.1 summarises the results.

The correction terms approach their infinite volume expectation rather quickly. For the particular mass  $\frac{m}{T} = 0.2$  we consider, the difference from the massless limit is smaller than the (fitting) errors, and thus, results are not presented explicitly. Note that we have an additional column  $[C_6]$ : we have added the term  $C_6 \left(\frac{\mu}{T}\right)^6$  to the Ansatz Eq.(4.16). The coefficient  $C_6$  is very small. The correction terms  $C_2$  and  $C_4$  are unchanged within the statistical errors.

Lattice	$C_2$	$C_4$	$[C_6]$
$4^3 \times 4$	4.387(1)	0.28(3)	[-]
$6^3 \times 4$	2.628(1)	1.70(5)	[0.0081(1)]
$8^3 \times 4$	2.315(1)	2.25(5)	[0.0046(1)]
$10^3 \times 4$	2.250(1)	2.49(5)	[0.0030(1)]
$\infty^3 \times 4$	2.25	2.6	-

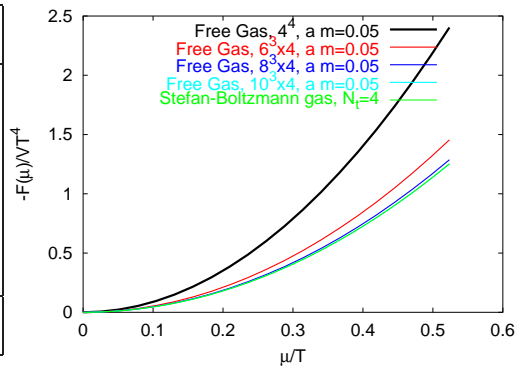


Table 4.1: The prediction for the free energy density based on the free gas model in the continuum at high temperature suffers from finite size and cut-off effects. The correction terms  $C_2$  and  $C_4$  help to quantify the systematics. The functional form in Eq.(4.16) nicely describes the data - the contribution of the additional term  $\left(\frac{\mu}{T}\right)^6$  is negligible (left table). We also plot the free energy density of the massless Stefan-Boltzmann gas for comparison (right). Already at the volume  $10^3$ , no difference is visible.

## 4.3 The Two Methods

### 4.3.1 Fourier Transformation

In order to design an algorithm which is able to measure an observable as a function of the quark, or rather baryon number, we need to understand how the expectation value of an observable  $O$  can be evaluated in the canonical ensemble. It is given by

$$\langle \hat{O} \rangle_B \equiv \frac{\frac{1}{2\pi} \int_{-\pi}^{\pi} d\bar{\mu}_I e^{-i3B\bar{\mu}_I} \int [DU] e^{-S_g[U;\beta]} \det M(U; i\bar{\mu}_I T) \hat{O}(U)}{Z_C(T, B)}. \quad (4.17)$$

We recognise at least three numerical prescriptions:

1. We treat  $\bar{\mu}_I$  as a dynamical degree of freedom, and supplement the ordinary Monte Carlo (Hybrid MC[87, 88], R-algorithm[89], PHMC[90], RHMC[91], ...) at fixed  $\bar{\mu}_I$  with a noisy Metropolis update of  $\bar{\mu}_I \rightarrow \bar{\mu}'_I$  keeping  $\{U\}$  fixed. The oscillatory part  $e^{-i3B\bar{\mu}_I}$  in the sample weight causes a sign problem for non-zero baryon number  $B$ . This approach breaks down for rather small  $B$  already.
2. Rather than allowing all imaginary chemical potentials, one can measure the ratio of grand canonical partition functions as

$$\begin{aligned} \frac{Z_{GC}(i\bar{\mu}_I T)}{Z_{GC}(i\bar{\mu}_{I_0} T)} &= \frac{\int [DU] e^{-S_g[U;\beta]} \det M(U; i\bar{\mu}_I T)}{\int [DU] e^{-S_g[U;\beta]} \det M(U; i\bar{\mu}_{I_0} T)} \\ &= \frac{\int [DU] e^{-S_g[U;\beta]} \frac{\det M(U; i\bar{\mu}_I T)}{\det M(U; i\bar{\mu}_{I_0} T)} \det M(U; i\bar{\mu}_{I_0} T)}{\int [DU] e^{-S_g[U;\beta]} \det M(U; i\bar{\mu}_{I_0} T)} \\ &\equiv \left\langle \frac{\det M(U; i\bar{\mu}_I T)}{\det M(U; i\bar{\mu}_{I_0} T)} \right\rangle_{\mu_{I_0}}. \end{aligned} \quad (4.18)$$

The range  $\bar{\mu}_I \in [-\pi, \pi]$  can be covered with a set of “patches” each centred on a different  $\bar{\mu}_0$ . Each grand canonical partition function can thus be measured with a certain statistical error, and the Fourier transformation has to be calculated only once. This approach, promoted e.g. by Ref. [92], also fails rapidly as  $B$  increases, because statistical noise overwhelms the small amplitudes of the high Fourier coefficients, which decrease *exponentially* in  $B$ . We thus need some kind of variance reduction.

3. The third approach provides such a variance reduction, but is computationally much more intensive. We exploit the fact, that all the  $\mu_I$ -dependence in the grand canonical partition function is contained in the fermion determinant, and calculate the Fourier components of the determinant of *each configuration exactly*:

$$\begin{aligned}
\frac{Z_C(T, B)}{Z_{GC}(i\bar{\mu}_{I_0}T)} &= \frac{\frac{1}{2\pi} \int_{-\pi}^{\pi} d\bar{\mu}_I e^{-i3B\bar{\mu}_I} \int [DU] e^{-S_g[U;\beta]} \det M(U; i\bar{\mu}_I T)}{Z_{GC}(i\bar{\mu}_{I_0}T)} \\
&= \frac{\int [DU] e^{-S_g[U;\beta]} \det M(U; i\bar{\mu}_{I_0}T) \left( \frac{1}{2\pi} \int_{-\pi}^{\pi} d\bar{\mu}_I e^{-i3B\bar{\mu}_I} \frac{\det M(U; i\bar{\mu}_I T)}{\det M(U; i\bar{\mu}_{I_0}T)} \right)}{Z_{GC}(i\bar{\mu}_{I_0}T)} \\
&\equiv \frac{\int [DU] e^{-S_g[U;\beta]} \det M(U; i\bar{\mu}_{I_0}T) \left( \frac{\hat{Z}_C(U; B)}{\det M(U; i\bar{\mu}_{I_0}T)} \right)}{Z_{GC}(i\bar{\mu}_{I_0}T)} \\
&\equiv \left\langle \frac{\hat{Z}_C(U; B)}{\det M(U; i\bar{\mu}_{I_0}T)} \right\rangle_{\mu_{I_0}}. \tag{4.19}
\end{aligned}$$

In a first project, QCD at zero baryon density, we use the first prescription. At  $B = 0$ ,  $e^{-i3B\bar{\mu}_I}|_{B=0} = 1$  and thus, the Boltzmann weight is real and positive. In this framework, we resolve the ‘‘Polyakov loop paradox’’, compare the confinement-deconfinement transition at  $\mu = 0$  with  $B = 0$ , and study the free energy as a function of the temperature and the imaginary chemical potential. In a second project, a canonical approach to Finite Density QCD, we implement the third prescription. We measure the free energy as a function of the temperature and the baryon number and determine the phase boundary of the phase transition from the hadronic matter phase to the quark-gluon plasma phase in the  $T$ - $\mu$  and  $T$ - $\rho$  plane.

### 4.3.2 Zero Baryon Number

In order to sample the  $B = 0$  canonical ensemble (Eq.(4.2)), we alternate two kinds of Metropolis steps: (i) proposing a new configuration  $\{U'\}$  at given imaginary chemical potential  $\mu_I$  as a candidate by Hybrid Monte Carlo, and (ii) suggesting a new imaginary chemical potential at given configuration  $\{U\}$ .

A candidate  $\{U'\}$  is accepted with ordinary Metropolis probability

$$Prob(U \rightarrow U') = \min(1, e^{-\Delta S}) . \quad (4.20)$$

The update of  $\mu_I \rightarrow \mu'_I$ , keeping  $\{U\}$  fixed, is based on the acceptance

$$Prob(\mu_I \rightarrow \mu'_I) = \min\left(1, \frac{\det^{N_f}(\mathcal{D}(\mu'_I) + m)}{\det^{N_f}(\mathcal{D}(\mu_I) + m)}\right) . \quad (4.21)$$

The ratio of determinants is evaluated with a stochastic estimator (see Appendix C), namely

$$\frac{\det^{N_f}(\mathcal{D}(\mu'_I) + m)}{\det^{N_f}(\mathcal{D}(\mu_I) + m)} = \langle e^{-|\mathcal{D}(\mu'_I) + m|^{-N_f/2}(\mathcal{D}(\mu_I) + m)^{N_f/2} \eta|^2 + |\eta|^2} \rangle_\eta \quad (4.22)$$

where  $\eta$  is a Gaussian complex vector. Since one Gaussian vector is sufficient, the computational overhead is negligible. In addition, one can perform a “ $Z_3$ -move” at any time to help ergodicity:

$$\mu_I \rightarrow \mu_I \pm \frac{2\pi T}{3} \quad U_4(\vec{x}, x_4 = x_{4_0}) \rightarrow U_4(\vec{x}, x_4 = x_{4_0}) e^{\mp i \frac{2\pi}{3}}, \quad \forall \vec{x} . \quad (4.23)$$

Such a “ $Z_3$ -move” is always accepted, since the configuration  $\{U, \mu_I\}$  and the one with a centre-rotated Polyakov loop, but shifted imaginary chemical potential,  $\{U \times e^{-i \frac{2\pi}{3}}, \mu_I + \frac{2\pi T}{3}\}$  have the same Dirac determinant, and thus the same sampling weight, as discussed at length in subsection 1.2.2.

A computational detail: For  $T > T_c$ , the  $\mu_I$ -distribution is sharply peaked around  $0, \pm \frac{2\pi T}{3}$ . To obtain the distribution accurately in the whole interval, we apply a multicanonical algorithm in the  $T > T_c$  regime for the larger lattices ( $6^3 \times 4$  and  $8^3 \times 4$ )[93]. For this, we bias the sampling of the imaginary chemical potential by modifying the acceptance probability

$$Prob^{\text{multi}}(\mu_I \rightarrow \mu'_I) = \min\left(1, \frac{\det^{N_f}(\mathcal{D}(\mu'_I) + m)}{\det^{N_f}(\mathcal{D}(\mu_I) + m)} e^{(bias(\mu'_I) - bias(\mu_I))}\right) , \quad (4.24)$$

with  $bias(\mu_I)$  chosen such that the sampled histogram becomes flat for all  $\mu_I$ <sup>7</sup>. The expectation value of an observable  $\hat{O}$  is then given by

$$\langle \hat{O} \rangle = \frac{1}{\sum_{\{U; \mu_I\}} e^{-bias(U; \mu_I)}} \sum_{\{U; \mu_I\}} \hat{O}(U; \mu_I) e^{-bias(U; \mu_I)}. \quad (4.25)$$

$\{U, \mu_I\}$  labels the sampled configurations  $\{U\}$  at imaginary chemical potential  $\mu_I$ .

### 4.3.3 Non-Zero Baryon Number

In the first part of this subsection, we follow Ref. [79]. As we will see, the canonical partition functions  $Z_C(T, B)$ , which allow the study of canonical ensembles at non-zero baryon number, are determined by the Fourier coefficients of the determinant. [94] noticed that the determinant of the fermion matrix can be exactly computed for any chemical potential at the cost of diagonalising a so-called “reduced matrix” (or “fermion transition matrix”)<sup>8</sup>. The fermion matrix  $M$  for four degenerate flavours of staggered quarks

$$M(x, x', \mu) = a\delta_{x, x'} + \frac{1}{2m} \sum_{i=1}^3 \eta_i(x) \left[ U_i(x) \delta_{x, x' - \hat{i}} - U_i^\dagger(x - \hat{i}) \delta_{x, x' + \hat{i}} \right] \quad (4.26)$$

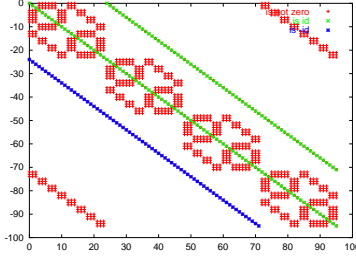
$$+ \frac{1}{2m} \eta_4(x) \left[ e^{\mu a} U_4(x) \delta_{x, x' - \hat{4}} - e^{-\mu a} U_4^\dagger(x - \hat{4}) \delta_{x, x' + \hat{4}} \right]. \quad (4.27)$$

is of size  $\mathbb{C}^{3VN_t \otimes 3VN_t}$ , where  $V$  is the spatial volume. Note we have chosen a slightly different convention  $M = M^{KS}/m$  (compare Eq.(1.47)). In the temporal gauge ( $U_4(\mathbf{x}, x_4) = \mathbb{1}$  except for  $x_4 = N_t - 1$ ), the staggered fermion matrix  $M$  can be reordered and written in the following block-form:

---

<sup>7</sup>A simple way to get an estimate of the function  $bias(\mu_I)$  is the following: One starts by sampling with no bias to produce a histogram  $hist(\mu_I)$  of the sampled  $\mu_I$ . One then fits  $bias(\mu_I)$  to  $\frac{1}{hist(\mu_I)}$  with a suitable Ansatz like  $a\mu_I^2 - b\mu_I^4$ , or uses a table.

<sup>8</sup>Z. Fodor and S. D. Katz[65] make use of this approach.



$$M = \begin{pmatrix} B_0 & \mathbf{1} & 0 & \dots & 0 & U_{N_t-1}^\dagger e^{-\mu a N_t} \\ -\mathbf{1} & B_1 & \mathbf{1} & 0 & \dots & 0 \\ 0 & -\mathbf{1} & B_2 & \mathbf{1} & 0 & \dots \\ & & & & \dots & \\ -U_{N_t-1} e^{\mu a N_t} & 0 & \dots & 0 & -\mathbf{1} & B_{N_t-1} \end{pmatrix}$$

The  $B_i$ 's are matrices of size  $\mathbb{C}^{3V \otimes 3V}$ . They contain the spatial part only, so the entries of each  $B_i$ -row consist of one identity and 18 non-trivial complex numbers: 3 colours  $\times$  6 neighbours.  $U_{N_t-1}^\dagger e^{-\mu a N_t}$  is a shorthand notation for a  $3V \times 3V$  block-diagonal matrix, where the  $3 \times 3$  blocks are built from the  $V$  temporal links  $U^\dagger(\vec{x}, x_4 = N_t - 1)$  that are not set to the identity in the temporal gauge. The introduction of a chemical potential is explicitly given by the  $e^{\pm \mu a N_t}$  term, which is the only dependency of the fermion matrix  $M$  on the chemical potential. We now explicitly show for  $N_t = 4$  how the reduced matrix  $P$  is obtained.

1. We multiply the last column by  $U_{N_t-1} e^{\mu a N_t}$ :

$$\det M = \det \begin{pmatrix} B_0 & \mathbf{1} & 0 & U_{N_t-1}^\dagger e^{-\mu a N_t} \\ -\mathbf{1} & B_1 & \mathbf{1} & 0 \\ 0 & -\mathbf{1} & B_2 & \mathbf{1} \\ -U_{N_t-1} e^{\mu a N_t} & 0 & -\mathbf{1} & B_{N_t-1} \end{pmatrix} = e^{-3V \mu a N_t} \det \begin{pmatrix} B_0 & \mathbf{1} & 0 & \mathbf{1} \\ -\mathbf{1} & B_1 & \mathbf{1} & 0 \\ 0 & -\mathbf{1} & B_2 & U_{N_t-1} e^{\mu a N_t} \\ -U_{N_t-1} e^{\mu a N_t} & 0 & -\mathbf{1} & B_{N_t-1} U_{N_t-1} e^{\mu a N_t} \end{pmatrix}$$

2. We multiply from the left by a specially crafted matrix, of which the determinant is the identity:

$$\begin{aligned} \det M &= e^{-3V \mu a N_t} \det \begin{pmatrix} \mathbf{1} & B_0 & 0 & 0 \\ 0 & \mathbf{1} & 0 & 0 \\ 0 & 0 & \mathbf{1} & B_2 \\ 0 & 0 & 0 & \mathbf{1} \end{pmatrix} \det \begin{pmatrix} B_0 & \mathbf{1} & 0 & \mathbf{1} \\ -\mathbf{1} & B_1 & \mathbf{1} & 0 \\ 0 & -\mathbf{1} & B_2 & U_{N_t-1} e^{\mu a N_t} \\ -U_{N_t-1} e^{\mu a N_t} & 0 & -\mathbf{1} & B_{N_t-1} U_{N_t-1} e^{\mu a N_t} \end{pmatrix} \\ &= e^{-3V \mu a N_t} \det \begin{pmatrix} 0 & \mathbf{1} + B_0 B_1 & B_0 & \mathbf{1} \\ -\mathbf{1} & B_1 & \mathbf{1} & 0 \\ -B_2 U_{N_t-1} e^{\mu a N_t} & -\mathbf{1} & 0 & (\mathbf{1} + B_2 B_{N_t-1}) U_{N_t-1} e^{\mu a N_t} \\ -U_{N_t-1} e^{\mu a N_t} & 0 & -\mathbf{1} & B_{N_t-1} U_{N_t-1} e^{\mu a N_t} \end{pmatrix} \end{aligned}$$

3. We multiply the first column by  $-1$  and cycle the columns of the matrix such that the first column becomes the last. This allows to write the matrix in the following block form:

$$\det M = e^{-3V \mu a N_t} \det \begin{pmatrix} \Omega_{01} & \mathbf{1} \\ -\mathbf{1} & \Omega_{23} U_{N_t-1} e^{\mu a N_t} \end{pmatrix}$$

$$\text{with } \Omega_{i,i+1} = \begin{pmatrix} B_i B_{i+1} + \mathbf{1} & B_i \\ B_{i+1} & \mathbf{1} \end{pmatrix} = \begin{pmatrix} B_i & \mathbf{1} \\ \mathbf{1} & 0 \end{pmatrix} \begin{pmatrix} B_{i+1} & \mathbf{1} \\ \mathbf{1} & 0 \end{pmatrix}$$

4. We multiply the last column by  $e^{-\mu a N_t}$  and define the reduced matrix  $P$ :

$$\det M = e^{+3V \mu a N_t} \det \begin{pmatrix} \Omega_{01} & e^{-\mu a N_t} \\ -\mathbf{1} & \Omega_{23} U_{N_t-1} \end{pmatrix} = e^{+3V \mu a N_t} \det (P + e^{-\mu a N_t})$$

$$\text{with } P = \left( \prod_{i=0,2}^{N_t-1} \Omega_{i,i+1} \right) U_{N_t-1} = \prod_{i=0,1}^{N_t-1} \begin{pmatrix} B_i & \mathbf{1} \\ \mathbf{1} & 0 \end{pmatrix} U_{N_t-1} \quad (4.28)$$

$P$  is independent of the chemical potential and of size  $\mathbb{C}^{6V \otimes 6V}$ . Let us denote its  $6V$  complex Eigenvalues by  $\lambda_i$ . Note that with Eq.(4.28), we can calculate  $\det M$  via the reduced matrix for arbitrary temporal extents  $N_t$ . The numerical effort scales like  $N_t^2$  for a given volume.

5. The determinant of the staggered fermion matrix can be calculated for arbitrary  $\mu$  using

$$\det M(U; \mu) = e^{3V \mu a N_t} \prod_{i=1}^{6V} (\lambda_i + e^{-\mu a N_t}) . \quad (4.29)$$

The Fourier expansion of the fermion determinant is

$$\det M(U; \mu) = \sum_{Q=-3V}^{Q=3V} \hat{Z}_C(U; Q) e^{-Q \mu a N_t} , \quad (4.30)$$

where  $Q$  is the quark number[95]. The sum is limited by  $|Q| \leq 3V$ . We argue as follows. Let us absorb (as per step 1 in the above derivation) the factor  $e^{\pm \mu a N_t}$  in  $U_{N_t-1}^\dagger$  ( $U_{N_t-1}$  respectively). Per Eq.(4.28), the number of Fourier modes of  $\det M(U; \mu)$  is equal to the one of  $\det P(U; \mu)$ . The size of the reduced matrix  $P$  is  $6V \times 6V$ . When its determinant is expanded using Cramer's rule, each term is the product of  $6V$  matrix elements, each of which can involve a temporal link (with the intrinsic chemical potential). Thus, a temporal link can appear 6 times at most, which leads to  $12V+1$  Fourier modes. However, since  $\det P(U; \mu) = \det P(U; -\mu)$ , the number of Fourier coefficients is reduced to  $6V+1$ . The expansion in Eq.(4.30) follows.

We can solve for the Fourier coefficients  $\hat{Z}_C(U; Q)$  by a matching procedure:

$$\begin{aligned}
\det M(U; \mu) &= e^{3V \mu a N_t} [\lambda_1 \cdots \lambda_{6V} + \dots + f(\lambda_1, \dots, \lambda_{6V}) e^{(-3V-Q)\mu a N_t} + \dots + 1 \cdot e^{-6V \mu a N_t}] \\
&= e^{3V \mu a N_t} [\hat{Z}_C(Q = -3V, \lambda_1 \cdots \lambda_{6V}) + \dots + \hat{Z}_C(Q, \lambda_1, \dots, \lambda_{6V}) e^{(-3V-Q)\mu a N_t} + \dots \\
&\quad + \hat{Z}_C(Q = 3V, \lambda_1 \cdots \lambda_{6V}) e^{-6V \mu a N_t}] \\
&= e^{3V \mu a N_t} e^{-3V \mu a N_t} [\hat{Z}_C(Q = -3V) e^{3V \mu a N_t} + \dots + \hat{Z}_C(Q = 0) + \dots + \hat{Z}_C(Q = 3V) e^{-3V \mu a N_t}] \\
&= \hat{Z}_C(Q = -3V) e^{3V \mu a N_t} + \dots + \hat{Z}_C(Q = 0) + \dots + \hat{Z}_C(Q = 3V) e^{-3V \mu a N_t} .
\end{aligned} \tag{4.31}$$

This delicate step requires a special multi-precision library<sup>9</sup>. The whole Fourier decomposition, in particular the computation of the Eigenvalues, is the computational intensive part of the simulation. It takes  $\mathcal{O}(V^3)$  operations. A numerical test can easily be performed: Since  $\hat{Z}_C(U; -Q) = \hat{Z}_C(U; Q)^*$  via inspection of Eq.(4.30), and in particular  $\hat{Z}_C(U; Q = 3V) = 1$  exactly, it must be fulfilled  $\hat{Z}_C(U; Q = -3V) = \prod_{i=1}^{6V} \lambda_i = 1$ .

From the construction of the canonical partition function, Eq.(1.105), it follows immediately that

$$Z_C(\beta, Q) = \int [DU] \hat{Z}_C(U; Q) e^{-S_g[U; \beta]} , \tag{4.32}$$

with  $Z_C(\beta, Q) = 0$  for  $Q$  not a multiple of 3. We thus consider the baryon number  $B = \frac{Q}{3}$  from now on. In Monte Carlo simulations, it is more convenient to express the canonical partition functions as observables

$$\begin{aligned}
\frac{Z_C(\beta, B)}{Z_{GC}(\beta_0 = \beta, \mu = i\mu_{I_0})} &= \frac{1}{Z_{GC}(\beta_0, i\mu_{I_0})} \int dU e^{-S_g[U; \beta_0]} \det M(U; i\mu_{I_0}) \\
&\quad \times \frac{1}{2\pi} \int_{-\pi}^{\pi} d\left(\frac{\mu_I}{T}\right) e^{-i3B \frac{\mu_I}{T}} \frac{\det M(U; i\mu_I)}{\det M(U; i\mu_{I_0})} \\
&= \left\langle \frac{1}{2\pi} \int_{-\pi}^{\pi} d\left(\frac{\mu_I}{T}\right) e^{-i3B \frac{\mu_I}{T}} \frac{\det M(U; i\mu_I)}{\det M(U; i\mu_{I_0})} \right\rangle_{\beta_0, i\mu_{I_0}} = \left\langle \frac{\hat{Z}_C(U; B)}{\det M(U; i\mu_{I_0})} \right\rangle_{\beta_0, i\mu_{I_0}} ,
\end{aligned} \tag{4.33}$$

---

<sup>9</sup>We use the GNU multi precision library (<http://www.swox.com/gmp>). We have cross-checked the results with other libraries, such as MAPM (<http://www.tc.umn.edu/ringx004/mapm-main.html>).



with  $\hat{Z}_C(U; B) = \frac{1}{2\pi} \int_{-\pi}^{\pi} d\left(\frac{\mu_I}{T}\right) e^{-i3B\frac{\mu_I}{T}} \det M(U; i\mu_I)$ , and  $Z_{GC}(\beta_0, i\mu_{I_0})$  is the grand canonical partition function sampled by Monte Carlo, here for notational simplicity at  $\beta_0 = \beta$  and  $\mu = i\mu_{I_0}$ . The  $\hat{Z}_C(U; B)$ 's are the Fourier coefficients of the fermion determinant for a given configuration  $\{U\}$ . Although the average in Eq.(4.33) should be real positive, the individual measurements are in general complex, sometimes with a negative real part. This is how the sign problem manifests itself in our approach. Moreover, a reliable estimate depends on a good overlap of our Monte Carlo ensemble with the canonical sector  $B$  at temperature  $\beta$ . We address this issue by following the idea of Ref. [65] and including both confined and deconfined configurations in our ensemble. Indeed, we supplement the ensemble  $(\beta_c(\mu = 0), 0)$  with additional critical ensembles at various couplings, which consist of configurations from both phases. In principle, any ensemble is allowed. We use the following set of ensembles:

1. at imaginary chemical potential in the whole periodic interval, denoted as  $(\beta_c(\mu_I), \mu_I)$ .

The critical line as a function of the imaginary chemical potential is

$$\beta_c(\mu_I) = 5.042(3) + 0.80(6)\mu_I^2 + O(\mu_I^4). \quad (4.34)$$

2. at non-zero isospin chemical potential, denoted as  $(\beta_c(\mu_{IS}), \mu_{IS})$ .

For small chemical potential, the curvature of the isospin chemical potential corresponds to the one of the real chemical potential

$$\beta_c(\mu_{IS}) = 5.042(3) - 0.80(2)\mu_{IS}^2 + O(\mu_{IS}^4). \quad (4.35)$$

Remember that at low temperature, one has to be careful not to exceed  $\mu_{IS} \gtrsim \frac{m_\pi}{2}$  [69]. Otherwise, one samples ensembles with configurations from the confined phase and the pion superfluid, see Fig. 4.2. The potential risks have been discussed in subsection 4.1.1.

3. at asymmetric coupling  $\xi$ , denoted as  $(\beta_c(\xi), \xi)$ .

We keep  $\mu = 0$  and modify the temporal part of the Dirac operator. We

introduce in

$$M \sim \frac{1}{2m} \eta_4(x) \left[ U_4(x) \delta_{x,x'-\hat{4}} - U_4^\dagger(x - \hat{4}) \delta_{x,x'+\hat{4}} \right] \quad (4.36)$$

an anisotropic coupling  $\xi \in \mathbb{R}$  by

$$M \sim \frac{1}{2m} \eta_4(x) \left[ \xi U_4(x) \delta_{x,x'-\hat{4}} - \xi U_4^\dagger(x - \hat{4}) \delta_{x,x'+\hat{4}} \right] \quad (4.37)$$

(compare with the fermion matrix with a chemical potential Eq.(4.26) and see Ref. [96] for a similar approach). The problem we want to solve with this particular choice of ensembles is the following. If we want to find the phase transition at low temperature, for example at  $\beta = 4.9$ , we have to reweight the critical ensembles at imaginary chemical potential from  $\beta(\mu_I) \geq 5.042$  over a huge “distance” in  $\beta$ . Also, the isospin chemical potential ensemble at  $\beta = 4.90$  might sample the pion superfluid rather than the quark gluon plasma. The presented modification of the Dirac operator shifts the phase transition to lower  $\beta$  for  $\xi > 1$ , see Table 4.2, because  $\xi > 1$  is equivalent to shrinking the temporal lattice spacing  $a \rightarrow \frac{a}{\xi}$  seen by the quarks.

$\xi$	$\beta_c(\xi)(approx.)$
1.00	5.042
1.10	5.013
1.25	4.970
1.375	4.935
1.515	4.900

Table 4.2: The (approximated) phase transition as a function of the asymmetry-parameter  $\xi$ .

Each of these ensembles has a good overlap with a certain canonical sector at a particular temperature<sup>10</sup>. We will illustrate this in more detail in the beginning of

<sup>10</sup>For example, it has been suggested by Ref. [97] that for a given  $B$  there is an optimal imaginary

section 4.5. We combine all this information about a particular canonical partition function  $Z_C(\beta, B)$  by Ferrenberg-Swendsen reweighting[98]. We discuss this non-trivial issue in detail in Appendix D. Here, we want to stress one point: We have to ensure that the individual ensembles have good overlap with their “neighbouring” ensembles, in particular because the ensembles at imaginary chemical potential are unphysical and the  $\xi$ -ensembles are generated with a modified Dirac operator. Assume we want to combine the measurements of two ensembles with no overlap:  $(\beta = 4.935, \mu = 0 \Leftrightarrow \xi = 1)$  and  $(\beta = 4.935, \xi = 1.375)$ , see Fig 4.4. By making

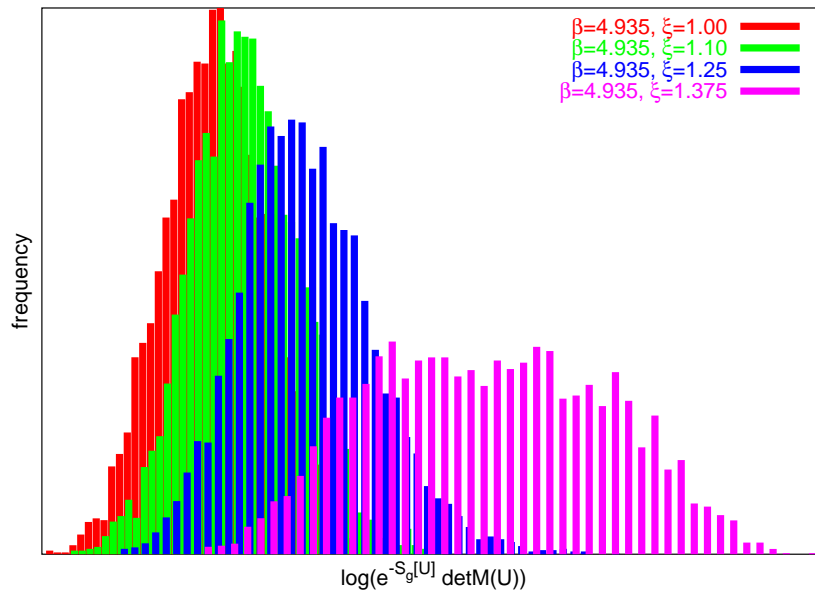


Figure 4.4: Illustration of the Factorisation method. The ensemble at  $\xi = 1.375$  is a critical ensemble. We want to combine it with an ensemble generated at  $\mu = 0$  (equal  $\xi = 1$ ). For a proper Ferrenberg-Swendsen reweighting, we have to ensure a good overlap by supplementing with two more ensembles at  $\xi = 1.1$  and  $\xi = 1.25$ .

use of the Factorisation method, see subsection 3.3.2, we can ensure the applicability of the Ferrenberg-Swendsen reweighting procedure. In this particular case, chemical potential  $\mu_I$ . Unfortunately, this does not seem to be so simple: The Laplace transformation Eq.(1.108) tells us, that the optimal choice of a chemical potential solves  $\frac{\partial f(T, \rho)}{\partial \rho} = 3\mu$ , where  $f(T, \rho)$  is the Helmholtz free energy density. For an imaginary chemical potential, this equation does not have a solution since the free energy density is real.

this means that we have to add two more ensembles ( $\beta = 4.935, \xi = 1.1$ ) and ( $\beta = 4.935, \xi = 1.25$ ) to the ensemble pool.

#### 4.3.4 Baryon density versus chemical potential

One of the main results in this project is the phase diagram as a function of the temperature  $T$  and the baryon density  $\rho = \frac{B}{V}$ . To compare with the literature, which focuses on the phase diagram in the  $T$ - $\mu$ -plane, we need to know how to relate  $\mu$  to  $\rho$ . We have two options. (i) We can express any expectation in the grand canonical ensemble by the canonical partition functions via the fugacity expansion, see Eq.(1.106),

$$Z_{GC}(T, \mu) = \int d\rho e^{3V\rho\frac{\mu}{T}} Z_C(T, \rho) \quad (4.38)$$

as

$$\begin{aligned} \langle \rho \rangle(\mu) &= \frac{1}{Z_{GC}(T, \mu)} \int d\rho \rho Z_C(T, \rho) e^{3V\rho\frac{\mu}{T}} \\ \langle B \rangle(\mu) &= \frac{1}{Z_{GC}(T, \mu)} \sum_B B Z_C(T, B) e^{3B\frac{\mu}{T}}. \end{aligned} \quad (4.39)$$

In practice, some of the canonical partition functions are very poorly determined and contribute essentially noise. As a whole, this approach works badly, as concluded by Ref. [79], still it might come in handy to perform cross-checks with (ii): the saddle point approximation. We can rewrite Eq.(4.38) as

$$Z_{GC}(T, \mu) = \int d\rho e^{-\frac{V}{T}(f(T, \rho) - 3\mu\rho)} \quad (4.40)$$

with the Helmholtz free energy density  $f(T, \rho) = -\frac{T}{V} \log Z_C(T, \rho)$ . For large volumes, the integral is dominated by a neighbourhood of  $\rho_{max}$ , where  $\rho_{max}$  is the maximum of  $-\frac{V}{T}(f(T, \rho) - 3\mu\rho)$  for a given chemical potential, ie.

$$\mu = \frac{1}{3} \frac{\partial f(\rho)}{\partial \rho} \Big|_{\rho_{max}} = f'(\rho_{max}). \quad (4.41)$$

While the first expression Eq.(4.39) is exact in any volume, the saddle point approximation Eq.(4.41) is so only in the thermodynamic limit and may have more than

one solution when solving for the baryon density. We illustrate this in Fig. 4.5 by plotting  $f'(\rho)$ , which equals  $\mu$  in the saddle point approximation, versus  $\rho$ . Assume a first order phase transition line, which we cross by varying the chemical potential  $\mu$ . Increasing  $\mu$  from zero,  $\rho$  increases very little. For some  $\mu > \mu_1$ , two more solutions appear, but by continuity, the system chooses the lowest value of the density. At some value  $\mu = \mu_2$  we reach the “local maximum” of a typical S-shaped curve, and the low-density solution disappears: the density must jump, discontinuously, to the high-density solution. Starting at large chemical potential, we will stay in the high-density phase until  $\mu = \mu_1$ . Then the high-density solution disappears, and  $\rho$  must jump to a low value. We obtain a text-book hysteresis plot.

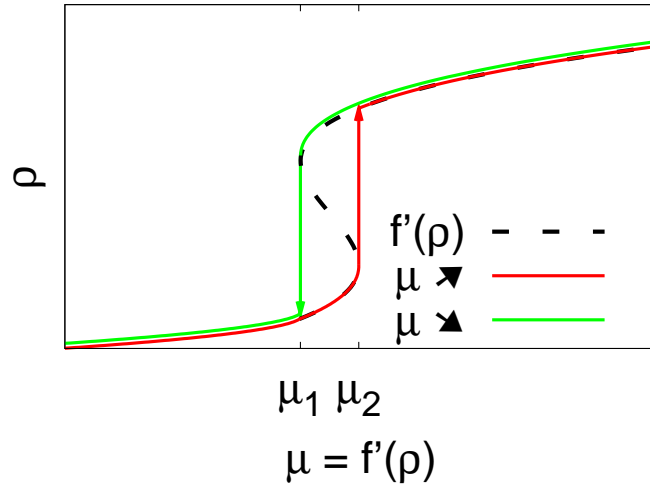


Figure 4.5: The plot illustrates the hysteresis in  $\rho(\mu)$  while crossing a first order transition. We start at zero chemical potential and increase it. Then, we start at large chemical potential and decrease it. Dashed, we plot the first derivative of the free energy, which typically shows an S-shape in the vicinity of a first order phase transition.

The canonical approach to Finite Density QCD allows to determine the Helmholtz free energy  $F(T, B)$ . We thus approximate the derivative by a finite difference<sup>11</sup> and

<sup>11</sup>The approximation of the derivative by a finite difference introduces an error  $\mathcal{O}(\frac{1}{V})$ .

obtain the saddle point approximation in the form

$$\frac{\mu(B)}{T} = \frac{F(T, B) - F(T, B - 1)}{3T}. \quad (4.42)$$

## 4.4 Results - Zero Baryon Number

While the grand canonical partition function  $Z_{GC}(T, \mu)$  with chemical potential  $\mu$  explicitly breaks the  $Z_3$  symmetry with the Dirac determinant, the canonical partition function at fixed baryon number  $Z_C(T, B)$  is manifestly  $Z_3$ -symmetric. We compare  $Z_{GC}(T, \mu = 0)$  and  $Z_C(T, B = 0)$  formally and by numerical simulations, in particular with respect to properties of the confinement-deconfinement transition. We resolve the ‘‘Polyakov loop paradox’’ and show that differences between the two ensembles, for physical observables characterising the phase transition, vanish with increasing lattice size. We identify the phase transition by measuring the susceptibility of the plaquette and of the chiral condensate, and discuss finite size effects via Binder cumulants. From the histogram of the sampled imaginary chemical potential  $\mu_I$ , we obtain the free energy as a function of  $\mu_I$  for free. We discuss it and demonstrate numerically that the two ensembles at  $\mu = 0$  and  $B = 0$  are equivalent in the thermodynamic limit.

We focus on four flavours of Kogut-Susskind fermions with degenerate mass  $\frac{m}{T} = 0.2$ . In this theory, the pion mass acquires a mass of about 350 MeV. Simulations are performed on lattices with extents  $4^3 \times 4$ ,  $6^3 \times 4$  and  $8^3 \times 4$  at seven temperatures<sup>12</sup>, ranging from  $\frac{T}{T_c} = 0.85$  to 1.1, with good overlap between the ‘‘neighbouring’’ ensembles. We analyse the results using Ferrenberg-Swendsen reweighting[98], see section D.4.

---

<sup>12</sup>We relate the coupling  $\beta$  to the temperature  $T$  via  $T = \frac{1}{a(\beta)N_t}$  and the two-loop  $\beta$ -function Eq.(1.61).

### 4.4.1 Polyakov Loop in the Canonical Ensemble

The expectation value of the Polyakov loop in the canonical ensemble is zero for any temperature. We show this explicitly in the following. The chemical potential is introduced on the lattice, see subsection 1.1.5, as

$$U_4(x) \rightarrow e^{+\mu a} U_4(x) \quad (4.43)$$

$$U_4^\dagger(x) \rightarrow e^{-\mu a} U_4^\dagger(x), \quad (4.44)$$

or equivalently as

$$U_4(\vec{x}, x_4 = x_{4_0}) \rightarrow e^{+N_t \mu a} U_4(\vec{x}, x_4 = x_{4_0}) \quad (4.45)$$

$$U_4^\dagger(\vec{x}, x_4 = x_{4_0}) \rightarrow e^{-N_t \mu a} U_4^\dagger(\vec{x}, x_4 = x_{4_0}), \quad (4.46)$$

on a given temporal hyperplane  $x_{4_0}$ . An imaginary chemical potential  $i\mu_I = i\frac{2\pi T k}{3}$  corresponds to a  $Z_3$  centre transformation, see subsection 1.2.1,

$$U_4(\vec{x}, x_4 = x_{4_0}) \rightarrow e^{iN_t a \frac{2\pi T k}{3}} U_4(x) = z(k) U_4(\vec{x}, x_4 = x_{4_0}). \quad (4.47)$$

As a consequence, the two configurations  $\{U, \mu_I\}$  and  $\{z(k)U, \mu_I - \frac{2\pi T k}{3}\}$  have the same value for the Dirac determinant  $\det M(U; \mu_I) = \det M(z(k)U; \mu_I - \frac{2\pi T k}{3})$ , but the Polyakov loop is centre-rotated. We can group the configurations of a canonical ensemble in triplets,

$$Z_C(T, B) = \frac{1}{2\pi} \int_{-\pi}^{\pi} d\left(\frac{\mu_I}{T}\right) e^{-i3B\frac{\mu_I}{T}} \int [DU] e^{-S_g[U; \beta]} \frac{1}{3} \sum_{k=0}^2 \det M(z(k)U_4(x_4 = x_{4_0}), \mu_I), \quad (4.48)$$

since  $\det M(U; \mu_I + \frac{2\pi T k}{3}) = \det M(z(k)U; \mu_I)$  and  $e^{-i3B\frac{1}{T}\frac{2\pi T k}{3}} = 1$  for  $B \in \mathbb{Z}$ . In each triplet, the average of the Polyakov loops is  $Pol_i \times \left(1 + e^{-i\frac{2\pi}{3}} + e^{i\frac{2\pi}{3}}\right) = 0$ , and therefore the ensemble average also vanishes

$$\langle Pol \rangle_{Z_C(T, B)} = 0 \quad (4.49)$$

for any integer baryon number and temperature.

In the ensemble generated by the grand canonical partition function

$$Z_{GC}(T, \mu) = \int [DU] e^{-S_g[U; \beta]} \det M(U; \mu) , \quad (4.50)$$

the expectation value of the Polyakov loop

$$\langle Pol \rangle_{Z_{GC}(T, \mu)} \neq 0 \quad (4.51)$$

is non-zero for any chemical potential and temperature. In the following, we show that the non-vanishing value is caused by canonical sectors with quark numbers, which are not a multiple of three. We express the grand canonical partition function via the fugacity expansion (for notational simplicity at  $\mu = 0$ )

$$\begin{aligned} Z_{GC}(T, \mu = 0) &= \sum_Q Z_C(T, Q) \quad \text{with } Z_C(T, Q) = 0 \text{ if } Q \neq 0 \pmod{3} \\ &\quad (Z_C(T, Q): \text{ see Eq.(1.105) on page 35}) \\ &= \dots + Z_C(0) + \cancel{Z}_C(1) + \cancel{Z}_C(2) + Z_C(3) + \cancel{Z}_C(4) + \dots \end{aligned} \quad (4.52)$$

with  $Q$  the quark number, and  $\cancel{Z}_C(\cdot)$  indicates  $Z_C(\cdot) = 0$ . The canonical partition functions can be written as  $Z_C(T, Q) = \sum_i W_i(Q)$ , where  $i$  labels the configurations, and  $W_i(Q)$  are the corresponding Boltzmann weights. The expectation value of the Polyakov then generically is given by

$$\begin{aligned} \langle Pol \rangle_{GC} &= \frac{\sum_Q \text{Num}(Q)}{Z_{GC}(T, \mu = 0)} \quad (4.53) \\ &= \frac{\dots + \cancel{\text{Num}}(0) + \text{Num}(1) + \text{Num}(2) + \cancel{\text{Num}}(3) + \text{Num}(4) + \dots}{\dots + Z_C(0) + \cancel{Z}_C(1) + \cancel{Z}_C(2) + Z_C(3) + \cancel{Z}_C(4) + \dots} \neq 0 , \end{aligned} \quad (4.54)$$

where  $\text{Num}(Q)$  is given by  $\text{Num}(Q) = \sum_i Pol_i W_i(Q)$  and vanishes if  $Q$  is a multiple of 3 due to Eq.(4.49). It follows that the contributions of canonical sectors with fractional baryon number to the Polyakov loop are unphysical, since the corresponding canonical expectation value

$$\langle Pol \rangle_{Z_C(T, Q \neq 0 \pmod{3})} = \frac{\text{Num}(Q \neq 0 \pmod{3})}{\cancel{Z}_C(Q \neq 0 \pmod{3})} = \infty . \quad (4.55)$$



Thus, the non-vanishing expectation value  $\langle Pol \rangle_{GC}$  is irrelevant for thermodynamic properties, since the canonical and the grand canonical ensembles are equivalent in the thermodynamic limit, and has to be considered as an artifact of keeping sectors with quark numbers not a multiple of three<sup>13</sup>. These canonical sectors, the so-called non-zero “triality sectors”, have zero partition function, and make no contribution to any expectation value, as we will show numerically in the following, except for observables sensitive to the centre  $Z_3$  like the Polyakov loop. In particular, they do not change the expectation value of the Polyakov loop correlator.

#### 4.4.2 Confinement-Deconfinement Transition

The phase transition is signaled by the peak in the susceptibility of the chiral condensate  $\langle \bar{\psi}\psi \rangle$ , which we measure as follows. First, we show that the expectation value of the chiral condensate is  $\frac{\partial \log Z_{GC}(T, \mu, m)}{\partial m}$ :

$$\begin{aligned}
\frac{\partial \log Z_{GC}(T, \mu, m)}{\partial m} &= \frac{1}{Z_{GC}(T, \mu, m)} \frac{\partial Z_{GC}(T, \mu, m)}{\partial m} \\
&= \frac{1}{Z_{GC}(T, \mu, m)} \int [DU][D\bar{\Psi}][D\Psi] \frac{\partial}{\partial m} e^{-S_g[U] - \bar{\Psi}M\Psi} \\
&= \frac{1}{Z_{GC}(T, \mu, m)} \int [DU][D\bar{\Psi}][D\Psi] (-\bar{\Psi}\Psi) e^{-S_g[U] - \bar{\Psi}(\not{D} + m - \mu\gamma_0)\Psi} \\
&= \langle -\bar{\Psi}\Psi \rangle .
\end{aligned} \tag{4.56}$$

---

<sup>13</sup>“Triality” is defined as the difference of the number of quarks and antiquarks modulo 3. We can say that non-zero triality states cause the explicit breaking of the  $Z_3$ -symmetry and therefore are responsible for a non-vanishing expectation value of the Polyakov loop. Furthermore, we can argue that non-zero triality states are unphysical: Triality is a strictly conserved quantity in any physical process. Once the universe has decided in which triality sector it wants to exist, it cannot change its triality. Since in the confined phase, there are colourless states only, it must be the zero triality sector.

We can interchange the path integral and  $\frac{\partial}{\partial m}$ , from which it follows

$$\begin{aligned}
\frac{\partial \log Z_{GC}(T, \mu, m)}{\partial m} &= \frac{1}{Z_{GC}(T, \mu, m)} \frac{\partial Z_{GC}(T, \mu, m)}{\partial m} \\
&= \frac{1}{Z_{GC}(T, \mu, m)} \int [DU] \frac{\partial}{\partial m} e^{-S_g[U] + \text{Tr} \log M(m)} \\
&= \frac{1}{Z_{GC}(T, \mu, m)} \int [DU] \left( \text{Tr} \left\{ M^{-1}(m) \frac{\partial M(m)}{\partial m} \right\} \right) e^{-S_g[U]} \det M(m) \\
&= \langle \text{Tr} \left\{ M^{-1}(m) \frac{\partial M(m)}{\partial m} \right\} \rangle. \tag{4.57}
\end{aligned}$$

Thus, the chiral condensate is calculated via the trace of  $M^{-1}(m) \frac{\partial M(m)}{\partial m}$ . Note that the trace is evaluated with stochastic estimators, rather than computed exactly. We plot the results from both ensembles as a function of  $\beta$  in Fig. 4.6.

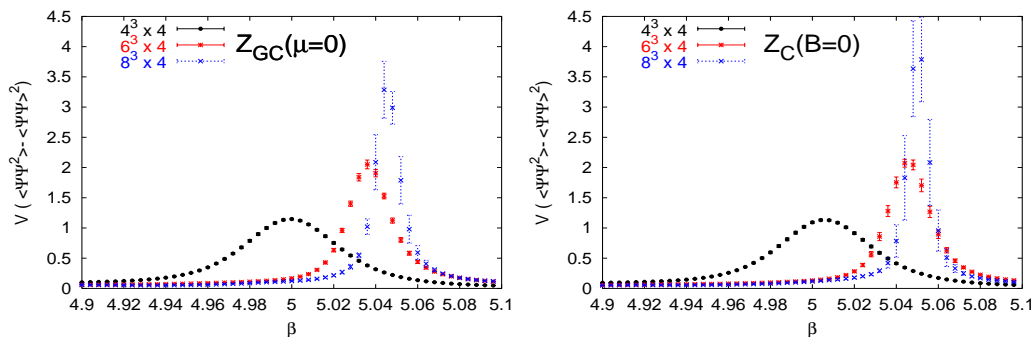


Figure 4.6: Susceptibility of  $\bar{\psi}\psi$  versus  $\beta$  for all volumes in both ensembles. left:  $Z_{GC}(T, \mu = 0)$ , right:  $Z_C(T, B = 0)$ . Even for the smallest,  $4^4$ , lattice, differences are barely visible.

On the  $4^3 \times 4$  lattice, a slight shift in the pseudo-critical  $\beta_c$  can be observed. It disappears for larger volumes. We observe the same behaviour for the specific heat. The small deviation is caused by contributions from higher baryon sectors, which are present in the  $\mu = 0$  ensemble. This is our first evidence to establish the equivalence of the two ensembles.

In quenched simulations, a  $Z_3$ -symmetrisation of the Polyakov loop is often enforced by hand, which is accompanied by reduced finite size effects[99]. Therefore, we could expect to observe such a reduction in the canonical formalism as well compared to

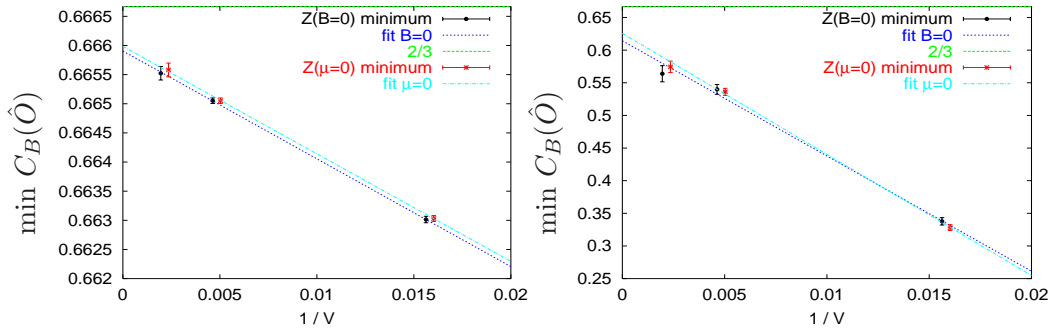


Figure 4.7: Binder cumulant minimum versus inverse volume for both ensembles (slightly shifted). left: plaquette, right: chiral condensate. The thermodynamic extrapolation does not tend to  $\frac{2}{3}$ , indicating a first order transition.

the grand canonical one. To compare the finite size effects in the two ensembles, we analyse the minimum of the Binder cumulant[100]

$$C_B(\hat{O}) = 1 - \frac{1}{3} \frac{\langle \hat{O}^4 \rangle}{\langle \hat{O}^2 \rangle^2} \quad (4.58)$$

versus the inverse volume  $1/V$  (see Fig. 4.7). For both the plaquette and the chiral condensate, the thermodynamic (linear) extrapolation does not tend to  $\frac{2}{3}$  - indicative of a first order phase transition<sup>14</sup>, confirming the finding in the literature[101]. However, for each volume, the measured cumulant values agree between the two ensembles within statistical errors, indicating equivalent finite size effects.

### 4.4.3 The Free Energy $F(T, \mu_I)$

In the grand canonical ensemble, the free energy (as a dimensionless quantity) is given in terms of the grand canonical partition function

$$\frac{\Delta F(T, \mu)}{VT^4} \equiv -\frac{1}{VT^3} \log \frac{Z_{GC}(T, \mu)}{Z_{GC}(T, 0)}. \quad (4.59)$$

<sup>14</sup>In the case of a second order transition,  $\langle \hat{O}^4 \rangle$  is equal to  $\langle \hat{O}^2 \rangle^2$  up to finite size corrections[100]. Thus,  $C_B(\hat{O}) \rightarrow \frac{2}{3}$  in the thermodynamic limit. In the case of a first order transition, the double peak structure of the distribution of the measurements manifests itself in a non-trivial value of the Binder cumulant.

A standard approach[72, 73] is to make a Taylor expansion in  $\mu$  about  $\mu = 0$ , where the derivatives entering the series may be expressed as complicated expectation values evaluated at  $\mu = 0$ . Remember that this expansion is in even powers of  $\mu$ . The lowest order expansion coefficient is then estimated by

$$\frac{\partial^2 \log Z_{GC}(T, \mu)}{\partial \mu^2} = \left\langle \frac{N_f}{4} \frac{\partial^2 (\log \det M)}{\partial^2 \mu} \right\rangle_{\mu=0} + \left\langle \left( \frac{N_f}{4} \frac{\partial (\log \det M)}{\partial \mu} \right)^2 \right\rangle_{\mu=0}. \quad (4.60)$$

and

$$\frac{\partial (\log \det M)}{\partial \mu} = \text{Tr} \left( M^{-1} \frac{\partial M}{\partial \mu} \right) \quad (4.61)$$

$$\frac{\partial^2 (\log \det M)}{\partial \mu^2} = \text{Tr} \left( M^{-1} \frac{\partial^2 M}{\partial \mu^2} \right) - \text{Tr} \left( M^{-1} \frac{\partial M}{\partial \mu} M^{-1} \frac{\partial M}{\partial \mu} \right) \quad (4.62)$$

In our approach, the free energy comes for free from the  $\mu_I$ -histogram in the canonical simulation, and moreover, to all orders. For low temperature, however, the histograms are quite noisy. Therefore we will, when needed, anticipate results from the more sophisticated method (see subsection 4.3.3), where we can calculate the grand canonical partition functions as a function of an arbitrary imaginary chemical potential as a consequence of the reweighting method that we apply, as described in Appendix D.

In Fig. 4.8 we show the free energy divided by  $VT^4$  versus  $\frac{\mu_I}{T}$  for  $\frac{T}{T_c} < 1$ ,  $\frac{T}{T_c} \simeq 1$  and  $\frac{T}{T_c} > 1$ . In all cases, we observe a minimum at  $\frac{\mu_I}{T} = 0$ . Therefore, in the thermodynamic limit, only  $\frac{\mu_I}{T} = 0 \pmod{\frac{2\pi}{3}}$  will survive. This establishes the equivalence of  $Z_C(T, B = 0)$  with  $Z_{GC}(T, \mu = 0)$ .

For  $\frac{T}{T_c} \sim 0.9$ , no singularities develop at  $\frac{\mu_I}{T} = \pm \frac{\pi}{3}$  in the thermodynamic limit, thus indicating a crossover, as expected from the phase diagram  $T$ - $\mu_I$ , see Fig. 1.4 on page 34. In Fig. 4.9, left plot, we show the free energy density, determined by the histogram method, which is very flat and noisy unfortunately. The periodicity of the free energy is  $\frac{2\pi T}{3}$ , and we exploit it by a Fourier expansion in  $3k \frac{\mu_I}{T}$  using the

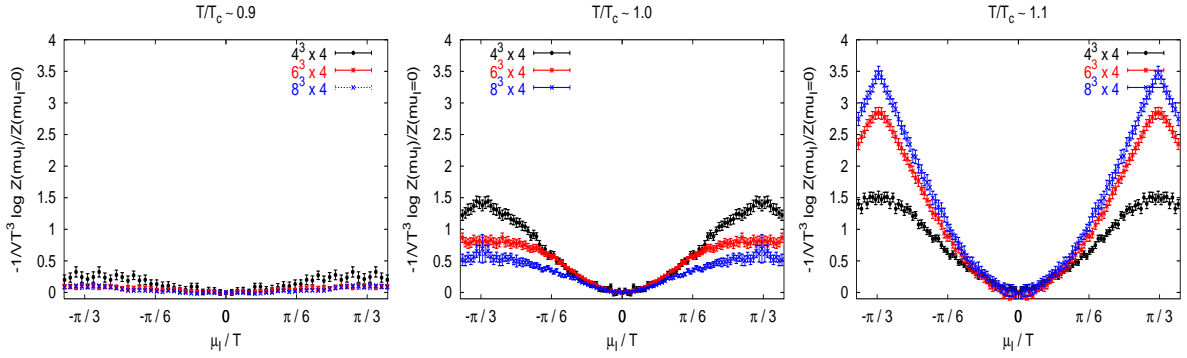


Figure 4.8:  $\frac{F(T, \mu_I)}{VT^4}$  as a function of  $\frac{\mu_I}{T}$  at the temperatures  $\frac{T}{T_c} \sim 0.9, 1.0, 1.1$  from left to right. The free energy density increases significantly while entering the high-temperature phase.

Ansatz

$$\frac{\Delta F(T, \mu_I)}{VT^4} = c \left( 1 - \cos\left(3\frac{\mu_I}{T}\right) \right) + d \cos\left(6\frac{\mu_I}{T}\right) + \dots \quad (4.63)$$

In order to improve the determination of the coefficients  $c, d, \dots$ , we use results based

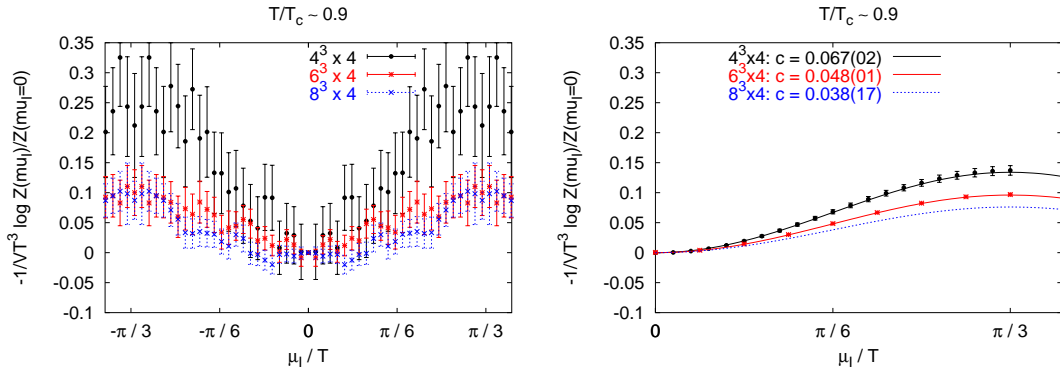


Figure 4.9:  $\frac{F(T, \mu_I)}{VT^4}$  as a function of  $\frac{\mu_I}{T}$  for  $\frac{T}{T_c} \sim 0.9$ . The histogram method is very noisy. We show a rescaled version of the left plot in Fig. 4.8 (left). We also present results based on the reweighting method described in subsection 4.3.3 (right). The results are in agreement with the histogram method, but allow for a more reliable description by a Fourier expansion. The first coefficient is sufficient to describe the data points. The reweighting method calculation is expensive and has not been done for the  $8^3 \times 4$  lattice. We thus draw the fit, which is based on histogram data.

on the reweighting method described in subsection 4.3.3. Within errors, the free en-

energy density is in agreement with the histogram method, but with much smaller statistical uncertainty. The fit is excellent already with one Fourier coefficient, with no indication for higher Fourier components, at least on the small lattices we consider. Note that in the hadron resonance gas model, see subsection 4.2.1, the Ansatz for the free energy as an imaginary chemical potential is  $\frac{\Delta F(T, \mu_I)}{VT^4} = f(T)(1 - \cos(\frac{3\mu_I}{T}))$ . We thus have a mean to measure the sum of resonances  $f(T)$ . For example in the case of a  $6^3 \times 4$  lattice,  $f(T \sim 0.9T_c) = 0.048(1)$ . Since our data can be so well described by this Ansatz, this confirms that the relevant degrees of freedom in the low-temperature phase are hadrons. The masses of the hadrons are much larger than the scale given by the temperature, since the free energy changes only slightly when varying the imaginary chemical potential, thus  $m_H \gg T_c \approx 160$  MeV.

For  $\frac{T}{T_c} \sim 1.1$  we expect a cusp at  $\mu_I = \pm \frac{\pi T}{3}$  ( $Z_3$ -transitions) to develop in the thermodynamic limit, due to the first order phase transition. Indeed, it appears clearly as the volume increases, see Fig. 4.10 for a comparison of the histogram results (left) versus the reweighting approach<sup>15</sup> (right).

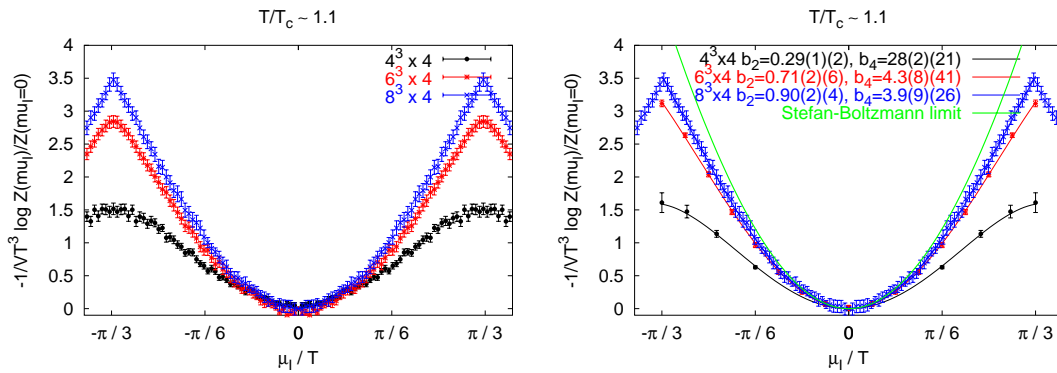


Figure 4.10:  $\frac{F(T, \mu_I)}{VT^4}$  as a function of  $\frac{\mu_I}{T}$  for  $\frac{T}{T_c} \sim 1.1$ . The histogram method (left). The reweighting method, however with  $8^3 \times 4$  results from the histogram (right). We can describe the data points very accurately by the free gas Ansatz. With increasing volume, the Stefan-Boltzmann limit ( $T \rightarrow \infty$ ) is approached very quickly already at  $\frac{T}{T_c} \sim 1.1$  due to the strong first order transition.

<sup>15</sup>The  $8^3 \times 4$ -data points are taken from the histogram method.

We can try to describe these results by a generic Taylor series in  $\frac{\mu_I}{T}$  as an Ansatz. We already have discussed such a simple model at high temperature, the free gas of massless quarks (see subsection 4.2.2). If we perform an analytical continuation from real to imaginary chemical potential, then the free energy of this model is given by

$$\frac{\Delta F(T, V, \mu_I)}{VT^4} = b_2(T)C_2 \frac{N_f}{2} \left(\frac{\mu_I}{T}\right)^2 - b_4(T)C_4 \frac{N_f}{4\pi^2} \left(\frac{\mu_I}{T}\right)^4 \quad (4.64)$$

in the thermodynamic limit. We consider the volume-dependent lattice corrections  $C_2$  and  $C_4$  (compare Table 4.1) and measure the deviation from this free gas model by two parameters  $b_2(T)$  and  $b_4(T)$ .

$T \sim 1.1T_c$	$4^3$	$6^3$	$8^3$	SB limit
$b_2(T)$	0.29(1)(2)	0.71(2)(6)	0.90(2)(4)	1
$b_4(T)$	28(2)(21)	4.3(8)(41)	3.9(9)(26)	1

Table 4.3: The coefficients of the free energy density expansion for  $\frac{T}{T_c} \sim 1.1$  come close to their  $T \rightarrow \infty$  value. In addition to the jackknife error, we specify a systematic error for the fitting Ansatz (see text). The error on the second coefficient  $b_4$  is so large that we cannot determine it properly.

We observe that the leading term approaches the Stefan Boltzmann limit rather fast while increasing the volume, see Fig. 4.10 and Table 4.3. This is somewhat surprising since this coincidence with the Stefan Boltzmann law will occur only at  $T \rightarrow \infty$  even in the thermodynamic limit. Deviations at  $T \sim 1.1T_c$  should persist even in the thermodynamic limit, which indicates the interactions of the quarks<sup>16</sup>. The reduction of  $b_2(T)$  from 1 is consistent with perturbative calculations[34], and its value agrees with Ref. [103], already for the  $8^3 \times 4$  lattice. We argue that indeed the relevant degrees of freedom at high temperature are very light quarks. The first indication is the success of describing our data with the massless quark gas model.

<sup>16</sup>It has been shown already that the free energy of the gluon sector deviates from the Stefan Boltzmann value  $\frac{8\pi^2}{45}$  by about 15%[102] even at  $\frac{T}{T_c} \sim 5$  (and more for lower temperatures). It thus would not be astonishing to observe deviations at finite temperature also in the quark sector.

The second indication comes from the observation that the high-temperature phase is strongly affected by the imaginary chemical potential, thus  $m_q \ll T_c \approx 160$  MeV.

The coefficients in Table 4.3 suffer from a systematic fitting error. One source is the fitting *range*: our Ansatz Eq.(4.64) does not reflect the  $\frac{2\pi}{3}$ -periodicity of  $\frac{\mu_I}{T}$ , therefore we are allowed to fit small  $\frac{\mu_I}{T}$  only. In this regime, the quartic term is subleading and hard to quantify. An estimate of the systematic fitting error can be obtained by varying the fitting range. Another source is the fitting *Ansatz*: we could add the next-order term  $(\frac{\mu_I}{T})^6$ , which changes  $C_4$  by a few percentages, or periodicise the Ansatz by hand via

$$\frac{\Delta F_{per}(T, V, \mu_I)}{VT^4} = -\frac{1}{VT^3} \log \frac{Z_{per}(T, V, \mu_I)}{Z_{per}(T, V, 0)} \quad (4.65)$$

with

$$Z_{per}(T, V, \mu_I) = \sum_{k=-\infty}^{\infty} e^{-VT^3 \left( b_2(T) C_2 \frac{N_f}{2} \left( \frac{\mu_I + 2\pi k}{T} \right)^2 - b_4(T) C_4 \frac{N_f}{4\pi^2} \left( \frac{\mu_I + 2\pi k}{T} \right)^4 \right)}. \quad (4.66)$$

In conclusion, we cannot determine  $b_4(T)$  accurately.

## 4.5 Results - Non-Zero Baryon Number

We now present results from the variance reducing canonical approach to study properties of QCD at temperature  $T$  and density  $\rho$ /chemical potential  $\mu$ . For the theory with four flavours of Kogut-Susskind fermions at mass  $\frac{m}{T} = 0.2$  ( $m_\pi \approx 350$  MeV), the transition between the hadronic and the plasma phase is first-order and gives rise to a co-existence region, part hadron part plasma. We will identify this co-existence region, obtain the phase diagram in the  $T$ - $\rho$  plane, then in the  $T$ - $\mu$  plane using the saddle point approximation Eq.(4.42). We will confirm that the two phases can be well described by simple models, the hadron resonance gas and the massless quark gas. We will measure the chiral condensate as a function of the baryon number. The result will also help to identify two phases: in the confined



phase the chiral condensate has a finite value, while in the quark gluon plasma it should be zero since chiral symmetry is restored. However, due to the non-vanishing quark mass, there is a residual chiral condensate. The dynamics of the first order phase transition is governed by the latent heat and the interface tension. We discuss a technique to measure them and present results. Note that the average Polyakov loop is of no use in our approach. Its expectation value is zero for any temperature in every canonical sector, as discussed in subsection 4.4.1.

This is a feasibility study, therefore we consider a small, coarse lattice  $6^3 \times 4$ . Since  $T_c \sim 160$  MeV, the lattice spacing  $a \sim 0.3\text{fm}$ , and the spatial volume is  $(6a)^3 \approx (1.8\text{fm})^3$ . We sample a variety of ensembles, each at around 5000 configurations, to address the overlap problem, as elaborated in subsection 4.3.3. See Table 4.4 for a detailed list. In addition to the ensembles listed in that table, we have 55 additional ones, given by the parameters  $(\beta, \mu_I)$ , with eleven  $\beta$ 's in  $\beta = 4.80, \dots, 5.10$  and the imaginary chemical potentials  $\mu_I = 0.0, 0.0654I, 0.1309I, 0.18512I, 0.2618$ . Note that our ensembles are generated such that the autocorrelation time  $\tau$  is smaller than one configuration except at the phase transition, where  $\tau$  is about  $1 \lesssim \tau \lesssim 5$ . The autocorrelation times are taken into account in the multi-histogram reweighting, as well as in the error analysis. In Fig. 4.11, we illustrate the overlap problem and the importance of critical ensembles. We plot the importance of the various ensembles  $\Omega_C$  (see Eq.(D.32)) in the canonical sectors  $B = 0, 8, 14$  at temperature  $\frac{T}{T_c} = 0.9$ . We observe that only ensembles sampled at around criticality, namely the ensembles  $(\beta = 5.05, \mu_I = 0.0)$ ,  $(\beta = 5.071, \mu_I = 0.1852)$  (not included in the pictures) and  $(\beta = 5.10, \mu_I = 0.2618)$ , contribute in the high-density (large  $B$ ), ie. quark-gluon plasma regime.

ensemble number	$\beta$	coupling type	coupling value
0	5.042	$\mu_I$	0.00
1	5.044	$\mu_I$	0.06
2	5.054	$\mu_I$	0.13
3	5.067	$\mu_I$	0.18
4	5.085	$\mu_I$	0.22
5	5.095	$\mu_I$	0.26
6	5.007	$\mu_I$	0.00
7	5.009	$\mu_I$	0.06
8	5.019	$\mu_I$	0.13
9	5.032	$\mu_I$	0.18
10	5.050	$\mu_I$	0.22
11	5.060	$\mu_I$	0.26
12	4.975	$\mu_I$	0.00
13	4.975	$\mu_I$	0.18
14	4.975	$\mu_I$	0.26
15	4.975	$\mu_I$	0.06
16	4.975	$\mu_I$	0.13
17	4.972	$\mu_I$	0.00
18	5.025	$\mu_I$	0.26
19	4.970	$\mu_{IS}$	0.20
20	4.990	$\mu_I$	0.26
21	4.970	$\xi$	1.25
22	4.970	$\xi$	1.10
23	4.935	$\xi$	1.00
24	4.935	$\xi$	1.10
25	4.935	$\xi$	1.25
26	4.935	$\xi$	1.375
27	4.955	$\mu_I$	0.26
28	5.013	$\xi$	1.10
29	4.90	$\xi$	1.00
30	4.90	$\xi$	1.10
31	4.90	$\xi$	1.25
32	4.90	$\xi$	1.375
33	4.90	$\xi$	1.515
34	4.90	$\xi$	1.45
35	4.92	$\mu_I$	0.26

Table 4.4: The various ensembles in our approach.

### 4.5.1 The Free Energy $F(T, \mu)$ and $F(T, B)$

The free energy is the fundamental quantity to describe a thermodynamic system. We present it as a function of the temperature  $T$  and the real chemical potential  $\mu$  as well as the baryon number  $B$ :

$$\begin{aligned} \Delta F(T, \mu) &= -T \log \frac{Z_{GC}(T, \mu)}{Z_{GC}(T, \mu = 0)} \\ F(T, B) &\equiv -T \log \frac{Z_C(T, B)}{Z_C(T, B = 0)}. \end{aligned} \quad (4.67)$$

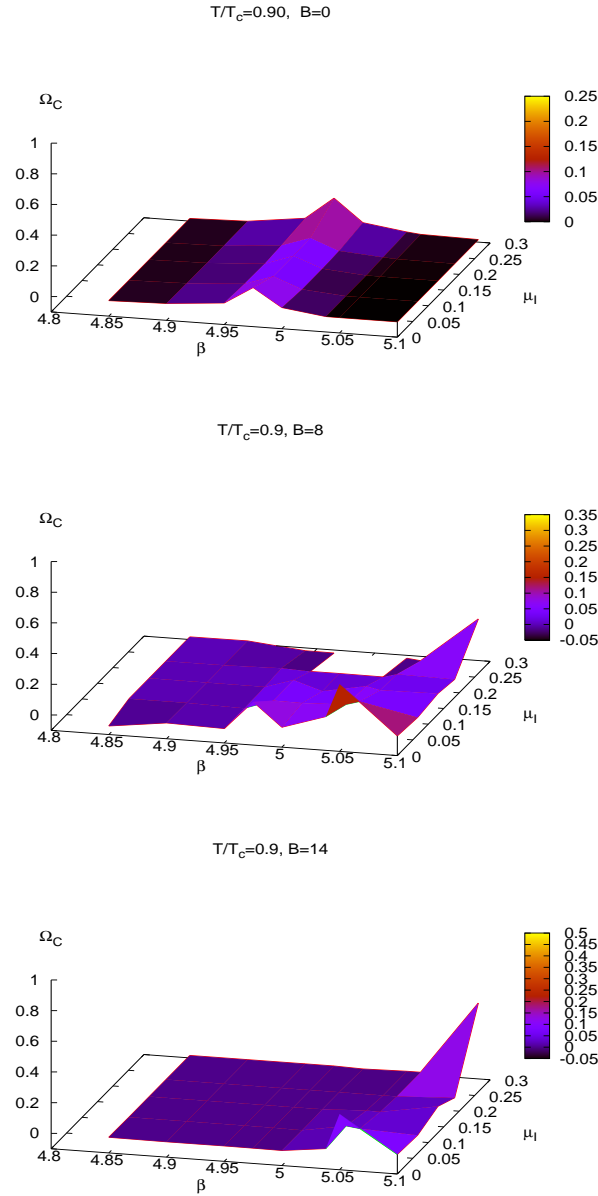


Figure 4.11: The importance  $\Omega_C$  of various ensembles (see text) at temperature  $T/T_c = 0.90$  ( $\beta = 4.98$ ), see Eq.(D.15) on page 197. In the  $B = 0$ -sector, the confining ensembles around  $\beta = 4.975$  contribute most (top). In the co-existence region ( $B = 8$ ) several ensembles contribute (middle). At large  $B$ , only the ensembles sampled around criticality contribute (bottom). This reflects the overlap-problem: for  $B = 14$ , we sample the quark-gluon plasma phase; ensembles in the confined regime have no information about this sector, hence only the ensembles sampled at around criticality contribute significantly.

In this section, we almost exclusively deal with the Helmholtz free energy  $F(T, B)$ . However, to establish the connection with the previous section, where we have studied the free energy as a function of the imaginary chemical potential, we first discuss  $\Delta F(T, \mu)$ . As per Eq.(D.6), we determine  $Z_{GC}(T, \mu)$  via Ferrenberg-Swendsen reweighting. An arbitrary normalisation constant cancels if we consider the ratio  $\frac{Z_{GC}(T, \mu)}{Z_{GC}(T, \mu=0)}$ . We want to show the inconsistency of  $\Delta F(T, \mu)$  with the free gas expression in the Stefan-Boltzmann limit, confirming results in Ref. [73] and the previous section.

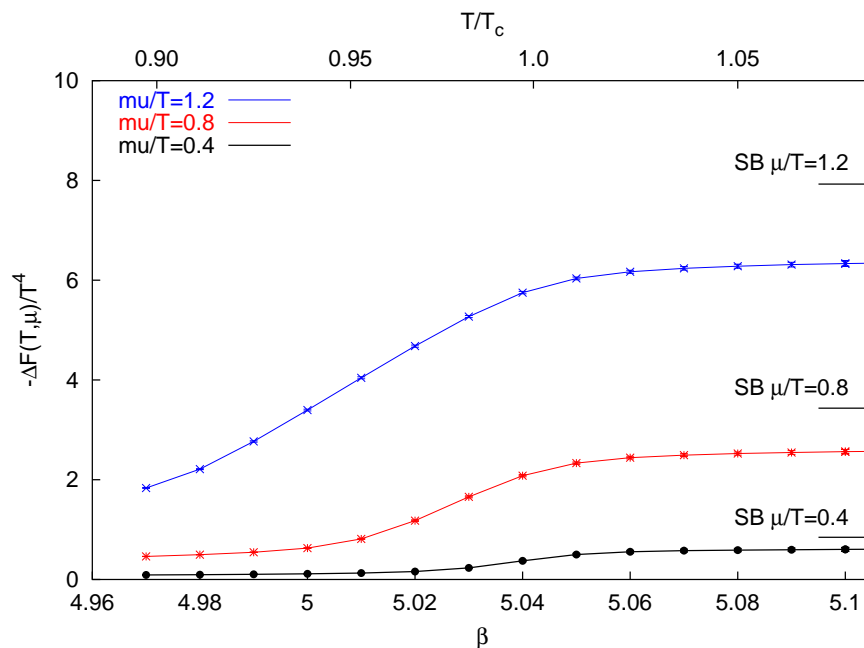


Figure 4.12:  $-\frac{\Delta F(T, \mu)}{T^4}$  as a function of the temperature at fixed real chemical potential  $\frac{\mu}{T} = 0.4, 0.8$  and  $1.2$ . The Stefan-Boltzmann values incorporate finite volume and cut-off corrections of the free gas on the lattice. At  $\frac{T}{T_c} = 1.1$ , the numerical values are about 30% smaller than the model calculation.

In Fig. 4.12 we plot  $\frac{\Delta F(T, \mu)}{VT^4}$  at fixed chemical potential while varying the temperature. A plateau is reached for rather low temperatures  $T \sim 1.1T_c$  already<sup>17</sup>. We compare

<sup>17</sup>We have chosen the inverse coupling  $\beta = 5.10$ , which gives a temperature  $T$  of about  $1.1 T_c$ . In the previous section, we discussed results at the same  $\beta$ -value.

its value with the free gas model calculation,

$$-\frac{\Delta F(T, V, \mu_I)}{VT^4} = C_2 \frac{N_f}{2} \left(\frac{\mu}{T}\right)^2 + C_4 \frac{N_f}{4\pi^2} \left(\frac{\mu}{T}\right)^4, \quad (4.68)$$

where we take the finite volume and cut-off corrections  $C_2$  and  $C_4$  into account, as listed in Table 4.1. We observe that the lattice results are below the free gas values. We quantify the deviation by requiring that

$$-\frac{\Delta F(T, V, \mu_I)}{VT^4} = \hat{b}_2(T) C_2 \frac{N_f}{2} \left(\frac{\mu}{T}\right)^2 + \hat{b}_4(T) C_4 \frac{N_f}{4\pi^2} \left(\frac{\mu}{T}\right)^4 \quad (4.69)$$

describes our high temperature plateaus for all chemical potential. Note that we have plotted only three particular values of  $\frac{\mu}{T}$  for simplicity. We obtain  $\hat{b}_2(T \sim 1.1T_c) = 0.70(2)$  and  $\hat{b}_4(T \sim 1.1T_c) = 3.0(2)$ . For small chemical potentials, our results deviate from the free gas Ansatz by about 30%, for  $\frac{\mu}{T} > 1$  even more. This discrepancy is caused by an interaction between the quarks. Ref. [34] shows that a finite coupling  $g(T)$  indeed decreases the leading coefficient in Eq.(4.68). Note that we cannot determine the value of the coupling  $g(T)$ , since also  $g(T)$ -dependent finite size corrections are affecting  $b_2(T)$ . In the previous section, where we extracted the free energy as a function of an imaginary chemical potential, we have determined  $b_2(T \sim 1.1T_c) = 0.71(2)$  ( $b_4(T \sim 1.1T_c)$  could not be extracted reliably), confirming the findings here. This indicates that the analytical continuation of the Taylor series works, at least for small chemical potential.

In the following, we discuss  $F(T, B)$  as a function of small baryon numbers  $B = 1, \dots, 4$  to check the feasibility of the method to explore few-nucleon systems at low temperature. We then extrapolate to the strong-coupling regime  $\beta \rightarrow 0$  and compare with analytical strong-coupling calculations.

In Fig. 4.13 (left), we illustrate the scans we are performing in the  $T$ - $\rho$  plane. Note that the arrows are not vertical, since we keep fixed the baryon number, not the density<sup>18</sup>. If we increase  $\beta$ , the lattice spacing  $a$  decreases. As a consequence, the

<sup>18</sup>The scans actually are performed along  $T \sim \rho^{\frac{1}{3}}$ .

density increases. In the right figure, we present the Helmholtz free energy at fixed baryon number  $B = 1, 2, 3, 4$  as a function of the temperature.

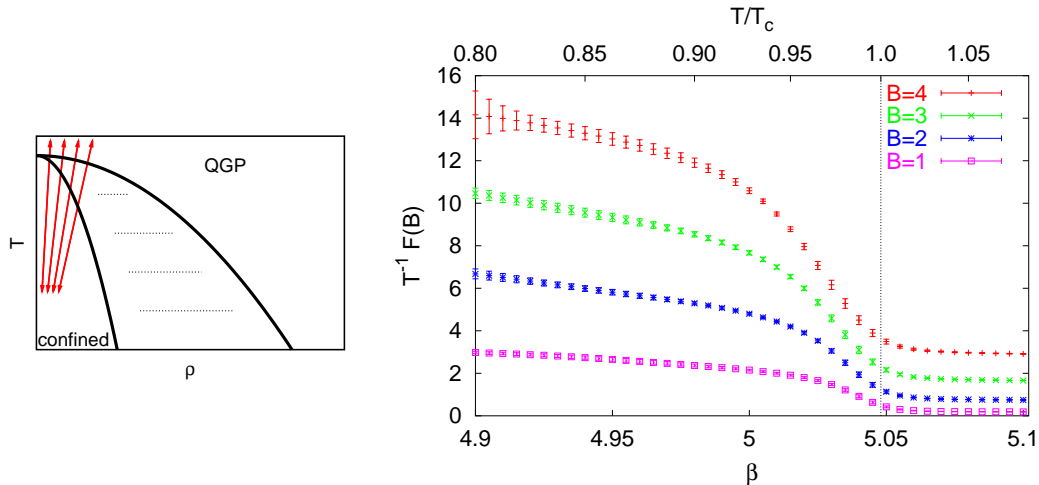


Figure 4.13: A sketch of our scan (left). The free energy at fixed baryon number as a function of the  $\beta/T$  (right). The vertical line indicates the critical temperature at  $B = 0$ . At low temperature, we deal with a system of weakly interacting heavy ( $m_B \gg T$ ) baryons  $F(T, B) \sim B$ , at high temperature we observe a weakly interacting gas of light ( $m_q \ll T$ ) quarks  $F(T, B) \sim B^2$ .

In the high-temperature phase  $T > T_c$ ,  $F(T, B)$  is almost independent of the temperature. Thus, compared to the temperature, the mass of the degree of freedom is either very large or very small. Motivated by the (relative) success of the free quark gas model in this regime, we calculate the Helmholtz free energy in this model for small  $B$ . For small  $\mu$ , the free energy as a function of the chemical potential is approximately  $F(\mu) \sim VT^2\mu^2$ , compare with Eq.(4.16). The grand canonical partition function thus is

$$Z_{GC}(T, \mu) \sim e^{VT\mu^2}, \quad (4.70)$$

and we obtain the canonical partition function by the Fourier transformation

$$Z_C(T, B) = \frac{1}{2\pi} \int_{-\pi}^{\pi} d\bar{\mu}_I e^{-i3B\bar{\mu}_I} Z_{GC}(i\bar{\mu}_I T) \sim e^{-\frac{B^2}{VT^3}}. \quad (4.71)$$

It follows that the Helmholtz free energy  $F(T, B) = -T \log \frac{Z_C(T, B)}{Z_C(0)} \sim B^2$ , as we observe with small deviations. These deviations may be caused by finite size effects,

and/or the inappropriateness of the simple model (for example there is a weak interaction between the quarks). Here, we cannot shed more light on this issue, but we will do so in the next subsection.

As  $T$  approaches  $T_c$  from below, the free energy drops dramatically. This region is indicative of the co-existence region, however, due to rounding effects, boundaries are hard to quantify. In the low-temperature phase  $T < T_c$ , the Helmholtz free energy increases approximately linearly with  $B$  at a given temperature. In addition, it decreases linearly in  $T$  at a given  $B$ . A very naive canonical partition function like

$$Z_C(T, B) = e^{-\frac{1}{T}(m|B| - ST)} \equiv d e^{-\frac{1}{T}m|B|} \quad \text{with } d \equiv e^{-S} \quad (4.72)$$

would already be sufficient to explain this behaviour. This partition function describes a system consisting of  $B$  baryons of the same kind: a baryon state with mass  $m$  at rest, with degeneracy  $d$  ( $S$  is the entropy). The assumption that we deal with static baryons is reasonable: the minimal non-trivial momentum is much larger than the temperature,  $p_{min} = \hbar k_{min} = \frac{2\pi}{N_s a} > T = \frac{1}{N_t a} \sim 160$  MeV. In other words it is unlikely to find baryon states with non-zero momentum. A numerical investigation shows however that we observe small deviations from this description. At fixed temperature, we check the difference  $I = F(B = 1) - F(B = 2)/2$ . We obtain  $I = -0.06(1)a^{-1} \approx -35(6)$  MeV, within errors independently of the temperature in the interval  $0.85 < \frac{T}{T_c} < 0.9$ . This may be caused by a small repulsive interaction. As a consequence, we either implement this interaction in the given model, or we consider a different one. We realise that Eq.(4.72) is a crude approximation of the hadron resonance gas model (one static resonance only). We will test our data against the hadron resonance gas in the next subsection and, indeed, find good agreement.

We can lower the temperature, or rather  $\beta$ , even further. We measure  $F(\beta, B = 1)$

and extrapolate to the strong coupling limit  $\beta \rightarrow 0$ . It will allow us to compare with predictions from different strong coupling calculations. The first comparison is made by considering the strong coupling spectrum of the four flavour theory. We use the Ansatz in Eq.(4.72) extended to two states with the masses  $m_0, m_1$  and degeneracies  $d_0, d_1$ . The masses are known[104, 105] a priori:  $am_0(\beta = 0) = 2.785$  and  $am_1(\beta = 0) = 3.113$ . The degeneracies can be calculated. In order to determine the various possibilities to combine three degenerate quarks into a symmetric state (under the exchange of a pair of quarks), we have to reduce  $4 \otimes 4 \otimes 4 = 20_S \oplus 20_M \oplus 20_M \oplus 4_A$ , where the subscript  $S$  refers to symmetric,  $M$  to mixed-symmetric and  $A$  to antisymmetric states. With four flavours, the “baryon octet”, which contains the “nucleon” becomes a 20-plet. The “baryon decuplet” becomes a 20-plet also. The total degeneracy is then (for the two lowest states)

$$\begin{aligned} J^P = \frac{1}{2}^+ & : 20 \times \left(2\frac{1}{2} + 1\right) = 40 \\ J^P = \frac{3}{2}^+ & : 20 \times \left(2\frac{3}{2} + 1\right) = 80 . \end{aligned}$$

The Ansatz thus becomes

$$Z(\beta) = d_0 e^{-\frac{(am_0)(\beta)}{aT}} + d_1 e^{-\frac{(am_1)(\beta)}{aT}} + \dots , \quad (4.73)$$

with  $d_0 = 40$  and  $d_1 = 80$ .  $\frac{1}{aT} = N_t$ , where  $N_t$  is the number of lattice sites in temporal direction. We expand the mass terms in  $\beta$ :  $(am_i)(\beta) = (am_i)(\beta = 0) + c_i\beta + \mathcal{O}(\beta^2)$  allows for a fit with the parameters  $c_0, c_1$ .

In Fig. 4.14, we plot our results of  $F(\beta, B)/B$  for  $B = 1$  and  $B > 2$ . We first consider the case  $B = 1$ , where  $F(\beta, B)/B = F(\beta, B)$ , and fit the Ansatz Eq.(4.73). If we consider one state ( $m_0$ ) only, the expansion coefficient  $c_0$  is small, which justifies our simple expansion. However, the fit<sup>19</sup> does not account for all data points, neither does the Ansatz with two states. The tendency however is that the inclusion of more states reduces the free energy of our Ansatz, thus Eq.(4.73) approaches the lattice

---

<sup>19</sup>In Fig. 4.14 we only indicate the free energy predicted by Eq.(4.73) at  $\beta = 0$ : “1-state” refers to the inclusion of only the state  $m_0$ ; “2-states” indicates that we use two states  $m_0$  and  $m_1$ .



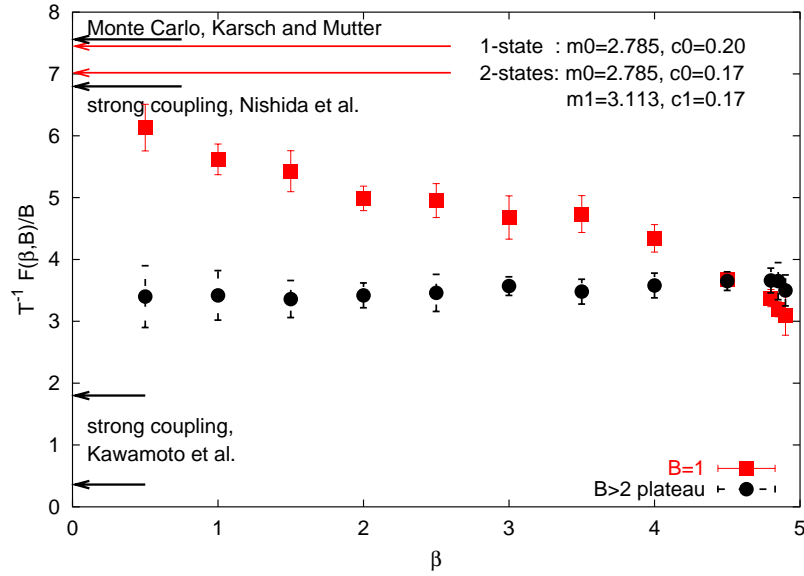


Figure 4.14: Strong coupling limit. We show  $F(\beta, B)/B$  for  $B = 1$  and  $B > 2$  (plateau). For  $B = 1$ ,  $F(\beta, B)/B = F(\beta, B)$ , we compare the free energy with predictions from a simple strong coupling Ansatz Eq.(4.73), labelled with “1-state” and “2-states”. The parameters  $c_0$  and  $c_1$  are obtained by a mediocre fit (not explicitly plotted). Further states are needed, which bend the strong-coupling prediction to lower values, thus the prediction will approach the lattice data.  $F(\beta, B)/B$  is also a crude approximation for the critical chemical potential[80]. We compare with predictions for the critical chemical potential at  $\beta = 0$  from Monte Carlo simulations and strong coupling calculations: “Monte Carlo, Karsch and Mutter”[106], “Nishida et al.”[107] and just recently “Kawamoto et al.”[108]. At  $B = 1$ , the interaction of the baryons is not included, which biases  $F(\beta, B)/B$  to larger values. At fixed  $\beta$ , a plateau in  $F(\beta, B)/B$  is reached at about  $B = 3$  already. We plot the particular plateau-values which are in between the various strong coupling calculations.

data. However, this would require further knowledge of the spectrum. In fact, if we allow in our simple Ansatz for non-zero momenta  $\epsilon_i^2(m_i, \vec{k}) = m_i^2 + \sum_{j=1}^3 \left(2 \sin \frac{k_j}{2}\right)^2$  and sum over these states, the prediction is  $T^{-1}F(\beta, B) = 4.80$  for the “1-state plus momenta”-Ansatz and  $T^{-1}F(\beta, B) = 4.31$  for the “2-states plus momenta”-Ansatz.

Strong coupling calculations have determined the critical chemical potential at  $\beta = 0$ . An old analysis using Monte Carlo simulations has found  $a\mu_c(\beta = 0) = 0.63$  (see Fig. 4.14 “Monte Carlo, Karsch and Mutter”[106]). The quantity shown is  $\frac{1}{aT}3a\mu_c$ ), a newer strong coupling calculation has obtained  $a\mu_c(\beta = 0) = 0.57$  (see

Fig. 4.14 “Nishida et al.” [107]). Their result indicates a rather large critical chemical potential. However, recently, another strong coupling analysis has been performed, where a baryon interaction term is incorporated for the first time. Ref. [108] then finds, depending on the strength of the interaction, a band  $a\mu_c(\beta = 0) \in [0.03, 0.15]$ . This band is indicated in Fig. 4.14 (“Kawamoto et al.”). As argued in Ref. [80],  $F(\beta, B)/B$  is an estimation of the critical chemical potential at a certain value of the coupling  $\beta$ , if a plateau of  $F(\beta, B)/B$  with increasing  $B$  is reached. We observe such a plateau for  $B = 3$  already. We show the plateau-value,  $B > 2$ , which is in between the strong coupling calculations. The value of the critical chemical potential at  $\beta = 0$  is important because it provides a limiting value for the critical line  $\mu_c(\beta)$ , which we study later.

$$\mathbf{4.5.2} \quad \frac{F(T, B) - F(T, B-1)}{3T} = \frac{\mu(B)}{T}$$

We assume the validity of the saddle point approximation to equate  $\frac{F(T, B) - F(T, B-1)}{3T}$  with  $\frac{\mu(B)}{T}$  following Eq.(4.42). This assumption is justified, as we will show in the next subsection. If we know  $\frac{\mu(B)}{T}$ , which relates  $\mu$  to  $\rho = \frac{B}{V}$ , we can compare the lattice results with model calculations for  $\rho(\mu)$ : we show that the low-density regime can be reasonably well described by a simple hadron resonance gas Ansatz Eq.(4.11),  $\frac{\rho}{T^3} = f(T) \sinh(\frac{\mu}{T})$  with  $f(T)$  as the only free parameter; the high-density regime almost corresponds to a gas of free massless quarks Eq.(4.15)  $\frac{\rho}{T^3} = \frac{N_f}{3} \left(\frac{\mu}{T}\right) + \frac{N_f}{3\pi^2} \left(\frac{\mu}{T}\right)^3$ . In Fig. 4.15, we show  $\frac{\mu}{T}$  as a function of the baryon number, at fixed temperature, as sketched in the left figure. We obtain accurate results up to high densities ( $\frac{\rho}{T^3} = 8$  corresponds to about 5 baryons/fm<sup>3</sup>) and large chemical potentials ( $\frac{\mu}{T} \sim 2$ ). Note that we find the same  $\frac{\rho}{T^3}(\frac{\mu}{T})$  dependence in the plasma phase at all temperatures.

In the low-temperature phase, it is remarkable that the hadron resonance gas Ansatz

$$\frac{\rho}{T^3} \left(\frac{\mu}{T}\right) = \tilde{f}(T) \sinh \frac{3\mu}{T} \quad (4.74)$$

accounts for all data points at small baryon number. We fit the sum of the hadron

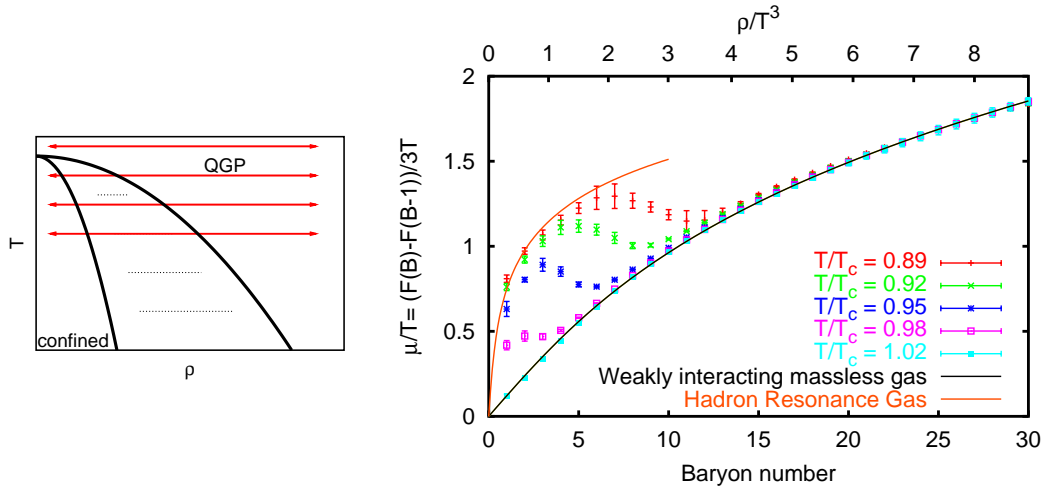


Figure 4.15: A sketch of our “scans” (left). The derivative of the free energy at fixed temperature as a function of the baryon number (density). In the saddle point approximation, the y-axis corresponds to  $\frac{\mu}{T}$

resonances  $\tilde{f}(T)$  and find  $\tilde{f}(T \sim 0.90T_c) = 0.05(1)$ , in agreement<sup>20</sup> with  $f(T \sim 0.90T_c) = 0.048(1)$  in subsection 4.4.3. In two independent studies, at imaginary chemical potential and at finite baryon density, we have described consistently the free energy and one of its derivatives with the hadron resonance gas model. The only free parameter was the sum of resonances  $f(T) = \tilde{f}(T)$ . As a side note, this result also indicates the validity of analytic continuation.  $\frac{\rho}{T^3} \left(\frac{\mu}{T}\right)$  shows no measurable deviation from  $f(T) \sin \frac{3\mu}{T}$ , whereas  $\frac{\rho}{T^3} \left(\frac{\mu}{T}\right)$  deviates from Eq.(4.74) dramatically as the phase transition is reached.

The high-temperature regime can be well described by the slightly modified free massless quark Ansatz

$$\frac{\rho}{T^3} \left(\frac{\mu}{T}\right) = \tilde{b}_2(T)C_2 \frac{N_f}{3} \left(\frac{\mu}{T}\right) + \tilde{b}_4(T)C_4 \frac{N_f}{3\pi^2} \left(\frac{\mu}{T}\right)^3, \quad (4.75)$$

with  $\tilde{b}_2(T = 1.1T_c) = 0.70(1)$  and  $\tilde{b}_4(T = 1.1T_c) = 2.97(3)$ . This appears to hold for any temperature if the *density* is large enough. Thus, we have found the low-

<sup>20</sup>We compare the results at same inverse coupling  $\beta = 4.95$ , which corresponds to a temperature slightly lower than  $\frac{T}{T_c} = 0.9$ .

temperature/large-density regime to be consistent with a quark-gluon plasma description. The coefficients, which quantify the deviation from the Stefan-Boltzmann gas, are in agreement with results from imaginary chemical potential (subsection 4.4.3) as well as real chemical potential (subsection 4.5.1). On the rather small lattice  $6^3 \times 4$ , we deviate by at about 30% from a free gas. The downward deviation from 1 ( $\tilde{b}_2(T = 1.1T_c) = 0.70(1)$ ) is consistent in sign with leading perturbative corrections[86].

For completeness, we cross-check the volume-dependent constants  $C_2$  and  $C_4$ . We calculate  $\frac{F(T,B)-F(T,B-1)}{3T}$  for the free quark gas on the lattice, which is obtained by setting all gauge links to the identity. The results are shown in Table 4.5. The new constants, labelled as  $\tilde{C}_2$  and  $\tilde{C}_4$  (“canonical results”), agree with the  $C_2$  and  $C_4$  (“grand-canonical results”) in Table 4.1.

Lattice	$\tilde{C}_2$	$\tilde{C}_4$
$4^3 \times 4$	4.39(8)	0.24(8)
$6^3 \times 4$	2.67(2)	1.75(3)
$8^3 \times 4$	2.33(1)	2.33(1)
$10^3 \times 4$	2.25(1)	2.52(1)
$\infty^3 \times 4$	2.25	2.6

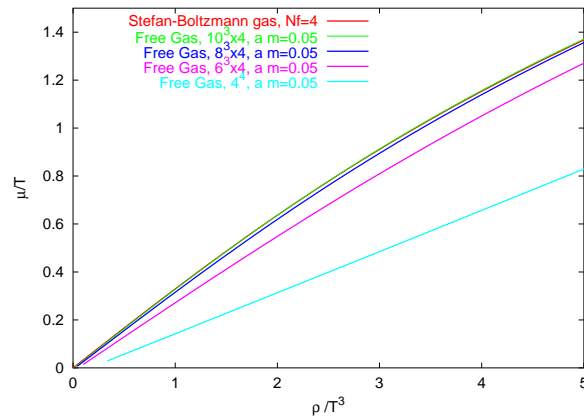


Table 4.5: The prediction for  $\frac{\mu}{T}(\frac{\rho}{T^3})$ , based on the free gas model in the continuum at high temperature, suffers from finite size and cut-off effects. The correction terms  $\tilde{C}_2$  and  $\tilde{C}_4$  help to quantify the systematics (left table). As expected, the correction factors are in agreement with Table 4.1 on page 115. We plot results of  $\frac{\mu}{T}(\frac{\rho}{T^3})$  from the free gas on the lattice at various lattice sizes and compare with the massless Stefan-Boltzmann gas (right). Already at the volume  $10^3$ , no difference is visible.

### 4.5.3 Maxwell Construction

The first order phase transition and the associated metastabilities between the two phases are clearly visible in the S-shape behaviour of  $\frac{\mu}{T}(B)$ , see the discussion in subsection 4.3.4. For a given temperature  $T$ , we identify the boundaries  $\rho_1$  and  $\rho_2$  of the co-existence region and the critical chemical potential  $\mu_c$  as follows. Equality

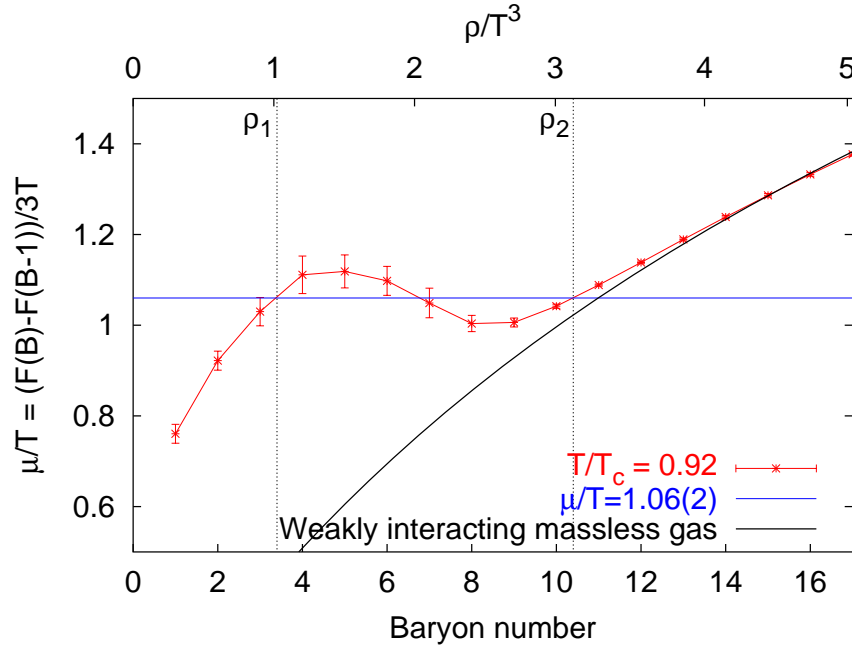


Figure 4.16: The Maxwell construction allows to extract the chemical potential, as well as the boundaries of the coexistence region.

of the free energy densities in the two phases  $f(\rho_1) - 3\mu_c\rho_1 = f(\rho_2) - 3\mu_c\rho_2$ , where  $f$  is the Helmholtz free energy  $f(\rho = \frac{B}{V}) = -\frac{T}{V} \log Z_C(\rho = \frac{B}{V})$ , implies

$$\int_{\rho_1}^{\rho_2} d\rho (f'(\rho) - 3\mu_c) = 0. \quad (4.76)$$

Since  $f'(\rho)$  is the quantity measured in Fig. 4.15, we determine  $\rho_1$ ,  $\rho_2$  and  $\mu_c$  by a “Maxwell construction”, illustrated in Fig. 4.16 for the temperature  $\frac{T}{T_c} = 0.92$ . The value of  $\frac{\mu}{T}$  defining the horizontal line is adjusted to make the areas of the two “bumps” in the S-shape equal. Here,  $\frac{\mu_c}{T} = 1.06(2)$  is the value of the critical chemical potential, with the boundaries of the co-existence region at  $\frac{\rho_1}{T^3} = 1.00(16)$  and

$$\frac{\rho_2}{T^3} = 3.15(32).$$

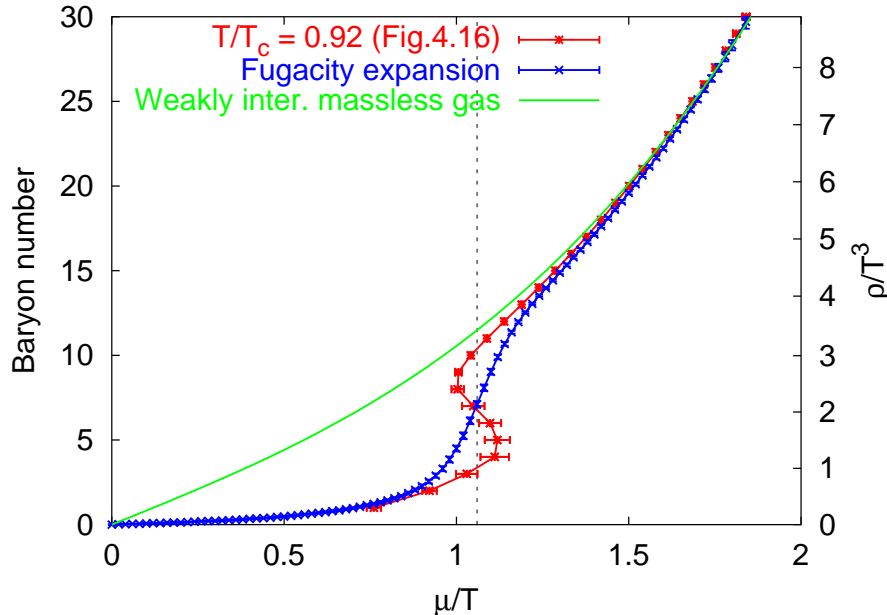


Figure 4.17: The saddle point approximation in comparison with the fugacity expansion. The same critical chemical potential  $\mu_c = 1.06(2)$  is indicated. However, the S-shape indicating the metastabilities is only visible via the saddle point approximation.

We can cross-check this result for the critical chemical potential by making use of the fugacity expansion Eq.(4.39), see Fig. 4.17. For a given chemical potential, we measure the baryon number  $\langle B \rangle(\mu)$ . We see a jump at the same value  $\frac{\mu}{T} = 1.06$ , but the rounding due to finite size effects is very strong.

#### 4.5.4 Phase Diagrams

We present the phase diagram in the  $T$ - $\mu$  as well as in the  $T$ - $\rho$ -plane<sup>21</sup>. The latter has been obtained for the first time. In Fig. 4.18, we summarise results from various methods, all for the same theory: four flavours of staggered quarks at  $\frac{m}{T} = 0.2$ ,

<sup>21</sup>Remember that we fix the temperature as a ratio  $\frac{T}{T_c}$  via the 2-loop  $\beta$ -function. Also, we set the scale by setting  $T_c = 160 \text{ MeV}$ . Then,  $a(\beta) = \frac{1}{T(\beta)N_t} \approx 0.3 \text{ fm}$ .

with  $N_t = 4$  time slices; only the spatial volume varies as indicated. We have re-

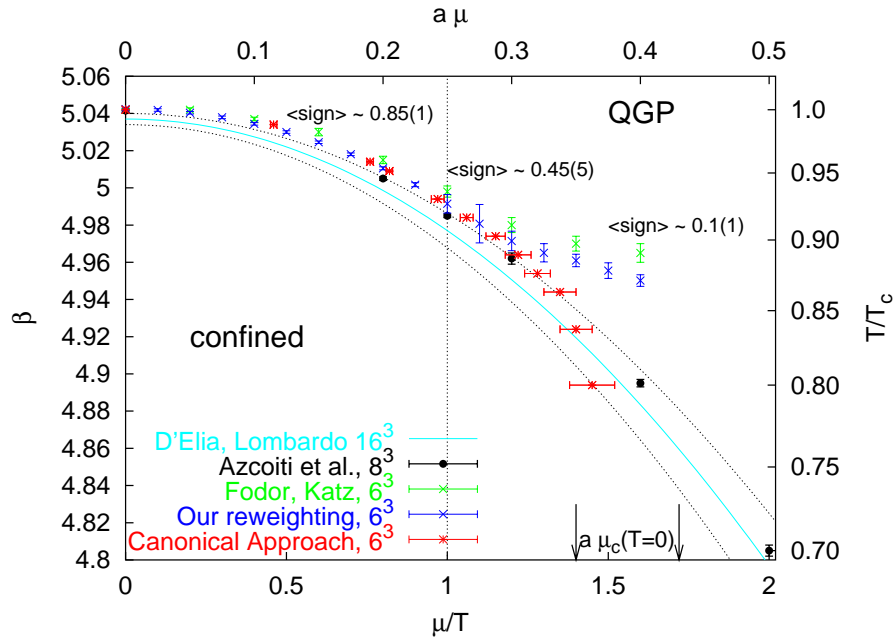


Figure 4.18: The phase diagram in the  $T$ - $\mu$ -plane for four degenerate flavours of staggered quarks with  $m_\pi \approx 350$  MeV.

peated (“Our reweighting”) the study of [65] (“Fodor,Katz”), using multi-parameter reweighting on one ensemble generated at  $(\beta_c, \mu = 0)$ . We identify the phase transition via the peak of the specific heat instead of Lee-Yang zeroes, and obtain consistent results. However, the “sign problem” dramatically grows with increasing chemical potential, as shown by the average sign in the figure. Moreover, our statistical error, based on jackknife blocks as in Ref. [65], does not reflect the true inaccuracy, since the blocks are not statistically uncorrelated, see Appendix B. In Fig. 4.19 (left), we explicitly show the weight of each configuration sampled at  $\beta_c(\mu = 0)$  when we reweight to  $(\beta = 4.94, a\mu = 0.35)$ . Two configurations carry  $\frac{2}{3}$  of the weight, indicating the breakdown of statistical sampling. This apparent overlap problem can be cured, see Fig. 4.19 (right). We supplement the reweighting of the one ensemble generated at  $(\beta_c, \mu = 0)$  with the ensembles listed in Table 4.4. Again, we identify the phase transition via the peak in the specific heat. The phase boundary “Our

reweighting, all ensembles” agrees with the results from the canonical approach, and clearly starts to deviate from the  $\beta_c(\mu = 0)$ -reweighting results at  $\frac{\mu}{T} \approx 1.2$ .

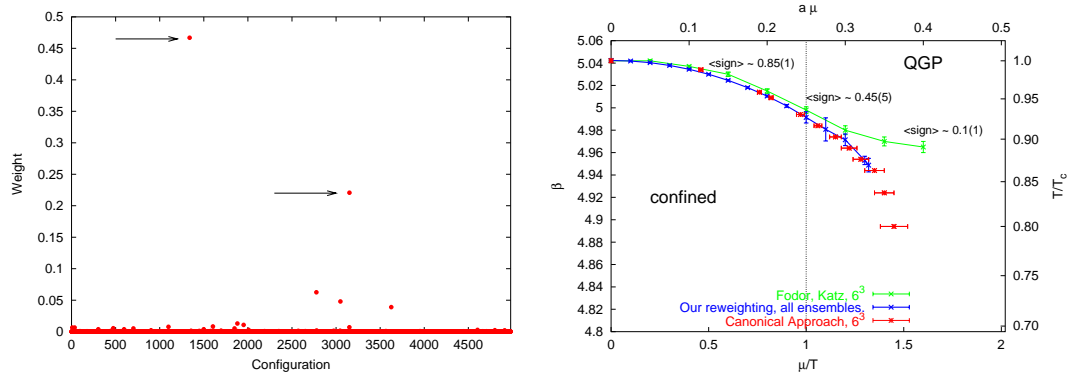


Figure 4.19: The breakdown of statistical sampling. Here we show the weight of each configuration sampled at  $\beta_c(\mu = 0)$  when we reweight to  $(\beta = 4.94, a\mu = 0.35)$ . The two arrows mark the only relevant configurations (left). The phase boundary, obtained via reweighting, agrees with our new results, if we include ensembles with better overlap with the large  $\mu$ -regime. Note, the lines are meant to guide the eye (right).

The parabolic fit[76] is consistent with the black points[96]. Both methods perform an analytic continuation from imaginary chemical potential, for which systematic errors are hard to quantify.

Our new results are shown in red. There is no strong inconsistency with other results, but we observe a clear sign of bending down starting at  $\frac{\mu}{T} \approx 1.3$ . In fact this should happen, if the critical line is to reach our strong-coupling results.

In Fig. 4.20, we plot the phase diagram in the  $T$ - $\rho$  plane. We reach reasonable accuracy down to  $\frac{T}{T_c} \approx 0.8$ . The densities at the boundaries of the co-existence region seem to remain constant at  $T < 0.85T_c$  already, with  $\rho_{\text{QGP}} = 1.8(3)\frac{B}{\text{fm}^3}$  and  $\rho_{\text{confined}} = 0.50(5)\frac{B}{\text{fm}^3}$ . For the following discussion we assume that the density  $\rho_{\text{confined}}$  gives an upper bound for nuclear matter density[109]: the baryons are so packed at this density that a phase transition starts to take place. Let us compare the value with the real world, where the nuclear matter density is  $0.17\frac{B}{\text{fm}^3}$ [110]. We thus have 3 times more baryons in the system. This is a reasonable value, since our quark mass is heavier than in real-world, from which one expects that the baryon



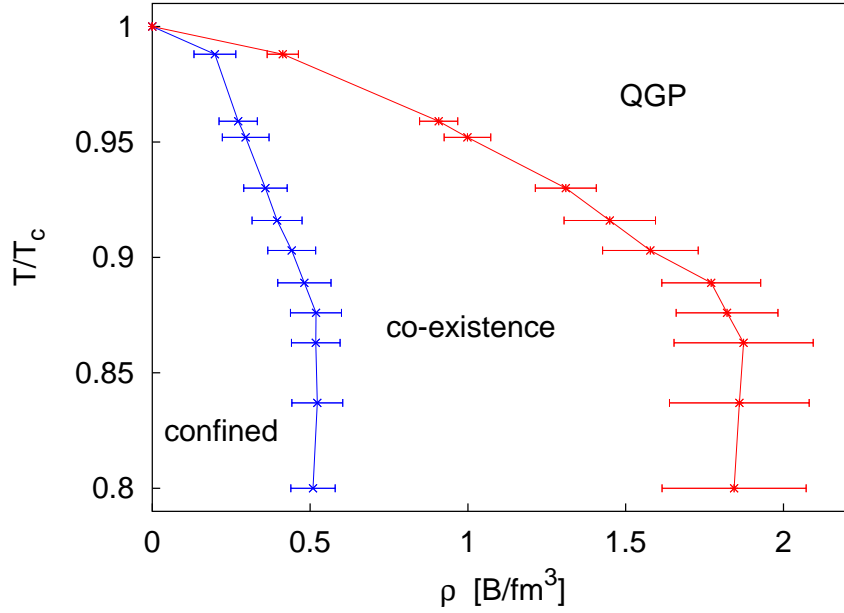


Figure 4.20: The phase diagram in the  $T$ - $\rho$ -plane for four degenerate flavours of staggered quarks with  $m_\pi \approx 350$  MeV.

shrinks. If we want to compensate for the factor 3 in the density, the diameter of a baryon shrinks by  $3^{-\frac{1}{3}} \sim 0.7$ .

### 4.5.5 Chiral Condensate

In chapter 1, we have discussed the notion of chiral symmetry with its order parameter, the chiral condensate. With massless quarks, the expectation value of  $\bar{\Psi}\Psi$  is non-zero in the confined phase, but zero in the deconfined phase. Here, we deal with non-zero quark masses, hence the pion acquires a mass. As a consequence, the chiral condensate never is zero. Still, it can be used to characterise the two phases at low and high density.

We first study the chiral condensate at zero chemical potential as a function of the temperature, see Fig. 4.21. The black points are our results for the chiral condensate  $\langle\bar{\Psi}\Psi\rangle$ , in red we plot the susceptibility  $\langle(\bar{\Psi}\Psi)^2\rangle - \langle\bar{\Psi}\Psi\rangle^2$ . Note that we have

multiplied the red values with a normalisation factor, such that both data sets fit nicely on the same figure. The phase transition occurs at  $\beta = 5.043(1)$ , in agreement with the literature. We note the residual of the chiral condensate at large  $\beta$ :  $\langle \bar{\Psi}\Psi \rangle = 0.255(12)$ . We will make use of this value in the following, when we study the chiral condensate as a function of the baryon number.

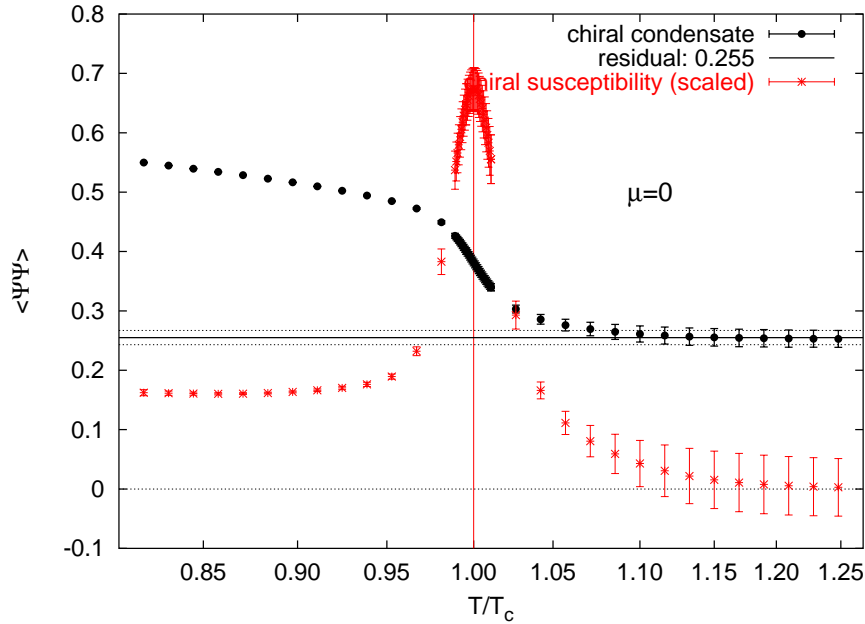


Figure 4.21: The chiral condensate as a function of the temperature at  $\mu = 0$ . The chiral symmetry is only approximate, hence there is a non-zero residual chiral condensate even at high temperature,  $\langle \bar{\Psi}\Psi \rangle = 0.255(12)$ .

In Fig. 4.22, we present the chiral condensate as a function of the baryon number at  $\frac{T}{T_c} = 0.94$ . We indicate with vertical lines the boundaries of the co-existence region at that temperature obtained via the saddle-point approximation. The residual chiral condensate at high temperature at zero chemical potential is also drawn. The value of the chiral condensate at  $B = 0$  agrees with the one at  $\mu = 0$  as expected. For small baryon numbers, the chiral condensate varies only slightly until it hits the co-existence region. A rather fast drop is observed, eventually  $\langle \bar{\Psi}\Psi \rangle$  remains constant at large  $B$ . It is nice to observe that this happens within the boundaries

given by the residual chiral condensate at  $\mu = 0$ .

We cannot read off the boundaries of the co-existence region in a clean way. Due to the finite volume, the rounding effects are simply too large. Furthermore, we rapidly lose accuracy if we lower the temperature. This is due to the method to extract the chiral condensate as a function of the baryon number, see below. The analysis is based on one ensemble only, given by the temperature we want to study. To avoid an overlap problem, we remain conservative and have studied a temperature not too far from the phase transition.

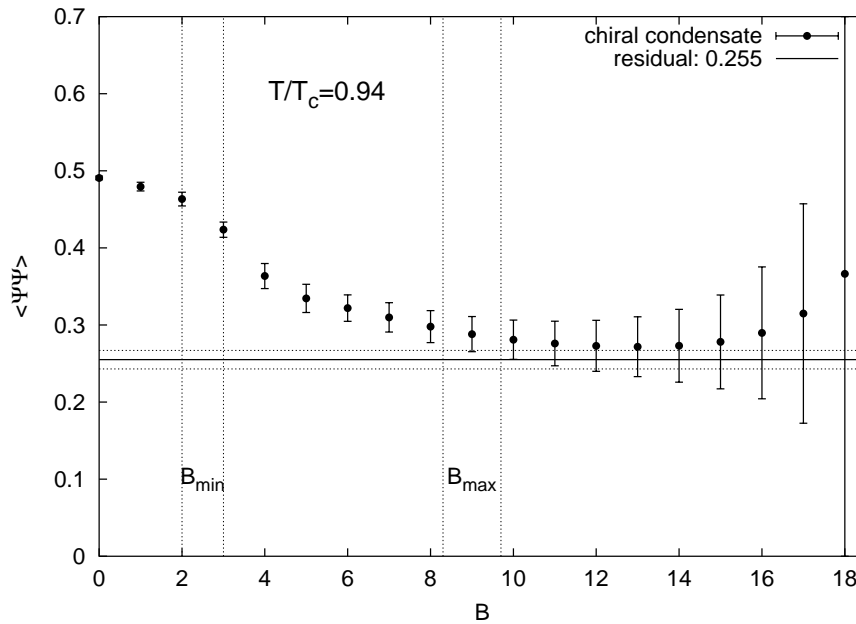


Figure 4.22: The chiral condensate as a function of the baryon number  $B$  at  $\frac{T}{T_c} = 0.94$ . The agreement of the residual chiral condensate at large baryon number with the one in the large-temperature regime at  $B = 0$  (resp.  $\mu = 0$ ) is an indication that the high-density regime can be identified with the quark-gluon plasma phase. The dotted lines, indicating the boundaries of the co-existence region, are taken from the previous subsection (via the Maxwell construction).

The problem in the study of the chiral condensate lies in the fact that the observable depends explicitly on the chemical potential. As a consequence, we cannot determine

the expectation value of  $\bar{\Psi}\Psi$  as simple as the one of the plaquette, which does not. However, we can measure  $\frac{\partial \log Z_C(T, B, m)}{\partial m}$ :

$$\begin{aligned}
\frac{\partial \log Z_C(T, B, m)}{\partial m} &= \frac{1}{Z_C(T, B, m)} \frac{\partial Z_C(T, B, m)}{\partial m} \\
&= \frac{1}{Z_C(T, B, m)} \frac{1}{2\pi} \int_{-\pi}^{\pi} d\left(\frac{\mu I}{T}\right) e^{-i3B\frac{\mu I}{T}} \int [DU][D\bar{\Psi}][D\Psi] \frac{\partial}{\partial m} e^{-S_g[U] - \bar{\Psi}M\Psi} \\
&= \frac{1}{Z_C(T, B, m)} \frac{1}{2\pi} \int_{-\pi}^{\pi} d\left(\frac{\mu I}{T}\right) e^{-i3B\frac{\mu I}{T}} \int [DU][D\bar{\Psi}][D\Psi] (-\bar{\Psi}\Psi) e^{-S_g[U] - \bar{\Psi}(D+m-\mu\gamma_0)\Psi} \\
&= \langle -\bar{\Psi}\Psi \rangle(B)
\end{aligned} \tag{4.77}$$

We write the derivative as a discrete difference and obtain

$$\langle -\bar{\Psi}\Psi \rangle = \frac{\partial \log Z_C(T, B, m)}{\partial m} \Big|_{m=\bar{m}} = \frac{\log Z_C(T, B, \bar{m} + \delta) - \log Z_C(T, B, \bar{m} - \delta)}{2\delta}. \tag{4.78}$$

The right hand side can be evaluated via

$$\begin{aligned}
\frac{Z_C(T, B, \bar{m} + \delta)}{Z_C(T, B, \bar{m} - \delta)} &= \frac{\frac{1}{Z_C(T, B, \bar{m})} \int [DU] \frac{1}{2\pi} \int_{-\pi}^{\pi} d\left(\frac{\mu I}{T}\right) e^{-i3B\frac{\mu I}{T}} \left(\frac{\det M(\bar{m} + \delta)}{\det M(\bar{m})}\right) e^{-S_g[U] \det M(\bar{m})}}{\frac{1}{Z_C(T, B, \bar{m})} \int [DU] \frac{1}{2\pi} \int_{-\pi}^{\pi} d\left(\frac{\mu I}{T}\right) e^{-i3B\frac{\mu I}{T}} \left(\frac{\det M(\bar{m} - \delta)}{\det M(\bar{m})}\right) e^{-S_g[U] \det M(\bar{m})}} \\
&= \frac{\langle \frac{Z_C(T, B, \bar{m} + \delta)}{\det M(\bar{m})} \rangle_{\bar{m}}}{\langle \frac{Z_C(T, B, \bar{m} - \delta)}{\det M(\bar{m})} \rangle_{\bar{m}}},
\end{aligned} \tag{4.79}$$

where we sample at  $m = \bar{m}$ .

## 4.5.6 Latent Heat

Quantities of central importance for the dynamics of a first order phase transition are the latent heat and the interface tension (discussed in the next subsection). In the literature, these quantities are studied while varying the temperature. Here, we also have access to the density driven transition properties. The latent heat quantifies the energy needed for the hadronic matter or quark-gluon plasma to undergo a change of phase while varying the density at fixed temperature.

We study the latent heat as follows. The internal energy density of the system is given by ( $U$ =internal energy)

$$\epsilon \equiv \frac{\langle U \rangle}{V} = \frac{T^2}{V} \frac{\partial}{\partial T} \log Z \tag{4.80}$$

with the temperature  $T = \frac{1}{a(\beta)N_t}$ . Since we have fixed the number of sites in temporal direction  $N_t = 4$ , we can vary the temperature by changing  $\beta$ . Thus,

$$\epsilon = \frac{T^2}{V} \frac{\partial \beta}{\partial T} \frac{\partial}{\partial \beta} \log Z = -\frac{6}{a^4} \langle Pla q \rangle a \frac{\partial \beta}{\partial a} \quad (4.81)$$

with  $\langle Pla q \rangle = \frac{1}{Z} \int [DU] \left( \frac{1}{6N_s^3 N_t} \sum_{\mu < \nu} \sum_x \frac{1}{N_c} \text{Re Tr } Pla q(x, \mu, \nu) \right) e^{-S_g[U]} \det M(U)$ . As  $\beta$ -function, we use the perturbative 2-loop expression given in Eq.(1.61) and obtain

$$a \frac{\partial \beta}{\partial a} = \frac{4\beta_0^3 N_c \beta}{2\beta_1 N_c - \beta_0 \beta}. \quad (4.82)$$

We express the latent heat  $L_h$  in the density driven transition in a dimensionless ratio

$$\frac{L_h}{T^4} \equiv \frac{\epsilon(B_{max}) - \epsilon(B_{min})}{T^4} = -6N_t^4 (\langle Pla q(B_{max}) \rangle - \langle Pla q(B_{min}) \rangle) a \frac{\partial \beta}{\partial a}, \quad (4.83)$$

where  $B_{min}$  and  $B_{max}$  correspond to the boundaries of the co-existence region. In Fig. 4.23 we show the results. In the left figure, we illustrate our construction. At temperature  $\frac{T}{T_c} = 0.92$ , we plot  $\langle Pla q(B) \rangle$ . The two phases are clearly separated. At small baryon number, we observe a moderate linear increase until we hit the phase boundary. A sharp linear increase follows, which bends into a constant behaviour. The rounding is due to finite size effects. It is hard to read off the boundaries of the co-existence region. We thus use the  $B_{min}$  and  $B_{max}$  values obtained from the Maxwell construction, indicated by vertical delimiters. The latent heat is then determined via Eq.(4.83), see the right figure. The dimensionless ratio  $\frac{L_h}{T^4}$  increases rapidly, and seems to remain constant for  $\frac{T}{T_c} < 0.96$ . We thus have indication that the strength of the phase transition increases as the temperature is lowered. Unfortunately, the errors are rather large.

We can cross-check these results in principle. Due to the first order nature of the transition, the histogram of the plaquette shows a two-peak structure. The distance between these peaks allows to determine the latent heat. Qualitatively, we can verify the above finding, but the error is even larger.

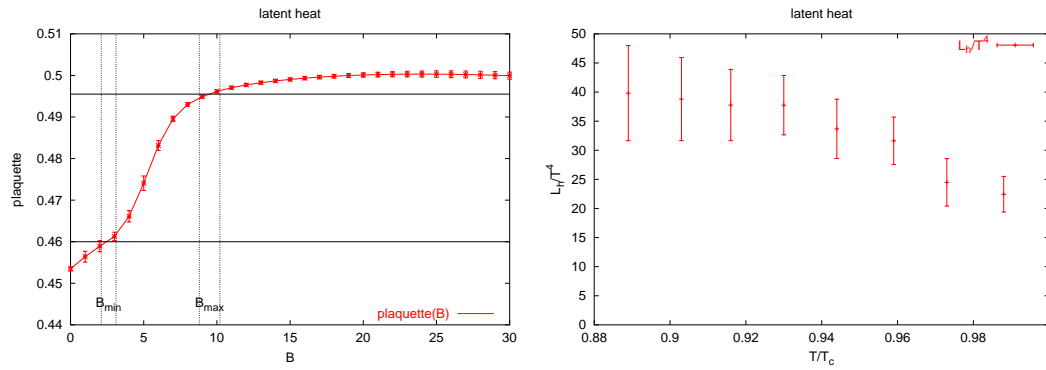


Figure 4.23: The plaquette expectation values as a function of the baryon number at fixed temperature  $\frac{T}{T_c} \approx 0.92$ . The boundaries of the co-existence region are indicated with vertical delimiters. We equal the distance of the two horizontal lines with  $\langle Plaq(B_{max}) \rangle - \langle Plaq(B_{min}) \rangle$  (left). The latent heat in a dimensionless ratio  $\frac{L_h}{T^4}$  as a function of  $\frac{T}{T_c}$  (right).

### 4.5.7 Interface Tension

We assume a nucleation process as the underlying mechanism of the first order transition from the low- to the high-density phase. In order to start the transition, a droplet of the high-density phase has to form which is accompanied by building an interface. Its energy cost is proportional to the area of the interface with the proportionality constant  $\sigma$ , which is called the interface tension. On a hypercubic lattice with periodic boundary conditions, the droplet grows until the two phases are separated by two planar (2+1)-dimensional non-interacting interfaces, see Fig. 4.24, left. The area of one interface thus is  $(N_s a)^2 (N_t a) = 2(N_s a)^2 / T$ . The transition completes at no additional cost by moving the interfaces. Eventually, the destruction of the two interfaces will release the energy the system had to pay in the first place. The change in the Helmholtz free energy is illustrated in Fig. 4.24, right.

The first bump<sup>22</sup>, whose area is labelled by  $A$  (dimensionless), encodes the free energy needed to create the two interfaces. We introduce the “reduced” interface tension by

$$\sigma_R = \frac{\sigma}{T} \quad (4.84)$$

<sup>22</sup>The construction is described in subsection 4.5.3.

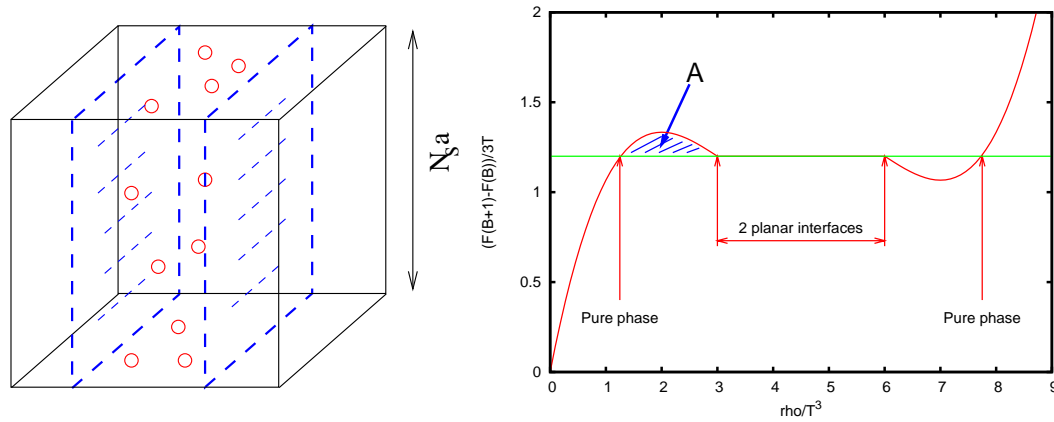


Figure 4.24: Illustration of the nucleation process. On a hypercubic lattice with periodic boundary condition, the two interfaces are planar (left). The area of the bump  $A$  corresponds to the free energy needed to create two planar interfaces and allows to extract the interface tension.

and extract it via (see Fig. 4.25)

$$\sigma_R = \frac{A}{2(N_s a)^2} . \quad (4.85)$$

Within the errors, the reduced interface tension remains fairly constant for  $\frac{T}{T_c} < 0.96$  at  $\sqrt{\sigma_R} \approx 45$  MeV as a function of the temperature. For pure  $SU(3)$ -Yang Mills theory, the reduced interface tension is  $\sqrt{\sigma_R} = 34(17)$  MeV on a  $64^3 \times 4$  lattice[19]. We thus conclude that the order of magnitude of our interface tension is reasonable.

We have presented a new method to extract the interface tension between the confined phase and the quark-gluon plasma of the density-driven transition, by exploiting fully the Maxwell construction.

## 4.6 Conclusions - Canonical Approach to Lattice QCD

We have presented a method to study QCD in a canonical framework. It is designed for few-nucleon systems at low temperature but proves also capable of exploring

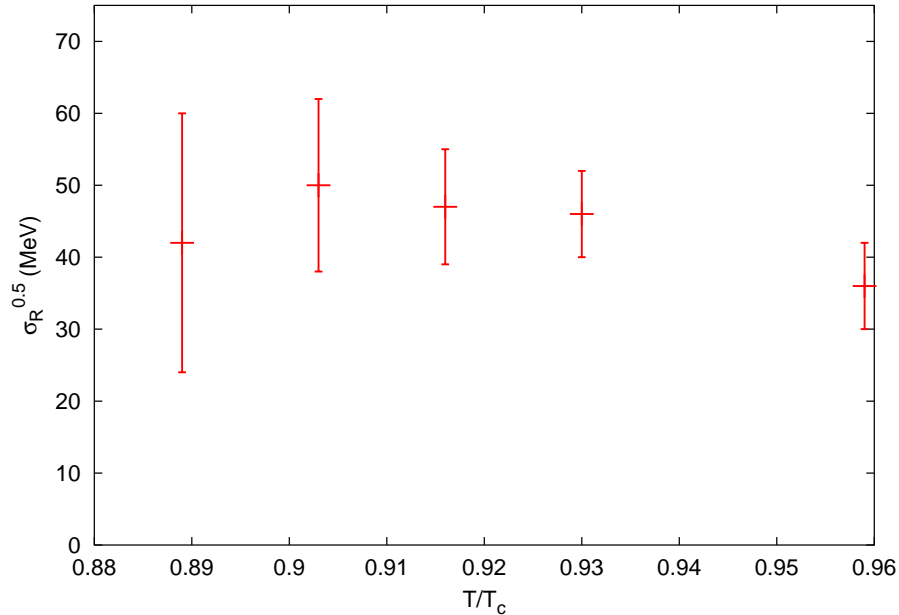


Figure 4.25: The reduced interface tension in physical units as a function of the temperature.

high-density regimes ( $\rho \lesssim \frac{5}{\text{fm}^3}$  or  $\frac{\mu}{T} \lesssim 2$ ) at temperatures  $T \gtrsim 0.8T_c$  on a  $6^3 \times 4$  lattice.

We measure the free energy as a function of the imaginary chemical potential  $\mu_I$ , real chemical potential  $\mu$  and the baryon number  $B$ . With the latter two, we identify the location of the phase transition between hadronic matter and quark-gluon plasma via the peak in the specific heat, and independently, by a Maxwell construction, which is based on the saddle point approximation. We find good agreement with the literature when  $\frac{\mu}{T} \lesssim 1$ . At larger chemical potential  $\mu$ , we observe a bending down of the critical line at  $\frac{\mu}{T} \gtrsim 1.3$ . This should happen if the critical line is to reach our strong coupling results. As a new result, we have obtained the  $T$ - $\rho$  phase diagram. Based on the Maxwell construction, we can extract the boundaries of the co-existence region quite reliably. As a result, we obtain the maximum nuclear matter density  $\rho_{\text{confined}} \sim 0.50(5) \frac{B}{\text{fm}^3}$  for a four flavour theory with  $m_\pi \approx 350$  MeV - three times larger than real-world nuclear matter density. We can cross-check the



estimates of the phase boundaries via the specific heat or the chiral condensate, however, this is much harder, due to finite size effects. We find rough agreement.

The two phases can be rather well described by the hadron resonance gas at low density and by an interacting massless gas at high density. In the confined phase, for example at  $\frac{T}{T_c} \sim 0.9$  ( $\beta = 4.95$ ), we find a good description of our data by

$$\frac{\rho}{T} \left( \frac{\mu}{T} \right) = f(T) \sinh \left( \frac{3\mu}{T} \right) \quad (4.86)$$

with  $f(T) = 0.048(1)$ , a value obtained from both real and imaginary chemical potential approaches. In the quark-gluon plasma phase, a slightly modified free gas Ansatz allows to account for all data points

$$\frac{\rho}{T^3} = C_2 \frac{N_f}{3} \left( \frac{\mu}{T} \right) + b_4(T) C_4 \frac{N_f}{3\pi^2} \left( \frac{\mu}{T} \right)^3. \quad (4.87)$$

We determine the finite-size and cut-off correction terms  $C_2$  and  $C_4$  by calculating the free energy of the free fermion gas on the lattice and find agreement with the literature for  $V \rightarrow \infty$ . The coefficients  $b_2(T)$  and  $b_4(T)$  are independent of the temperature for large enough temperatures and densities, and we find  $b_2(T \sim 1.1T_c) = 0.70(1)$  and  $b_4(T \sim 1.1T_c) = 2.97(3)$ . The leading order term  $b_2$  is confirmed by results at imaginary chemical potential. We thus observe deviations from the Stefan Boltzmann free gas of at about 30% just above  $T_c$ .

We study the dynamics of the density-driven phase transition by calculating the latent heat  $L_h \approx 20 - 40 T^4$  for temperatures around  $(0.88 - 0.99)T_c$  and the interface tension  $\sqrt{\sigma} \sim 45$  MeV. The order of magnitude of these quantities seem reasonable ( $\sqrt{\sigma_R} \approx 34(17)$  MeV for the pure  $SU(3)$  theory). However, further studies, for example at larger quark mass, are needed.

The determination of the canonical partition functions requires the calculation of the Fourier transformation (in imaginary chemical potential) of the grand canonical par-

tition function. We have presented two methods: a computationally cheap version, where the imaginary chemical potential is treated as a dynamical degree of freedom; and an expensive method, which enjoys a substantial variance reduction provided by the Fourier transformation of *each* determinant. A peculiarity of the canonical approach is that the expectation value of the Polyakov loop is zero for any temperature and baryon number. In the grand canonical ensemble, however, the Polyakov loop is always non-zero. This gives rise to questions about the equivalence of the two ensembles. We have shown that they do agree since their free energy densities are equal in the thermodynamic limit. We furthermore have resolved the so-called “Polyakov loop paradox” by realising that the non-physical non-zero triality sectors, ie. canonical sectors of quark numbers not a multiple of three, are responsible for the non-vanishing Polyakov loop expectation value. These non-zero triality states can be included or excluded without affecting the expectation values of observables sensitive to the phase transition in the thermodynamic limit.

The numerical problems of the canonical approach are different for the two methods presented. The numerically cheap version suffers from the sign problem already for small  $B$ . We thus use it to explore the zero baryon density region only. The other, more expensive method shows large fluctuations in the co-existence region. These fluctuations are not caused by the numerical method, but by the physics of the system, which does not like to stay in the co-existence region because of the additional interface free energy.

# Chapter 5

## 3-state Potts Model

### 5.1 Motivation

The 3-dimensional 3-state Potts model and the Finite Temperature QCD with infinitely heavy quarks share the same  $Z_3$  global symmetry, and in both theories the order parameter shows a first order phase transition [24, 25]. When an external magnetic field is turned on in the Potts model, this  $Z_3$  symmetry is explicitly broken and the first order phase transition is weakened, becoming second order for a certain strength of the magnetic field and crossover beyond. In the case of Finite Temperature QCD, the inverse of the quark mass plays the role of the external magnetic field in the 3-D 3-state Potts model. The first order phase transition of the quenched theory (infinitely heavy quark limit) weakens, and turns into a second order transition for a critical, heavy but not infinite, dynamical quark mass [111, 112], see Fig. 5.1. A universality argument then implies that the critical properties of the two theories, Potts and QCD, will be the same at this second-order point. Since the 3-D 3-state Potts model is simpler than QCD and can be simulated on a large lattice, its numerical investigation will give us more detailed quantitative information on the critical properties of Finite Temperature QCD with heavy quarks. In particular we can determine the curvature of the surface of second-order endpoints (Fig. 5.1,

large mass regime) as a function of the chemical potential  $\mu$  in QCD.  $\mu$  also becomes

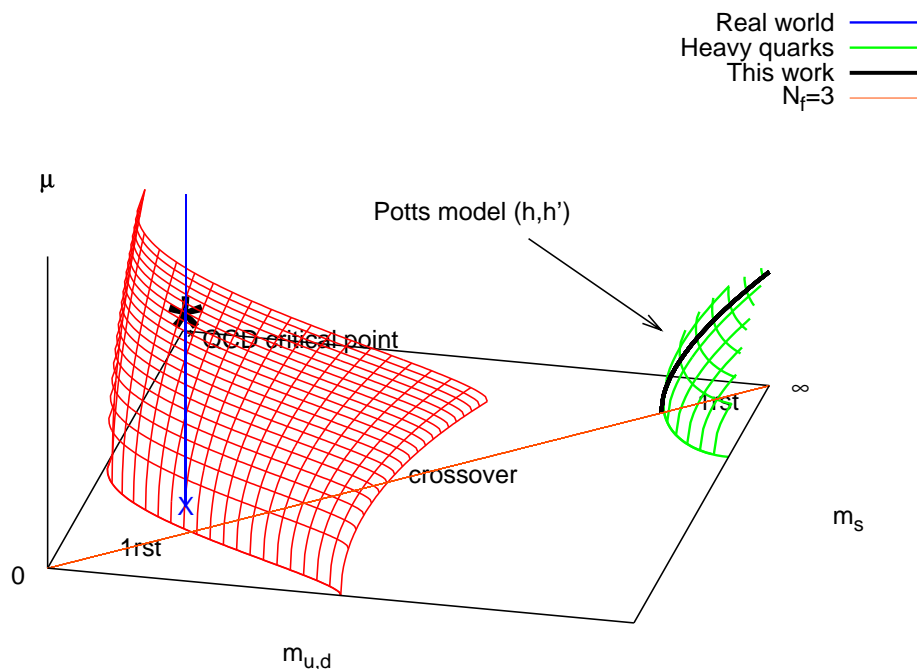


Figure 5.1: The order of the QCD phase transition from hadronic matter phase to the quark-gluon plasma phase in the plane of the degenerate “up/down”-quark masses  $m_u = m_d$ , “strange”-quark mass  $m_s$  and the chemical potential  $\mu$ . The  $N_f = 3$  line refers to the case of 3 degenerate quark flavours with mass  $M$ . The blue  $X$  refers to real-world physics, ie. physical quark masses. In our sketch, the vertical line pierces the surface of second order endpoints at a particular value of the chemical potential. If this QCD critical point indeed exists, such a positive curvature  $\frac{\partial^2 M(\mu)}{\partial \mu^2} \Big|_{\mu=0}$  is likely. However, if the curvature is negative, there is no critical endpoint, which leads to exotic scenarios of the QCD phase diagram. In this work, we determine  $\frac{M}{T} \left( \frac{\mu}{T} \right)$  at large quark masses via the Potts model and show that the first order region shrinks under the influence of  $\mu$ .

an external magnetic field in the Potts model. Following Ref. [113], we revisit this mapping  $(m_{u,d} = m_s = M, \mu)_{QCD} \rightarrow \text{external fields } (h, h')_{Potts}$ , and determine the phase diagram for an arbitrary chemical potential, real or imaginary. Analytic continuation of the phase transition line between real and imaginary chemical potential can be tested with precision. Our results show that the chemical potential weakens

the heavy-quark deconfinement transition in QCD. We determine the canonical partition functions and show that the S-shape behaviour of  $\frac{F(T,B)-F(T,B-1)}{3T}$  at the first order transition is realised as in our QCD study.

## 5.2 Method

The effect of a quark chemical potential on hot QCD with static quark sources can be formulated in the following grand canonical ensemble:

$$\begin{aligned}
Z(\mu) &= \sum_{n,\bar{n}} Z_{n,\bar{n}} e^{\frac{\mu}{T}(n-\bar{n})} \\
&= \sum_{n,\bar{n}} \int [DU] \frac{1}{n!} (\Phi[U])^n \frac{1}{\bar{n}!} (\Phi[U]^*)^{\bar{n}} e^{-S_g[U] - \frac{n}{T}(M-\mu) - \frac{\bar{n}}{T}(M+\mu)} \\
&= \int [DU] e^{-S_g[U] + e^{-\frac{1}{T}(M-\mu)} \Phi[U] + e^{-\frac{1}{T}(M+\mu)} \Phi[U]^*}, \tag{5.1}
\end{aligned}$$

where  $Z_{n,\bar{n}}$  is the canonical partition function with  $n$  quarks and  $\bar{n}$  anti-quarks,  $U$  is the SU(3) gauge field,  $S_g$  is the gauge action,  $\Phi[U]$  is the Polyakov loop,  $\Phi[U]^*$  the anti-Polyakov loop,  $M$  is the heavy quark mass and  $\mu$  is the quark chemical potential. When there is no chemical potential ( $\mu = 0$ ), the action in Eq.(5.1) is real. If  $\mu \neq 0$ , the action becomes complex and Monte Carlo simulation is difficult because of the ‘‘sign problem’’: the usual probabilistic interpretation of Eq.(5.1) is not possible.

Symmetry considerations tell us that the important dynamics of the gauge field are those of the Polyakov loop and the anti-Polyakov loop. Thus, one can simplify  $S_g[U]$  and consider instead the interaction of Polyakov loops, modelled by a Potts term. We introduce the  $Z_3$  spin  $\Phi(\vec{x}) \in [1, e^{-i\frac{2\pi}{3}}, e^{+i\frac{2\pi}{3}}]$  and write the corresponding lattice Hamiltonian for the 3-D 3-state Potts model

$$H = -\kappa \sum_{i,\vec{x}} \delta_{\Phi(\vec{x}),\Phi(\vec{x}+i)} - \sum_{\vec{x}} [h\Phi(\vec{x}) + h'\Phi^*(\vec{x})], \tag{5.2}$$

where  $\kappa$  is the effective coupling of neighbouring  $Z_3$  spins, and the external fields

$$\begin{aligned} h &= e^{-\frac{1}{T}(M-\mu)} \equiv h_M e^{\frac{\mu}{T}} = h_M e^{\bar{\mu}} \\ h' &= e^{-\frac{1}{T}(M+\mu)} \equiv h_M e^{-\frac{\mu}{T}} = h_M e^{-\bar{\mu}} \end{aligned} \quad (5.3)$$

with  $h_M = e^{-\frac{M}{T}}$  and  $\bar{\mu} = \frac{\mu}{T}$ . If  $h \neq h'^*$ , this Hamiltonian is also complex. However, the partition function remains real [113]. The partition function includes summation over all the possible  $Z_3$  spin configurations. Introducing “bonds” with a certain probability among parallel  $Z_3$  spins and defining a “cluster” made of the sites connected by the bonds, we can divide the summation into the sum over clusters and that within a cluster. Then, after analytically summing over  $Z_3$  spin orientations within each cluster, the partition function in terms of cluster configurations is given by

$$Z(\mu) = \int [Db] (e^\kappa - 1)^{N_b} \prod_C \left[ e^{2h_M |C| \cosh \bar{\mu}} + 2e^{-h_M |C| \cosh \bar{\mu}} \cos(\sqrt{3}h_M |C| \sinh \bar{\mu}) \right] \quad (5.4)$$

where  $Db$  is the sum over all the possible bond configurations,  $N_b$  is the number of bonds in a given cluster configuration, and  $|C|$  is the number of sites in a given cluster.  $Z$  is real and is free from the “sign problem” since the second term which can be negative due to the presence of  $\cos(\sqrt{3}h_M |C| \sinh \bar{\mu})$  is always smaller than the first term. However, the “solution” of the complex action problem in the 3-D 3-state Potts model is different from the  $SU(2)$  gauge theory case [114] and from the four-fermi theory case [115], where the action itself can be shown to be real even with a real chemical potential. In the Potts model, the action is complex, and a change of variables (from spins to bonds) is necessary to recover a real effective action and show that the partition function of the model remains real.

The ( $h = h'$ ) case (that is, zero chemical potential) has been studied in Ref. [116]. The ( $h' = 0$ ) case (that is,  $M, \mu \rightarrow \infty$  while  $M/\mu$  is fixed) has been investigated in Ref. [113]. Since we are also interested in testing the analytic continuation of imaginary chemical potential results to real chemical potential, instead of taking  $h' = 0$  limit, we study here the full parameter space of arbitrary  $(h, h')$ .

For the case of an imaginary chemical potential ( $\mu \rightarrow \mu_I$ , i.e.,  $h' = h_M e^{-i\bar{\mu}_I} = h^*$ ), the partition function,  $Z_I$ , becomes

$$\begin{aligned} Z_I(\mu_I) &= \int Db(e^\kappa - 1)^{N_b} \prod_C \left[ e^{2h_M|C|\cos(\bar{\mu}_I)} e^{2h_M|C|\cos(\bar{\mu}_I + \frac{2\pi}{3})} e^{2h_M|C|\cos(\bar{\mu}_I - \frac{2\pi}{3})} \right] \\ &= \int Db(e^\kappa - 1)^{N_b} \prod_C \left[ e^{2h_M|C|\cos\bar{\mu}_I} + 2e^{-h_M|C|\cos\bar{\mu}_I} \cosh(\sqrt{3}h_M|C|\sin\bar{\mu}_I) \right]. \end{aligned} \quad (5.5)$$

Since  $\cosh(i\bar{\mu}) = \cos(\bar{\mu})$ ,  $\sinh(i\bar{\mu}) = i\sin(\bar{\mu})$  and  $\cos(i\theta) = \cosh(\theta)$ , the relation  $Z(\mu \rightarrow i\mu_I) = Z_I(\mu_I)$  is quite obvious and the analytic continuation between  $Z$  and  $Z_I$  is transparent. The Roberge-Weiss symmetry [18],  $Z_I(\frac{\mu_I}{T}) = Z_I(\frac{\mu_I}{T} + \frac{2\pi k}{3})$ , can also be seen clearly in Eq.(5.5).

## 5.3 Real Chemical Potential

Using the Swendsen-Wang cluster algorithm [117] on Eq.(5.4), we simulate the 3-D 3-state Potts model. The actual simulation is performed along the  $h = h'$  line in the  $(h, h')$  parameter space and the data are re-weighted for arbitrary  $(h, h')$ . Although the reweighting factor is not always positive, this strategy turns out to be more efficient than sampling Eq.(5.4), because the ensuing sign problem is very mild. Simulations are performed on lattice volumes  $56^3$ ,  $64^3$ , and  $72^3$ . Typically  $\sim 2$  million data samples are collected per simulation point. The critical point could be identified via the Binder cumulant introduced in Eq.(4.58) on page 133. Here, we require the third order cumulant  $\langle (\hat{O} - \langle \hat{O} \rangle)^3 \rangle$  of the absolute value of the magnetisation  $\langle \hat{O} \rangle = \langle |\sum_{\vec{x}} \Phi(\vec{x})| \rangle$  to vanish. At that point, we evaluate the connected Binder cumulant

$$B_4(\hat{O}) = 1 - \frac{1}{3} \frac{\langle (\hat{O} - \langle \hat{O} \rangle)^4 \rangle}{\langle (\hat{O} - \langle \hat{O} \rangle)^2 \rangle^2}. \quad (5.6)$$

Since the universality class of the 3-D 3-state Potts model is that of the 3-D Ising model,  $B_4$  for the Potts model at the critical point should be equal to that of the

Ising model ( $= 1.604(1)$ ). Fig. 5.2 (left) shows  $B_4$  as a function of  $h$  (here,  $h' = h$ ). From this, we find that the critical end point is at  $(\kappa_c, h_c) = (0.54940(4), 0.000255(5))$  in comparison with the value given in Ref. [116],  $(0.54938(2), 0.000258(3))$ . Similarly, for the  $h' = 0$  case, Fig. 5.2 (right), we obtain that  $(\kappa_c, h_c) = (0.54947(1), 0.000465(5))$  (Ref. [113] reported  $(\kappa_c, h_c) = (0.549463(13), 0.000470(2))$ ).

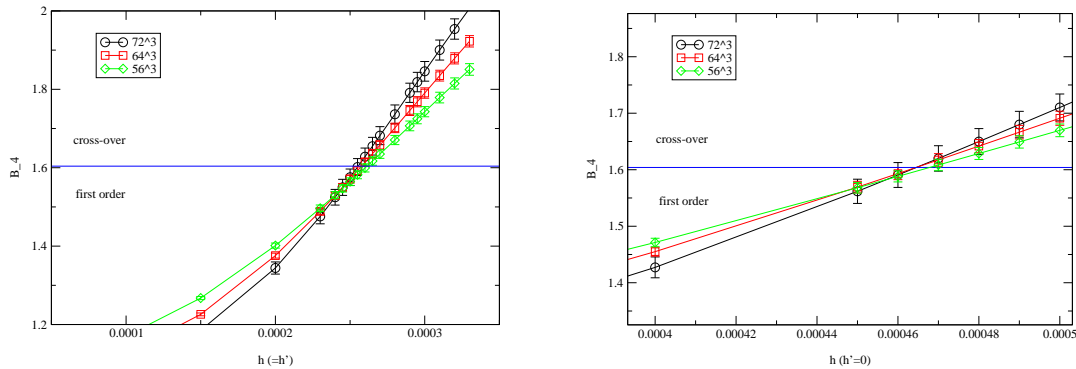


Figure 5.2: The Binder cumulant  $B_4$  for magnetisation versus  $h$  ( $h = h'$ ) (left).  $B_4$  for magnetisation vs  $h$  ( $h' = 0$ ) (right).

The critical end point can be located for arbitrary  $h$  and  $h'$ . Fig. 5.3 (left) shows the  $(h, h')$  parameters for the second order phase transition. Here, rather than  $(h, h')$ , we use the variables  $\frac{M}{T}$  and  $\frac{\mu}{T}$ , which can be related to QCD due to the universality argument as per Eq.(5.3). The line in the figure is from the asymptotic value, ( $h = h_c, h' = 0$ ). Since  $h = e^{-\frac{M}{T} + \frac{\mu}{T}}$ , the relation  $h_c = e^{-\frac{M}{T} + \frac{\mu}{T}}$  for given  $h_c$  defines a line in the parameter space  $(\frac{M}{T}, \frac{\mu}{T})$ . In Fig. 5.3 (left), the simulation data lies above this asymptotic line. This shows that the anti-Polyakov loop in Finite Temperature QCD plays an important role in critical parameter space and should not be neglected in considering the critical properties of the theory. To further compare our results with the limit studied in Ref. [113], we show  $\frac{T}{M}$  vs.  $\frac{\mu}{M}$  in Fig. 5.3 (right). As  $\frac{\mu}{M}$  increases, our simulation data approach the asymptotic line as expected. This plot clearly shows that the range of  $\frac{T}{M}$  values for which the transition is first-order shrinks as the chemical potential is turned on. In fact, the transition disappears altogether



for  $\frac{\mu}{M} > 1$ . So the effect of the chemical potential is to *weaken* the phase transition.

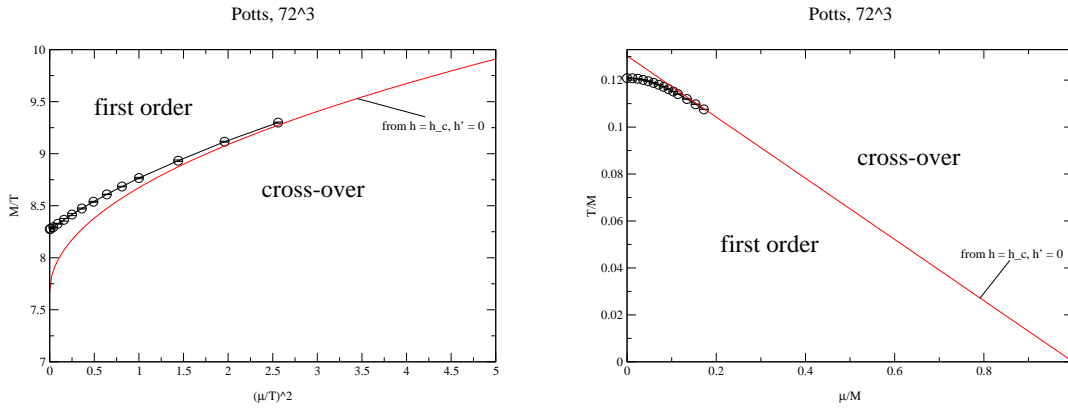


Figure 5.3:  $\frac{M}{T}$  for second order transition versus  $(\frac{\mu}{T})^2$  (left).  $\frac{T}{M}$  for second order transition versus  $\frac{\mu}{M}$  (right).

Fig. 5.3 (left) suggests an interesting comparison with the Finite Temperature QCD phase diagram. Let us imagine increasing the chemical potential from zero, following the arrow in Fig. 5.4 (left). Without chemical potential, the quark mass is chosen such that the transition is first order. With a non-zero chemical potential, this first order phase transition weakens. At a certain chemical potential, the system shows a second order phase transition. With chemical potential larger than this critical value, the system shows a crossover. On the other hand, consider Fig. 5.4 (right), which is analogous to Fig. 5.4 (left). This figure is a schematic phase diagram for three-flavour QCD with *light* quarks suggested in Ref. [118] and summarises the conventional wisdom, compare Fig. 5.1. Without chemical potential, 3-flavour QCD shows a first order phase transition when the quark mass is smaller than a certain mass  $m_c(0)$ . Let us say that we start with a system where the quark mass is larger than  $m_c(0)$ . Then, this 3-flavour QCD system has a crossover. In this case, increasing the chemical potential makes the transition stronger: a second order phase transition appears when the chemical potential hits a certain magnitude. If the chemical potential is increased further, the system undergoes a first order phase transition. Therefore, the 3 light flavour QCD system shows (crossover  $\rightarrow$  second

order phase transition  $\rightarrow$  first order phase transition) as the chemical potential is increased. In contrast, the heavy quark QCD system suggested by 3-D  $Z_3$  Potts model will undergo (first order phase transition  $\rightarrow$  second order phase transition  $\rightarrow$  crossover) as the chemical potential is increased. Interestingly, some recent light-quark QCD simulations give support to the possibility that the conventional wisdom scenario above might be at fault [119], so that the influence of the chemical potential in the light-quark and the heavy-quark cases would be similar.

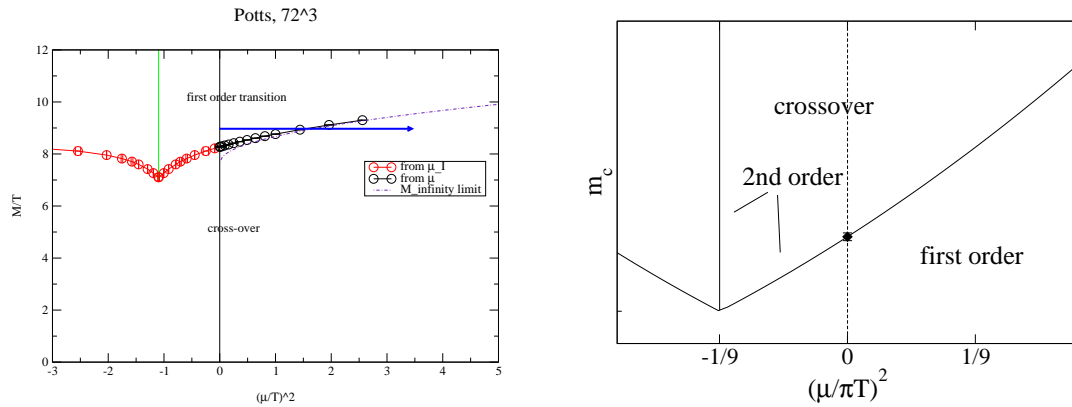


Figure 5.4:  $\frac{M}{T}$  for second order transition versus  $(\frac{\mu}{T})^2$  (left). schematic QCD phase diagram for 3 light quarks from [120] (right).

## 5.4 Imaginary vs Real Chemical Potential

For the case of an imaginary chemical potential, one can perform a direct sampling of Eq.(5.2), or reweight the  $h = h'$  data used for the real chemical potential study. As before, the critical point is located by use of the magnetisation Binder cumulant and  $B_4 = 1.604$  crossing point.

In Fig. 5.4 (left), we put together the critical end point parameters obtained from the imaginary chemical potential case and those from the real chemical potential case (note the similarity with the schematic phase diagram for 3 light flavour QCD

shown in Fig. 5.4 (right)). Although the proximity of the  $Z_3$  transition at  $\mu_I = \frac{\pi}{3}$  introduces curvature in the imaginary chemical potential result, the small real  $\mu$  result is smoothly connected to the small imaginary  $\mu_I$  result and the analytic continuation poses no serious problem even on a large lattice volume such as  $72^3$ . However, the critical line shows significant curvature, which limits the accuracy of the extrapolation from imaginary to real  $\mu$ . A 4th order polynomial  $\frac{M}{T} = 8.273 + 0.585(\frac{\mu}{T})^2 - 0.174(\frac{\mu}{T})^4 + 0.160(\frac{\mu}{T})^6 - 0.071(\frac{\mu}{T})^8$  is necessary to describe the critical line from  $(\frac{\mu}{T})^2 = -(\frac{\pi}{3})^2$  to 1.5.

## 5.5 Canonical Ensemble

For a given  $\frac{M}{T}$ , the system undergoes a phase transition at some critical chemical potential  $\frac{\mu}{T}$ . Here, we study the behaviour of  $\frac{\mu}{T}(\frac{\rho}{T^3})$  in the vicinity of a second order critical point. We expect the S-shape, which we have observed in the first-order transition study in subsection 4.3.4 on page 126, to flatten to a plateau, indicating the absence of the metastabilities<sup>1</sup>. The canonical partition functions can be calculated as in chapter 4. The Helmholtz free energy of  $B$  baryons is given by

$$F(T, B) \equiv -T \log \frac{Z_C(T, B)}{Z_C(T, B=0)} \quad (5.7)$$

with

$$\begin{aligned} Z_C(T, B) &= \frac{1}{2\pi} \int_{-\pi}^{\pi} d\left(\frac{\mu_I}{T}\right) e^{-i3B\frac{\mu_I}{T}} Z_{GC}(T, \mu = i\mu_I) \\ &= \frac{1}{2\pi} \int_{-\pi}^{\pi} d\left(\frac{\mu_I}{T}\right) e^{-i3B\frac{\mu_I}{T}} \int [DU] e^{-S_g[U] + e^{-\frac{1}{T}(M-\mu)}\Phi[U] + e^{-\frac{1}{T}(M+\mu)}\Phi[U]^*} \\ &= \int [DU] \left( \frac{1}{2\pi} \int_{-\pi}^{\pi} d\left(\frac{\mu_I}{T}\right) e^{-i3B\frac{\mu_I}{T} + e^{\frac{i\mu_I}{T}}\Phi[U] + e^{-\frac{i\mu_I}{T}}\Phi[U]^*} \right) e^{-S_g[U] + h_M\Phi[U] + h_M\Phi[U]^*} \\ &\equiv \int [DU] \hat{Z}_C(B) e^{-S_g[U] + h_M(\Phi[U] + \Phi[U]^*)}. \end{aligned} \quad (5.8)$$

---

<sup>1</sup>At  $h = 0$ , the first order transition in the Potts system is weak. An increase in  $h$  further decreases the strength of the transition since we approach the second order critical point, compare Fig. 5.2

The Fourier coefficients  $\hat{Z}_C(B)$  can be identified with a Bessel function of first kind  $J_n(z)$

$$\begin{aligned}
\hat{Z}_C(B) &= \frac{1}{2\pi} \int_{-\pi}^{\pi} d\left(\frac{\mu_I}{T}\right) e^{-i3B\frac{\mu_I}{T} + e\frac{i\mu_I}{T}\Phi[U] + e^{-\frac{i\mu_I}{T}\Phi[U]^*}} \\
&= \frac{1}{2\pi} \int_{-\pi}^{\pi} d\left(\frac{\mu_I}{T}\right) e^{-i3B\frac{\mu_I}{T} + 2\operatorname{Re}\Phi[U]\cos\frac{\mu_I}{T} - 2\operatorname{Im}\Phi[U]\sin\frac{\mu_I}{T}} \\
&= \frac{1}{2\pi} \int_{-\pi}^{\pi} d\left(\frac{\mu_I}{T}\right) e^{-i3B\frac{\mu_I}{T} + 2|\Phi[U]|\cos\left(\frac{\mu_I}{T} - \theta\right)} \\
&= \frac{1}{2\pi} \int_{-\pi}^{\pi} d\left(\frac{\mu_I}{T}\right) e^{-i3B\frac{\mu_I}{T} + 2|\Phi[U]|\cos\left(\frac{\mu_I}{T} - \theta\right)} \\
&= e^{-i3B\Theta[U]} I_{3B}(2|\Phi[U]|) .
\end{aligned} \tag{5.9}$$

with  $\Theta[U] = \arccos \frac{\operatorname{Re}\Phi[U]}{|\Phi[U]|} = \arg(\Phi[U])$ .

In Fig. 5.5, we compare  $\frac{\mu}{T}(B) = \frac{F(T,B) - F(T,B-1)}{3T}$  with the grand canonical expectation value  $\langle B \rangle_{GC}(\frac{\mu}{T})$ . The baryon number is measured by evaluating  $\langle B \rangle_{GC} = \frac{\partial \log Z(\mu)}{\partial \mu}$ , where  $Z(\mu)$  is given by Eq.(5.1). The parameters are chosen such that we are at a second order endpoint: for the  $48^3$  lattice  $\frac{M}{T} = 8.8805$ ; for the  $96^3$  lattice  $\frac{M}{T} = 9.028$ . Both approaches, the canonical as well as the grand canonical, indicate the same corresponding chemical potential. We observe a plateau-like behaviour, indicating the second order nature of the transition. Note that for the smaller lattice the resolution of the density is limited, and hence, we do not observe the approach  $\frac{\mu}{T} \rightarrow 0$  for  $B \rightarrow 0$ . These simple checks confirm the applicability of the canonical approach to identify the critical chemical potential.

## 5.6 Conclusions - 3-state Potts Model

We have extended earlier work on the 3-D  $Z_3$  Potts model with one external field coupled to  $\Phi(\vec{x})$  [113] or to  $\Phi(\vec{x}) + \Phi^*(\vec{x})$  [116] to the full general case  $h\Phi(\vec{x}) + h'\Phi^*(\vec{x})$ , and presented a complete picture of the phase diagram in the  $(\kappa, h, h')$  parameter space. Our investigation also gives us a handle on heavy quark QCD at finite den-

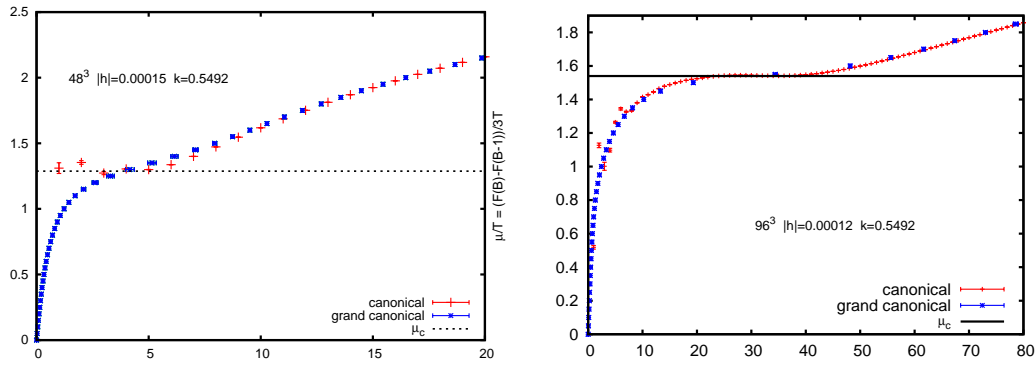


Figure 5.5: The chemical potential  $\frac{\mu}{T}$  as a function of the baryon number  $B$  on a  $48^3$  lattice at mass  $\frac{M}{T} = 8.8805$  (left), and on a  $96^3$  lattice at mass  $\frac{M}{T} = 9.028$  (right). The critical chemical potentials are indicated equivalently by the canonical approach and by the grand canonical framework. Note that at the smaller volume, the resolution of the density is coarse.

sity and temperature which shares the same global symmetry, allowing us to make statements about the heavy quark QCD phase diagram in the finite temperature, finite density, and heavy quark mass parameter space.

For a real chemical potential, the partition function of the Potts model is shown to be real even though the action itself is complex. The sign problem is mild. Simulation results show that turning on a chemical potential  $\mu$  makes the finite temperature transition weaker, so that the region of parameter space corresponding to a first-order transition shrinks under the influence of  $\mu$ . This implies that a similar phenomenon occurs in the phase diagram of heavy quark QCD, see Fig. 5.1.

For an imaginary chemical potential, the action of the Potts model is real and the model is easy to study. Since both real chemical potential and imaginary chemical potential can be simulated, analytic continuation from imaginary to real chemical potential can be tested. We find that analytic continuation works satisfactorily, even with large lattice volumes such as  $72^3$ .

We also can study the Helmholtz free energy. We determine the critical chemical potential as a function of the baryon density, and find good agreement with grand canonical calculations at real  $\mu$ .

In short, the 3-D  $Z_3$  Potts model has a rich structure and provides us with a useful “proving ground” for studying the finite temperature and density phase structure of QCD.

# Chapter 6

## Outlook

In the context of 3-dimensional  $SU(2)$  Lattice Gauge Theory with two static adjoint charges, we have shown for the first time the phenomenon of string breaking from first principles using the Wilson loop observable only. The string breaks at a length  $R_b \approx 1.0\text{fm}$ . We were able to measure Wilson loops up to the extent  $R \times T \sim 1.2\text{fm} \times 4.0\text{fm}$ . The variance reduction technique by Lüscher and Weisz addresses the exponential decrease of the signal in  $T$ . The required computer time scales approximately like  $T^3$ [51]. The exponential decrease in  $R$  remains. For similar models, like the  $Z_{N_c}$  or  $U(1)$  gauge theory, there are algorithms[121], which allow to go beyond this limitation.

Our results settle the question whether string breaking can be observed from first principles using only the Wilson loop observable. The natural extension is to study string breaking in the context of 4-dimensional QCD with dynamical fermions<sup>1</sup>. As outlined in chapter 2, the required large lattice size was beyond our computer capacity, but progress is happening: just recently, Ref. [122] has convincingly observed string breaking with two flavours of Wilson fermions using the multichannel approach.

---

<sup>1</sup>Note that the presented variance reduction method, which requires a decomposition of the action in local pieces, is not directly applicable in the presence of dynamical fermions.

In Lattice QCD with four flavours of staggered quarks with mass  $\frac{m}{T} = 0.2$ , we have studied the phase diagram for  $\frac{T}{T_c} \gtrsim 0.8$  and  $\frac{\mu}{T} \lesssim 2$  with a new canonical approach - a success, when compared to other methods, which are limited to  $\frac{\mu}{T} \lesssim 1$ .

Our new method provides a framework, which allows to determine the phase boundary to even lower temperatures. However, we observe that with the considered ensembles, we cannot lower the temperature further: we lose the signal of the Helmholtz free energy  $F(B)$ , which is obtained from the ratio of partition functions  $\frac{Z_C(B)}{Z_C(0)}$ . This ratio decreases exponentially like  $e^{-Bm_B/T}$ , where  $m_B$  is the mass of the baryon. New ensembles, which have a good overlap with the confined, co-existence and deconfined regime at low temperature, have to be found (see below). The study of QCD in a canonical formalism has just begun. Many promising developments and generalisations can be explored. We can vary various simulation parameters, such as the volume  $V$ , the quark mass  $m$ , the temperature  $T = \frac{1}{aN_t}$ , the number of quark flavours  $N_f$  or the number of colours  $N_c$ . The essential goal is to approach real-world and/or experimental conditions more closely. Here are some possibilities:

1. The increase of the spatial volume  $V$  is mandatory to obtain physically reliable results. (i) The thermodynamic limit has to be taken. (ii) We need to make sure for a certain matter density that the number of baryons  $B = \rho V$  in the system can be described as a statistical ensemble: the small maximal density in the hadronic phase ( $\rho_1 \sim 0.5 \frac{B}{\text{fm}^3}$ , see subsection 4.5.4) requires a significant volume (ie.  $V \gtrsim 10^3$ ) before enough baryons are present to justify a statistical treatment. From a numerical point of view, increasing the volume is computationally expensive: the effort grows like  $V^3$ . The calculation can be distributed among several processors, however a fast interconnection is needed. Nowadays, the calculation of the eigenvalues of the reduced matrix, which consumes 99% or more percents of the total computation time, is already feasible on a  $16^3 \times 4$  lattice. Assuming a several petaflop machine, it should be



possible for our strategy to double the spatial extent from 1.8 fm to 3.6 fm (or change the volume from about  $6 \text{ fm}^3$  to about  $50 \text{ fm}^3$ ), which might well be in the regime of the thermodynamic limit. At the same time, we can consider finer lattices, e.g. we reduce the lattice spacing from 0.3 fm to 0.15 fm. The required lattice then is of extent  $24^3 \times N_t$ . Note that the temporal extent  $N_t$  has only a linear influence on the numerical effort. A problem, however, may be caused by the required baryon *numbers* in order to achieve the same baryon *densities*. In any case, ensembles with a good overlap with the desired canonical sectors are mandatory.

2. At the quark mass  $\frac{m}{T} = 0.2$ ,  $N_f = 4$ , the phase transition is believed to be first order for any chemical potential. As per Fig. 1.6 on page 39, it is likely that an increase in the quark mass weakens the phase transition also for the four flavour theory. An initial study indeed shows that the phase transition becomes a crossover at zero chemical potential for  $\frac{m}{T} = 0.28$ . If the transition at  $T = 0$  still is first order, the existence of a second order endpoint like in the case of real-world QCD follows. In this framework, we thus can test the capacity of our method to identify this critical endpoint. At least, it might provide a determination of the curvature  $\frac{\partial^2 m(\mu)}{\partial \mu^2} \Big|_{\mu=0}$  of the surface of second-order endpoints at *small* quark masses, compare with Fig. 5.1. The technical difficulty is the identification of the second order endpoint on a small lattice. In the context of a computationally inexpensive laboratory of heavy-quark QCD, namely the Potts model, we have determined this curvature at large quark masses. A careful finite size scaling analysis is needed, which is possible in the Potts model. We have observed that in a small volume, the canonical formalism gives a false signal for a weak first order transition when it should be a second order transition, while the grand-canonical approach indicates mistakenly a crossover. These finite size effects have to be taken into account in further studies.

3. By changing the spatial extent  $N_t$ , we can vary the temperature via  $T = \frac{1}{a(\beta)N_t}$ . By increasing  $N_t$ , lower temperatures become accessible, and thus the study of nuclear matter and nuclear interactions on the lattice from first principles is possible in principle. Fig. 6.1 shows preliminary results hinting that, perhaps, the formation of nuclear matter may be observed. The free energy per baryon  $F(B)/B$  is displayed as a function of the baryon density  $\rho$ , for four temperatures  $T \leq \frac{2}{3}T_c$  ( $T_c$  is also shown for comparison). All simulations were performed on  $4^3 \times N_t$  lattices,  $\beta = 5.0$ , with four flavours of staggered fermions ( $am = 0.05$ ), so that the physical volume is strictly constant and the relative temperatures are known exactly. The scale has been fixed by setting  $T_c = 160$  MeV. One clearly sees that the free energy per baryon is minimised when  $\rho \approx 4/\text{fm}^3$ . The baryon mass comes out at it should be  $\sim 1$  GeV, and the binding energy per baryon is about 200 MeV. A further investigation is mandatory: what is the effect of increasing the physical volume? What happens if we change the quark mass or the number of quark flavours?
4. We can vary the number of quark flavours  $N_f$ . While quarks come in six flavours, three of them are so heavy that the thermodynamics of QCD at 200 MeV can be reproduced at  $N_f = 2 + 1$  ( $m_u = m_d = m$ ,  $m_s > m$ ) flavours. For  $T \ll 200$  MeV  $N_f = 2$  may be adequate. To adjust the number of flavours in the simulation, we either make use of the square root trick with staggered fermions or implement Wilson fermions<sup>2</sup>. In both approaches, technical aspects of the Fourier expansion of the fermion determinant in  $e^{i\frac{\mu}{T}}$  have to be worked out carefully.

It has been suggested[123] (since we study four degenerate flavours of medium-

---

<sup>2</sup>Ref. [81] uses Wilson fermions, however they calculate the values of the determinant at different chemical potentials by brute-force, ie. they build the fermion matrix  $M$  from scratch for each chemical potential. This limits their investigation to baryon sectors  $B = 0, 1, 2$  only.

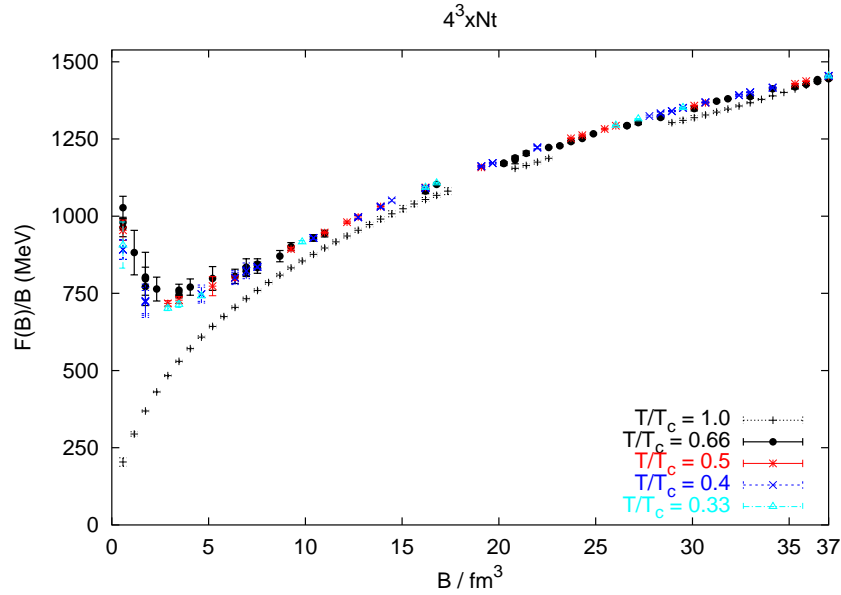


Figure 6.1: Dimensionless free energy per baryon,  $T^{-1}F(B)/B$ , as a function of the baryon density in units of baryons per  $\text{fm}^3$ . The lowest temperature is about 53 MeV.

heavy quarks) that the minimum in Fig. 6.1 may be related to “strange matter” [124], ie. nuclear matter with a large fraction of strange quarks. The stability of this “strange matter”, which might explain why we perhaps see nuclear matter at  $T = 53$  MeV and above in the four-flavour case, should be larger if we consider more flavours (and smaller for fewer flavours). We thus might study  $N_f = 8$ , which poses no technical difficulties, and the nuclear binding should be even more pronounced.

5. It also might be interesting to change the number of colours. For  $N_c = 4$ , a strong coupling calculation [125] finds a  $T = 0$  transition at a value of the baryon chemical potential significantly smaller than  $m_B$ . This indicates strong nuclear binding and gives rise to the assumption that it might be easier to identify the nuclear matter transition in an  $SU(4)$  model than in an  $SU(3)$  model also at finite temperature. Moreover, the sign problem might be milder, since it is absent at  $\beta = 0$ .

6. In Heavy-Ion collision experiments, up- and down-quark numbers are different and conserved separately (up to weak corrections). We can introduce an isospin chemical potential, which controls the ratio of up- and down-quarks. We thus improve the reproduction of experimental conditions, and the phase diagram becomes richer[126].

From an algorithmic point of view, we have observed two properties, which could be exploited further. (i) A symmetry property of the Fourier coefficients of the determinant  $\hat{Z}_C(B) = \hat{Z}_C^*(-B)$  indicates, in principle, a possible reduction of the size of the reduced matrix  $P$  by a factor 2. The determination of its Eigenvalues would then gain a factor 8 in speed. (ii)  $\hat{Z}_C(B)$  and  $\hat{Z}_C(B-1)$  are strongly correlated as per Fig. 6.2. Can we find improved estimators for the important quantity  $\frac{Z_C(B)}{Z_C(B-1)}$ , where  $Z_C(B)$  are the canonical partition functions?

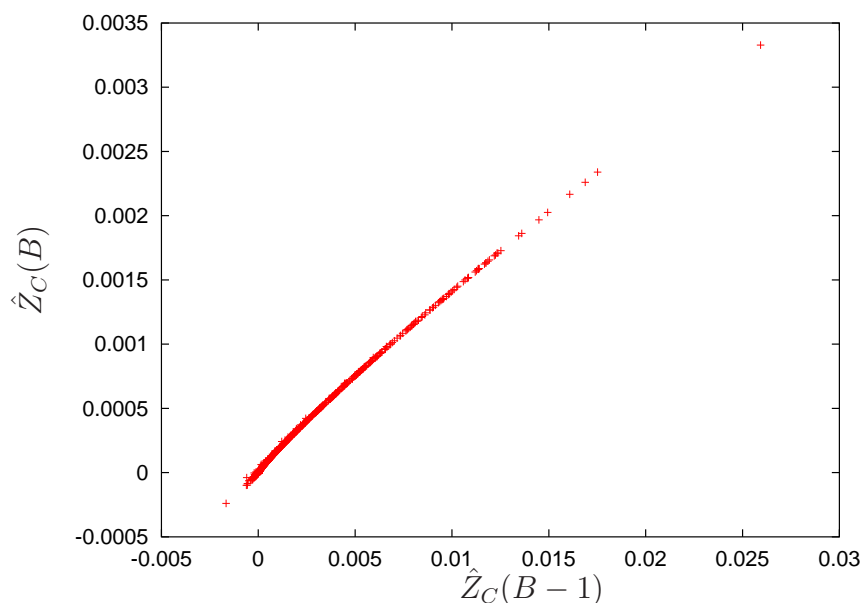


Figure 6.2: Strong correlations between the individual measurements of  $\hat{Z}_C(B)$  and  $\hat{Z}_C(B-1)$  on a given configuration are observed. Here, we show a particularly clear example at  $B = 7$ ,  $\beta = 5.070$ ,  $\frac{m}{T} = 0.28$ .

This short list indicates in how many directions this study can be continued to explore regimes, “where no man has gone before”.



# Appendix A

## $r_I$ and the free scalar propagator

We follow [55] and define forces by

$$F(r_I) = -\frac{V(r) - V(r - a)}{a} \quad (\text{A.1})$$

where  $r_I$  is chosen such that the force evaluated from Eq.(A.1) coincides with

$$F(r_I) = C_2 \frac{g_0^2}{2\pi r_I}, \quad (\text{A.2})$$

the force in the continuum at tree level (ie. from a Coulomb potential  $\log r$  in two dimensions). This results in

$$r_I = -\frac{a}{2\pi(G(r, 0) - G(r - a, 0))}, \quad (\text{A.3})$$

where  $G(x, y)$  is the massless scalar lattice propagator in 2 dimensions defined by

$$-\Delta G(x, y) = \delta(x, y) \quad (\text{A.4})$$

We simply solve for  $G(x = n_1 a, y = n_2 a)$  by Fourier transform, namely

$$G(n_1 a, n_2 a) = \frac{1}{N^2} \sum_{l_1=1, l_2=1}^N \frac{\cos(\frac{2\pi}{N} \sum_1^2 l_i n_i)}{\sum_{i=1}^2 2 - 2 \cos(\frac{2\pi}{N} l_i)}, \quad (\text{A.5})$$

where  $N \gg n_1, n_2$  is the number of discretisation points, taken sufficiently large that  $G(n_1 a, n_2 a)$  is known to 4-digit accuracy. Finally, we set the zero-mode contribution so that  $G(0, 0) = 0.0$ . A summary of our results in the range we consider is given in Table A.1.

$r/a$	$G(r, 0)$		
0	0.0000		
1	-0.2500	$(r - \frac{a}{2})/a$	$r_I/a$
2	-0.3634	2.5	2.3790
3	-0.4303	3.5	3.4080
4	-0.4770	4.5	4.4333
5	-0.5129	5.5	5.4505
6	-0.5421	6.5	6.4435
7	-0.5668	7.5	7.4721
8	-0.5881	8.5	8.4657
9	-0.6069	9.5	9.4735
10	-0.6237		
11	-0.6389		

Table A.1: (left) The scalar lattice propagator  $G(r, 0)$  in 2d. (right) The naive derivation points  $(r - \frac{a}{2})$  compared with  $r_I$  in the range we consider.



# Appendix B

## Error analysis

The correct estimation of the statistical error of an expectation value based on a stochastic simulation is difficult. Here, we outline the 'common practice'-method: jackknife error analysis of binned data, and comment on the 'best practice'-method: bootstrap error analysis. In the second section, we discuss the error estimation of a reweighted observable.

### B.1 Binned Jackknife Error Estimation

We consider  $N$  measurements  $O_i$  from an importance sampling Monte Carlo simulation. The expectation value of the observable  $\langle O \rangle$  can be estimated as the average

$$\bar{O} = \frac{1}{N} \sum_{i=1}^N O_i . \quad (\text{B.1})$$

The naive error is given by

$$\Delta \bar{O} = \sqrt{\frac{1}{N(N-1)} \sum_{i=1}^N (O_i - \bar{O})^2} . \quad (\text{B.2})$$

In practice, we have to deal with autocorrelations between the individual measurements, and often we have to estimate the error of functions, which depend (possibly non-linearly) on the expectation values of some quantities. In the following, I present

the idea behind the binned jackknife error estimation[127], and then comment on the issue of autocorrelations.

1. Based on all measurements, we calculate the average  $\bar{Y} = f(\bar{O}^1, \bar{O}^2, \dots)$ , where  $\bar{O}^i$  is the average of the observable  $O^i$ .
2. We divide the  $N$  measurements into  $M$  blocks. The block size  $\frac{N}{M}$  is a crucial quantity, since the error estimated by this procedure depends on  $\frac{N}{M}$  due to the, usually non-zero, autocorrelation time  $\tau$ . I will comment on this “feature” below.
3. For each  $m = 1, \dots, M$  we remove the block  $m$  and calculate the jackknife variable  $\bar{Y}_m = f(\bar{O}^1_m, \bar{O}^2_m, \dots)$ , where the subscript  $m$  shall denote, that the average is evaluated based on the remaining  $N - \frac{N}{M}$  measurements.
4. The error estimate is then given by

$$\Delta\bar{Y} = \sqrt{\frac{M-1}{M} \sum_{m=1}^M (\bar{Y}_m - \bar{Y})^2}. \quad (\text{B.3})$$

As mentioned, the estimated jackknife error varies with the block size  $\frac{N}{M}$ . In the following we assume that  $\frac{N}{M} \ll N$ . As long as the block size is smaller than the autocorrelation time  $\tau$ , the error increases as we increase the block size. The reason for this is the fact, that our blocks are still correlated. When the block size becomes larger (than  $\tau$ ), the error starts to flatten to a plateau value and then oscillates around its correct value. The blocks will be statistically uncorrelated. Usually, the plateau value is taken as the jackknife error estimate. This procedure is known in the literature as “binning analysis” and it helps to determine an adequate block size for a given set of measurements as well as the autocorrelation time.

The bootstrap method is closely related to jackknife, but it takes the underlying sampling distribution into account.

1. Based on all measurements, we calculate the average  $\bar{Y} = f(\bar{O}^1, \bar{O}^2, \dots)$ , where  $\bar{O}^i$  is the average of the observable  $O^i$ .
2. We divide the  $N$  measurements into  $M$  blocks, such that the block size  $\frac{N}{M} \gg \tau$ , where  $\tau$  is the largest autocorrelation time of the individual ones of each observables  $O^1, O^2, \dots$ .
3. New: From the set of  $M$  blocks, we pick randomly  $M$  blocks, not trying to avoid double sampling. Thus, some blocks may not get selected at all, some once, some twice etc.
4. We calculate the quantity of interest over the selected data, denoted as  $\bar{B}_b$ .
5. New: We repeat the previous two steps a large number of times  $N_B$ , typically  $N_B \gg M$ .
6. The error estimate is then given by

$$\Delta\bar{Y} = \sqrt{\frac{1}{N_B - 1} \sum_{b=1}^{N_B} (\bar{B}_b - \bar{Y})^2}. \quad (\text{B.4})$$

## B.2 Example: Statistical Error Estimate in the Reweighting Procedure

In the reweighting method, there is a variety of sources of errors[128]. Here, we discuss the statistical error only. Assume an infinite set of measurements of two observables  $O_i^1 = (Ow)_i = O_i w_i$  and  $O_i^2 = w_i$ . Our function  $f(\bar{O}^1, \bar{O}^2) = \frac{\bar{O}^1}{\bar{O}^2}$  is the “true value”. In practice we have  $N$  measurements, however.

Let us now denote the average of  $K$  samples of our  $N$  measurements  $a_1, \dots, a_K$  as  $\bar{O}^1_K$ , from which we obtain an estimate  $f(\bar{O}^1_K, \bar{O}^2_K)$ . The average over many sets of samples then is  $\overline{f(\bar{O}^1_K, \bar{O}^2_K)}$ . We define the bias as

$$bias = \overline{f(\bar{O}^1_K, \bar{O}^2_K)} - f(\bar{O}^1, \bar{O}^2). \quad (\text{B.5})$$

A linear function  $g(\overline{O^1}, \overline{O^2}) = \overline{O^1} + \overline{O^2}$  has no bias, but the reweighting function  $f$  given above has a non-vanishing bias. The estimated relative error of the expectation value of  $O$

$$\langle O \rangle = \frac{\langle Ow \rangle_{||}}{\langle w \rangle_{||}} \approx \frac{\overline{Ow}}{\overline{w}} \quad (\text{B.6})$$

is

$$\left( \frac{\Delta \langle O \rangle}{\langle O \rangle} \right)^2 \approx \left( \frac{\Delta \overline{Ow}}{\overline{Ow}} \right)^2 + \left( \frac{\Delta \overline{w}}{\overline{w}} \right)^2 - 2 \text{cov}(Ow, w) + \dots, \quad (\text{B.7})$$

where  $\text{cov}$  is the covariance of  $Ow$  and  $w$

$$\text{cov}(Ow, w) = \frac{1}{N-1} \left( \sum_{i=1}^N O_i w_i^2 - \sum_{i=1}^N O_i w_i \sum_{i=1}^N w_i \right). \quad (\text{B.8})$$

In practice, we calculate the error estimate of a reweighted quantity via the binned jackknifed procedure describe above.

# Appendix C

## Stochastic Estimator

A ratio of determinants can be estimated using a single Gaussian complex vector[7]:

$$\frac{\det^{N_f}(\mathcal{D}(\mu'_I) + m)}{\det^{N_f}(\mathcal{D}(\mu_I) + m)} = \frac{\det^{N_f} M(\mu'_I)}{\det^{N_f} M(\mu_I)} = \frac{\int d\phi^\dagger d\phi e^{-\phi^\dagger \frac{1}{M^{N_f}(\mu'_I)} \phi}}{\int d\phi^\dagger d\phi e^{-\phi^\dagger \frac{1}{M^{N_f}(\mu_I)} \phi}} \quad (\text{C.1})$$

$$= \frac{\int d\eta^\dagger d\eta |J(\phi, \eta, \mu_I)| e^{-\eta^\dagger M^{N_f/2}(\mu_I) M^{-N_f/2}(\mu'_I) M^{-N_f/2}(\mu'_I) M^{N_f/2}(\mu_I) \eta}}{\int d\eta^\dagger d\eta |J(\phi, \eta, \mu_I)| e^{-\eta^\dagger \eta}} \quad (\text{C.2})$$

where we have substituted  $\phi = M^{N_f/2}(\mu_I)\eta$ . Note, that in the above notation, the Jacobian  $|J(\phi, \eta, \mu_I)|$  is  $\det M^{N_f}(\mu_I)$ , which is independent of  $\eta$ .

$$\frac{\det^{N_f}(\mathcal{D}(\mu'_I) + m)}{\det^{N_f}(\mathcal{D}(\mu_I) + m)} = \frac{\int d\eta^\dagger d\eta e^{-|M^{-N_f/2}(\mu'_I) M^{N_f/2}(\mu_I)\eta|^2} e^{-|\eta|^2 + |\eta|^2}}{\int d\eta^\dagger d\eta e^{-|\eta|^2}} \quad (\text{C.3})$$

$$= \langle e^{-|M^{-N_f/2}(\mu'_I) M^{N_f/2}(\mu_I)\eta|^2 + |\eta|^2} \rangle_\eta \quad (\text{C.4})$$

and  $\langle \cdot \rangle_\eta$  tells us that  $\eta$  has to be sampled with the distribution  $\int d\eta^\dagger d\eta e^{-|\eta|^2}$ .

# Appendix D

## Ferrenberg-Swendsen reweighting

Ferrenberg-Swendsen or multi-histogram reweighting[98] is a method, which allows us to “expand” results from Monte Carlo simulations at some particular values of the involved couplings (temperature  $\beta$ , chemical potential  $\mu$ , ...), to *any other* value of these couplings ( $\beta_r, \mu_r$ ) sufficiently close to the simulation parameters without performing any additional simulations. It is necessary that the “target” ensemble, given by  $(\beta_r, \mu_r)$ , has a non-vanishing overlap with at least one of the Monte Carlo ensembles, otherwise the results become unphysical. This would pose no problem if the error estimation, as discussed in Appendix B, is trustworthy. Note that in this thesis, we check for the overlap explicitly.

We present the method with a certain amount of verbosity. There are two steps, which can be looked at independently.

1. An iterative procedure, which solves a self-consistency equation for the so-called “optimised partition functions”, and
2. the virtual reweighting procedure, which allows to calculate the value of the partition function, and furthermore, the expectation value of observables at “arbitrary” values of the couplings. In practice, reweighting works well for interpolation in the coupling space, however not for extrapolation.

## D.1 The Self-Consistency Equation

The grand canonical partition function is given by

$$Z_{GC}(\beta, \mu) = \int [DU] e^{-S_g[U; \beta]} \det M(U; \mu) \equiv \int [DU] W[U; \beta, \mu]. \quad (\text{D.1})$$

In this particular case, we have two couplings: the temperature  $\beta$  and the chemical potential  $\mu$ . We assume that the couplings are chosen such that the weight  $W$  can be sampled by ordinary Monte Carlo methods. For the following, consider a discrete configuration space for simplicity. The sum over configurations cannot be performed exactly. Instead, importance sampling is used, so that  $n$  configurations are visited, selected from the ensemble with probability  $\frac{W[U; \beta, \mu]}{Z_{GC}(\beta, \mu)}$ . Then, the number of times a given configuration  $U$  will appear in the sample is (when averaged over many identical Monte Carlo simulations)

$$c(U) = n \frac{W[U; \beta, \mu]}{Z_{GC}(\beta, \mu)} \quad (\text{D.2})$$

Consider several simulations  $j = 1..R$  performed with different sets of weights  $(\beta_j, \mu_j)$ , consisting of a number of configurations given by  $n_j$ . The grand canonical partition functions are

$$Z_j = \int [DU] W[U; \beta_j, \mu_j]. \quad (\text{D.3})$$

All these simulations still do not cover the full configuration space. Many configurations have not been sampled, while some others have been sampled several times. But altogether, the ensemble of all sampled configurations can be used to evaluate a partition function with arbitrary couplings  $W[U; \beta, \mu]$ , via

$$Z_{GC}(\beta, \mu) \sim \sum_{\text{distinct sampled } U} W[U; \beta, \mu] \quad (\text{D.4})$$

However, one must avoid overcounting. The number of times a given configuration  $U$  appears in the sample  $j$  is given by Eq.(D.2). Therefore, configuration  $U$  appears in the ensemble of all sampled configurations a number of times equal to

$$\sum_j n_j \frac{W[U; \beta_j, \mu_j]}{Z_j} \quad (\text{D.5})$$

Taking this multiplicity factor out, one arrives at the Ferrenberg-Swendsen expression for the grand canonical partition function  $Z_{GC}(\beta, \mu)$ :

$$Z_{GC}(\beta, \mu) = \sum_{\text{sampled } U} \frac{1}{\sum_j n_j \frac{W[U; \beta_j, \mu_j]}{Z_j}} W[U; \beta, \mu] \quad (\text{D.6})$$

In particular, this holds for all the sampled partition functions, thus the self-consistency equation can be written as

$$Z_k = \sum_{\text{sampled } U} \frac{W[U; \beta_k, \mu_k]}{\sum_j n_j \frac{W[U; \beta_j, \mu_j]}{Z_j}}, \quad (\text{D.7})$$

and more explicit with  $\sum_{\text{sampled } U} = \sum_{s=1}^R \sum_{i_s=1}^{n_s}$

$$Z_k = \sum_{s=1}^R \sum_{i_s=1}^{n_s} \frac{e^{-S_g[s, i_s; \beta_k]} \det M(s, i_s; \mu_k)}{\sum_{j=1}^R \sum_{i_j=1}^{n_j} \frac{e^{-S_g[s, i_s; \beta_j]} \det M(s, i_s; \mu_j)}{Z_j}}. \quad (\text{D.8})$$

The weight of each configuration  $U$ , now more specifically denoted as  $(s, i_s)$ , has to be known for each set of sampled couplings. We will now show that this is trivial for the gauge action  $S_g[s, i_s; \beta]$ , but more difficult for the determinant.

### D.1.1 Gauge action

The lattice gauge action Eq.(1.27) is independent of  $\mu$ , and  $\beta$  can be factored out:

$$S[s, i_s; \beta] = \beta \sum_p \left( 1 - \frac{1}{N_c} \text{Re Tr } p_{s, i_s} \right), \quad (\text{D.9})$$

where  $\sum_p$  is the sum over all plaquettes and  $N_c$  is the number of colours. The gauge part of the weight-function thus is easily obtained for any configuration at any coupling  $\beta$ .

### D.1.2 Fermion determinant

The fermion determinant is independent of  $\beta$ , but  $\mu$  cannot be factored out. The brute-force way would be to calculate the determinant for each configuration by creating the fermion matrix  $M$  from scratch for any involved chemical potential.



Fortunately, we know the Eigenvalues of the reduced matrix Eq.(4.29), with which we can express the determinant as

$$\det M(\mu) = e^{3V\mu N_t} \prod_{i=1}^{6V} (\lambda_i + e^{-\mu N_t}) ,$$

for real, as well as imaginary chemical potential. This allows the evaluation of  $\det M(\mu)$  for any  $\mu$ , once the  $\lambda_i$ 's have been computed.

At finite isospin chemical potential  $\mu_{IS}$ , the fermion part of the weight is given by

$$W_f[s, i_s; \mu_{IS}] = \sqrt{\det M(\mu = \mu_{IS}) \det M(\mu = -\mu_{IS})} . \quad (\text{D.10})$$

Unfortunately, supplementing the ensemble with configurations generated at non-trivial  $\xi$ -values is expensive. In this case, we cannot make use of the above trick, but have to re-calculate the Eigenvalues  $\lambda_i$  for every  $\xi \neq 1$ .

## D.2 Autocorrelation-Time

The previous derivation of Eq.(D.6) assumes that all configurations were uncorrelated from each other. This is hardly the case, in particular around a first order phase transition. In fact, each simulation  $j$  is a Markov chain with autocorrelation time  $\tau_j$ , and in general, one samples in the transition regime more configurations than in others. Eventually, the estimate of the total weight of the critical ensembles is too large. We can restore the proper statistical weights by a rescaling of the weights:

$$W[U; \beta_j, \mu_j] \rightarrow \frac{W[U; \beta_j, \mu_j]}{1 + 2\tau_j} \quad (\text{D.11})$$

This leads to the modified Eq.(D.7):

$$Z_k = \sum_{s=1}^R \sum_{i_s=1}^{n_s} \frac{e^{-S_g[s, i_s; \beta_k]} \det M(s, i_s; \mu_k) / (1 + 2\tau_k)}{\sum_j n_j \frac{e^{-S_g[s, i_s; \beta_j]} \det M(s, i_s; \mu_j) / (1 + 2\tau_j)}{Z_j}} , \quad (\text{D.12})$$

which we use, after estimating the  $\tau_j$ 's of the plaquette values. We have observed that the reweighting results do not change within the statistical error if we consider

the autocorrelation times of different observables. In particular, our ensembles are generated such that the autocorrelation time is smaller than one configuration except at the phase transition, where  $\tau$  is about  $1 \lesssim \tau \lesssim 5$ .

### D.3 Reweighting to Arbitrary Coupling

The expectation value of an observable  $\hat{O}$  in general is given by

$$\langle \hat{O} \rangle_{\beta, \mu} = \sum_{s=1}^R \sum_{i_s=1}^{n_s} \hat{O}(s, i_s) \omega(s, i_s; \beta, \mu). \quad (\text{D.13})$$

If  $R = 1$  and the Markov chain is generated using importance sampling at couplings  $(\beta_1 = \beta, \mu_1 = \mu)$  (no reweighting), the weight-function  $\omega$  simply is  $\omega = \frac{1}{n_s}$ . In general,

$$\omega(s, i_s; \beta, \mu) = \frac{1}{Z_{GC}(\beta, \mu)} \frac{W[s, i_s; \beta, \mu]}{\sum_{j=1}^R n_j \frac{W[s, i_s; \beta_j, \mu_j]}{Z_j}} \quad (\text{D.14})$$

and  $Z_{GC}(\beta, \mu)$  is given by Eq.(D.6). We have omitted the autocorrelation time for notational simplicity. The weights used in the first step of the Ferrenberg-Swendsen reweighting method, namely solving the self-consistency equation Eq.(D.7), are sampling weights, so they are positive. In the second step, there is no such a restriction: we can reweight to real chemical potential, where the determinant is complex. The difficulty, however, is to control the statistical error.

It is advantageous to cover as much configuration space as possible, so that a new  $Z_{GC}(\beta, \mu)$  can be evaluated correctly even when the weights  $W[s, i_s; \beta, \mu]$  are very different from any of the sampling weights  $W[s, i_s; \beta_j, \mu_j]$ . However, if the sampling weights  $W[s, i_s; \beta_j, \mu_j]$  are very different from each other, each simulation  $j$  will concentrate on a given part of configuration space, and the sum  $\sum_j n_j \frac{W[s, i_s; \beta_j, \mu_j]}{Z_j}$  for any configuration  $(s, i_s)$  will be dominated by just one term. This is known as the overlap problem. This will make the convergence of the set of equations Eqs.(D.7) difficult. There is a subtle consequence for the error estimation. In an extreme case,

when most of the weight is carried by one single configuration, any error estimation is questionable.

It is convenient to define the total weight of a Monte Carlo ensemble by

$$\Omega(s) = \sum_{i_s=1}^{n_s} \omega(s, i_s; \beta, \mu) . \quad (\text{D.15})$$

The sum  $\sum_s \Omega(s) = \sum_s \sum_{i_s=1}^{n_s} \omega(s, i_s; \beta, \mu)$  has to be the identity exactly - a simple test for numerical round-off errors.

## D.4 Zero Baryon Density

, and the Fourier transformation is sampled independently of the temperature  $\beta$ .

We treat the imaginary chemical potential  $\mu_I$  as an additional degree of freedom, like the gauge configuration  $U$ . We thus make use of the reweighting procedure by the following formulation. The expectation value of an observable at some target temperature  $\beta$  in the zero baryon sector is given by

$$\langle \hat{O} \rangle_{B=0, \beta} = \frac{1}{Z_C(\beta, B=0)} \frac{1}{2\pi} \int_{-\pi}^{\pi} d\bar{\mu}_I \int [DU] \hat{O} e^{-S_g[U; \beta]} \det M(U; i\bar{\mu}_I T) \quad (\text{D.16})$$

$$= \frac{1}{Z_C(\beta, B=0)} \sum_{s=1}^R \sum_{i_s=1}^{n_s} \hat{O}(s, i_s) \omega(s, i_s; \beta) \quad (\text{D.17})$$

Our ensembles, denoted by  $j$ , are not sampled at  $\beta$ , but at various  $\beta_j$ 's. The function  $\omega$ , the correct weight distribution Eq.(D.14), thus is given by

$$\omega(s, i_s; \beta) = \frac{1}{\mathcal{N}} \frac{e^{-\beta S_g[s, i_s]}}{\sum_{j=1}^R n_j \frac{e^{-\beta_j S_g[s, i_s]}}{Z_j}} , \quad (\text{D.18})$$

where  $\mathcal{N}$  is a normalisation constant, which is cancelled by  $Z_C(B=0, \beta)$

$$Z_C(\beta, B=0) = \frac{1}{\mathcal{N}} \sum_{s=1}^R \sum_{i_s=1}^{n_s} \frac{1}{\sum_{j=1}^R n_j \frac{e^{-(\beta_j - \beta) S_g[s, i_s]}}{Z_j}} . \quad (\text{D.19})$$

## D.5 Canonical Partition Functions

In subsection 4.3.3 we have claimed that Eq.(4.33) allows for Ferrenberg-Swendsen reweighting, in order to improve the accuracy on the canonical partition functions. Again, the key for understanding is given by realising that

$$\begin{aligned} \frac{Z_C(\beta_k, B)}{Z_{MC}(\beta_k, i\mu_k)} &= \frac{\int [DU] \hat{Z}_C(U; B) \frac{\det M(U; i\mu_k)}{\det M(U; i\mu_k)} e^{-S_g[U; \beta_k]}}{\int DU e^{-S_g[U; \beta_k]} \det M(U; \mu_k)} \\ &= \left\langle \frac{\hat{Z}_C(U; B)}{\det M(U; i\mu_k)} \right\rangle_{\beta_k, i\mu_k} = \sum_{i_k} \frac{\hat{Z}_C(k, i_k; B)}{\det M(k, i_k; i\mu_k)}, \end{aligned} \quad (\text{D.20})$$

with  $\hat{Z}_C(U; B) = \frac{1}{2\pi} \int_{-\pi}^{\pi} d\bar{\mu}_I e^{-i3B\bar{\mu}_I} \det M(U; i\bar{\mu}_I T)$  are the Fourier coefficients of the determinant. The canonical partition function with respect to a different  $\beta$  is given by

$$\frac{Z_C(\beta, B)}{Z_{MC}(\beta_k, i\mu_k)} = \frac{1}{Z_{MC} \mathcal{N}_{\parallel}(\beta_k, i\mu_k)} \sum_{i_k} \frac{\hat{Z}_C(k, i_k; B)}{\det M(k, i_k; i\mu_k)} e^{S_g[U; \beta_k] - S_g[U; \beta]}. \quad (\text{D.21})$$

The arbitrary normalisation factor  $\mathcal{N}_{\parallel}$  is irrelevant for physical observables. If we want to perform a multi-histogram reweighting using various ensembles, we have to be careful to add ‘‘apples to apples’’, since each ensemble has a different normalisation,  $Z_{MC}(\beta_k, i\mu_k)$ . We solve this problem by expressing the canonical partition functions at a target coupling  $\beta$  with respect to a *reference* grand canonical partition function at the couplings  $(\beta_0, \mu_0)$ . Generically, we write

$$\frac{Z_C(\beta, B)}{Z_{ref}(\beta_0, \mu_0)} = \frac{1}{Z_{ref}(\beta_0, \mu_0)} \int [DU] \hat{Z}_C(U; B) e^{-S_g[U; \beta]}. \quad (\text{D.22})$$

Based on our  $s$  ensembles, the denominator  $Z_{ref}(\beta_0, \mu_0)$ , although not explicitly needed, can be calculated via the self-consistency equation Eq.(D.8)

$$Z_{ref}(\beta_0, \mu_0) = \sum_{s, i_s} \frac{e^{-S_g[s, i_s; \beta_0]} \det M(s, i_s; \mu_0)}{\sum_j n_j \frac{e^{-S_g[s, i_s; \beta_j]} \det M(s, i_s; \mu_j)}{Z_j}} \quad (\text{D.23})$$

The numerator  $Z_C(\beta, B)$  is independent of the chemical potential. In terms of the sampled configurations, we write

$$Z_C(\beta, B) = \frac{1}{\mathcal{N}} \sum_{s, i_s} \frac{Z_C(s, i_s; B) e^{-S_g[s, i_s; \beta]}}{\sum_j n_j \frac{e^{-S_g[s, i_s; \beta_j]} \det M(s, i_s; \mu_j)}{Z_j}} \quad (\text{D.24})$$

The overall normalisation factor  $\mathcal{N}$  drops out for physical observables.

For notational convenience in the following, we multiply the numerator in Eq.(D.24) with the identity  $\frac{\det M(s, i_s; \mu_0)}{\det M(s, i_s; \mu_0)}$  and define

$$\begin{aligned} \frac{Z_C(\beta, B)}{Z_{ref}(\beta_0, \mu_0)} &= \frac{1}{Z_{ref}(\beta_0, \mu_0)} \frac{1}{\mathcal{N}} \sum_{s, i_s} \frac{Z_C(s, i_s; B) \frac{\det M(s, i_s; \mu_0)}{\det M(s, i_s; \mu_0)} e^{-S_g[s, i_s; \beta]}}{\sum_j n_j \frac{e^{-S_g[s, i_s; \beta_j]} \det M(s, i_s; \mu_j)}{Z_j}} \\ &\equiv \left[ \frac{\hat{Z}_C(s, i_s; B)}{\det M(s, i_s; \mu_0)} \right]_{\beta_0, \mu_0}^\beta \end{aligned} \quad (\text{D.25})$$

## D.6 Canonical Observables

The expectation value of an observable  $\hat{O}$  in the canonical sector  $B$  is given by

$$\langle \hat{O} \rangle_{B, \beta} = \frac{1}{Z_C(\beta, B)} \int [DU] e^{-S_g[U; \beta]} \frac{1}{2\pi} \int_{-\pi}^{\pi} d\bar{\mu}_I e^{-i3B\bar{\mu}_I} \det M(U; i\mu_I) \hat{O} \quad (\text{D.26})$$

$$= \frac{Z_{ref}(\beta, \mu_0)}{Z_C(\beta, B)} \frac{1}{Z_{ref}(\beta, \mu_0)} \int [DU] e^{-S_g[U; \beta]} \det M(U; \mu_0) \times \quad (\text{D.27})$$

$$\times \frac{1}{\det M(U; \mu_0)} \frac{1}{2\pi} \int_{-\pi}^{\pi} d\bar{\mu}_I e^{-i3B\bar{\mu}_I} \det M(U; i\mu_I) \hat{O} \quad (\text{D.28})$$

$$= \frac{Z_{ref}(\beta, \mu_0)}{Z_C(\beta, B)} \left[ \frac{1}{2\pi} \int_{-\pi}^{\pi} d\bar{\mu}_I e^{-i3B\bar{\mu}_I} \frac{\det M(U; i\mu_I)}{\det M(U; \mu_0)} \hat{O} \right]_{\beta, \mu_0}^\beta, \quad (\text{D.29})$$

where we have chosen the reference temperature  $\beta_0 = \beta$  for simplicity.

Observables, which are independent of the chemical potential, can be measured as follows. The expectation value is given by

$$\langle \hat{O} \rangle_{B, \beta} = \frac{\left[ \hat{O} \frac{\hat{Z}_C(U; B)}{\det M(U; \mu_0)} \right]_{\beta, \mu_0}^\beta}{\left[ \frac{\hat{Z}_C(U; B)}{\det M(U; \mu_0)} \right]_{\beta, \mu_0}^\beta} \equiv \sum_{s, i_s} \hat{O}(s, i_s) \omega_C(s, i_s; B, \beta), \quad (\text{D.30})$$

and we define the canonical weight-function  $\omega_C(s, i_s; B, \beta)$  as

$$\omega_C(s, i_s; B, \beta) = \frac{\frac{\hat{Z}_C(s, i_s; B) e^{-S_g[s, i_s; \beta]}}{\sum_j n_j \frac{e^{-S_g[s, i_s; \beta_j]} \det M(s, i_s; \mu_j)}{Z_j}}}{\sum_{s', i'_s} \frac{\hat{Z}_C(s', i'_s; B) e^{-S_g[s', i'_s; \beta]}}{\sum_j n_j \frac{e^{-S_g[s', i'_s; \beta_j]} \det M(s', i'_s; \mu_j)}{Z_j}}}. \quad (\text{D.31})$$

Note that this expression is independent of  $\mu_0$ . Like in subsection D.3, the sum over all weights  $\sum_{s,i_s} \omega_C(s, i_s; B, \beta) = 1$  can provide a simple test for limitations due to machine precision. In order to determine the importance of each ensemble for a given canonical sector, we consider the average weight of one configuration in a given ensemble:

$$\Omega_C(s; B, \beta) = N_C \frac{1}{n_s} \sum_{i_s=1}^{n_s} \omega_C(s, i_s; B, \beta) \quad (\text{D.32})$$

where the constant factor  $N_C$  is given by the condition

$$\sum_s \Omega_C(s; B, \beta) = 1 \quad (\text{D.33})$$

# Bibliography

- [1] K. G. Wilson, Phys. Rev. D **10** (1974) 2445.
- [2] K. Osterwalder and R. Schrader, Commun. Math. Phys. **31** (1973) 83; K. Osterwalder and R. Schrader, Commun. Math. Phys. **42**, 281 (1975).
- [3] M. Luscher, Commun. Math. Phys. **54** (1977) 283.
- [4] M. E. Peskin and D. V. Schroeder, An Introduction to Quantum Field Theory, ISBN 0-201-50397-2, p.672ff.
- [5] J. Gasser and H. Leutwyler, Annals Phys. **158** (1984) 142. B. Moussallam, arXiv:hep-ph/0407246.
- [6] C. Christou, A. Feo, H. Panagopoulos and E. Vicari, Nucl. Phys. B **525** (1998) 387 [Erratum-ibid. B **608** (2001) 479] .
- [7] Z. Bai, M. Fahey and G. Golub,, J. Comput. Appl. Math. 74 (1996) 71.
- [8] H. B. Nielsen and M. Ninomiya, Phys. Lett. B **105** (1981) 219.
- [9] P. H. Ginsparg and K. G. Wilson, Phys. Rev. D **25** (1982) 2649.
- [10] P. Hernandez, K. Jansen and M. Luscher, Nucl. Phys. B **552**, 363 (1999) .
- [11] R. Gupta, arXiv:hep-lat/9807028.
- [12] H. Kluberg-Stern, A. Morel, O. Napoly and B. Petersson, “Flavors Of Lagrangian Susskind Fermions,” Nucl. Phys. B **220** (1983) 447.

- [13] E. Marinari, G. Parisi and C. Rebbi, Nucl. Phys. B **190** (1981) 734.
- [14] B. Bunk, M. Della Morte, K. Jansen and F. Knechtli, Nucl. Phys. B **697** (2004) 343 .
- [15] J. I. Kapusta, Finite Temperature Field Theory, ISBN 0-521-44945-6.
- [16] P. Hasenfratz and F. Karsch, Phys. Lett. B **125** (1983) 308.
- [17] G. 't Hooft, Nucl. Phys. B **153** (1979) 141.
- [18] A. Roberge and N. Weiss, Nucl. Phys. B **275** (1986) 734.
- [19] P. de Forcrand, B. Lucini and M. Vettorazzo, arXiv:hep-lat/0409148.
- [20] C. Borgs and E. Seiler, Nucl. Phys. B **215** (1983) 125.
- [21] K. Adcox *et al.* [PHENIX Collaboration], Nucl. Phys. A **757** (2005) 184 .
- [22] M. A. Stephanov, Prog. Theor. Phys. Suppl. **153** (2004) 139 .M. A. Halasz, A. D. Jackson, R. E. Shrock, M. A. Stephanov and J. J. M. Verbaarschot, Phys. Rev. D **58** (1998) 096007.
- [23] M. G. Alford, Nucl. Phys. Proc. Suppl. **117**, 65 (2003) .
- [24] B. Svetitsky and L. G. Yaffe, Nucl. Phys. B **210** (1982) 423; L. G. Yaffe and B. Svetitsky, Phys. Rev. D **26** (1982) 963.
- [25] A. Gocksch and M. Ogilvie, Phys. Rev. D **31** (1985) 877.
- [26] R. D. Pisarski and F. Wilczek, Phys. Rev. D **29** (1984) 338.
- [27] S. Gavin, A. Gocksch and R. D. Pisarski, Phys. Rev. D **49** (1994) 3079 .
- [28] A. M. Polyakov, Phys. Lett. B **72** (1978) 477.
- [29] F. Karsch, E. Laermann and A. Peikert, Nucl. Phys. B **605** (2001) 579 .



- [30] N. Weiss, Phys. Rev. D **24** (1981) 475. C. DeTar and L. D. McLerran, Phys. Lett. B **119** (1982) 171; Y. Hatta and K. Fukushima, Phys. Rev. D **69** (2004) 097502 .
- [31] F. Karsch, K. Redlich and A. Tawfik, Eur. Phys. J. C **29** (2003) 549.
- [32] F. Karsch, K. Redlich and A. Tawfik, Phys. Lett. B **571** (2003) 67.
- [33] F. Karsch, Prog. Theor. Phys. Suppl. **153**, 106 (2004) .
- [34] C. R. Allton *et al.*, arXiv:hep-lat/0501030.
- [35] E. Laermann, C. DeTar, O. Kaczmarek and F. Karsch, Nucl. Phys. Proc. Suppl. **73** (1999) 447.
- [36] C. Michael, Nucl. Phys. Proc. Suppl. **26** (1992) 417; O. Philipsen and H. Wittig, Phys. Rev. Lett. **81** (1998) 4056 [Erratum-ibid. **83** (1999) 2684]; F. Knechtli and R. Sommer [ALPHA collaboration], Phys. Lett. B **440** (1998) 345; O. Philipsen and H. Wittig, Phys. Lett. B **451** (1999) 146; C. DeTar, U. M. Heller and P. Lacey, Nucl. Phys. Proc. Suppl. **83** (2000) 310; P. de Forcrand and O. Philipsen, Phys. Lett. B **475** (2000) 280; P. Pennanen and C. Michael [UKQCD Collaboration], arXiv:hep-lat/0001015; C. W. Bernard *et al.* [MILC Collaboration], Nucl. Phys. Proc. Suppl. **94** (2001) 546; G. S. Bali, H. Neff, T. Duessel, T. Lippert and K. Schilling [SESAM Collaboration], Phys. Rev. D **71** (2005) 114513 .
- [37] P. W. Stephenson, Nucl. Phys. B **550** (1999) 427.
- [38] K. D. Born *et al.*, Phys. Lett. B **329** (1994) 325; U. M. Heller *et al.*, Phys. Lett. B **335** (1994) 71; U. Glässner *et al.* [SESAM Collaboration], Phys. Lett. B **383** (1996) 98; S. Aoki *et al.* [CP-PACS Collaboration], Nucl. Phys. Proc. Suppl. **73** (1999) 216; G. S. Bali *et al.* [TXL Collaboration], Phys. Rev. D **62** (2000) 054503; B. Bolder *et al.*, Phys. Rev. D **63** (2001) 074504; H. D. Trottier and K. Y. Wong, arXiv:hep-lat/0209048.

- [39] G. I. Poulis and H. D. Trottier, Phys. Lett. B **400** (1997) 358.
- [40] F. Gliozzi and P. Provero, Nucl. Phys. Proc. Suppl. **83** (2000) 461.
- [41] S. Kratochvila and P. de Forcrand, arXiv:hep-lat/0209094.
- [42] S. Kratochvila and P. de Forcrand, Nucl. Phys. B **671** (2003) 103 .
- [43] F. Gliozzi and A. Rago, Nucl. Phys. B **714** (2005) 91 .
- [44] M. Lüscher and U. Wolff, Nucl. Phys. B **339** (1990) 222.
- [45] I. T. Drummond, Phys. Lett. B **434** (1998) 92.
- [46] K. Kallio and H. D. Trottier, Phys. Rev. D **66** (2002) 034503.
- [47] L. D. McLerran and B. Svetitsky, Phys. Rev. D **24** (1981) 450.
- [48] Y. Schröder, DESY-THESIS-1999-021.
- [49] G. Parisi, R. Petronzio and F. Rapuano, Phys. Lett. B **128** (1983) 418.
- [50] C. Michael, Nucl. Phys. B **259** (1985) 58.
- [51] M. Lüscher and P. Weisz, JHEP **0109** (2001) 010.
- [52] P. Majumdar, arXiv:hep-lat/0208068.
- [53] J. Engels, F. Karsch, E. Laermann, C. Legeland, M. Lütgemeier, B. Petersson and T. Scheideler, Nucl. Phys. Proc. Suppl. **53** (1997) 420.
- [54] M. Pepe, private communication.
- [55] R. Sommer, Nucl. Phys. B **411** (1994) 839.
- [56] M. J. Teper, Phys. Rev. D **59** (1999) 014512.
- [57] M. Lüscher, Nucl. Phys. B **180** (1981) 317.

- [58] S. Perantonis, A. Huntley and C. Michael, Nucl. Phys. B **326** (1989) 544.
- [59] O. Philipsen, private communication.
- [60] G. S. Bali, Phys. Rev. D **62** (2000) 114503.
- [61] M. Troyer and U. J. Wiese, Phys. Rev. Lett. **94** (2005) 170201.
- [62] P. Crompton, private communication.
- [63] B. Petersson, Nucl. Phys. Proc. Suppl. **30** (1993) 66.
- [64] Z. Fodor and S. D. Katz, JHEP **0404** (2004) 050 .
- [65] Z. Fodor and S. D. Katz, Phys. Lett. B **534**, 87 (2002).
- [66] S. Ejiri, arXiv:hep-lat/0506023.
- [67] I. M. Barbour, C. T. H. Davies and Z. Sabeur, Phys. Lett. B **215** (1988) 567;  
I. M. Barbour, S. E. Morrison, E. G. Klepfish, J. B. Kogut and M. P. Lombardo,  
Phys. Rev. D **56** (1997) 7063 .I. M. Barbour, S. E. Morrison, E. G. Klepfish,  
J. B. Kogut and M. P. Lombardo, Nucl. Phys. Proc. Suppl. **60A** (1998) 220 .
- [68] M. G. Alford, Nucl. Phys. Proc. Suppl. **73**, 161 (1999) .
- [69] K. Splittorff, arXiv:hep-lat/0505001.
- [70] J. B. Kogut and D. K. Sinclair, Phys. Rev. D **66** (2002) 034505 .
- [71] A. Nakamura and T. Takaishi, Nucl. Phys. Proc. Suppl. **129** (2004) 629 .
- [72] C. R. Allton *et al.*, Phys. Rev. D **66** (2002) 074507.
- [73] C. R. Allton *et al.*, Phys. Rev. D **68** (2003) 014507.
- [74] R. V. Gavai and S. Gupta, Phys. Rev. D **68** (2003) 034506 .
- [75] P. de Forcrand and O. Philipsen, Nucl. Phys. B **642** (2002) 290 .

- [76] M. D'Elia and M. P. Lombardo, Phys. Rev. D **67** (2003) 014505 .
- [77] V. Azcoiti, G. Di Carlo, A. Galante and V. Laliena, arXiv:hep-lat/0503010.
- [78] D. E. Miller and K. Redlich, Phys. Rev. D **35** (1987) 2524; K. F. S. Liu, Int. J. Mod. Phys. B **16** (2002) 2017 .
- [79] A. Hasenfratz and D. Toussaint, Nucl. Phys. B **371** (1992) 539.
- [80] S. Kratochvila and P. de Forcrand, arXiv:hep-lat/0409072.
- [81] A. Alexandru, M. Faber, I. Horvath and K. F. Liu, arXiv:hep-lat/0410002.
- [82] V. Azcoiti and A. Galante, Phys. Lett. B **444** (1998) 421.
- [83] S. Kratochvila and P. de Forcrand, Prog. Theor. Phys. Suppl. **153** (2004) 330 [Nucl. Phys. Proc. Suppl. **129** (2004) 533] .
- [84] M. Oleszczuk and J. Polonyi, Annals Phys. **227** (1993) 76; M. Oleszczuk, Nucl. Phys. B Proc. Suppl. **39** (1995) 471; O. Borisenko, M. Faber and G. Zinovev, Nucl. Phys. B **444** (1995) 563. K. Fukushima, Annals Phys. **304** (2003) 72.
- [85] R. Hagedorn and J. Rafelski, CERN-TH-2947 *Invited lecture given at Int. Symp. on Statistical Mechanics of Quarks and Hadrons, Bielefeld, Germany, Aug 24-31, 1980*; J. Rafelski and R. Hagedorn, CERN-TH-2969 *Invited talk given at Int. Symp. on Statistical Mechanics of Quarks and Hadrons, Bielefeld, West Germany Aug 24-31, 1980*.
- [86] J. Letessier and J. Rafelski, Phys. Rev. C **67** (2003) 031902 .
- [87] S. Duane, A. D. Kennedy, B. J. Pendleton and D. Roweth, Phys. Lett. B **195** (1987) 216.
- [88] K. Bitar, A. D. Kennedy, R. Horsley, S. Meyer and P. Rossi, Nucl. Phys. B **313**, 377 (1989).

- [89] S. A. Gottlieb, W. Liu, D. Toussaint, R. L. Renken and R. L. Sugar, Phys. Rev. D **35** (1987) 2531.
- [90] P. de Forcrand and T. Takaishi, Nucl. Phys. Proc. Suppl. **53** (1997) 968 .R. Frezzotti and K. Jansen, Phys. Lett. B **402** (1997) 328 .
- [91] A. D. Kennedy, I. Horvath and S. Sint, Nucl. Phys. Proc. Suppl. **73** (1999) 834.
- [92] M. G. Alford, A. Kapustin and F. Wilczek, Phys. Rev. D **59** (1999) 054502 .
- [93] B. A. Berg and T. Neuhaus, Phys. Rev. Lett. **68** (1992) 9 [arXiv:hep-lat/9202004].
- [94] P. E. Gibbs, Phys. Lett. B **172** (1986) 53.
- [95] R. Aloisio, V. Azcoiti, G. Di Carlo, A. Galante and A. F. Grillo, Phys. Lett. B **453** (1999) 275 [arXiv:hep-lat/9811033].
- [96] V. Azcoiti, G. Di Carlo, A. Galante and V. Laliena, arXiv:hep-lat/0409160.
- [97] P. R. Crompton, Nucl. Phys. Proc. Suppl. **119** (2003) 550.
- [98] A. M. Ferrenberg and R. H. Swendsen, Phys. Rev. Lett. **61** (1988) 2635;  
A. M. Ferrenberg and R. H. Swendsen, Phys. Rev. Lett. **63** (1989) 1195.
- [99] G. Martinelli, G. Parisi, R. Petronzio and F. Rapuano, Phys. Lett. B **122**, 283 (1983).
- [100] K. Binder, Z. Phys. B **43** (1981) 119.
- [101] M. Fukugita and A. Ukawa, Phys. Rev. Lett. **57** (1986) 503.
- [102] G. Boyd, J. Engels, F. Karsch, E. Laermann, C. Legeland, M. Lutgemeier and B. Petersson, Nucl. Phys. B **469** (1996) 419 .
- [103] M. D'Elia and M. P. Lombardo, Phys. Rev. D **70** (2004) 074509; M. D'Elia, F. Di Renzo and M. P. Lombardo, arXiv:hep-lat/0511029.

- [104] H. Kluberg-Stern, A. Morel and B. Petersson, Nucl. Phys. B **215** (1983) 527; T. Jolicoeur, H. Kluberg-Stern, M. Lev, A. Morel and B. Petersson, Nucl. Phys. B **235** (1984) 455. J. M. Drouffe and H. Kluberg-Stern, Nucl. Phys. B **260** (1985) 253.
- [105] D. Hochberg and J. Hoek, Nucl. Phys. B **270** (1986) 603.
- [106] F. Karsch and K. H. Mutter, Nucl. Phys. B **313** (1989) 541.
- [107] Y. Nishida, Phys. Rev. D **69** (2004) 094501.
- [108] N. Kawamoto, K. Miura, A. Ohnishi and T. Ohnuma, arXiv:hep-lat/0512023.
- [109] M. A. Halasz, A. D. Jackson, R. E. Shrock, M. A. Stephanov and J. J. M. Verbaarschot, Phys. Rev. D **58** (1998) 096007 [arXiv:hep-ph/9804290].
- [110] H. A. Bethe, Phys. Rev. **167** (1968) 879; H. A. Bethe, Ann. Rev. Nucl. Sci. **21** (1971) 93.
- [111] P. Hasenfratz et al, Phys. Lett. **B133** (1983) 221.
- [112] C. Alexandrou et al, Phys. Rev. **D60** (1999) 034504.
- [113] M. Alford et al, Nucl. Phys. **B602** (2001) 61.
- [114] P. Giudice and A. Papa, Phys. Rev. **D69** (2004) 094509.
- [115] V. Azcoiti et. al, JHEP **0412** (2004) 010.
- [116] F. Karsch and S. Stickan, Phys. Lett. **B488** (2000) 319.
- [117] R. H. Swendsen and J. Wang, Phys. Rev. Lett. **58** (1987) 86.
- [118] Ph. de Forcrand and O. Philipsen, Nucl. Phys. **B673** (2003) 170.
- [119] O. Philipsen, arXiv:hep-lat/0510077.
- [120] O. Philipsen and P. de Forcrand, arXiv:hep-lat/0409034.

- [121] P. de Forcrand, M. D'Elia and M. Pepe, Phys. Rev. Lett. **86** (2001) 1438; P. de Forcrand and O. Jahn, Nucl. Phys. A **755** (2005) 475; M. Panero, JHEP **0505** (2005) 066.
- [122] G. S. Bali, H. Neff, T. Duessel, T. Lippert and K. Schilling [SESAM Collaboration], Phys. Rev. D **71** (2005) 114513.
- [123] M. Shaposhnikov, private communication.
- [124] P. Wang, D. B. Leinweber, A. W. Thomas and A. G. Williams, arXiv:nucl-th/0407056.
- [125] E. Dagotto, A. Moreo and U. Wolff, Coupling Phys. Lett. B **186** (1987) 395; E. Dagotto, A. Moreo and U. Wolff, Phys. Rev. Lett. **57** (1986) 1292.
- [126] D. Toublan and J. B. Kogut, Phys. Lett. B **564** (2003) 212 [arXiv:hep-ph/0301183].
- [127] R. G. Miller, *The jackknife - a review*, Biometrika **61** (1974) 1-15.
- [128] M. E. J. Newman, R. G. Palmer, J. Stat. Phys. **97** (1999) 1011.





# List of Tables

1.1	Various transcriptions of the Dirac operator and their relation to doublers, chiral symmetry, flavour symmetry and ultra-locality. . . . .	15
3.1	Generalised Factorisation Method. An overview of various choices. . .	92
4.1	The prediction for the free energy density based on the free gas model in the continuum at high temperature suffers from finite size and cut-off effects. The correction terms $C_2$ and $C_4$ help to quantify the systematics. The functional form in Eq.(4.16) nicely describes the data - the contribution of the additional term $(\frac{\mu}{T})^6$ is negligible (left table). We also plot the free energy density of the massless Stefan-Boltzmann gas for comparison (right). Already at the volume $10^3$ , no difference is visible. . . . .	115
4.2	The (approximated) phase transition as a function of the asymmetry-parameter $\xi$ . . . . .	124
4.3	The coefficients of the free energy density expansion for $\frac{T}{T_c} \sim 1.1$ come close to their $T \rightarrow \infty$ value. In addition to the jackknife error, we specify a systematic error for the fitting Ansatz (see text). The error on the second coefficient $b_4$ is so large that we cannot determine it properly. . . . .	137
4.4	The various ensembles in our approach. . . . .	140

4.5	The prediction for $\frac{\mu}{T}(\frac{\rho}{T^3})$ , based on the free gas model in the continuum at high temperature, suffers from finite size and cut-off effects. The correction terms $\tilde{C}_2$ and $\tilde{C}_4$ help to quantify the systematics (left table). As expected, the correction factors are in agreement with Table 4.1 on page 115. We plot results of $\frac{\mu}{T}(\frac{\rho}{T^3})$ from the free gas on the lattice at various lattice sizes and compare with the massless Stefan-Boltzmann gas (right). Already at the volume $10^3$ , no difference is visible. . . . .	150
A.1	(left) The scalar lattice propagator $G(r, 0)$ in 2d. (right) The naive derivation points $(r - \frac{a}{2})$ compared with $r_I$ in the range we consider.	186

# List of Figures

1.1	The fundamental particles in the standard model (left). The four interactions in nature are the gravity, the electromagnetic force, the weak force and the strong force. Note that gravity is not part of the standard model (right, taken from <a href="http://particleadventure.org/particleadventure">http://particleadventure.org/particleadventure</a> ).	1
1.2	A plaquette and its contour.	10
1.3	Field Theory at Finite Temperature. The cylinder represents the periodic boundary conditions in the temporal direction.	26
1.4	Phase diagram of $Z_{GC}(i\mu_I)$ in the $(\mu_I, T)$ -plane for $N_c = 3$ . The arrows indicate the orientation of the Polyakov loop. The vertical lines signals the “order-order” $Z_3$ transitions, which are first order. Properties of the “order-disorder” $Z_3$ transitions (curved lines) depend on the parameters (number of flavours, quark mass) of the theory.	34
1.5	Conjectured phase diagram of real-world QCD in the $(T, \mu)$ -plane.	37
1.6	The order of the phase transition from the hadronic matter phase to the quark-gluon plasma one in the plane of the degenerate “up/down”-quark masses $m_u = m_d$ and “strange”-quark mass $m_s$ . The blue $X$ refers to real-world physics, ie. physical quark masses.	39
1.7	Two static charges $Q$ and $\bar{Q}$ will be screened, if the energy stored in the flux tube of length $R$ is large enough to create a matter-antimatter pair $g\bar{g}$ .	41

2.1	The Wilson loop channel. Information about the groundstate energy, the so-called static potential, can be extracted. . . . .	49
2.2	Hierarchical scheme. Using the three-level method as described in the text decreases the statistical error exponentially. While a one-level approach only allows to sample over the temporal links, a multi-level approach also makes it possible to update the interior spatial links, which improves the error reduction. . . . .	59
2.3	The improved spatial transporters. After each calculation of second-level averages $\left[ \mathbf{T}(R, na) \right] \left[ \mathbf{T}(R, (n+1)a) \right]$ , we form staple-shaped transporter including smeared spatial links at the time-slice $(n+2)a$ . . . . .	61
2.4	Interacting gluelumps at distance $R$ . Four "clovers" are stuck on a link-link-correlator tensor of temporal extent $T$ . . . . .	63
2.5	The adjoint and fundamental static potentials $V(R)$ (the latter multiplied by the Casimir factor $\frac{8}{3}$ ) versus $R$ using Wilson loops only. The adjoint static potential remains approximately constant for $R \geq R_b \approx 10a$ proving string breaking. The unbroken-string state energy is also drawn. The horizontal line at $2.06(3)a^{-1}$ represents twice the mass of a gluelump. . . . .	68
2.6	Adjoint Wilson loop data versus $T$ , for $R = 11a$ and $R = 12a$ , obtained from a diagonalisation procedure Eq.(2.56), applied to Wilson loops, considering three different levels of smearing. A two-mass Ansatz accounts for all data points. Single-exponentials (dotted lines) do not. At large $T$ , the broken-string groundstate is exposed. Note how small a signal can be measured. . . . .	71
2.7	The static adjoint potential $V(R)$ versus $R$ (same as in Fig. 2.5) and the first excited unbroken-string state energy using Wilson loops only. We also show the energy $\tilde{E}_1(R)$ (Eq.(2.59)) resulting from the relativistic Nambu string theory. The horizontal line at $2.06(3)a^{-1}$ represents twice the mass of a gluelump. . . . .	74

2.8	Agreement of the static adjoint potential $V(R)$ versus $R$ , extracted from the two-gluelump correlator and the one extracted from Wilson loops only (same as in Fig. 2.5, but shifted to the right for clarity). The deviations at $R = 8a$ and $R = 9a$ are due to a large value of the turning point $T_P$ , as explained in the text. . . . .	75
2.9	The static adjoint potentials $V(R)$ versus $R$ using the multichannel Ansatz. The agreement with the static potential extracted from Wilson loops only (same as in Fig. 2.5, shifted to the right for clarity) is good. The unbroken-string state energy is also drawn (dashed line). The horizontal line at $2.06(3)a^{-1}$ represents twice the mass of a gluelump. . . . .	77
2.10	The static potential $V(R)$ , the first and the second excited states energies using the multichannel Ansatz. We also show the energy $\tilde{E}_1(R)$ (Eq.(2.59)) resulting from the relativistic bosonic string theory. The horizontal line at $2.06(3)a^{-1}$ represents twice the mass of a gluelump. . . . .	78
2.11	Polyakov loop method. The static adjoint potential $V(R)$ versus $R$ extracted from the correlator of two adjoint Polyakov loops agrees very well with that measured using Wilson loops only (same as in Fig. 2.5, shifted to the right for clarity). The flattening of the potential can be observed, although we cannot extract the value at $R = 12a$ due to large fluctuations. . . . .	79
2.12	Ratio of forces $\frac{F_{\text{adj}}(R)}{F_{\text{fund}}(R)}$ as a function of the spatial separation. The horizontal line at $\frac{8}{3}$ indicates the Casimir ratio expected from perturbation theory. We see clear deviation at distances larger than $R = 2a$ . The ratio seems to decrease linearly while increasing $R$ . . . . .	81

3.1	Simple illustration of the overlap problem. A typical example of a sampled distribution versus the correct distribution with vanishing overlap. No relevant “configurations” are sampled (left). The sampled distribution at $\lambda = 0$ shows a rather good overlap with the distribution at $\lambda \neq 0$ (right). . . . .	89
3.2	The Brute-Force method. The histogram of the sampling variable $t$ in comparison with the exact integrand (top left). The expectation value $\frac{Z(\lambda)}{Z(0)} = \langle \cos(\lambda t) \rangle$ in comparison with the exact result (top right). The histogram of the observable $\cos(\lambda t)$ as a measure of the “sign problem” (bottom left). The expectation value $\langle \sin(\lambda t) \rangle$ (bottom right) as an indicator for ergodicity, and a check of the correct evaluation of the statistical error. . . . .	91
3.3	The Factorisation method. The histogram of the sampling variable $t$ in comparison with the exact integrand (top left) for various $\lambda$ . The expectation value $\frac{Z(\lambda)}{Z(0)} = \langle \cos(\lambda t) \rangle$ in comparison with the exact result (top right). The expectation value $\frac{Z(k)}{Z(k-1)}$ in comparison with the analytic result (bottom left). Successive values of $\lambda_1$ in the Optimal Factorisation method (bottom right). . . . .	93
3.4	Quantification of the “sign problem”. $\langle \frac{\cos(\lambda_1 t)}{\epsilon +  \cos((\lambda_1 - \frac{\lambda}{2n})t) } \rangle_{Standard}$ drops to zero fast, while increasing $\lambda_1$ (left). Another way to see the sign problem is by checking correlations between the numerator and the denominator. The more often the numerator has different sign than the denominator, the stronger the sign problem is. Here, we plot for $\lambda_1 = 6.0$ (right). Note that we consider one factor of the factorisation formula Eq.(3.11). The expectation value of this factor thus is of order $\mathcal{O}(1)$ . . . . .	95

3.5	The Factorisation method as a mean to solve the “Overlap problem”. Schematically, the Factorisation method allows to conciliate the sampled distribution with the physical distribution, if we find a way to sample “intermediate” distributions (left). The toy model considered here does not suffer from an “overlap problem”: We sample preferably configurations $\{t\}$ , which are important for the oscillating, correct distribution. . . . .	96
3.6	The Contour Integral. The integrand stops oscillating around the saddle point. A deformed contour may help to reduce the “sign problem” substantially. Here, $\lambda = 2.0$ is plotted to increase the visibility. . . . .	97
3.7	The Contour Integral. We fix $y_0 = \frac{\lambda}{2}$ and vary $t_0$ . Although we vary $t_0$ in a huge range, the choice of $y_0 = \frac{\lambda}{2}$ seems not to extend the range of $\lambda$ measurable. . . . .	98
3.8	The Contour Integral. We fix $t_0 = 100$ and vary $y_0$ . For $\frac{\lambda}{6} \leq y_0 \leq \frac{\lambda}{4}$ , we can recover the analytic result at least up to $\lambda = 6$ . . . . .	99
3.9	The Contour Integral. The choice $y_0 = \frac{\lambda}{4}$ solves the “sign problem” for this toy model. . . . .	99
3.10	The Contour Integral. The numerator has small errors for $y_0 = \frac{\lambda}{2}$ (top left), while the denominator has small errors for $y_0 = \frac{\lambda}{20} \approx$ undeformed (top right). With the choice $y_0 = \frac{\lambda}{4}$ , we observe strong correlation between the numerator and the denominator in Eq.(3.22). We plot the case “positive numerator” (bottom left) and “negative numerator” (bottom right). . . . .	101
4.1	Simplified conjectured phase diagram of real-world QCD in the $(T, \mu)$ -plane (left), in the $(T, \rho)$ -plane (right). The dotted lines represent a crossover, the solid lines a first order phase transition. The single dots show the position of the second order critical endpoint. . . . .	105

4.2	The conjectured phase diagram in the plane of temperature $T$ and isospin chemical potential $\mu_{IS}$ . For an isospin chemical potential $\mu_{IS} > \frac{m_\pi}{2}$ a pion condensate is built. . . . .	107
4.3	Distribution of the complex Polyakov loop in the grand canonical (top) and canonical (bottom) ensembles in the volumes $4^3 \times 4$ (left), $6^3 \times 4$ (right). In the thermodynamic limit, the distributions agree for both ensembles, up to two additional $Z_3$ -rotations in the canonical ensemble. . . . .	110
4.4	Illustration of the Factorisation method. The ensemble at $\xi = 1.375$ is a critical ensemble. We want to combine it with an ensemble generated at $\mu = 0$ (equal $\xi = 1$ ). For a proper Ferrenberg-Swendsen reweighting, we have to ensure a good overlap by supplementing with two more ensembles at $\xi = 1.1$ and $\xi = 1.25$ . . . . .	125
4.5	The plot illustrates the hysteresis in $\rho(\mu)$ while crossing a first order transition. We start at zero chemical potential and increase it. Then, we start at large chemical potential and decrease it. Dashed, we plot the first derivative of the free energy, which typically shows an S-shape in the vicinity of a first order phase transition. . . . .	127
4.6	Susceptibility of $\bar{\psi}\psi$ versus $\beta$ for all volumes in both ensembles. left: $Z_{GC}(T, \mu = 0)$ , right: $Z_C(T, B = 0)$ . Even for the smallest, $4^4$ , lattice, differences are barely visible. . . . .	132
4.7	Binder cumulant minimum versus inverse volume for both ensembles (slightly shifted). left: plaquette, right: chiral condensate. The thermodynamic extrapolation does not tend to $\frac{2}{3}$ , indicating a first order transition. . . . .	133
4.8	$\frac{F(T, \mu_I)}{VT^4}$ as a function of $\frac{\mu_I}{T}$ at the temperatures $\frac{T}{T_c} \sim 0.9, 1.0, 1.1$ from left to right. The free energy density increases significantly while entering the high-temperature phase. . . . .	135



4.9	$\frac{F(T, \mu_I)}{VT^4}$ as a function of $\frac{\mu_I}{T}$ for $\frac{T}{T_c} \sim 0.9$ . The histogram method is very noisy. We show a rescaled version of the left plot in Fig. 4.8 (left). We also present results based on the reweighting method described in subsection 4.3.3 (right). The results are in agreement with the histogram method, but allow for a more reliable description by a Fourier expansion. The first coefficient is sufficient to describe the data points. The reweighting method calculation is expensive and has not been done for the $8^3 \times 4$ lattice. We thus draw the fit, which is based on histogram data. . . . .	135
4.10	$\frac{F(T, \mu_I)}{VT^4}$ as a function of $\frac{\mu_I}{T}$ for $\frac{T}{T_c} \sim 1.1$ . The histogram method (left). The reweighting method, however with $8^3 \times 4$ results from the histogram (right). We can describe the data points very accurately by the free gas Ansatz. With increasing volume, the Stefan-Boltzmann limit ( $T \rightarrow \infty$ ) is approached very quickly already at $\frac{T}{T_c} \sim 1.1$ due to the strong first order transition. . . . .	136
4.11	The importance $\Omega_C$ of various ensembles (see text) at temperature $T/T_c = 0.90$ ( $\beta = 4.98$ ), see Eq.(D.15) on page 197. In the $B = 0$ -sector, the confining ensembles around $\beta = 4.975$ contribute most (top). In the co-existence region ( $B = 8$ ) several ensembles contribute (middle). At large $B$ , only the ensembles sampled around criticality contribute (bottom). This reflects the overlap-problem: for $B = 14$ , we sample the quark-gluon plasma phase; ensembles in the confined regime have no information about this sector, hence only the ensembles sampled at around criticality contribute significantly. . . .	141
4.12	$-\frac{\Delta F(T, \mu)}{T^4}$ as a function of the temperature at fixed real chemical potential $\frac{\mu}{T} = 0.4, 0.8$ and $1.2$ . The Stefan-Boltzmann values incorporate finite volume and cut-off corrections of the free gas on the lattice. At $\frac{T}{T_c} = 1.1$ , the numerical values are about 30% smaller than the model calculation. . . . .	142

- 4.13 A sketch of our scan (left). The free energy at fixed baryon number as a function of the  $\beta/T$  (right). The vertical line indicates the critical temperature at  $B = 0$ . At low temperature, we deal with a system of weakly interacting heavy ( $m_B \gg T$ ) baryons  $F(T, B) \sim B$ , at high temperature we observe a weakly interacting gas of light ( $m_q \ll T$ ) quarks  $F(T, B) \sim B^2$ . . . . . 144
- 4.14 Strong coupling limit. We show  $F(\beta, B)/B$  for  $B = 1$  and  $B > 2$  (plateau). For  $B = 1$ ,  $F(\beta, B)/B = F(\beta, B)$ , we compare the free energy with predictions from a simple strong coupling Ansatz Eq.(4.73), labelled with “1-state” and “2-states”. The parameters  $c_0$  and  $c_1$  are obtained by a mediocre fit (not explicitly plotted). Further states are needed, which bend the strong-coupling prediction to lower values, thus the prediction will approach the lattice data.  $F(\beta, B)/B$  is also a crude approximation for the critical chemical potential[80]. We compare with predictions for the critical chemical potential at  $\beta = 0$  from Monte Carlo simulations and strong coupling calculations: “Monte Carlo, Karsch and Mutter”[106], “Nishida et al.”[107] and just recently “Kawamoto et al.”[108]. At  $B = 1$ , the interaction of the baryons is not included, which biases  $F(\beta, B)/B$  to larger values. At fixed  $\beta$ , a plateau in  $F(\beta, B)/B$  is reached at about  $B = 3$  already. We plot the particular plateau-values which are in between the various strong coupling calculations. . . . . 147
- 4.15 A sketch of our “scans” (left). The derivative of the free energy at fixed temperature as a function of the baryon number (density). In the saddle point approximation, the y-axis corresponds to  $\frac{\mu}{T}$  . . . . . 149
- 4.16 The Maxwell construction allows to extract the chemical potential, as well as the boundaries of the coexistence region. . . . . 151

4.17	The saddle point approximation in comparison with the fugacity expansion. The same critical chemical potential $\mu_c = 1.06(2)$ is indicated. However, the S-shape indicating the metastabilities is only visible via the saddle point approximation. . . . .	152
4.18	The phase diagram in the $T$ - $\mu$ -plane for four degenerate flavours of staggered quarks with $m_\pi \approx 350$ MeV. . . . .	153
4.19	The breakdown of statistical sampling. Here we show the weight of each configuration sampled at $\beta_c(\mu = 0)$ when we reweight to $(\beta = 4.94, a\mu = 0.35)$ . The two arrows mark the only relevant configurations (left). The phase boundary, obtained via reweighting, agrees with our new results, if we include ensembles with better overlap with the large $\mu$ -regime. Note, the lines are meant to guide the eye (right).	154
4.20	The phase diagram in the $T$ - $\rho$ -plane for four degenerate flavours of staggered quarks with $m_\pi \approx 350$ MeV. . . . .	155
4.21	The chiral condensate as a function of the temperature at $\mu = 0$ . The chiral symmetry is only approximate, hence there is a non-zero residual chiral condensate even at high temperature, $\langle \bar{\Psi}\Psi \rangle = 0.255(12)$ .	156
4.22	The chiral condensate as a function of the baryon number $B$ at $\frac{T}{T_c} = 0.94$ . The agreement of the residual chiral condensate at large baryon number with the one in the large-temperature regime at $B = 0$ (resp. $\mu = 0$ ) is an indication that the high-density regime can be identified with the quark-gluon plasma phase. The dotted lines, indicating the boundaries of the co-existence region, are taken from the previous subsection (via the Maxwell construction). . . . .	157
4.23	The plaquette expectation values as a function of the baryon number at fixed temperature $\frac{T}{T_c} \approx 0.92$ . The boundaries of the co-existence region are indicated with vertical delimiters. We equal the distance of the two horizontal lines with $\langle Pla_q(B_{max}) \rangle - \langle Pla_q(B_{min}) \rangle$ (left). The latent heat in a dimensionless ratio $\frac{L_h}{T^4}$ as a function of $\frac{T}{T_c}$ (right).	160

4.24	Illustration of the nucleation process. On a hypercubic lattice with periodic boundary condition, the two interfaces are planar (left). The area of the bump $A$ corresponds to the free energy needed to create two planar interfaces and allows to extract the interface tension. . . .	161
4.25	The reduced interface tension in physical units as a function of the temperature. . . . .	162
5.1	The order of the QCD phase transition from hadronic matter phase to the quark-gluon plasma phase in the plane of the degenerate “up/down”-quark masses $m_u = m_d$ , “strange”-quark mass $m_s$ and the chemical potential $\mu$ . The $N_f = 3$ line refers to the case of 3 degenerate quark flavours with mass $M$ . The blue $X$ refers to real-world physics, ie. physical quark masses. In our sketch, the vertical line pierces the surface of second order endpoints at a particular value of the chemical potential. If this QCD critical point indeed exists, such a positive curvature $\frac{\partial^2 M(\mu)}{\partial \mu^2} _{\mu=0}$ is likely. However, if the curvature is negative, there is no critical endpoint, which leads to exotic scenarios of the QCD phase diagram. In this work, we determine $\frac{M}{T}(\frac{\mu}{T})$ at large quark masses via the Potts model and show that the first order region shrinks under the influence of $\mu$ . . . . .	166
5.2	The Binder cumulant $B_4$ for magnetisation versus $h$ ( $h = h'$ ) (left). $B_4$ for magnetisation vs $h$ ( $h' = 0$ ) (right). . . . .	170
5.3	$\frac{M}{T}$ for second order transition versus $(\frac{\mu}{T})^2$ (left). $\frac{T}{M}$ for second order transition versus $\frac{\mu}{M}$ (right). . . . .	171
5.4	$\frac{M}{T}$ for second order transition versus $(\frac{\mu}{T})^2$ (left). schematic QCD phase diagram for 3 light quarks from [120] (right). . . . .	172

5.5	The chemical potential $\frac{\mu}{T}$ as a function of the baryon number $B$ on a $48^3$ lattice at mass $\frac{M}{T} = 8.8805$ (left), and on a $96^3$ lattice at mass $\frac{M}{T} = 9.028$ (right). The critical chemical potentials are indicated equivalently by the canonical approach and by the grand canonical framework. Note that at the smaller volume, the resolution of the density is coarse. . . . .	175
6.1	Dimensionless free energy per baryon, $T^{-1}F(B)/B$ , as a function of the baryon density in units of baryons per $\text{fm}^3$ . The lowest temperature is about 53 MeV. . . . .	181
6.2	Strong correlations between the individual measurements of $\hat{Z}_C(B)$ and $\hat{Z}_C(B - 1)$ on a given configuration are observed. Here, we show a particularly clear example at $B = 7$ , $\beta = 5.070$ , $\frac{m}{T} = 0.28$ . . . . .	182



# Acknowledgments

I would like to thank my supervisor, Dr. Philippe de Forcrand, for proposing such interesting projects to me, for his help and encouragement - and also for the pressure he sometimes put on me - throughout the whole time we were working together.

Many thanks to Prof. Dr. Matthias Troyer, for accepting me as his PhD-Student. I am very grateful for the computer resources he made available to me and enjoyed useful discussions.

It was a pleasure to share the office with various people, who have shown the patience to listen to my monologues and answered my questions thoroughly. In particular I thank Oliver Jahn, Michele Vettorazzo and Urs Wenger. All of the above were involved in the process of proofreading first drafts of the manuscript. I thank them and Urs Burch for having the nerves to do so.

The numerical simulations of this thesis have been performed on the Asgard and Hreidar Beowulf Clusters at ETH Zürich, and at the Minnesota Supercomputing Institute. I thank the respective staff for their kind and competent support, in particular George Sigut.

Finally, I will always remember the great time I had with my teammates and colleagues at the Institute for Theoretical Physics, ETHZ.

Financial support by the ETH Zürich is gratefully acknowledged.





### *Personal Data*

Name	Kratochvila, Slavo Borja
Date of birth	February 8th, 1976
Place of birth	Uster ZH, Switzerland
Nationality	Swiss
Marital status	Unmarried
Present address	Institute for Theoretical Physics ETH Zürich CH - 8093 Zürich-Hönggerberg Email: slavo@kratochvila.com

### *Schools*

1983 - 1989	Primary school, Schattdorf/Altdorf UR
1989 - 1996	Gymnasium, Kollegium Karl Borromäus, Altdorf UR

### *University*

1996 - 2001	ETH Zürich, Studies in Physics
2001	ETH Zürich, Diploma in Theoretical Physics “Testing Dimensional Reduction in non-abelian SU(2) Gauge Theory” Supervisor: Prof. Dr. Zoltan Kunszt and Dr. Philippe de Forcrand
2001 - 2005	ETH Zürich, PhD. student of Prof. Dr. Matthias Troyer “Extracting Physics from Weak Signals in Lattice Gauge Theory” Supervisor: Dr. Philippe de Forcrand

